Strain balanced epitaxial stacks of quantum dots and quantum posts

Diego Alonso Álvarez

Molecular Beam Epitaxy Group
Instituto de Microelectrónica de Madrid
Consejo Superior de Investigaciones Científicas

A thesis submitted for the degree of
Doctor of Physics

December 2011

Work supervised by:
Dr. Benito Alén Millán
Dr. José M. Ripalda Cobián

Disertation given at the Universidad Autonoma de Madrid

Contents

Abstract - Resumen

English version

Quantum nanostructures are a promising way of improving the performance of many optoelectronic devices. Due to the simplicity of integration with current semiconductor technology, one of the most common and studied nanostructures are InAs quantum dots (QDs) epitaxially grown on GaAs. These self-assembled QDs normally show excellent optical properties with strong light emission/absorption and well defined transition energies. The former is related with the quality of the material and the number of QDs present in the structure. The latter depends on the QD size, shape and composition. In some applications only one layer of QDs is needed in the device, such as in single photon emitters. Other devices, as it is the case of lasers, require from 3 to 10 QDs layers and, in general, they do not need to be very closely spaced. In these cases, the properties of each QDs layer can be controlled independently from each other and the accumulation of the elastic energy due to the lattice mismatch do not severely degrades the structure. On the contrary, infrared photodetectors and novel concepts such as the intermediate band solar cell, need the stacking of tenths or even hundreds of closely spaced QDs layers to have an appreciably electrical response to the incoming light. Under these conditions, QDs tend to pile up forming vertical columns, to electrically couple if the spacer is thin enough and to show an evolution in size and shape with each layer. Additionally, the elastic energy is typically relieved in the form of dislocations with the resulting material degradation.

One of the suggested methods to enable the fabrication of large stacks of QDs without material degradation and keeping good QDs homogeneity is using the strain balanced technique. This technique, originally developed for QWs, consist on introducing a material with smaller lattice parameter than the matrix between each QDs layer. In this way, the compressive stress introduced by the QDs is compensated by the tensile stress due to this layer, delaying the formation of dislocations. In GaAs, the materials that can compensate the stress of InAs QDs are different alloys of GaAsP, GaInP or GaAsN. In order to calculate the compensating layer composition and thickness, several criteria inherited from the strain balancing of QWs are normally used. However, this approach does not take into account

the 3D shape of these nanostructures nor the effect of the inhomogeneous strain fields in the formation of the compensating layer.

It is the motivation of this work to fully characterize and understand the strain balancing process of InAs QDs stacks using to that end the accumulated stress measurement monitoring as a novel and powerful approach to study this kind of materials.

The mechano-optical stress sensor (MOSS) technique is an in-situ and real time characterization technique that can be used, among other applications, during growth of InAs QDs to monitor the stress they introduce in the material. The technique is based on determining the stress accumulated on the sample by measuring its bending, using to that aim the deflection of two laser beams impinging on the sample surface. In our system, the sample has to be lever-shaped and fix from one of its ends to a special sample holder. An aperture of enough size made on the centre of the holder allows the lever to bend freely. The separation of the reflected spots at a certain distance from the sample surface can then be related with the stress accumulated in the sample.

The work we have done can be divided into three large parts. In the first part, we have used MOSS to characterize the stress that single InAs QDs and GaAsP layers accumulate. We have found that the stress that accumulates a QDs layer is well beyond the theoretical predictions, which clearly have a large impact into the strain balance criteria that relies on those predictions. Simulation of the process using a finite element method support this findings and corroborates, from an experimental point of view, the hypothesis made by several authors one decade ago about the In migration from the WL to the nanostructures assisted by the present strain fields.

Using the above calibration, we have been able of fabricating fully strain balanced QDs stacks monitoring, at the same time, the stress evolution of the sample using MOSS. Our results reveal that under perfect strain balanced conditions the stack actually degrades, leading to the lack of QD formation beyond certain layer and bad optical properties. Further work in this line using partly strain balance structures has led us to the conclusion that there is a strong interconnection between the inhomogeneous train fields created by the QDs, the compensating layer characteristics and the quality of the sample. We have found that the QDs

strain fields affect the formation of the compensating layer as much as they affect the formation of the next QDs layer. This is of particular relevance when using a compensating ternary alloy, as presented in the optimized stacks, where severe composition modulation is expected. In general these studies indicate that, on the contrary to strain balanced QWs, in QDs it is not enough to achieve a zero stress condition on average. Other factors, such as the compensating layer composition (binary or ternary alloy) and its position inside the spacer, critically affect the final material quality. We supported this findings with the fabrication of a stack of 50 InAs QDs layers which showed homogeneous nanostructure formation in the whole stack and relatively narrow photoluminescence emission. The success of this stack was consequence of the use of nominally pure GaP monolayers to achieve the compensation, in agreement to previous findings.

We then addressed the fabrication of quantum posts, which are the limit of vertically coupled QDs when the spacer between layers reduces to only few monolayers. This relatively new nanostructures present properties midway between those of QDs and quantum wires, their height can be controlled by varying the number of periods in a short period superlattice and, when embedded in a device, the fabrication processing follows the standard and mature techniques known for III-V semiconductor technology. The limit to their height is an excessive stress accumulation that can be partly relieved by using strain balancing techniques. Using this approach we have fabricated strain balanced InAs/GaAsP QPs 120 nm high, with low size dispersion and dislocation density as confirmed by transmission electron microscopy and their narrow photoluminescence emission spectrum. The vanishing vertical confinement in this nanostructures has an impact in the polarization of the light emitted/absorbed by them. Our QPs exhibit dominant transverse magnetic mode (TM) emission only for light emitted through one of the edges of the sample, in the [1-10] direction, being the transverse electric (TE) mode dominant in the other azimuth [110]. Unexpectedly, giant linear polarization is found for light emitted in the growth direction. The various effects that can contribute to the observed effect are the shape anisotropy of the QPs, lateral composition modulations in the matrix or the anisotropic nature of atomic bonds in the superlattice.

Finally, using MOSS to characterized the growth of QPs (non strain

balanced, in this case) has enabled the observation of an enhancement of the In detachment from the WL and its migration to the QPs themselves, where they introduce less stress. This phenomenon, observed as an inversion of the accumulated stress sequence during the InAs/GaAs growth, is closely related with the In segregation described above for QDs but enhanced by the strong strain fields present in this case, which is the main driving force during QPs growth, and the formation of a liquid-like phase at the sample surface.

In summary, in this work we have used the MOSS technique to characterize the growth of QDs, from single layers to stacks of strain balanced QDs and QPs of unprecedented height. In our studies we describe not only basic phenomena related to In migration process but also reveal the impact of the inhomogeneous strain fields created by the QDs in the formation of the strain balanced layer and also the extraordinary polarization properties of large QPs. These results not only contribute to the basic knowledge on the nanostructures but also serves as a starting point for the optimization and fabrication of strain balanced stacks with technological application.

Versión en español

La utilización de nanoestructuras cuánticas es un modo muy prometedor de mejorar las propiedades de muchos dispositivos optoelectrónicos. Debido a la sencillez que ofrecen de integrarse en la tecnología actual de semiconductores, uno de los sistemas mejor estudiados es el de puntos cuánticos (quantum dots, QDs) de InAs fabricados epitaxialmente sobre GaAs. Este tipo de QDs autoensamblados presentan habitualmente excelentres propiedades ópticas, con intensa emision/absorción de luz a energías bien definidas. Lo primero está relacionado con la calidad cristalina del material y el número de QDs presentes en la estructura. Lo segundo, por su parte, depende de la forma de los QDs, su composición y su tamaño. Para algunas aplicaciones, es suficiente con incluir una sola capa de QDs en la zona activa del dispositivo. Tal es el caso de los emisores de un solo fotón. Otras, como es el caso de los láseres, requieren el apilamiento de varias capas de nanoestructuras, de 3 a 10 típicamente, no siendo necesario además que estén especialmente juntas. En estos casos, las propiedades ópticas de las nanoestructuras en cada capa pueden controlarse de forma independiente y no se corre el peligro de que la acumulación excesiva de energía elástica degrade la estructura. Finalmente, otros dispositivos tales como los detectores de infrarrojo basados en QDs o dispositivos más novedosos como las células solares de banda intermedia, requieren para su funcionamiento el apilamiento de decenas o incluso cientos de capas de QDs poco separadas entre si con objeto de aumentar la respuesta eléctrica de la estructura a la luz incidente. En estas condiciones, los QDs tienden a apilarse formando columnas verticales, se acoplan electricamente y sufren una evolución de tamaños de capa en capa. Como resultado, la energía elástica acumulada tiende a relajarse mediante la formación de dislocaciones, resultando en una degradación del material.

Uno de los métodos sugeridos para permitir la fabricación de esos grandes apilamientos sin que se produzca la degradación del material es la técnica de compensación de tensión. Esta técnica, desarrollada originalmente para pozos cuánticos, consiste en introducir un material con menor parámetro de red que el substrato entre capa y capa de QDs. De este modo, la tensión compresiva que introducen estos se ve compensada por la tensión expansiva que introduce dicho material, retrasando la formación de dislocaciones en la estructura. En el caso de que el substrato sea GaAs,

diferentes materiales que pueden compensar la tensión que introducen los QDs de InAs son aleaciones diversas de GaAsP, GaInP o GaAsN. Con objeto de calcular la composición y espesor óptimos de la capa compensadora, históricamente se han utilizado varios criterios heredados de la compensación de pozos cuánticos. No obstante, estos criterios no tenían en cuenta la forma tridimensional de los QDs o el efecto de los campos de tensión inhomogeneos, algo que resulta de capital importancia, como veremos más adelante.

La motivación de este trabajo es, por lo tanto, caracterizar y entender integramente el proceso de compensación de QDs de InAs apilados usando para ello una novedosa aproximación consistente en monitorizar la tensión que se acumula en la muestra durante su fabricación.

La técnica del sensor de tensión mecano-óptico (mechano-optical stress sensor, MOSS) es una técnica de medida *in-situ* y en tiempo real cuya aplicación, entre otras muchas, es el monitorizado de la tensión que una capa de QDs de InAs introduce en el resto de la estructura. La técnica se basa en determinar la tensión que se acumula en la muestra midiendo su curvatura, usando para ello la deflexión de dos haces laser reflejados en su superficie. En nuestro sistema, la muestra debe tener forma de palanca y estar sujeta al portamuestras solo por un extremo. Este debe contar con un hueco en el medio que permita a la palanca curvarse sin restricciones. La separación existente entre los haces láser reflejados a cierta distancia de la muestra se puede relacionar, en estas condiciones, con la tensión que se acumula en ella.

El trabajo realizado se puede dividir en tres grandes bloques. En el primero, hemos usado la técnica MOSS para caracterizar la tensión que acumulan las capas de QDs de InAs y las capas compensadoras de GaAsP. Mediante estas medidas, hemos encontrado que la tensión que acumula una capa de QDs es mucho mayor que lo estimado teóricamente, con el impacto que esta discrepancia tiene, por lo tanto, en los criterios teóricos de compensación de tensión. La simulación del proceso usando un método de elementos finitos apoya estos resultados y corrobora, desde un punto de vista experimental, las hipotesis realizadas por varios autores hace casi una década sobre la presencia de procesos de migración de In desde la capa de mojado hacia los QDs, asistidos por sus campos de tensiones.

Usando esta calibración previa, hemos sido capaces de fabricar

apilamientos de QDs completamente compensados en tensión, monitorizando la evolución de dicha tensión mediante la técnica MOSS. Nuestros resultados revelan que incluso en condiciones de compensación perfectas, el apilamiento se degrada, dando lugar a la ausencia de formación de QDs más allá de cierta capa y a unas malas propiedades ópticas del material. Continuando el trabajo en esta línea usando estructuras parcialmente compensadas llegamos a la conclusión de que hay una estrecha relacción entre los campos de tensión inhomogeneos creados por los QDs, las características de la capa compensadora y la calidad de la muestra. Nuestros resultas indican que dichos campos inhomogeneous afectan la formación de la capa compensadora del mismo modo que afectan la formación de la siguiente capa de QDs. Este efecto cobra especial importancia si la capa compensadora es un compuesto ternario, tal y como utilizábamos en nuestras muestras, en cuyo caso sería esperable una severa modulación de composición en dicha capa. En general, estos estudios apuntan a que, contrariamente a lo que ocurre en pozos cuánticos, en QDs no es suficiente con lograr una compensación de tensión completa en promedio y que otros factores, como la composición (compuesto binartio o ternario) y posición de la capa compensadora dentro del espaciador, afectan criticamente a la calidad final del material. Estos resultados se han visto apoyados por la fabricación exitosa de un apilamiento de 50 capas de QDs de InAs, manteniendo una formación homogenea de las nanoestructuras a lo largo de todo el apilamiento y una emissión de fotoluminiscencia relativamente estrecha. El exito de este proceso ha sido consecuencia, precisamente, del uso de capas compensadoras muy delgadas y fabricadas nominalmente con un compuesto binario, el GaP.

También hemos estudiado la fabricación de postes cuánticos (quantum posts, QP) que son el límite de QDs acoplados verticalmente cuando el espaciador entre capas se reduce a solo unas pocas monocapas atómicas. Estas nanoestructuras, de relativamente reciente descubrimiento, presentan propiedades que se encuentran a medio camino entre las de los puntos cuánticos y los hilos cuánticos. Su altura puede ser controlada variando el número de periodos de la superred de la que surgen y, cuando están integrados en un dispositivo, su procesado utiliza técnicas bién conocidas de la tecnología de materiales semiconductores

III-V. El límite de altura que se puede conseguir viene definido, al igual que en los QDs, por una acumulación excesiva de tensión en la muestra, algo que puede paliarse mediante el uso de la técnica de compensación de tensión. Mediante esta aproximación, hemos fabricado QPs compensados de InAs/GaAsP con una altura de 120 nm, y una baja dispersión de tamaños y densidad de dislocaciones, según queda confirmado por las medidas del microscopio electrónico de transmisión y la estrecha emisión de fotoluminiscencia. El casi nulo confinamiento vertical de estas nanoestructuras tiene un gran impacto en las propiedades de la luz emitida/absorbida por estas nanoestructuras. Nuestros QPs presentan emisión dominada por el modo transversal magnético (TM) sólo para la luz emitida por uno de los bordes de la muestra, en la dirección [1-10], siendo el modo transversal eléctrico (TE) dominante en el otro acimut [110]. Sorprendentemente, la luz emitida en la dirección de crecimiento [001] se encuentra tremendamente polarizada, siendo casi lineal. Entre los efectos que consideramos pueden estar afectando a estos resultados se encuentra la anisotropía de forma de los QPs, modulación de composición en la matriz que los rodea y así como la presencia de enlaces aómicos anisótropos en las intercaras de la superred.

Finalmente hemos usado la técnica MOSS para caracterizar el crecimiento de QPs no compensados en tensión. En estas estructuras hemos observado un incremento del desprendimiento de átomos de In desde la capa de mojado y su migración hacia los QPs, donde introducen menos tensión. Este fenómeno, observado como una inversión en el la tensión acumulada durante el crecimiento del InAs, está claramente relacionado con la segregación de In mencionada más arriba pero aumentado, en este caso, tanto por la presencia de los campos de tensiones que son la fuerza motora para la formación de QPs, como por un fundido parcial de la superficie de la muestra.

En resumen, en este trabajo hemos usado la técnica MOSS para la caracterización de QDs y, de forma pionera, para el estudio de su apilamiento y compensación de tensión, dando lugar además a QPs con una longitud sin precedentes. Nuestros estudios no solo describen fenómenos de caracter fundamental, como los procesos de migración de In, sino también otros con interés tecnológico, como el impacto de los campos de deformación inhomogéneos en la formación de la capa compensadora de

tensión y las extraordinarias propiedades de polarización de los QPs. Como consecuencia, estos resultados no solo contribuyen al conocimiento básico sobre este tipo de nanoestructuras, sino que tamibién sirven como punto de partida para la optimización y el desarrollo de apilamientos compensados en tensión con interés tecnológico.

Acronyms

List of common acronyms used along this work. We include the Section where they are first mentioned or described.

Acronym	**Meaning**	**Sec.**
AFM	Atomic Force Microscopy	3.4
BEP	Beam Equivalent Pressure	2.1.1
CB	Conduction Band	3.1
CL	Compensating Layer	5.1
EL	Electroluminescence spectroscopy	3.2
FTIR	Fourier Transform Infrared spectroscopy	3.7
IBSC	Intermediate Band Solar Cell	5.7.1
IMM	Instituto de Microelectrónica de Madrid	1.6
MBE	Molecular Beam Epitaxy	2.1.1
MOSS	Mechano-Optical Stress Sensor	4.1
PC	Photocurrent spectroscopy	3.3
PECVD	Plasma Enhanced Chemical Vapour Deposition	2.2.2
PL	Photoluminescence spectroscopy	3.1
QD	Quantum Dot	1.2.1
QDIP	QD Infra-red Photodetector	1.1
QWR	Quantum wire	1.2.1
QW	Quantum well	1.2.1
QP	Quantum post	1.4
RHEED	Reflection Hight Energy Electron Diffraction	2.1.3
TE	Transverse Electric	6.1
TM	Transverse Magnetic	6.1
TRPL	Time Resolved Photoluminescence	3.1.1
UHV	Ultra High Vacuum	2.1.1
UCA	University of Cádiz	3.5
VB	Valence Band	3.1
VCQD	Vertically Coupled QDs	5.1
WL	Wetting layer	1.3.2
XRD	X-Ray Diffraction	3.6

Chapter 1

Introduction

Contents

1.1 A bit of history

In 1970, Esaki *et al.* proposed a new kind of materials based on periodic variations of alloy composition or of impurity density introduced during epitaxial growth of semiconductors. That variation, with a period on the order of 10 nm, was predicted to have a large impact into the electronic and optical properties of the material.[1]

And it was true: that was the birth of quantum semiconductor heterostructures.

It took very little time to researchers to envision the potential of these structures and to begin to study their properties. The most basic structure was named quantum well (QW) and consisted in a very thin layer of a low bandgap semiconductor sandwiched between two layers of another one with larger bandgap. It was shown that QWs had a very particular density of states due to the quantum confinement and that their emission wavelength could be easily tuned by varying the well thickness and/or composition. By 1982, Arakawa *et al.* had already suggested the use of the new materials in the active region of lasers to reduce the threshold current and the temperature dependence.[2]

But QWs were only the beginning. Further research performed in the 80's naturally lead to the discovery and development of quantum dots (QDs), nanostructures with quantum confinement in the three spatial directions and with discrete energy levels and density of states.

The first QDs were made of CdS, as colloids in a liquid solution, and of CuCl, as the result of a phase decomposition in a supersaturated glass. [3, 4] The exploitation of epitaxial techniques to fabricate QDs in semiconductor monocrystals meant another breakthrough in semiconductor technology. This approach allowed to include QDs in optoelectronic devices, such as lasers, further reducing their threshold current.

The potential range applications of all these quantum nanostrucutures is enormous. Some technologies are already mature and being mass produced, such as quantum well or dot lasers for telecomunications. Others are almost ready to be released, such as QDs infrared photodetectors and optical amplifiers. Finally, many are in the earliest stage of development and need further research to fulfil the expectations, as it is the case of QDs for quantum information technologies and for next generation solar cells.

Depending on the application, it might be enough to include only one QD into the device, as it is the case of single photon emitters. For such devices, one of the problems to be solved is to place the QD with the correct properties (emission wavelength, intensity...) in the correct position in order to couple the emitted radiation to a photonic cavity or to a waveguide, for example.[5, 6]

For memory devices, where the goal is to store information, one probably wants a single layer of QDs with long lifetimes. This means that electrons and holes that represent the stored information must be kept inside the nanostructure very long time until they are "read".[7, 8]

However, these single layer or single QD applications are the least common. Most of the time, several layers of QDs are needed to get the desired effect. In QDs lasers, for example, from three to ten QDs layers are typically grown in a stack as the active material. The stack is then confined by cladding layers and Bragg reflectors to obtain the light amplification.[9–11]

The same can be applied to quantum dot infrared photodetectors (QDIPs), which exploit their intraband absorption properties. That intraband absorption for normal incident light is forbidden in QWs but it might be very intense in QDs. Nevertheless, electrical response to incoming light scales with the number of layers and to have an appreciably signal QDIPs with up to 70 QDs layers have been reported.[12] We will discuss later the selection rules for light absorption in quantum heterostructures.

Finally, advanced solar cell concepts, such as the intermediate band solar cell (IBSC), have the very same requirements as infrared photodetectors but with the extra handicap of having to extract the photogenerated carriers without any extra applied bias, simply by diffusion.

As shown by Ng *et al.*, stacking QDs leads to a severe degradation of the material with the formation of threading dislocations and "volcano like" structures.[13] This is a consequence of the lattice mismatch between the QDs material and the substrate that increases elastic energy of the structure, layer after layer, until it is released producing plastic relaxation.

The effect is also present in strained QWs, as shown by Matthews and Blakeslee, setting a critical thickness that a stack can reach before the formation of dislocations.[14] In QDs this effect might become worse because of the 3D shape of the nanostrcutures, that introduces an inhomogeneous component in the strain. This leads to the surface undulation and the "volcano like" structures mentioned before.

There are, essentially, four approaches to overcome this limitation. The first one, the most obvious, is to use only few QDs layers so the critical thickness for plastic relaxation is not reached. This might be reasonable for

lasers, where five layers are normally enough, but not for phototedectors or solar cells. The second option is to use large spacers between the QDs layers. This solution relies in that the strain introduced by a QDs layer can be accommodated by the surrounding crystal matrix if this is large enough to avoid the interaction with the following QDs layer. This can be an appropriate solution in QDIPs, where there is an applied voltage that helps the photogenerated carriers to reach the electric contacts, but in solar cells this collection relies on the free diffusion of those carriers. If the stack is very large, it will be more probable for the carriers to find a trap (a QD or a defect, for example) than to reach the electric contact within their diffusion length. An additional possibility is using lower In content QDs, which intrinsically introduces less stress to the sample. This can be done by directly growing InGaAs QDs or using more advanced approaches such as submonolayer QDs.[15]

Finally, the last option is to apply a strain balanced technique to compensate the compressive strain introduced by the QDs with a tensile strain in the spacer. This technique is explained in detail in Section 1.5 and has being extensively used with QWs. The extension of the technique to the QDs constitutes the core of the work presented here.

1.2 From bulk to QDs

All the properties of quantum nanostructures have their origin into their reduced size in one or more directions. This small size combined with the difference in the bandgaps of the materials of the nanostructure and the matrix allows a precise control of the emission wavelength, intensity or polarization. In this section and the next one we introduce some basic concepts about quantum nanostructures, in particular about quantum dots, that will be useful in following chapters.

1.2.1 Quantum confinement

The most basic nanostructure is a type-I quantum well. As mentioned before, it forms when a low bangap semiconductor layer is sandwiched between two layers of a higher bandgap material. Electrons and holes are then confined in the low bandgap material unless some energy is provided

to overcome the barrier potential (rising the temperature, for example). To have quantum effects, the thickness of the QW must be on the order (or smaller) than the de Broglie wavelength of carriers in that material:

$$\lambda = \frac{\hbar}{\sqrt{3m^* k_b T}} \tag{1.1}$$

where $\hbar$ is the Plank's constant, k_B is the Boltzmann's constant, T is the temperature and m^* is the effective mass of the carrier (electron or hole). In most semiconductors, m^* is smaller than the free electron mass, m_0. As an example, for GaAs $m_e^* = 0.067m_0$ and $m_{hh}^* = 0.5m_0$. This indicates that the de Broglie wavelengths are in the range 10 to 100 nm at low temperatures.

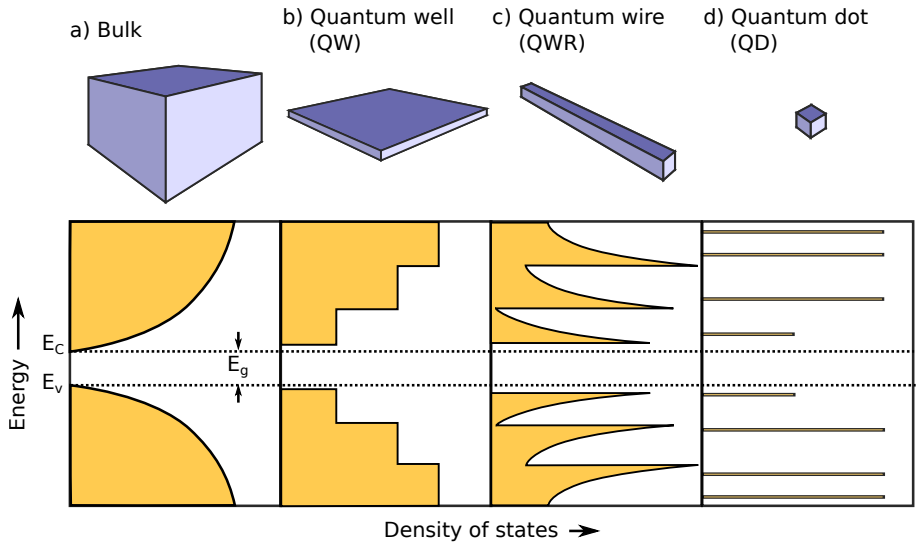

Figure 1.1: Schematic representation of the density of states as a function of energy for the four basic structures: a) bulk, b) QW, c)QWR and d) QD. Shaded areas correspond to available electronic states in each system. Image adapted from Ref. [16].

If this is fulfilled, the density of states as a function of the energy change from the smooth dependence in bulk materials to a stepped shape (Figure 1.1a and b, respectively). When quantum confinement takes place in two directions, then the nanostructure is called quantum wire (QWR)

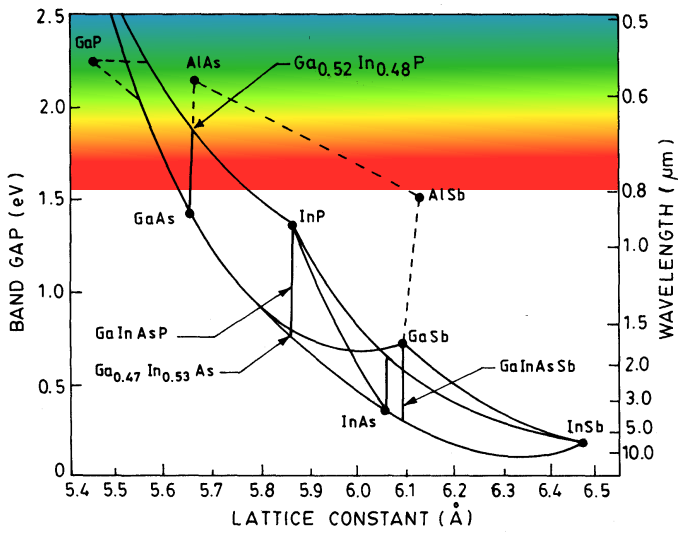

Figure 1.2: Bandgap of most important semiconductors as a function of their lattice parameter. Image adapted from Ref. [17].

and the density of states becomes spiky (Figure 1.1c). Finally, when the confinement happens in the three spatial dimensions, we talk about quantum dots, which present isolated energy levels (Figure 1.1d). This clear energy splitting between confined states is which makes QDs such intriguing and useful nanostructures, also receiving for this reason the name of "artificial atoms".

1.2.2 Semiconductor heterostructures

Bulk semiconductor materials, among which are the III-V compounds, are very well studied. The two most important properties are their bandgap energy and their lattice parameter. Figure 1.2 shows the relationship between those two magnitudes for some materials. The importance of this relationship became more important after Esaki's pioneer work. Combining two materials with different bandgap allows, among other possibilities, to control the carrier confinement or to design waveguides by varying periodically the refraction index. Yet the choice of materials to be combined is limited by their lattice parameter.

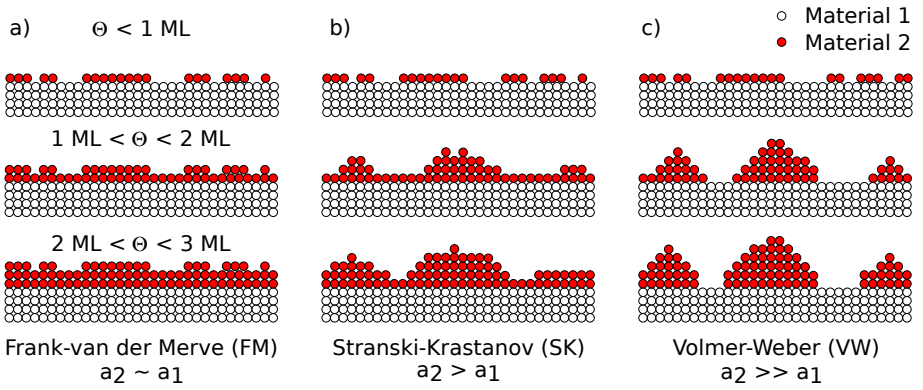

Figure 1.3: The three growth modes, depending on the lattice parameter between the two materials involved in the heterostructure. Image adapted from Ref. [16]

We can divide the heteroepitaxial systems into those formed by two components with similar lattice parameter (lattice matched materials) and those with different lattice parameter (lattice mismatched materials). The former have been the most extensively used since they lack of the inconvenience of the stresses accumulated in the interfaces of mismatched materials. However, semiconductor heterostructures must be grown over substrates, and those commercially available with high quality are limited to only a few materials (GaAs, GaSb, InP, Si...), making unavoidable to work with lattice mismatched materials.

The way a mismatched heteroepitaxy proceeds is determined by a trade-off between the surface energy of the deposited layer, the interface and the substrate, as well as the lattice mismatch of the materials involved. If the sum of the surface and interface energies is smaller than the surface energy of the substrate, then the growth proceeds layer-by-layer and it is known as Frank-van der Merve (FM) growth mode (Figure 1.3a). This is the case when $Ga_{0.47}In_{0.53}As$ grows on InP or when $Ga_{0.52}In_{0.48}P$ grows on GaAs.

When the heteroepitaxy takes place between materials with different lattice parameters, the growth is initially layer-by-layer and then changes to the 3D island formation. In this kind of growth, known as Stranski-Krastanow (SK) growth mode, the epitaxial layer adapts its

lattice parameter to that of the substrate, increasing the elastic energy until it reaches a critical value, when there is a relaxation of the surface (Figure 1.3a). If this process is plastic it leads to the formation of dislocations along the interface. On the other hand, if it is elastic, then it leads to the formation of coherent 3D islands, defect free. When the size of those 3D nuclei reaches several nanometers, then we talk about self-assembled nanostructures. If they are surrounded by a semicondcutor material of larger bandgap and have a size smaller than the de Broglie wavelength of carriers in that material (Equation 1.1), we talk about self assembled quantum dots or wires, depending on their general shape. An example of this would be the growth of InAs on GaAs with a lattice mismatch of $\sim$7%.

Finally, if the substrate surface energy is smaller than the sum of the layer and interface energies, then the growth leads from the beginning to the formation of three dimensional islands (Volmer-Weber growth mode, VW) (see Figure 1.3c). This is the case of InAs grown on GaP, where the lattice mismatch is 11%.

In the following section there is a detailed description of several methods used to fabricate quantum dots.

1.3 The QDs basics

In this section we review, from a basic point of view, the process of fabricating QDs and some concepts about quantum confinement in these 0D nanostructures using the harmonic oscillator model.

In a very rough classification, there are two ways of fabricating QDs: using colloidal or epitaxial techniques. Although this work has been done exclusively using the second approach, we will briefly comment the first one because of its large impact in science, industry and economy.

1.3.1 Colloidal QDs

Colloidal QDs are obtained from a wet chemical process from a precursor material. There are many materials that can be used to form QDs, being the most common the II-VI semiconductors: CdSe, CdS, ZnO, ZnS or PbS.[19, 20] Recent advances in synthesis methods have allowed to obtain

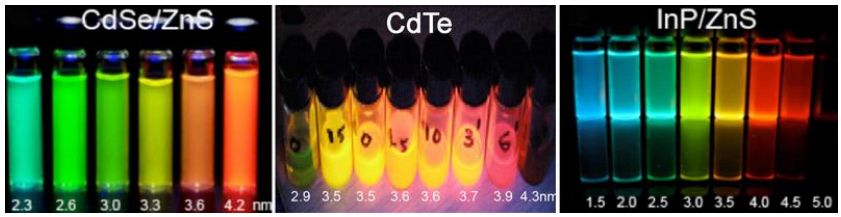

Figure 1.4: Colloidal QDs of different materials and sizes, showing the variety of emission wavelengths in the visible range. Image adapted from Ref. [18].

structures formed by a core of one material covered by another one, called shell. This core-shell QDs combine two materials such as HgS/CdS, InAs/InP or even a mix of III-V/II-VI semiconductors, as it is the case of structures formed by InAs/CdSe.[21] The quantum efficiency of devices with these core-shell QDs in the active region is much higher because the shell avoids non-radiative recombination in surface states.

The size of colloidal QDs ranges from 1 to 10 nm and they are generally spherical, although the exact geometry depends on the synthesis conditions. The size control allows to tune the emission properties of the CdSe QDs in the whole visible range and that of PbSe, PbS, or CdTe in the near infrarred (Figure 1.4).

Currently, the main application of these QDs is in light emitting devices (LEDs), a mature technology that is already in the production line. Another application that has devoted much attention is its use as cell markers and contrast agents in medical applications through a bio-functionalization of the QDs.[18, 22, 23]

Despite the large interest and effort in using these QDs in solid state optoelectronic devices, such as lasers and high efficient solar cells, the success has been very limited due to the need of high quality, monolithic crystals to avoid loses.[24]

1.3.2 Epitaxial QDs

QDs from QWs

The first technique developed to obtain epitaxial QDs is based on including a lateral confinement in QWs by using lithographic techniques. The main advantage is the ability to chose the position and size of the QD (within

the system resolution) and the compatibility of these techniques with the large scale integration processes of semiconductor devices found in the industry. On the other hand, it implies several problems such as sample erosion during the etching process (whether dry or wet), changes in the material stoichiometry or the formation of surface states, all of them with a detrimental effect in the QDs luminescence.[25]

Another approach, using AlGaAs/GaAs QWs as the base material, consist on irradiating the sample with high energy laser pulses that lead to the interdifusion of materials. The laser pulse produces the melt and recristalization of the material on a local scale, leading to well defined interfaces that separate the regions with and without interdifusion, the quantum dots. This process affects the quality of the material and, generally, produces point defects.[25]

Finally, it is possible to create QDs from QWs using highly strained layers and a pattern carved on the surface. Due to the variation of the strain field, this structures results in local lateral confinement in the QW. Despite the absence of defects, the degree of confinement is very small and QWs must be place near the surface to be affected by the pattern, which increases the recombination probability of carrier in surface states.[26] In the same line, it is possible to use self-assembled QDs, described below, to create the strain field that produces lateral confinemetent in a QW placed above them.[27]

QDs from QWRs

Following the ideas set in the previous paragraphs of increasing the confinement in systems with larger degrees of freedom, it is also possible to form QDs from QWRs. In recent years, a very efficient method has been developed to grow QWRs from a metalic particle that works as catalyst. In this system, the QDs are formed by varying the QWR composition as the growth proceeds. In this way, it has been reported GaAsP QDs embeded in GaP nanowires and LEDs based on InP with an InAsP QD in the active region.[28]

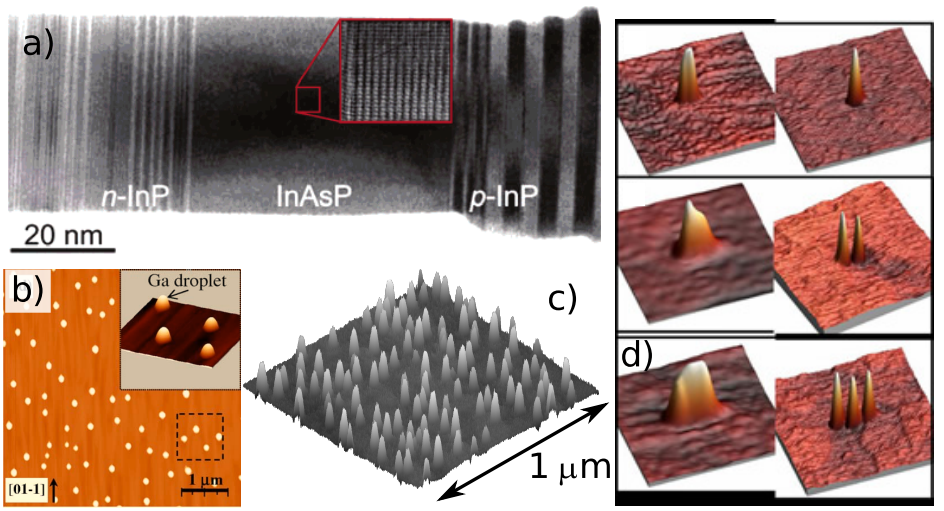

Figure 1.5: Examples of epitaxial quantum dots fabricated with different methods. a) From a QWR [28], b) using droplet epitaxy [29], c) SK quantum dots and d) QDs grown on patterned substrates [31].

Droplet QDs

Quantum dots can also be fabricated from metallic droplets made of Ga, In, Al... The growth of these droplets follows the VM growth mode at low temperature and with a III/V flux ratio very high. After the droplet formation, they are crystallized using a flux of the group V element, changing from an amorphous structure to a zinc-blende crystal. The optical properties of these nanostrcutures are comparable to those fabricated using the SK method.[29] Using this approach, QDs made of GaAs/AlGaAs or InAs/GaAs have been fabricated.[29, 30]

Stransky-Krastanow QDs

However, the most extended QDs fabrication method is based in the Stransky -Krastanow growth mode which, as explained above, depends on the materials lattice mismatch. The InAs/GaAs system is, by far, the better studied combination with a lattice mismatch of 7%. In this case, the critical thickness is around 1,65 ML of InAs at a substrate temperature of 510°C and the relaxation process produces nanometre sized islands.

These islands are spread randomly in the sample surface and although they usually have some average characteristics, there is always a certain dispersion in their size, shape and/or composition.

Once covered, the SK QDs do not suffer from the problems associated with other methods of defects or surface state recombination. This method of fabrication has the particularity that all the QDs are connected by an In(Ga)As layer at their base. This bidimensional structure consist on only few monolayers that behaves as a very thin QW and that is called wetting layer (WL).

One important process during the growth of InAs/GaAs QDs is the intermixing of atomic spices with the substrate and the capping. For this reason, nominally pure InAs QDs are actually In(Ga)As alloys with varying composition along the growth axis. Studies performed with cross section scanning tunnel microscopy (x-STM) have shown that In concentration is smaller in the base of the QD (80%) than in the apex (∼100%).[32]

Another important property of these QDs is its surface density. Depending on the application it might be convenient to work with ensembles of high or low densities. In lasers or solar cells, for example, it is required to have densities on the order of 10^{10} cm^{-2} or larger. On the contrary, in micro-photoluminescence experiments it is convenient to have much lower densities, around 10^{8} cm^{-2}, in order to study the properties of individual QDs. The surface density of QDs can be varied from 10^{11} cm^{-2} to 10^{8} cm^{-2}, depending on the growth conditions: substrate temperature, growth rate and amount of deposited material.

QDs grown on patterned substrates

Closely related with the SK QDs are the QDs grown in patterned substrates. In this case, prior to the QDs fabrication, the sample surface is patterned with the desired motifs that will act as preferential nucleation sites for the QDs. These motifs are commonly carved either by local or large area oxidation techniques.[31, 33] The advantage over the self-assembled process is that QDs distribution and density is fixed to that of the pattern and that their size and shape can be controlled to some extend by varying the properties of the pattern (depth and width of the holes, orientation...).

1.3.3 The harmonic oscillator model

To describe the energy levels of QDs, there are many theoretical models which take into account aspects so important for the quantum confinement as the size, shape, the stoichiometry or the strain fields. However, the basic properties of the QDs can be discussed in a very simple way using an harmonic oscillator potential in the effective mass approximation:

$$V_{QD} = \frac{1}{2} m^* \Sigma_{i=x,y,z} \omega_i^2 i^2 \tag{1.2}$$

where m^* is the electron or heavy hole effective mass and ω_i is the oscillator frequency for each of the spatial directions (we can assign x and y to the crystallographic directions [110] and [1-10], and z to the grow direction [001]). The hamiltonian of a carrier confined by the potential defined in Equation 1.2 is separable,

$$H = \frac{p^2}{2m^*} + V_{QD} \tag{1.3}$$

and can be solved easily to obtain the energy level structure:

$$E_C(n_i) = \Sigma_{i=x,y,z} \left(\frac{1}{2} + n_i \right) \hbar\omega_i, \qquad n_i = 0, 1, 2... \tag{1.4}$$

The energy levels defined by Equation 1.4 describe quite accurately the emission spectrum obtained from colloidal QDs, which have a spherical symmetry and in which the electronic structure mainly depends on the quantum confinement.[34] However, QDs growth by the SK mode are not spherical and the strain fields play an important role into the band mixing and position of the energy levels. As it is found in the literature, epitaxial QDs more commonly have the shape of a truncate pyramid, disks or lenses.[35–37] All of them have in common that the size in the growth direction (h) is much smaller than in the plane (d). Typical aspect ratios (h/d) for InAs/GaAs QDs range from 0.3 to 0.1. In these cases, it is necessary to use more advanced models, such as 8×8 $\boldsymbol{k} \cdot \boldsymbol{p}$ or pseudopotential methods, in order to reproduce the experimental results.[38] Nevertheless, although the application of the previous parabolic model needs to be restricted (at most) to describe the potential in the plane

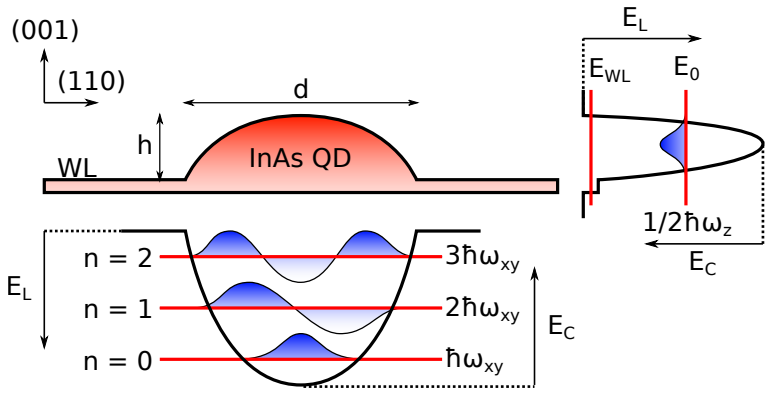

Figure 1.6: Schematic representation of the harmonic oscillator model.

and not in the growth direction, the general qualitative information it gives still applies and we can further discuss QDs properties based on it.

In Figure 1.6 we show an schematic representation of the harmonic oscillator model. In the growth direction [001] there is only one confined level with energy E_0 dependent on the QD height (h) and the depth of the potential well formed by the InAs in a GaAs matrix. The larger the height of the QDs, the larger would be localization energy (E_L) of the level (or, conversely, smaller $\hbar\omega_z$). On the contrary, when h is small, the localization energy of the ground state becomes very small, getting closer to the band edge, and the separation of the allowed states also increases. This has important consequences in the behaviour of devices with QDs in their active region: small QDs will suffer more severely the effect of thermal scape.

The confinement in the plane would be given by a two dimensional parabolic potential. The bond states of this potential define the spectral positions of the excited states of the carriers confined in the QD. The value of these states depends on the diameter of the nanostructure (in general, large d gives smaller $\hbar\omega$). They are usually closer to the conduction band than to the valence band since the effective mass of electrons is much smaller, although this depends on the corresponding band offsets. The lowest three states have energies $\hbar\omega$, $2\hbar\omega$ and $3\hbar\omega$ and a degeneracy (having into account the spin) of 2, 4 and 6.

The QDs size has also an important effect in the inhomogeneous

broadening of the photoluminescene emission bands in QDs ensembles. If there is a wide dispersion of sizes, the bands broaden due to the different position of the energy levels in each QD.

Lei *et al.* have recently measured the localization energy with respect the conduction (valence) band of electrons (holes) confined in InAs/GaAs QDs grown by MBE emitting at 1.04 eV at low temperature.[39] The values they have found using capacitance-voltage spectroscopy are 269 meV for electrons and 185 meV for holes. This same work shows that the separation between the allowed states in their QDs is $\hbar\omega = 8$ meV in the valence band and $\hbar\omega = 48$ meV in the conduction band. Similar results were obtained by Granados *et al.* finding 230 meV confinement energy for electrons ground state and $\hbar\omega = 70$ meV for the state separation, suggesting smaller size QDs.[40]

1.4 The aspect ratio of QDs

Quantum well infrared photodetectors (QWIPs) have been fabricated and have many advantages over other technologies. however, they also suffer from some drawbacks, being the most important that intraband (or inter-subband) absorption for normal incident light (perpendicular to the QW plane) is forbidden in the conduction band.[38] As a consequence of this, it is necessary to use complicated geometries to make the incoming radiation to reach the QWs by one of the edges, not from the plane, in order to exploit that intraband absorption.[41]

The fabrication of infrared photodetectors and intermediate band solar cells, both of which rely on the strength of this transition to work, strongly benefits thus by the development of QDs technology. In these nanostructures, intraband transitions between conduction band levels are allowed for normal incident light, contrary to the QWs, consequence mainly on the band mixing that takes place.

However, despite the promise of a very high performance of these QDs mid infrared devices (QDIPs and IBSC), there are several issues that are still unresolved. Apart to the need of stacking many QDs layers already commented, they have in common that *realistic QDs* do have to be sensitive to normal incident radiation, which is not always the case.

This assessment is true for colloidal QDs due to its small and almost

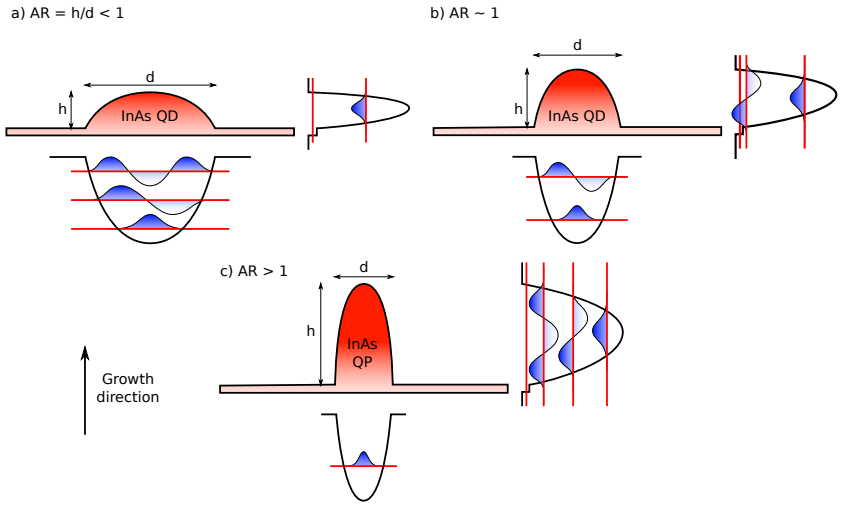

Figure 1.7: Change in the energy levels diagram for different shaped QDs. a) Standard SK QDs. b) QDs as high as wide. c) Larger-than-one AR QDs, or QPs.

perfectly spherical shape. But SK QDs are normally very shallow, with aspect ratios of 0.3 at most, normally smaller. This shallow shape reduces the band mixing and hence the strength of the intraband absorption. As a result, it is experimentally found that in typical SK QDs the absorption is normally greatly reduced compared with the case light propagates in the plane, as it has been shown in InAs/GaAs QDs.[42, 43] Moreover, in the limiting case, that absorption becomes indistinguishable from that observed in QWs, as it has been found in Ge/Si QDs superlattices.[44]

In the light of these results it seems necessary to modify the QDs from a shallow, lens-like shape (Figure 1.7a) to a narrow, columnar-like, structure (Figure 1.7c). In other words, to invert the aspect ratio of the QDs while keeping a reduced lateral size.

Achieving this new shape with standard self assembled techniques as those described in Section 1.3.2 is basically impossible. However, there is a relatively recent growth procedure that allows to grow this kind of vertical QDs and that might be the answer to boost the mid infrared response of these devices.

The technique consists on growing a very short period superlattice (SL) on top of a QDs layer (lets assume an InAs/GaAs SL on top of

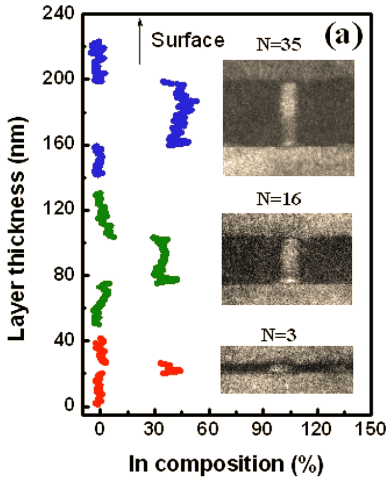

Figure 1.8: QPs of different heights as a function of the number of periods of the SL (N) and the In content of the QPs. Image adapted from Ref. [45]

InAs QDs).[45] Due to the strong strain fields generated by the InAs QDs, In adatoms of the SL will migrate towards the top of a buried QD. The resulting structure are In-rich columns surrounded by a Ga-rich matrix. The height of these quantum posts (QPs, also called quantum rods or nanorods) is controlled by the number of periods of the SL and the lateral dimension by the size of the QDs of the seed and the relative thickness of the InAs and GaAs layers of the SL (Figure 1.8). In many aspects, QPs can be seen as the limit of stacked QDs when the spacer between the layers is reduced to few monolayers.

The possible benefits of QPs do not limit to the enhanced intraband absorption, something that is not yet demonstrated. Most of the research performed so far in QPs has been focused into their polarization properties, which might be exploited in the fabrication of polarization controlled semiconductor optical amplifiers (SOAs).[45, 46] A final issue that has attracted much attention is that they are predicted to have very large radiative lifetimes, in which case they could be used for storage applications.[8]

More details about the fabrication of QPs and their properties in the framework of strain balanced materials will be discussed in Chapter 6.

1.5 Strain compensation

Strain compensation (strain balancing or strain symmetrization, as it is also known) is a technique to growth heterostructures of materials with different lattice parameter while keeping good crystal quality. It consist on alternating the growth of a material under compressive stress with another one under tensile stress. As it is shown below, this kind of structure leads to a situation where the average in-plain stress is zero and the formation of defects is mitigated.

The technique was first used by Miller *et al.* in 1991 to improve the quality of InGaAs multiple quantum well (MQW) lasers grown on InP.[47] Miller intentionally introduced a tensile strain in the barriers between QWs improving the material quality when a large number of QWs were grown. They demonstrated that following this scheme, the PL signal of a compensated sample was narrower and twice as intense as that of an uncompensated structure.

The research in this strain balanced structures was very intense during the 90's, leading to a large improvement of the quality of MQWs for laser applications.[48, 49] However, the number of stacked QWs that were used in these works was very small and the strain balanced process was, to a large extent, a trial-and-error method using the PL intensity and x-ray diffraction measurements as figures of merit to asses the quality of the structures.

The first mathematical estimation of the appropriate strain balanced condition was performed by Dutta *el al.*, using an equivalent strain thickness products for the QW and barrier materials. In its basic form, this "thickness weighted" (TW) condition can be expressed as [49]:

$$t_b\epsilon_b + t_{QW}\epsilon_{QW} = 0 \tag{1.5}$$

where t_b, t_{QW}, ϵ_b and ϵ_{QW} are the barrier and quantum well thicknesses and lattice mismatch, respectively. The latter is defined as:

$$\epsilon_{b(QW)} = \frac{a_{b(QW)} - a_{subs}}{a_{b(QW)}} \tag{1.6}$$

with a_b, a_{QW} and a_{subs} the barrier, quantum well and substrate unstrained lattice parameters, respectively.

In 1999, Ekins-Daukes *et al.* introduced a more simple mathematical formalism for the process, searching for a way to increase the number and quality of InGaAs QWs in a solar cell.[50] In his work, Ekins-Daukes considered as criterion to achieve the complete strain compensation in a MQW structure to have an average lattice parameter in the superlattice $\langle a \rangle$ equal to that of the substrate:

$$\langle a \rangle = \frac{t_b a_b - t_{QW} a_{QW}}{t_b + t_{QW}} = a_{subs} \tag{1.7}$$

This criterion, called "average lattice" (AL), also led to a large improvement of the material quality, the reduction of the dark current of the solar cell and, in general, to an unprecedented performance in this kind of devices.

Despite the success of this method, in 2002, Ekins-Daukes reviewed the strain-balance condition, considering two other criteria that might better describe the perfect strain symetrization.[51] The first one was Dutta's criterion, modified to include a dependence on the material elastic constants (hereafter named "modified thickness weighted" (MTW)):

$$A_b t_b \epsilon_b + A_{QW} t_{QW} \epsilon_{QW} = 0 \tag{1.8}$$

where $A_{b(QW)}$ depends on the stiffness coeficients (c_{ij}) and takes the following form in cubic lattice materials (GaAs, InAs, InP...):

$$A = c_{11} + c_{12} + 2\frac{c_{12}^2}{c_{11}} \tag{1.9}$$

The second criterion introduced by Ekins-Daukes was based on the requirement to achieve zero average in-plane stress in the tensile/compressive strained layer combination. To this aim, he calculated the strain energy of the two layer combination using classical elasticity theory and then derived an expression for the zero in-plane stress (ZS) condition. Assuming that the material has a cubic crystal structure and that the layers are pseudomorphically strained onto an (001) surface, then the strain elastic energy density (U) of one of the layers can be expressed as:

$$U = \left[c_{11} + c_{12} + 2\frac{c_{12}^2}{c_{11}} \right] \epsilon^2 = A\epsilon^2 \tag{1.10}$$

Table 1.1: Different criteria used to evaluate the strain balanced condition.

Criterion	Equation	Ref.
Average Lattice (AL)	$t_b a_b - t_{QW} a_{QW} = (t_b + t_{QW}) a_{subs}$	[50]
Thickness Weighted (TW)	$t_b \epsilon_b + t_{QW} \epsilon_{QW} = 0$	[49]
Modified TW (MTW)	$A_b t_b \epsilon_b + A_{QW} t_{QW} \epsilon_{QW} = 0$	[51]
Zero Stress (ZS)	$A_b \epsilon_b t_b a_{QW} + A_{QW} \epsilon_{QW} t_{QW} a_b = 0$	[51]

and the average strain energy density in the barrier/QW combination:

$$\langle U \rangle = \frac{U_b t_b + U_{QW} t_{QW}}{t_b + t_{QW}} = \frac{A_b \epsilon_b^2 t_b + A_{QW} \epsilon_{QW}^2 t_{QW}}{t_b + t_{QW}} \tag{1.11}$$

The in-plane stress can be obtained by differentiating $\langle U \rangle$ with respect the strain in one layer, ϵ_b or ϵ_{QW}. Since the layers are grown pseudomorphically, using Equation 1.6 it can be seen that the two strains are related by:

$$\epsilon_{QW} = \frac{a_b}{a_{QW}} \epsilon_b + \frac{a_b - a_{QW}}{a_{QW}} \tag{1.12}$$

The in-plain stress results in:

$$X = \frac{\partial \langle U \rangle}{\partial \epsilon_b} = \frac{2}{t_b + t_{QW}} \left(A_b \epsilon_b t_b + A_{QW} \epsilon_{QW} t_{QW} \frac{a_b}{a_{QW}} \right) \tag{1.13}$$

And the zero in-plane stress condition, $X = 0$:

$$A_b \epsilon_b t_b a_{QW} + A_{QW} \epsilon_{QW} t_{QW} a_b = 0 \tag{1.14}$$

It should be noted that in deriving Equation 1.13 it is assumed that the layer thicknesses do not depend on the strain, something that is not strictly true, in general. Table 1.1 summarizes the four criteria, each of them leading to different combination of composition and thicknesses for the barrier and the QWs.

To get a quantitative idea of the differences among the criteria, we have calculated the thickness of a $GaAs_{1-x}P_x$ barrier needed to compensate a 8 ML thick $In_{0.2}Ga_{0.8}As$ QW grown on a GaAs (001) substrate. The P content of the barrier is varied from $x = 0$ (no compensation) to $x = 1$

(pure GaP). As it can be seen in Figure 1.9, there are two clear tendencies: AL and TW on one hand; MTW and ZS, on the other. This difference is the direct consequence of taking into account the elastic constants of the barrier and the QW and highlights the importance of a correct choice of the criterion.

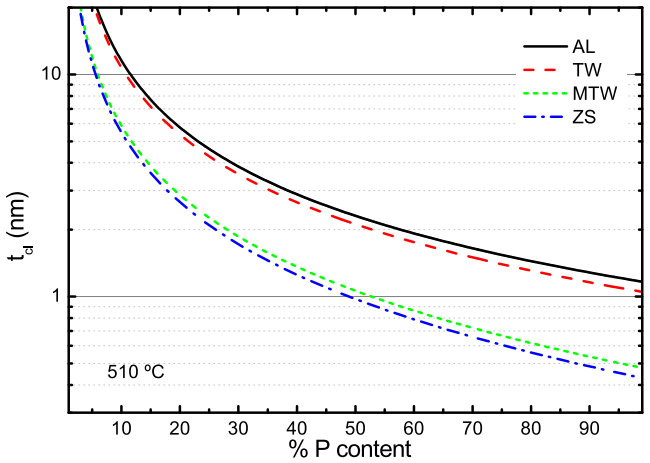

Figure 1.9: GaAsP barrier thickness as a function of the P content needed to compensate a 8 ML thick $In_{0.2}Ga_{0.8}As$ QW according to the different criteria.

The AL and TW criteria always give barrier thickness larger than the other two criteria which can be even twice the value predicted by the ZS criterion. If this one is taken as the most reliable in view of the its physical basis, using the AL or TW criteria will lead to overcompensated superlattices.

From a practical point of view, this technique works fairly well. Currently an InGaAs/GaAsP multiple quantum well (MQW) solar cell delivered by QuantaSol, an Spin-Off of the Quantum Photovoltaic Group at Imperial College London, has the world record efficiency for a single junction device (28.3%). Its integration in double and triple junction devices is in process.

1.6 Motivation and structure of the work

In the light of the summary presented in this introductory chapter, there are two basic aspects of QDs that have to be addressed in order to fabricate efficient devices. On one hand, it is necessary to stack many QDs layers to increase the contribution of the QDs to the device performance. This has to be done without degrading the crystal and optical quality of the devices.

On the other hand, there is an important work to be done in shape engineer SK QDs in order to get better mid-infrared response, to exploit enhanced polarization characteristics or larger radiation lifetimes. This means to study and control the properties of the QPs briefly introduced in the previous section.

In this work we address these two questions by using the strain balanced technique already apply in QWs but with a novel approach: using a mechano-optical stress sensor to *in-situ* monitor and optimize the accumulated stress and the strain balanced parameters.

The memory is organised as follows:

Chapter 2 is devoted to the sample fabrication techniques. It is divided into two parts: the first one addresses the description of the molecular beam epitaxy (MBE) reactor where samples are grown under very controlled conditions. It includes a discussion on the epitaxial growth of III-V semiconductors and the most important parameters that influence the process. In the second part we describe all the techniques needed to fabricate a device (typically, a PiN diode) from the as-grown structures fabricated in the MBE reactor. It includes the conditions used in wet etching and UV lithography used in this work, among other techniques.

Next chapter, Chapter 3, includes the characterization techniques that have been used to probe the properties of the samples. These techniques range from the structural analysis (atomic force microscopy, transmission electron microscopy...), optical analysis (photoluminescence, fourier-transform infrared spectroscopy...) and optoelectronic analysis (photocurrent spectroscopy, electroluminescence...). We will describe the fundamentals of the techniques and their implementation.

In Chapter 4 we introduce the fundamentals of the mechano-optical stress sensor technique and its implementation at the Instituto de Microelectrónica de Madrid (IMM). In this chapter, and as a presentation

of the capabilities of the experimental set-up, we also perform systematic measurements of the stress accumulated in InAs/GaAs QDs grown in different conditions and GaAsP layers of varying P content. This information will be used in the next chapters to design optimized strain balanced structures.

In Chapter 5 we enter into the detail of applying the strain balanced technique to QDs. First, we comment the work performed so far in this field by other groups and the current status of the technology. The core of the chapter is the application of the in-situ accumulated stress characterization to grow strain balanced structures, comparing the results with the theoretical approaches. Then, we discuss the effect of the inhomogeneous strain fields in the compensating layer, a topic never considered in the literature. Finally, we use all this information to fabricate a large stack of QDs, where we demonstrate the feasibility of fabricating this kind of structures and the conditions in which it can be done.

The last chapter, Chapter 6, is devoted to quantum posts. We begin the chapter explaining the detail of their fabrication, the properties found by other authors and the possible applications of these nanostructures. Next, we describe the fabrication of QPs including a strain balance process that has allowed us to fabricate QPs of extraordinary length. We comment on their specific properties and a theoretical description of the recombination dynamics of carriers in these nanostructures, a key point to be considered when using them as memory units.

The final chapter contains a summary of the main results of this work, including open questions and a brief description of future work to be done.

Bibliography

[1] L. Esaki and R. Tsu, "Superlattice and negative differential conductivity in semiconductors," *IBM Journal of Research and Development*, vol. 14, no. 1, pp. 61–65, 1970.

[2] Y. Arakawa and H. Sakaki, "Multidimensional quantum well laser and temperature dependence of its threshold current," *Applied Physics Letters*, vol. 40, no. 11, pp. 939–941, 1982.

[3] A. Ekimov and A. Onushchenko, "Quantum size effect in three-dimensional microscopic semiconductor crystals," *ZhETF Pis ma Redaktsiiu*, vol. 34, p. 363, 1981.

[4] L. Brus, "Electron–electron and electron-hole interactions in small semiconductor crystallites: the size dependence of the lowest excited electronic state," *The Journal of chemical physics*, vol. 80, p. 4403, 1984.

[5] J. Martín-Sánchez, G. Muñoz-Matutano, J. Herranz, J. Canet-Ferrer, B. Alén, Y. González, P. Alonso-González, D. Fuster, L. González, J. Martínez-Pastor, and F. Briones, "Single photon emission from site-controlled InAs quantum dots grown on GaAs(001) patterned substrates," *ACS nano*, vol. 3, pp. 1513–7, June 2009.

[6] L. J. Martinez, B. Alén, I. Prieto, D. Fuster, L. González, Y. González, M. L. Dotor, and P. A. Postigo, "Room temperature continuous wave operation in a photonic crystalmicrocavity laser with a single layer of InAs/InP self-assembled quantum wires," *Opt. Express*, vol. 17, pp. 14993–15000, Aug 2009.

[7] M. Geller, C. Kapteyn, L. M?ller-Kirsch, R. Heitz, and D. Bimberg, "450 meV hole localization in GaSb/GaAs quantum dots," *Appl. Phys. Lett.*, vol. 82, pp. 2706–2708, 2003.

[8] H. J. Krenner, C. E. Pryor, J. He, and P. M. Petroff, "A semiconductor exciton memory cell based on a single quantum nanostructure.," *Nano Letters*, vol. 8, no. 6, pp. 1750–5, 2008.

[9] D. L. Huffaker, G. Park, Z. Zou, O. B. Shchekin, and D. G. Deppe, "1.3 μm room-temperature GaAs-based quantum-dot laser," *Applied Physics Letters*, vol. 73, no. 18, p. 2564, 1998.

[10] J. Tatebayashi, Y. Arakawa, N. Hatori, H. Ebe, M. Sugawara, H. Sudo, and A. Kuramata, "InAs/GaAs self-assembled quantum-dot lasers grown by metalorganic chemical vapor deposition—Effects of postgrowth annealing on stacked InAs quantum dots," *Appl. Phys. Lett.*, vol. 85, no. 6, pp. 1024–1026, 2004.

[11] F. Suárez, D. Granados, M. L. Dotor, and J. M. García, "Laser devices with stacked layers of InGaAs/GaAs quantum rings," *Nanotechnology*, vol. 15, no. 4, p. S126, 2004.

[12] S. Chakrabarti, a. D. Stiff-Roberts, X. H. Su, P. Bhattacharya, G. Ariyawansa, and a. G. U. Perera, "High-performance mid-infrared quantum dot infrared photodetectors," *Journal of Physics D: Applied Physics*, vol. 38, pp. 2135–2141, July 2005.

[13] J. T. Ng, U. Bangert, and M. Missous, "Formation and role of defects in stacked large binary InAs/GaAs quantum dot structures," *emicond. Sci. Technol.*, vol. 22, no. 2, pp. 80–85, 2007.

[14] J. Matthews and A. Blakeslee, "Defects in epitaxial multilayers: I. misfit dislocations," *Journal of Crystal Growth*, vol. 27, pp. 118–125, 1974.

[15] Z. Xu, D. Birkedal, J. M. Hvam, Z. Zhao, Y. Liu, K. Yang, A. Kanjilal, and J. Sadowski, "Structure and optical anisotropy of vertically correlated submonolayer InAs/GaAs quantum dots," vol. 82, no. 22, pp. 3859–3861, 2003.

[16] A. Taboada, *Controlling the shape, size and composition of III-V semiconductor nanostructures: quantum rings and quantum dots.* PhD thesis, Instituto de Microelectrónica de Madrid (CNM-CSIC), 2010.

[17] D. N. Bose, "Growth and characterization of compound semiconductors for optoelectronics," *LaserNews*, vol. 10, April 1999.

[18] "Biomedical Engineering in Advanced Applications of Quantum, Oscillatory, and Nanotechnological Systems (BEAAQONS)." `http://www.bmed.mcgill.ca/dotty/projects.html`, 2011.

[19] C. Murray, C. Kagan, and M. Bawendi, "Self-organization of cdse nanocrystallites into three-dimensional quantum dot superlattices," *Science*, vol. 270, no. 5240, p. 1335, 1995.

[20] L. Bakueva, I. Gorelikov, S. Musikhin, X. Zhao, E. Sargent, and E. Kumacheva, "PbS Quantum Dots with Stable Efficient Luminescence in the Near-IR Spectral Range," *Advanced Materials*, vol. 16, no. 11, pp. 926–929, 2004.

[21] R. Little, M. El-Sayed, G. Bryant, and S. Burke, "Formation of quantum-dot quantum-well heteronanostructures with large lattice mismatch: ZnS/CdS/ZnS," *The Journal of Chemical Physics*, vol. 114, p. 1813, 2001.

[22] J. Caruge, J. Halpert, V. Wood, V. Bulovic, and M. Bawendi, "Colloidal quantum-dot light-emitting diodes with metal-oxide charge transport layers," *Energy (eV)*, vol. 4, pp. 4–6, 2008.

[23] P. Anikeeva, J. Halpert, M. Bawendi, and V. Bulovic, "Quantum dot light-emitting devices with electroluminescence tunable over the entire visible spectrum," *Nano letters*, vol. 9, no. 7, pp. 2532–2536, 2009.

[24] S. Emin, S. Singh, L. Han, N. Satoh, and A. Islam, "Colloidal quantum dot solar cells," *Solar Energy*, 2011.

[25] D. Bimberg, M. Grundmann, and N. N. Ledentsov, *Quantum dot heterostructures.* Wiley, 1998.

[26] K. Kash, D. Mahoney, B. Van der Gaag, A. Gozdz, J. Harbison, and L. Florez, "Observation of quantum dot levels produced by strain modulation of GaAs-AlGaAs quantum wells," *Journal of Vacuum Science & Technology B: Microelectronics and Nanometer Structures*, vol. 10, no. 4, pp. 2030–2033, 1992.

[27] J. Riikonen, J. Sormunen, M. Mattila, M. Sopanen, and H. Lipsanen, "InGaAs/InP Quantum Dots Induced by Self-Organized InAs Stressor-Islands," *Japanese Journal of Applied Physics*, vol. 44, no. 17, pp. L518–L520, 2005.

[28] E. D. Minot, F. Kelkensberg, M. van Kouwen, J. A. van Dam, L. P. Kouwenhoven, V. Zwiller, M. T. Borgström, O. Wunnicke, M. A. Verheijen, and E. P. A. M. Bakkers, "Single quantum dot nanowire leds," *Nano Letters*, vol. 7, no. 2, pp. 367–371, 2007.

[29] Z. M. Wang, B. L. Liang, K. A. Sablon, and G. J. Salamo, "Nanoholes fabricated by self-assembled gallium nanodrill on gaas(100)," vol. 90, no. 11, p. 113120, 2007.

[30] P. Alonso-González, B. Alén, D. Fuster, Y. González, L. González, and J. Martínez-Pastor, "Formation and optical characterization of single InAs quantum dots grown on GaAs nanoholes," vol. 91, no. 16, p. 163104, 2007.

[31] J. Martín-Sánchez, P. Alonso-González, J. Herranz, Y. González, and L. González, "Site-controlled lateral arrangements of InAs quantum dots grown on GaAs(001) patterned substrates by atomic force microscopy local oxidation nanolithography," *Nanotechnology*, vol. 20, no. 12, p. 125302, 2009.

[32] A. G. Taboada, A. M. Sánchez, A. M. Beltrán, M. Bozkurt, D. Alonso-Álvarez, B. Alén, A. Rivera, J. M. Ripalda, J. M. Llorens, J. Martín-Sánchez, Y. González, J. M. Ulloa, J. M. García, S. I. Molina, and P. M. Koenraad, "Structural and optical changes induced by incorporation of antimony into InAs/GaAs(001) quantum dots," *Phys. Rev. B*, vol. 82, p. 235316, Dec 2010.

[33] P. Alonso-González, L. González, Y. González, D. Fuster, I. Fernández-Martínez, J. Martín-Sánchez, and L. Abelmann, "New process for high optical quality InAs quantum dots grown on patterned GaAs(001) substrates," *Nanotechnology*, vol. 18, no. 35, p. 355302, 2007.

[34] F. W. Wise, "Lead salt quantum dots: the limit of strong quantum confinement.," *Accounts of chemical research*, vol. 33, pp. 773–80, Nov. 2000.

[35] M. Grundmann, O. Stier, and D. Bimberg, "InAs/GaAs pyramidal quantum dots: Strain distribution, optical phonons, and electronic structure," *Physical Review B*, vol. 52, no. 16, pp. 11969–11981, 1995.

[36] R. Nötzel, J. Temmyo, A. Kozen, T. Tamamura, T. Fukui, and H. Hasegawa, "Self-organization of strained GaInAs microstructures on InP (311) substrates grown by metalorganic vapor-phase epitaxy," *Applied physics letters*, vol. 66, p. 2525, 1995.

[37] S. Farfad, R. Leon, D. Leonard, J. Merz, and P. Petroff, "Phonons and radiative recombination in self-assembled quantum dots," *Physical Review B*, vol. 52, no. 8, p. 5752, 1995.

[38] J. Singh, *Electronic and optoelectronic properties of semiconductor structures*. Cambridge University Press, 2003.

[39] W. Lei, M. Offer, A. Lorke, C. Notthoff, C. Meier, O. Wibbelhoff, and A. Wieck, "Probing the band structure of InAs/ GaAs quantum dots by capacitance-voltage and photoluminescence spectroscopy," *Applied Physics Letters*, vol. 92, p. 193111, 2008.

[40] D. Granados and J. M. García, "Determination of the energy levels on InAs quantum dots with respect to the GaAs conduction band," *Nanotechnology*, vol. 16, no. 5, p. S282, 2005.

[41] K. Choi, C. Monroy, V. Swaminathan, T. Tamir, M. Leung, J. Devitt, D. Forrai, and D. Endres, "Optimization of corrugated-QWIPs for large format, high quantum efficiency, and multi-color FPAs," *Infrared physics & technology*, vol. 50, no. 2-3, pp. 124–135, 2007.

[42] S. Sauvage, P. Boucaud, F. H. Julien, J.-M. Gérard, and V. Thierry-Mieg, "Intraband absorption in n-doped InAs/GaAs quantum dots," vol. 71, no. 19, pp. 2785–2787, 1997.

[43] S. Chua, S. Xu, X. Zhang, X. Wang, and T. Mei, "Polarization dependence of intraband absorption in self-organized quantum dots," *Applied physics*, vol. 73, no. 14, pp. 1997–1999, 1998.

[44] W. Wu, J. Liu, and Y. Tang, "Infrared spectroscopy of intraband transitions in ge/si quantum dot superlattices," *Superlattices and microstructures*, vol. 26, no. 3, 1999.

[45] L. H. Li, P. Ridha, G. Patriarche, N. Chauvin, and a. Fiore, "Shape-engineered epitaxial InGaAs quantum rods for laser applications," *Applied Physics Letters*, vol. 92, no. 12, p. 121102, 2008.

[46] T. Kita, O. Wada, H. Ebe, Y. Nakata, and M. Sugawara, "Polarization-Independent Photoluminescence from Columnar InAs/GaAs Self-Assembled Quantum Dots," *Japanese Journal of Applied Physics*, vol. 41, no. Part 2, No. 10B, pp. L1143–L1145, 2002.

[47] B. Miller, U. Koren, M. Young, and M. Chien, "Strain compensated strained layer superlattices for 1.5 micron wavelength lasers," *LEOS 1991 Summer Topical Meetings on Epitaxial Materials and In-Situ Processing for Optoelectronic Devices. Photonics and Optoelectronics*, pp. 16–17, 1991.

[48] G. Zhang and a. Ovtchinnikov, "Strain-compensated InGaAs/GaAsP/GaInAsP/GaInP quantum well lasers (l=0.98 um) grown by gas-source molecular beam epitaxy," *Applied Physics Letters*, vol. 62, no. 14, p. 1644, 1993.

[49] N. Dutta, W. Hobson, D. Vakhshoori, H. Han, P. Freeman, J. de Jong, and J. Lopata, "Strain compensated InGaAs-GaAsP-InGaP laser," *IEEE Photonics Technology Letters*, vol. 8, pp. 852–854, July 1996.

[50] N. J. Ekins-Daukes, K. W. J. Barnham, J. P. Connolly, J. S. Roberts, J. C. Clark, G. Hill, and M. Mazzer, "Strain-balanced GaAsP/InGaAs quantum well solar cells," *Applied Physics Letters*, vol. 75, no. 26, p. 4195, 1999.

[51] N. Ekins-Daukes, K. Kawaguchi, and J. Zhang, "Strain-balanced criteria for multiple quantum well structures and its signature in x-ray rocking curves," *Crystal Growth & Design*, vol. 2, no. 4, pp. 287–292, 2002.

Chapter 2

Molecular Beam Epitaxy and sample processing

In this chapter there is an introduction to the MBE growth process, its implementation at the IMM and the additional techniques used to fabricate devices from the bare epitaxies. In the first part of the chapter, there is a general overview of the MBE technique (2.1.1); then a description of the main parameters that influence the growth of the samples and common conditions used in this work (2.1.2); after that, we introduce the most important in situ characterization technique in MBE systems, the reflection high energy electron diffraction (RHEED) measurements (2.1.3); and finally we will describe the characteristics and capabilities of the MBE reactors available at IMM (2.1.4). In the second part, we describe the main steps that are needed to fabricate devices from the epitaxies fabricated in the MBE reactors. These includes a description of the processing schemas applied along this work (2.2.1), the UV lithography (2.2.2), wet etching (2.2.2), metal deposition to fabricate the contacts (2.2.2), SiO_x deposition (2.2.2) and encapsulation (2.2.2).

Contents

2.1 Molecular beam epitaxy (MBE)

2.1.1 Overview

The origin of MBE can be found back in the early 70's, when it was developed as a technique to grow epitaxial layers of very high purity semiconductor compounds.[1, 2] Thereafter, it has evolved and become a generalized technique to grow different materials, such as III-V, II-VI or Si/Ge compounds. With MBE it is possible to fabricate epitaxial materials with abrupt interfaces and a very precise control of the thickness, doping level and composition of the layers. This capability is essential for the development of new photonic and optoelectronic devices.[1]

The high quality of the materials fabricated in an MBE reactor requires ultra high vacuum conditions (UHV), with base pressures lower than 10^{-10} mbar. For this reason, such reactors usually count with a combination of vacuum pumps (rotatory, turbomolecular, roots and ionic pumps), Ti sublimation filaments and liquid nitrogen cryopumps, as well as periodic baking processes to remove molecules adsorbed in the reactor walls.

In Figure 2.1 there is a schematic representation of an MBE growth process.[4] The different materials are heated in effusion cells and high purity molecular beams are projected onto the sample. The partial pressure of the beams (or beam equivalent pressure, BEP) is controlled by the temperature of the cells which can be monitored by thermocouples placed in their base. That pressure can be measure directly with a mobile ionization manometer that can be situated in place of the sample

[1] Part of the MBE section is adapted from A.G.Taboada thesis, with permission from the author.[3]

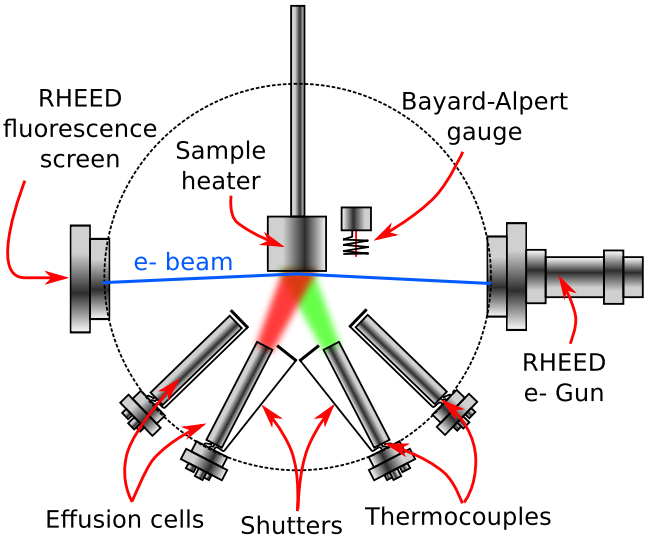

Figure 2.1: Schematic representation of the MBE growth process, including the main parts of the system.

when needed. Additionally, the molecular beams can be interrupted with pneumatically actuated shutters to select the materials that reach the sample at each time. The substrate temperature is monitored with a thermocouple and controlled with a tantalum filament. Using the cells and substrate temperatures and the shutters it is possible to achieve the optimum growth conditions, so the reactions between the elements on the surface of the substrates result in the formation of high purity crystalline epitaxial layers.

2.1.2 Parameters and conditions

In 1982 Freller *et al.* developed the three temperatures method to grow InAs and InSb thin films.[5] They found that for each pinning rate of evaporated particles, there is a critical substrate temperature (T_s) beyond which there is not continuous condensation on the substrate surface. In other words, for each T_s there is a minimum particle flux that must be surpassed in order to have condensation. That flux is directly proportional to the temperatures of the material sources.

Most III-V semiconductors are formed by elements that have very different partial pressures and high dissociation rate during the evaporation process. Group V element (P, As, Sb) is more volatile than the group III (Ga, In, Al) and, as a consequence, for high enough temperatures, the later will be melted but with a vapour pressure several orders of magnitude smaller that the former. For this reason, it is not possible to get a III-V semiconductor compound using a single effusion cell and hence to get an stoichiometric compound it is necessary to work with different temperatures for each cell.

Following the work of Freller, the three temperatures considered (group III and V cells temperatures and substrate temperature) must fulfil the relationship $T_V < T_s < T_{III}$. In this way, combining different material beams, the growth rate of the epitaxial layer is determined by the condensation of group III element on the surface. Since the free energy of decomposition of the compound is larger than that required to evaporate the most volatile element, the fraction of it which does not incorporate evaporates back to the chamber.

One of the main advantages of MBE growth lies on the possibility of fabricating heteroepitaxial materials, such as InAs or AlAs on InP or GaAs, for example. As mentioned before, it is possible to obtain abrupt interfaces with high degree of control to the limit of an atomic monolayer thanks to the fast response of the pneumatic shutters. Likewise, the MBE growth rate, typically from 0.2 μm/h to 1.5 μm/h, allows to further tune the thickness, composition and doping of the materials. Moreover, the low substrate temperatures required in conventional MBE growth (580°C for growing GaAs) limits the diffusion of dopants and improves the quality of the interfaces. In this sense, MBE has an advantage over other epitaxial grow techniques, such as metal-organic chemical vapour deposition (MOCVD) or metal-organic vapour phase deposition (MOVPE) where substrate temperatures are typically much higher. Additionally, the low pressures used during MBE growth implies that the beams are in a molecular regime, with a high degree of directionality, which increases the efficiency of the shutters. In comparison, in MOCVD and MOVPE the particle flux is in a viscous regime with multiple collisions between the molecules inside the beams.

Growth kinetics

During the MBE growth of III-V semiconductor compounds, there are different simultaneous processes that affect the growth kinetics:[6]

- Adsorption of evaporated atoms and molecules.
- Surface migration and dissociation of adsorbed molecules.
- Incorporation of atoms to the crystal lattice.
- Desorption of particles incorporated and not incorporated to the crystal lattice.

MBE growth is kinetically controlled by the adsorption of the group V element whereas the growth rate is governed by the group III element. These elements (Ga, Al, In) have a sticking coefficient on the (100) GaAs surface of almost unity in the temperature regime commonly used (450 C to 620 C). This means that each atom that reaches the surface, stays there. On the contrary, the adsorption probability of group V elements is smaller and depends critically on the substrate temperature and the population of group III atoms on the surface. An important fraction of group V atoms is desorbed so it is convenient to work with particle fluxes of group V element at least one order of magnitude larger than those of group III.

Two other parameters have a large impact in the MBE growth process. The first one is the surface reconstruction of the substrate, that is explained below. The second one is related with the strain fields present in the surface due to buried nanostructures. As it is discuss in Section 5.5 this fields might favour the formation of one or other alloy on a local scale.

Surface reconstruction of GaAs

Most III-V semiconductor materials are characterized by a zinc-blende crystal structure.[2] In its (001) face, it presents alternating planes of group III and V atoms.[7] The crystal structure on the surface of this materials is noticeable different from that in bulk.The presence of dangling bonds

[2]N-based compounds, such as GaN or InN, have a wurtzite structure, but we will no consider them in this work.

leads to the rearranging of the outer atoms in order to minimize the surface energy. There are different mechanisms to reach that situation such as hibridization of surface bonds, their coupling, formation of vacancies or partial relaxation of the atomic positions.

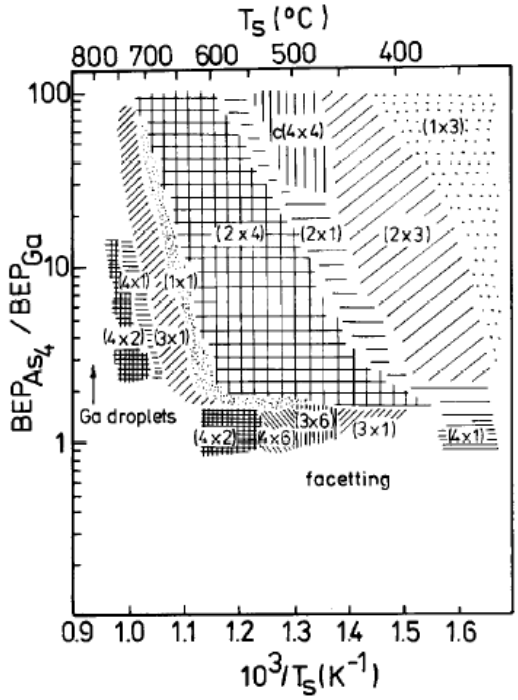

Figure 2.2: Phase diagram of the GaAs (001) surface reconstructions as a function of the substrate temperature and As/Ga flux ratio. Image adapted from Ref. [8].

The GaAs (001) surface might end in Ga or As atoms, leaving in both cases two dangling bonds. The experimental conditions set the way in which atoms rearrange in order to minimize the surface energy of the semiconductor. In Figure 2.2 we show a phase diagram of the GaAs (001) surface reconstructions as a function of the substrate temperature and As/Ga flux ratios. The final surface reconstruction will be the one that, minimizing the surface energy, accomplishes with the following principles:[8]

- It must be accessible for the kinematic conditions of the experiment.
- The surface is generally electrically self-compensated. That means that dangling bonds of the most electronegative element must be filled and those of the electropositive, empty. In this way, the surface keeps the semiconductor character. Half-filled bonds might lead to metallic behaviours.
- Given a certain surface stochiometry, the atomic geometry is determined by a reduction of surface bonds by means of re-hibridization with other bonds.

The material used as substrate along this thesis work is GaAs (001). It might show a large variety of reconstructions, from those As-rich such as c(4×4) or (2×2) to those Ga-rich as (4×2), (6×6) or (4×6).[3]All the samples grown in this work have been fabricated using a substrate temperature from 480 C to 650 C and As BEP between 10^{-6} and 2×10^{-6} mbar. In this situation and assuming static conditions, surface dimers arrange in periodic positions along [110] and [1-10] directions.

Usually, MBE growth of GaAs begins and finishes with the (2×4) surface reconstruction, which make it one of the better studied. This reconstruction is characterized for being stabilized in the group V element with As dimers aligned along the [1-10] direction.[10] The electronic restrictions stated above imply that the last monolayer can not be completed. Figure 2.3 shows the most common configurations for the unit cell in this reconstruction. β(2×4) and β2(2×4) contain the maximum As content permitted by the restrictions of electronic stability (around 75%), being the latter more stable, with two dimers in the first layer and one in the third one. It leads to the smallest surface energy. As the substrate temperature is increased or the As pressure reduced, it is favourable the formation of the phase α(2×4), with more Ga. The unit cell is similar to the β2(2×4) but with Ga atoms in the place of one of the As dimers. On the contrary, reducing the substrate temperature or increasing the As pressure,

[3]The nomenclature (n×m) refers to the unit cell of the periodic arrangement of dimers in the GaAs (001) surface. The size of the unit cell will be proportional to the unit cell of the bulk material. A (2×4) reconstruction, for example, will have a size 2a in the [110] direction and 4b in the [1-10], being a and b the lattice parameters of the crystal lattice along those two directions, respectively.

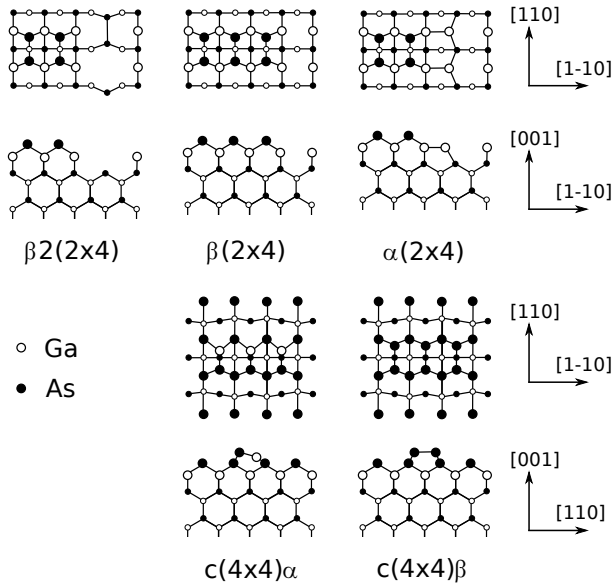

Figure 2.3: Unit cells of the most important phases of the (2×4) and c(4×4) reconstructions of GaAs (001). Image adapted from Ref. [9].

first produces the richest As phase of the (2×4) reconstruction, the $\gamma(2\times4)$, and then a complete new reconstruction, the c(4×4) with two layers of As atoms. At typical growth conditions, the dominant configuration is the phase c(4×4)α which has a first layer of only As bonds and a second layer of As-Ga bonds [110] oriented. Further reduction of the temperature lead to the c(4×4)β, with two layers of As bonds.

2.1.3 Reflection high energy electron diffraction measurements (RHEED)

As discussed above, the particular surface reconstruction have a large impact in the adsorption and migration of atoms and, hence, in the kinetics of the growth process. For that reason, it is important to monitor the status of the surface, which in MBE can be done with reflection high energy electron diffraction (RHEED) measurements.

This technique uses a gun that emits a beam of monochromatic electrons, with energies between 5 and 50 keV, and that hits the substrate

at a very glazing angle (less than 3°). The incidence angle can be controlled with a magnetic field of varying intensity in the direction perpendicular to the beam. In this situation, the penetration depth of electrons into the material is in the order of a few monolayers and, if we assume that electrons reflect in those monolayers, we can consider the surface as a bi-dimensional diffraction grid. Reciprocal lattice vectors will be perpendicular to the plane formed by the normal to the sample surface and the electron beam. The intersection of the Ewald's sphere with that periodic distribution of vectors give a diffraction pattern characteristic of the surface reconstruction (Figure 2.4).[11] In the ideal situation, the intersection pattern consists on a set of bright dots in a fluorescence detector screen (phosphor screen, in our MBE systems) arranged in a semi-circumference arc perpendicular to the sample plane (Figure 2.4, right-top image). In a more realistic case, there is dispersion in the electron energies and thermal vibrations of the surface atoms. Additionally, sample surface might have steps. In this situation the ideal dot distribution became an arrangement of diffraction rods with certain thickness (Figure 2.4, right-bottom image).[12]

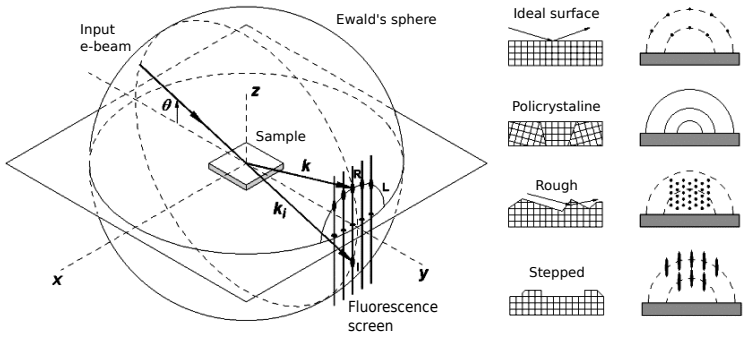

Figure 2.4: Schematic representation of the e-beam diffraction pattern formation on a fluorescence screen. Figure adapted from Ref. [13]

Apart from the surface reconstruction, RHEED allows to monitor the desorption of native oxide from the substrate surface, estimate its temperature o calculate the growth rate of the material. Additionally, it can be used to identify the transition from a bi-dimensional to a tree-dimensional surface, extremely useful during the growth of quantum

dots.

When a substrate is introduced in the MBE reactor, it shows a diffraction pattern characteristic of an amorphous material, as the native oxide: several concentric bright halos. As the substrate temperature is increased under an As flux (in case of a GaAs substrate), those halos progressively become bright spots at positions defined by the periodicity of the crystal surface. That is the indication of a complete removal of the native oxide. As explained above, surfaces tend to rearrange to minimize the free surface energy. Each reconstruction depends on the substrate temperature and the stoichiometry of the surface. As a consequence, it is possible to reproduce changes in the reconstruction under fix conditions (constant group V element flux) and use them as reliable estimations of the substrate temperature. In particular, using a constant As4 flux (As BEP = 2×10^{-6} mbar), we can take as a reference the temperature of native oxide desorption (600°C) and the change in the surface reconstruction from the (2×4) to the c(4×4) (510°C).[14, 15]

One of the applications that makes RHEED such a useful tool in an MBE reactor is the measurement of the growth rate. This allows, also, to calibrate the fluxes of different materials, control the composition of the alloys and the thickness of quantum wells or superlattices. This kind of control is based on the study of the intensity oscillation in the diffraction pattern (see Figure 2.5).[10] The periodicity of such oscillations corresponds to the time needed to form a complete monolayer. The intensity variation of the oscillations is larger for the electron beam directly reflected by the surface than in the diffracted spots. In GaAs, a monolayer is defined as a complete Ga layer plus a complete As layer and has a thickness of 2.823 Å.

When the electron beam hits a surface perfectly flat, the reflectivity is large and the intensity of the reflected spot, maximum. When the shutter of a group III element is open, the RHEED intensity reduces and the signal begins to oscillate. Within the kinematic approximation of electron diffraction, we can assume that this reduction is due to the formation of 2D islands on the surface. The presence of those islands contribute to the destructive interference of electrons diffracted by different atomic planes since the wavelength associated with the incident beam is smaller than the height of the islands. In this way, the minimum intensity is found for half

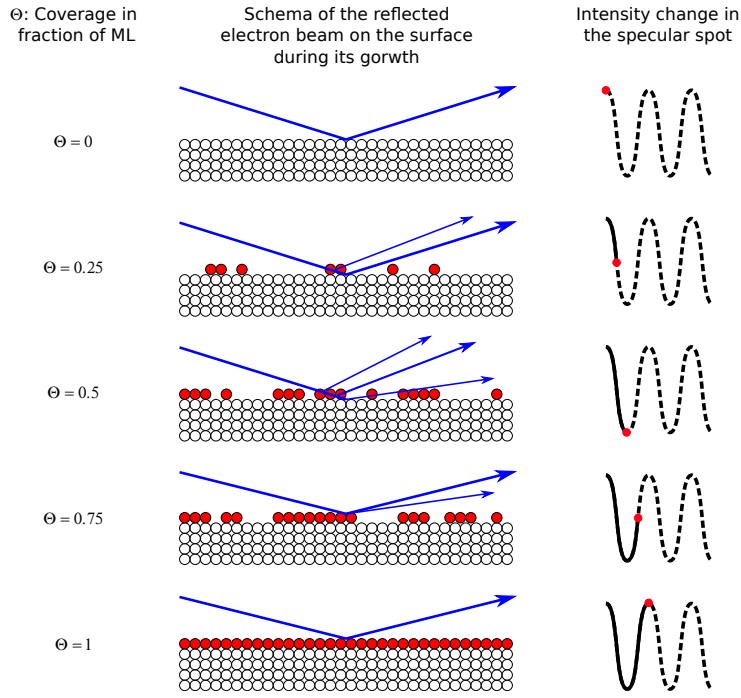

Figure 2.5: Evolution of the specular reflection intensity as the growth of a ML proceeds. Image adapted from Ref. [10].

monolayer, when the surface roughness is maximum. The period finishes in the initial point when the monolayer is completed. In the real case, there is a damping in the oscillations consequence of a phase difference between the growth kinetics and the formation of bidimensional islands on the second monolayer before the first one is completed.[4]

The study of the evolution of RHEED oscillations during the growth of III-V semiconductors for several temperatures and flux relations together with an study over stepped substrates lead to a precise picture of the mechanism present in the process: layer by layer growth, step-flow and three dimensional growth mode.[16, 17]

If MBE growth is performed on a surface perfectly flat, defect free and under perfect growth conditions, the dominant process is bi-dimensional growth or layer by layer.[7] In these conditions, group III atoms have enough energy to migrate along the surface and find other atoms of the

same kind leading to the formation of preferential nucleation centres. Then, they evolve to form bidimensional island and, finally, complete monolayers.

On the other hand, if there is a regular distribution of steps, the step edges work as preferential nucleation centres and the growth proceed expanding the steps until all the available surface is covered. In this growth mode, there is no oscillations of the RHEED pattern.[16]

Finally, it is possible to observe three dimensional growth if the conditions are not optimal: low substrate temperature or a flux ratio (Φ_{As}/Φ_{Ga}) too small.[4]As the mobility of group III atoms reduces, the growth becomes three dimensional in the preferential nucleation places. This can also happen if the substrate is not flat and defect free. In this case, blurred spots of low intensity appear in the RHEED pattern

2.1.4 MBE reactor at the IMM

At Instituto de Microelectrónica de Madrid (IMM) there are three reactors. Two of them are home-made, designed and fabricated at IMM, and the third one is a commercial RIBER Compact 21 reactor. The latter has not been used in this work so the description will be focused in the other two, called MBE II and MBE III.

In Figure 2.6 there is a schematic representation of the reactors, which have a specular layout. All the chambers of the two systems are interconnected with vacuum valves and can be isolated when necessary. This allows to minimize the contact of the main chamber with the outer environment. Both systems count with an introduction chamber that is never connected with the rest of the system unless its base pressure is lower than 5×10^{-7} mbar using a rotatory and a turbomolecular pumps. Additionally, before substrates enter into the prechamber, they undergo a soft baking with 500 W halogen lamps to partly remove the water absorbed in the samples and the walls of the introduction chamber during the loading operation.

The prechamber uses ionic pumps to achieve the UHV regime. Both prechambers are interconnected with an auxiliary chamber. In the

[4] Φ is defined as the number of atoms that reach a surface per unit of surface and time.

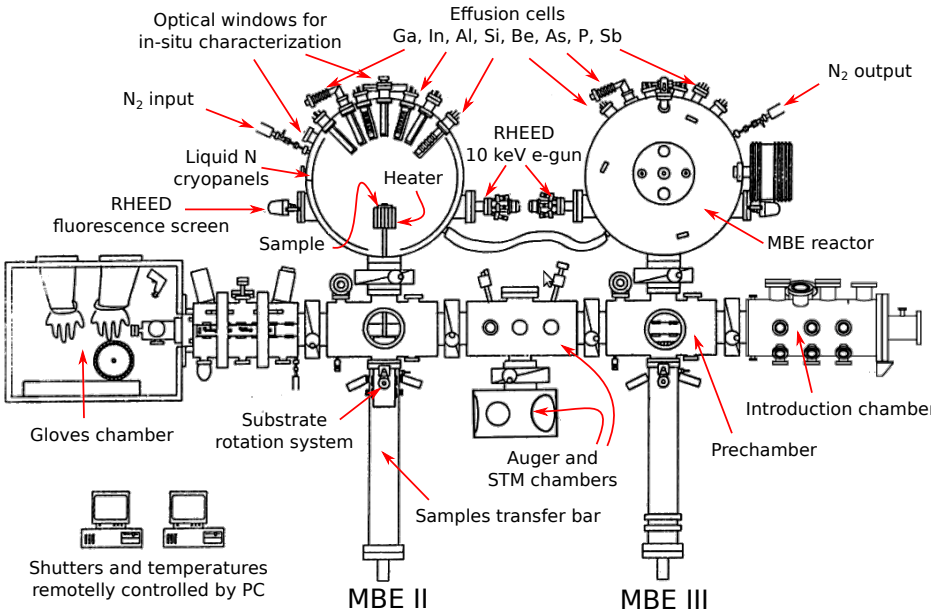

Figure 2.6: Diagram of the two MBE systems used in this work.[3]

prechamber, the substrates are transferred to the main heater and are degassed between 200°C and 300°C. The heater is made by a tantalum resistance with a zig-zag pattern to ensure a homogeneous temperature in all the substrate. The heater temperature is measured with a W-Re thermocouple placed at is centre and controlled with an Eurotherm (process controlled by temperature feedback).

Finally, samples mounted in the heater enter into the reactors. They count with independent ionic pumps, Ti sublimation filaments and liquid nitrogen traps, where most of the residual gases condense. Both systems have effusion cells for Ga, In, Al, Be, Si, As and P, and additionally, MBE II have a Sb effusion cell, also home-made. The general working principles of the effusion cells are very simple. The material, of very high purity, is placed in a crucible heated by a resistance. The cell temperature is measured with a W-Re thermocouple at its base. Using the thermocouple measurement and an electronic feedback, the effusion cells keep the appropriate temperature for the sublimation of the materials. The vapour pressures can be maintained low enough to achieve growth rates

well below a monolayer per second.

In Table 2.1 we show typical cell temperatures and growth rates/BEP /doping level for the materials used in this work. It should be noticed that these temperatures suffer from large variations depending on the material amount that remains inside the effusion cell, so this values are just an example of the order of magnitude. As materials are spent, temperatures must be increased to keep the same growth conditions. As it can be seen, group III elements temperatures are larger than typical substrate temperatures (450-650°C) and this, in turn, larger than group V element temperature, in agreement with the three temperatures theory of Freller *et al.* explained above (Section 2.1.2).

Table 2.1: Typical cell temperatures and resulting growth conditions on GaAs (001). The doping level given considers a growth rate of 0.5 ML/s. For As cracker, which does not have thermocouple, the temperature is given in amperes (A). For the P cell a presure range is given since it depends also on the opening screw.

Material	**T (°C)**	**R (ML/s)**	**Pressure (mbar)**	Dop. **(cm^{-3})**
Ga	950	0.5	-	-
In	729	0.02	-	-
Al	1126	0.42	-	-
Si	1160	-	-	2×10^{18}
Be	830	-	-	2×10^{18}
As	243	-	2×10^{-6}	-
As cracker	2 A	-	-	-
P	20-40	-	10^{-7}-5×10^{-6}	-
P cracker	850	-	-	-

The effusion cell, similarly to the main heater, are made with refractory materials that have very low vapour pressures at the working temperatures. Common materials are tantalum, tungsten and molybdenum for the structure of the cell, the heaters and the shutters. The isolating materials are pyrolytic boron nitride and sintered alumina. These elements are used for the crucibles and wall bushings. The cells are refrigerated with pure water that continuously flows through a stainless steel tube that surrounds them. Shutters are controlled with electro-pneumatic actuators that allow

an open/close time on the order of 0.1 s.

The design of the effusion cells is slightly different depending on the type of material to evaporate. Flux of group III elements (Ga, In, Al) and dopants (Si, Be) is controlled with a mobile screen whereas for group V elements (As, P, Sb) it is interrupted by sealing the end of the crucible. Using the effusion cells of the group V elements available in the reactors at IMM, we can work with compound tetramers, dimmers or even atomic fluxes in the case of Sb. A tungsten or tantalum filament placed at the end of the cell can be heated up to 1000°C, thermally dissociating group V tetramers. This filament, called cracker, count with an additional thermocouple. The cracker and the heater of the crucible are independent, which simplify the choice of the specie of the element to work with. Our As cell interrupts the flux with a fast quartz stopper instead of needle valves, hermetic but slow, and screens, not hermetic but fast. This improvement allows to work with Φ_{ON}/Φ_{OFF} As ratios of 200, one order of magnitude larger than conventional cells.

P effusion cell has a slightly different working principle. Commercial P we used is a *red* phosphorous ingot that is directly placed inside the crucible. In this form, P can not be used for epitaxial growth and it needs first to be transformed into *white* P.[18] To this end, usually on a different day that the sample growth, the P cell is heated which evaporates part of the red P and partly transforms it into white P, which sticks on the walls of the cell. The cell can be hermetically closed with a pneumatically actuated screw whose aperture can be adjusted by hand. This white P has a relatively high vapour pressure at room temperature so, when the screw is open, it sublimates and enters into the reactor chamber. The P BEP is thus controlled by the opening of the screw and the temperature of the walls of the cell. This temperature is in the range 0-60°C and can be varied with continuous water flow through a coil around the cell. The cell cracker allows to break the white P tetramers into dimers, which have higher reactivity.

Group V element fluxes are measured with a mobile Bayard-Alpert gauge that can be placed at the sample position. During growth, this manometer is shifted towards one side to leave space for the heater with the sample. The relationship between the pressures measured at the sample position P_s and the intermediate position P_{int} is given by:

$$P_s(As) = 1.58 P_{int}(As) \quad (2.1)$$
$$P_s(P) = 2 P_{int}(P) \quad (2.2)$$

Notice that the pressure measured with this manometer include all atomic spices of the given element. All BEP given along this work are the pressures measured at the intermediate position, P_{int}.

2.2 Sample processing

Once the desired structure has been fabricated by MBE, typically including several QDs layers in the intrinsic region of a PiN diode, it is necessary to process that epitaxy and define the devices and metallic contacts in order to perform electrical measurements. In this work, we have used two processing schemas to fabricate the devices, each of them gathering some advantages and disadvantages.

2.2.1 Processing schemas

Schema 1:

This schema is one of the most simple processings that can be envisage in a PiN diode with top-bottom architecture and keeping the possibility of performing optical measurements in the device. It has three steps:

1. **Definition of mesas** to isolate different devices on the same sample. It includes one *UV lithography* and *wet etching* steps.

2. **Metal deposition** to fabricate the top ohmic contact. It includes a *UV lithography* step and the *metal deposition* itself.

3. **Encapsulation of the devices**, which implies to connect with gold wires and conductive epoxy or silver paint the top and bottom contacts to external pads.

This schema present the advantage of being very simple, with few steps, and compact, allowing the definition of many devices in a small piece of

sample. Its main disadvantage is that the bonding of the top contact is done in the mesa itself which might damage the device and degrade its electrical properties.[19] The closeness of the bonding to the optical window also might affect the optical properties because of shadowing of the bond or the silver paint, if this is used.

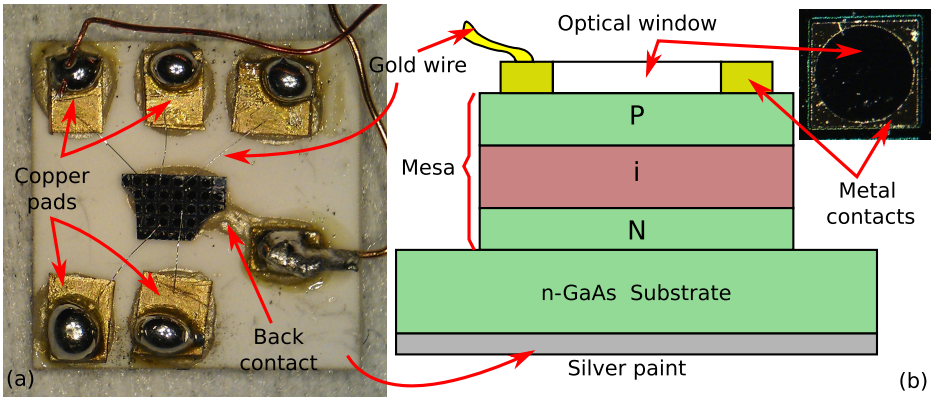

Figure 2.7: (a) Photograph of an encapsulated sample processed following the schema 1. (b) Schematic representation of a cros section of the sample, where it can be seen the different layers that includes the processing.

In Figure 2.7 it can be seen a photograph of a sample process according to this schema and a picture of the cross section of one of the devices, where a profile of the different layers can be seen.

Schema 2:

This schema, also with a top-bottom architecture, is a refinement of the previous one which aims to separate the bonding region and the device region, reducing the probability of damaging the device during bonding. It has five steps:

1. **Definition of mesas** to isolate different devices on the same sample. It includes one *UV lithography* and *wet etching* steps.

2. **SiO_x deposition** to isolate the bottom N-region from the surface.

3. **SiO_x etching** to open an optical window on top of the mesa and make accessible the top p-region. It includes one *UV lithography* and *wet etching* steps.

4. **Metal deposition** to fabricate the top ohmic contact. It includes a *UV lithography* step and the *metal deposition* itself.

5. **Encapsulation of the devices**, which implies to connect with gold wires and conductive epoxy or silver paint the top and bottom contacts to external pads.

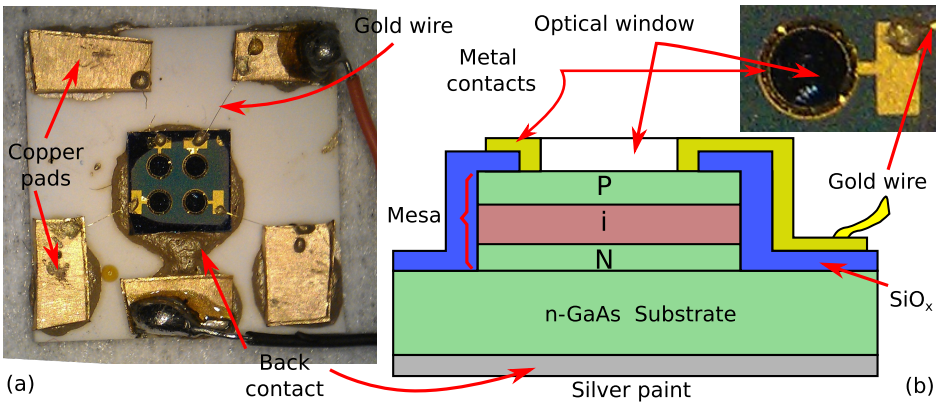

Figure 2.8: (a) Photograph of an encapsulated sample processed following the schema 2. (b) Schematic representation of a cros section of the sample, where it can be seen the different layers that includes the processing.

As it can be seen in Figure 2.8a, this schema requires more space per device and more steps for its fabrication, thus with an increased probability of failure in any of them. It also might have larger contact resistance that schema 1 given the smaller contacting area. However this is important only at high currents, situation that will not be the case in our experiments. The blueish region around the circular mesas are the parts of the surface that are covered with SiO_x, whereas the optical windows are the black, circles in the middle of each device. In Figure 2.8b we also show a cross section of one of the devices with the profile of the layers.

2.2.2 Processing techniques and conditions

Next we describe the different steps that are necessary in the two schemas described above.

Basic sample cleaning

One common step that is used recursively during sample processing is its surface cleaning from dust particles, photoresist or grease. The latter is not usually a problem, given that the sample is never touch except with tweezers but the former might greatly affect the lithography process.

The standard cleaning protocol consist in successive washes (typically two rounds) with acetone, isopropanol and deionized water. The remaining water is completely removed by blowing the sample with dry nitrogen.

UV lithography

UV lithography is used to define motifs in a photoresist spinned on the sample that would later serve as mask for an etching or deposition process. In Figure 2.9 we summarise the process of defining a photoresist mask.

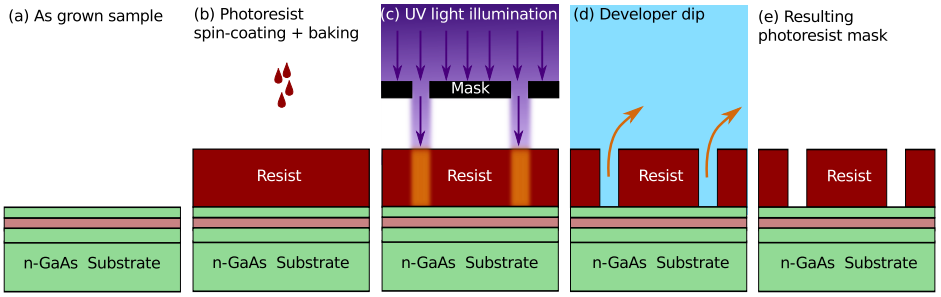

Figure 2.9: Different steps of the UV lithography process: (a) sample cleaning, (b) photoresist spin-coating and baking, (c) UV light exposure, (d) developer dip and (e) resulting photoresist mask.

The photoresist (Microposit S1813) is spread over the sample using a spin coater. Typical conditions in samples of about 5×5 mm require a single drop of the resist from a pipette spinned at 5000 rpm during 45 s. The resulting film thickness is between 1 and 2 μm, according to the specifications (Figure 2.9b). The sample is then introduced in an oven at

90°C for 30 minutes to bake and harden the resist. This step was later improved by placing the sample in a hot-plate at 115°C for 5 minutes with identical results.

Once the resist is baked, the sample is placed in a UV lithography alignment system. This equipment allows to align a UV mask with the sample with micrometer precision and illuminate the regions not covered by the mask with UV light (Figure 2.9c). Given that in this work the resolution did not need to be very high, we used inexpensive UV masks made of printed transparencies with a resolution of 5-10 μm. Higher resolution can be obtain by using high quality masks made of chrome on quartz glass. Typical exposure times used in this work range from 15 to 40 s, depending on the ageing of the photoresist and the UV lamp.

The regions of the resist exposed by the UV light are altered and become soluble in a special substance called the developer (Microposit MF-319) (Figure 2.9d).[5] When the sample is dipped into this substance, the resist of those areas is removed and the UV mask pattern is revealed in the resist that remains in the sample surface (Figure 2.9e).

Wet etching

This step is used to etch part of the material of the sample in order to define the mesas or open the optical windows. We have used two recipes, for GaAs and SiO_x etching, although the steps are the same in both cases.

1. **Recipe 1:** GaAs etching.

   There are several recipes in the literature that allow to etch GaAs (001) surfaces. Typical etchants are Br_2/methanol, $H_2O_2/NH_4OH/H_2O$, $H_2SO_4/H_2O_2/H_2O$, H_2SO_4/H_2O_2/HCl, or HCl/H_2O.[20, 21] Most of them consist in oxidising the GaAs surface with the oxidant (eg. H_2O_2) and removing the oxide from the surface with the acid (eg. H_2SO_4). The difference of each recipe is in the etching rate, the selectivity of the etched surfaces and their smoothness.

   The etchant used in this work uses a solution of water, otophosphoric acid and hydrogen peroxide in the following proportion:

[5] That is the case of positive photoresist, such as Microposit S1813. In the case of negative photoresist, the illuminated regions are those that become insoluble.

$$H_3PO_4 : 2 + H_2O_2 : 1 + H_2O : 17 \tag{2.3}$$

At room temperature, we find that this solution has an etching rate of 5-6 nm/s, in agreement with reported values.[21] It should be noted that this etch rate might be affected by the ageing of the etchant in very long (or parallel) processes and the presence of other chemical species in the sample with slower etch rates, such as InGaAs alloys. With the proportions used in the above recipe, for example, the etch rate of InGaAs is between 3 and 4 times slower than that of GaAs.[21]

In this work we use this recipe to define the mesas and thus the etching depth is that required to reach the substrate (between 1 and 7 μm, depending on the sample structure).

2. **Recipe 2:** SiO_x etching.

   By far, the most commonly used etching recipe for silicon oxide is buffered HF, also called buffered oxide etch (BOE). It consist in a solution of hydrofluoric acid (HF) and ammonium fluoride (NH_4F). If HF is used pure (in the 49% dilution commercially available), the etch is extremely fast, >30 nm/s, and it also removes the resist mask. The addition of NH_4F allows to control the pH of the solution, to avoid the latter effect, and further diluting the mixture in water reduces the etch rate in order to have a higher degree of control over the process.[22]

   The solution composition used in this work is:

$$NH_4F : 6 + HF : 1 + H_2O : 100 \tag{2.4}$$

   In this conditions, the etch rate found for the chemical vapour deposited silicon oxide (see Section 2.2.2) is 2-4 nm/s. Given that this solution is used to open the optical window in the processing schema 2, the GaAs serves as stop layer and there is no danger of over etching the sample. Nevertheless, it is not convenient to leave the sample in this solution too much time beyond the calculated value to etch the SiO_x layer since the process is isotropic and there might be a fast lateral etching beneath the resist mask.

HF is a very hazardous substance that must be manipulated with extreme care. For these reason, other recipes suggested in the literature are those that use KOH, which offers much lower etch rates, smoother surfaces and larger security.[23]

Regardless of the recipe used, the process of etching the sample is the same. We first define the resist mask with the motifs we want to etch in the sample using the steps explained in the previous section (Figure 2.10a). The sample is then dipped in the given solution during the calculated time, stirring it during the whole process to homogenise the solution as the etching proceeds (Figure 2.10b). Due to ageing effects of the etchant (specially if several samples are being etched at the same time) the etch depth might be smaller than the desired value so it is convenient to check it with a profilemeter and resume the process if it is below the expected value. It is good practice to etch the sample in several short steps than in a single larger one to better control the depth and avoid undesirable lateral etching (Figure 2.10c).

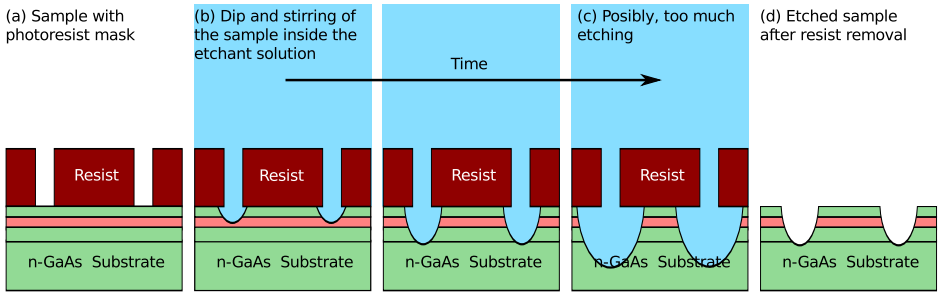

Figure 2.10: Different steps of the wet etching process (we illustrate recipe 1, although recipe 2 have the same steps but etching SiO_x): (a) photoresist mask definition, (b) wet etching, (c) an example of excesive etching and (d) resist removal and resulting mesa definition.

Once the etching has finished, the reaction is stopped by dipping the sample in deionized water and the resist is removed by using the basic cleaning process described above, leaving in the sample surface the etched motifs (Figure 2.10d).

Metals deposition

The fabrication of the metallic contacts is a crucial step in order to obtain reliable and reproducible devices. There are a good number of works where several metallisation schemas are used in order to get good ohmic contacts over n- and p-type GaAs, with low contact resistance and robust mechanical properties.[24–28]

In our case, the metal contact only need to be defined for the top p-type terminal. For the the back contact (n-type) we make use of the In utilized for sticking the sample to the holder during the MBE growth. This In is deeply diffused inside the n-type substrate, given the high temperatures used during growth, and thus constitutes a very convenient ohmic contact.

Two similar metallisation schemas have been used in this work for the p-type contact. The first one consisted in a simple Ti/Au bilayer. In the second one, we inserted a Pt layer between Ti and Au to avoid excessive Au interdifusion in the sample during the post deposition thermal annealing (see below).[28]. The exact structures we have used are:

- Ti (20 nm) + Au (200 nm)
- Ti (5 nm) + Pt (10 nm) + Au (40 nm)

Even though both structures give similar electrical properties, we preferred the second one given that the lift-off process was easier as a consequence of the smaller metal thickness.

The metal deposition is performed in an electron beam metal evaporation system under high vacuum conditions (base pressure $<10^{-7}$ mbar). The system counts with a rotatory crucible holder that allows to easily change the material to evaporate among the six available positions without opening the chamber, which increases the materials purity. Typical metals that can be evaporated in this system are Au, Pt, Ge, Cr, Al, Ni, Co and Ti.

In order to fabricate the metal contacts, we first define the regions where they have to be deposited with a photoresist mask following the aforementioned UV lithography process (Figure 2.11a). Before introducing the sample in the prechamber of the metal evaporator, it is dipped few seconds in a BOE solution in order to remove the native oxide, which improves the adherence of the materials and reduces the contact

resistance. To communicate the evaporation chamber and the prechamber, the pressure of the latter must be lower than $<10^{-6}$ mbar).

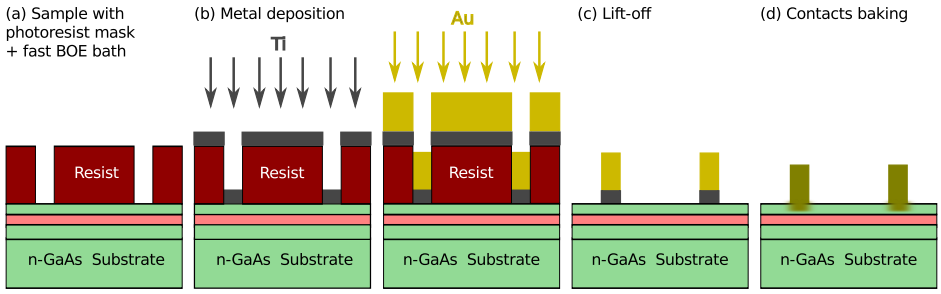

Figure 2.11: Different stages of the metal deposition process: (a) photoresist mask definition and native oxide removal, (b) metal deposition, (c) lift-off and (d) contacts baking.

The deposition of the metals proceeds sequentially, using deposition rates between 0.5 and 1.5 Å/s, depending on the material and the current of the e-gun (Figure 2.11b). The growth rate is monitored with a quartz crystal microbalance placed close to the sample. Before changing from one material to the next one, the crucible is allowed to cold down for a few minutes. In principle, the deposition of metals is highly directional, meaning that steps or shadowed regions will not be covered. However, thanks to the isotropic character of the wet etching process we use, steps are not strictly vertical but show a smooth curvature. This allows to have continuous films of metals conformal to the surface steps, as we need in the processing schema 2. Nevertheless, in the sidewalls of the steps, the metal thickness would probably be smaller.

Once the metallisation is completed, the sample is removed from the evaporator system and introduced in an acetone bath. Normally, this bath is enough for lifting-off the resist and the metal deposited on top of it, leaving the metallic contacts only in the unmasked regions (Figure 2.11c). However, either because of large metal thickness, resist ageing or its hardening during the metal deposition, sometimes it is necessary to aid the lift-off process with an ultrasonic bath.

The final step in the metallization process is the baking of the contact to allow them to diffuse into the semiconductor and lead to the desired low resistance ohmic contact (Figure 2.11d). The baking process was first

carried out in a hot plate under nitrogen atmosphere to avoid Ti oxidation and then in a rapid thermal annealing (RTA) system, also under nitrogen atmosphere. The peak temperature is 350°C with a duration of 90 s in both cases, being the main difference the heating and cool down process, which in the hot plate takes 50 and 300 s, respectively, whereas in the RTA these times are much faster.

SiO_x growth

Silicon oxide has been extensively used in the microelectronic industry to serve as the insulator layer in metal-oxide-semiconductor (MOS) devices, such as MOSFET transistors, which are the basic units in the fabrication of microprocessors.[29] Another common application of SiO_x is for passivation purposes in order to reduce surface recombination in Si and III-V semiconductors.[30, 31]

In this case, we benefit from both uses of the SiO_x. On the one hand, using SiO_x allows to place the top metallic contact out from the mesa, by isolating the metal pad and the transmission line from the underlying n-type GaAs region (Figure 2.8b). On the other hand, part of the surface and lateral walls of the mesa become passivated, preventing the appearance of parasitic parallel routes for the current between the P and N regions.

To deposit the SiO_x on the sample we use a plasma enhanced chemical vapour deposition (PECVD) system. This method allows the fabrication of SiO_x films over any surface, contrary to thermal oxidation method that can only be used on Si substrates.

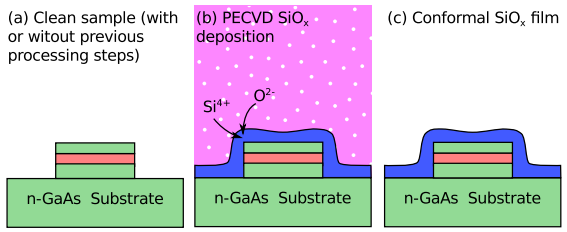

Figure 2.12: Different stages of the SiO_x: (a) cleaning of the sample, (b) SiO_x deposition in the PECVD chamber and (c) resulting SiO_x film.

In order to deposit SiO_x on our samples, they have to be perfectly clean of dust and resist (Figure 2.12a). The sample is placed on a hot plate

inside the reaction chamber whose temperature must be ∼300°C during the growth process in order to have high quality, high oxygen content SiO_x. The reaction chamber is then evacuated down to few mbar and purge with dry nitrogen to prevent the formation of undesired chemical species. Then, a mixture of silane (SiH_4) and oxigen (O_2) is introduced in the chamber and a radio-frequency signal initiates the plasma reaction by partly ionizing the molecules in the chamber. Using plasma is necesary in order to keep low temperature reactions and avoid the decomposition of the semiconductor material or metal diffusion, if there is any in the sample (Figure 2.12b). Growth rate of SiO_x in our system is 0.5 nm/s.

It should be noted that growth of SiO_x is conformal and that surfaces and sidewalls are equally covered (Figure 2.12c). Actually, it is found that in "rough" regions (next to the sample edge or etched steps) the film thickness is slightly larger due to an increased viscosity of the plasma and enhanced chemical reactions. This can be seen with the naked eye as a color change of the film in those regions.

Encapsulation

The final step of the sample processing is the encapsulation of the device with the appropriate external contacts. In our case, the encapsulation process begins by sticking the sample to an alumina holder 1×1 cm wide with several copper pads near the edges. We use silver paint or conductive epoxy to perform the sticking, which allows also to connect the back of the sample with one of the pads and complete the back contact (Figures 2.7a and 2.8a).

The gold wire between the top contacts and the copper pads is usually connected with a wire bonding or ball bonding system. In these systems, the gold wire crosses a small capillary tube inside a ceramic tip that is connected to an electromechanical apparatus and a magnifying glass. The sample (with the alumina) is placed in hot plate that heats it up to 180-200°C. With the aid of the magnifying glass, the tip is positioned over the small metallic top contact of a given device of the sample and then the bonding is launched. When this happens, the tip approaches the sample until touching it, presses the gold wire against the contact applying at the same time ultrasonic vibrations, and then withdraws. If the process succeeds, the gold wire would be welded to the contact and the remaining

wire would slide through the capillary tube. The tip is then moved to a free copper pad of the alumina and the process is repeated, cutting the gold wire at the end and finishing the bonding process.

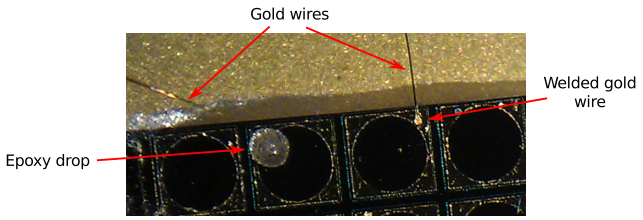

Figure 2.13: Spilled epoxy (left) and correct welded (rigth) wire bonding of two devices that use schema 1.

It might happen that the gold wire does not weld to the contact. In those cases, rather than keep trying which usually degrades the contact and the device, it is often better to make the bonding by hand using conductive epoxy of silver paint. This is a delicate operation that might lead in some cases to the spillage of the epoxy out of the contact. Specially in schema 1, where the bonding region is close to the optical window, this spilling normally partly covers the optical window and hence reduces the illuminated area in electroptical experiments. In Figure 2.13 we show a correct welded wire and a spilled epoxy contact of two devices in the sample. In general, epoxy contacts lead to higher contact resistance.

Bibliography

[1] A. Cho, "GaAs Epitaxy by a Molecular Beam Method: Observations of Surface Structure on the (001) Face," *Journal of Applied Physics*, vol. 42, no. 5, pp. 2074–2081, 1971.

[2] A. Cho, "Impurity profiles of GaAs epitaxial layers doped with Sn, Si, and Ge grown with molecular beam epitaxy," *Journal of Applied Physics*, vol. 46, no. 4, pp. 1733–1735, 1975.

[3] A. Taboada, *Controlling the shape, size and composition of III-V semiconductor nanostructures: quantum rings and quantum dots.* PhD thesis, Instituto de Microelectrónica de Madrid (CNM-CSIC), 2010.

[4] Y. González, *Crecimiento y caracterización de GaAs sobre Si por epitaxia de haces moleculares.* PhD thesis, Universidad Complutense de Madrid, 1991.

[5] H. Freller and K. Günther, "Three-temperature method as an origin of molecular beam epitaxy," *Thin Solid Films*, vol. 88, no. 4, pp. 291 – 307, 1982.

[6] A. Madhukar, "Far from equilibrium vapour phase growth of lattice matched III-V compound semiconductor interfaces: Some basic concepts and monte-carlo computer simulations," *Surface Science*, vol. 132, no. 1-3, pp. 344 – 374, 1983.

[7] N. W. Ashcroft and D. N. Mermin, *Solid state physics*. Toronto: Thomson Learning, 1 ed., Jan. 1976.

[8] A. Ohtake, "Surface reconstructions on GaAs(001)," *Surface Science Reports*, vol. 63, no. 7, pp. 295 – 327, 2008.

[9] A. Ohtake, M. Ozeki, T. Yasuda, and T. Hanada, "Atomic structure of the GaAs(001) $-$ (2×4) surface under As flux," *Physical Review B*, vol. 65, p. 165315, Apr 2002.

[10] V. P. LaBella, M. R. Krause, Z. Ding, and P. M. Thibado, "Arsenic-rich GaAs (001) surface structure," *Surface Science Reports*, vol. 60, no. 1-4, pp. 1 – 53, 2005.

[11] J. E. Mahan, K. M. Geib, G. Y. Robinson, and R. G. Long, "A review of the geometrical fundamentals of reflection high energy electron diffraction with application to silicon surfaces," vol. 8, no. 5, pp. 3692–3700, 1990.

[12] R. Farrow, *Molecular Beam Epitaxy - Applications to Key Materials*. William Andrew Publishing/Noyes, 1995.

[13] "Image reproduced from the website:." `www.las.inpe.br/~cesar/Infrared/rheed.htm`.

[14] J. Zhou, Q. Xue, H. Chaya, T. Hashizume, and T. Sakurai, "Surface ordering of the molecular beam epitaxially grown GaAs (001) 2x4 As reconstruction," vol. 64, no. 5, pp. 583–585, 1994.

[15] Y. Asaoka, "Desorption process of GaAs surface native oxide controlled by direct Ga-beam irradiation," *Journal of Crystal Growth*, vol. 251, no. 1-4, pp. 40 – 45, 2003. Proceedings of the Twelfth International Conference on Molecular Beam Epitaxy.

[16] J. H. Neave, P. J. Dobson, B. A. Joyce, and J. Zhang, "Reflection high energy electron diffraction oscillations from vicinal surfaces: a new approach to surface diffusion measurements," vol. 47, no. 2, pp. 100–102, 1985.

[17] J. M. V. Hove, P. R. Pukite, and P. I. Cohen, "The dependence of rheed oscillations on mbe growth parameters," vol. 3, no. 2, pp. 563–567, 1985.

[18] "More information about phosphorus allotropes can be found in the Wikipedia and references therein:." http://en.wikipedia.org/wiki/Allotropes_of_phosphorus.

[19] I. Rey-Stolle and C. Algora, "Analysis of wirebonding techniques for contacting high concentrator solar cells," *Advanced Packaging, IEEE Transactions on*, vol. 26, pp. 47 – 53, feb. 2003.

[20] M. Rei Vilar, J. El Beghdadi, F. Debontridder, R. Artzi, R. Naaman, A. Ferraria, and A. Botelho do Rego, "Characterization of wet-etched gaas (100) surfaces," *Surface and Interface Analysis*, vol. 37, no. 8, pp. 673–682, 2005.

[21] "A relation of etchants for III-V semiconductors and references can be found in:." http://terpconnect.umd.edu/~browns/wetetch.html.

[22] H. Proksche, G. Nagorsen, and D. Ross, "The Influence of NH_4F on the Etch Rates of Undoped SiO_2 in Buffered Oxide Etch," *Journal of The Electrochemical Society*, vol. 139, no. 2, pp. 521–524, 1992.

[23] H. Seidel, L. Csepregi, A. Heuberger, and H. Baumgärtel, "Anisotropic etching of crystalline silicon in alkaline solutions," *Journal of The Electrochemical Society*, vol. 137, no. 11, pp. 3612–3626, 1990.

[24] L. Allen, L. Hung, K. Kavanagh, J. Phillips, A. Yu, and J. Mayer, "Ohmic contacts to n-GaAs using In/Pd metallization," *Applied Physics Letters*, vol. 51, p. 326, 1987.

[25] F. Ren, "Use of Ti in ohmic metal contacts to p-GaAs," *Journal of Vacuum Science & Technology B: Microelectronics and Nanometer Structures*, vol. 13, p. 293, Mar. 1995.

[26] M. P. Patkar, T. P. Chin, J. M. Woodall, M. S. Lundstrom, and M. R. Melloch, "Very low resistance nonalloyed ohmic contacts using low-temperature molecular beam epitaxy of GaAs," vol. 66, no. July 1994, pp. 1994–1996, 1995.

[27] E. D. Marshall, B. Zhang, L. C. Wang, P. F. Jiao, W. X. Chen, T. Sawada, S. S. Lau, K. L. Kavanagh, and T. F. Kuech, "Nonalloyed ohmic contacts to n-GaAs by solid phase epitaxy of Ge," vol. 62, no. 3, pp. 942–947, 1987.

[28] G. Stareev, "Formation of extremely low resistance Ti/Pt/Au ohmic contacts to p?GaAs," vol. 62, no. 22, pp. 2801–2803, 1993.

[29] "More information about MOSFETs can be found in the Wikipedia and references therein:." http://en.wikipedia.org/wiki/MOSFET.

[30] N. Grant and K. McIntosh, "Passivation of a (100) silicon surface by silicon dioxide grown in nitric acid," *Electron Device Letters, IEEE*, vol. 30, pp. 922 –924, sept. 2009.

[31] C. Huang, J.-R. Chen, and S. Huang, "Silicon dioxide passivation of gallium arsenide by liquid phase deposition," *Materials Chemistry and Physics*, vol. 70, no. 1, pp. 78 – 83, 2001.

Chapter 3

Characterization Techniques

In this Chapter there is a review of the common characterization techniques used along the thesis work. The aim is to present the basic principles of the theory behind each technique and its implementation at Instituto de Microelectrónica de Madrid rather than going into much detail. Further information can be found in the corresponding references.

Contents

3.1 Photoluminescence spectroscopy (PL)

Photoluminescence spectroscopy is, probably, the most widely used technique to characterize semiconductor nanostructures. It gives a first

hint of the quality of the sample, the density of the nanostructures, their size, etc.

In its basic form it consists on illuminating the sample with an excitation source (normally a laser), whose energy is above the bandgap of the material, and recording the re-emitted light. The whole process can be divided into three steps (see Figure 3.1).

1. An electron absorbs a photon coming from the laser (γ_{ex}) and is promoted to the conduction band (CB), leaving a hole in the valence band (VB).

2. The electron (hole) rapidly loses part of its energy by emission of phonons and carrier-carrier interactions until it reaches the conduction (valence) band edge. During this step, carriers might be trapped by a nanostructure, losing more energy when they fall into an empty confined level. In general, carriers tend to reach the lowest energy level available. This process is called thermalization.

3. Finally, if the transition is allowed by the selection rules, the electron and hole recombine emitting a photon with an energy equal to the difference of the energy of the levels involved in the transition (γ_{pl}).

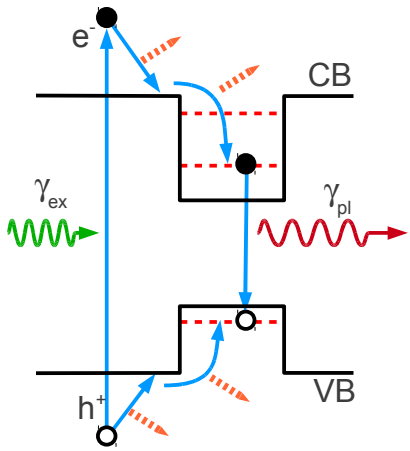

Figure 3.1: Description of the PL fundamentals

This simple picture is strongly influenced by several factors, which study represent the most interesting part of PL measurements. In general, we should have the following considerations:

1. **Emission energy**: The peak energy of the PL band is directly related with the energy levels involved in the transition. It gives information about the size, shape and composition of the nanostructures, all together, and the height of the confinement barriers.

2. **Width**: PL experiments performed in this work are *macro-PL* measurements, which means that we measure ensembles of thousands of nanostructures. Since they are self assembled, there is a dispersion in sizes and shapes that leads to a different transition energy for each nanostructure and, hence, to an inhomogeneous broadening of the PL peak.

3. **Intensity**: The PL intensity is consequence of a trade-off among several processes, each of them with a characteristic rate (k). The processes with larger rates will dominate the PL emission. Lets assume that we are interested in the PL emission from the electron ground state to the hole ground state (see Figure 3.2). The intensity will be larger if processes that populate ground state (process 1 or 1+2) and the radiative emission (process 3) are faster than those that depopulate ground state (processes 4 and 5) and non-radiative emission (process 6). A similar description can be done for holes. At low temperature, the characteristic time ($\tau = 1/k$) of processes 1 and 2 are on the order of picoseconds whereas process 3 is around 1 nanosecond. Processes 4, 5 and 6 are much slower. In Table 3.1 there is a summary of some of the things that affect these rates.

Figure 3.3 represent the photoluminescence setup at IMM. This system is characterized by its simplicity and versatility. There are three laser sources, described in table 3.2, whose light can be focused into an area of around 200 μm at the sample surface. Samples are mounted in a close cycle helium cryostat that allows to vary the temperature in the 20 K to 300 K range (APD Cryogenic Displex DE-201).

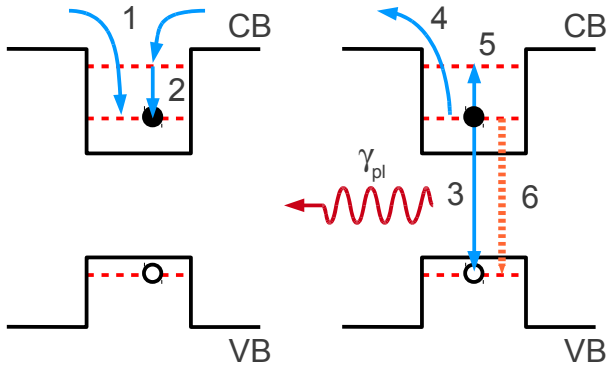

Figure 3.2: Processes that influence the PL intensity. (1) Relaxation from the matrix; (2) relaxation from an excited state; (3) radiative recombination; (4) thermal or tunnel extraction of carriers to the matrix; (5) thermal promotion of carriers to an excited state; (6) non radiative recombination processes (Auger recombination, carrier trapping by defects...)

PL radiation is dispersed with a 0.3 m Spectra Pro 2300i monocromator using a 600 grooves/mm grating and recorded with one of the three detectors available, depending on the application. The chosen output of the monocromator can be selected with a mobile mirror. The InGaAs array have 256 channels and work in the 900 to 1850 nm range (Hamamatsu G9205-256W). Its dark current decreases when it is cooled down to -20 C with a Peltier plate. The Ge photodiode works at a reverse bias of 300 V and can be used to detect PL emission with wavelengths between 700 and 1700 nm. It is refrigerated with liquid nitrogen (North Coast Scientific Corporation EO-817L). It is more sensitive that the InGaAs array but, being single channel, the acquisition times are much longer. To work with this detector the excitation source must be optically modulated at a certain frequency (around 177 Hz, in general), signal that is used as reference channel for a lock-in amplifier (EG&G Princeton Applied Research 5207). The germanium detector generates an output voltage, proportional to the signal intensity, that is recorded by the amplifier. The last detector is a photomultiplier tube (PMT), that can be used in place of the Ge detector (Hamamatsu H10330A-75). Due to its fast response, this detector is used mainly for time resolved measurements. The detection range goes from 950 to 1700 nm.

Table 3.1: Main factors that influence the PL intensity.

Oscilator strength	This gives the fundamental intensity of the PL peak and it is related with the overlap of the electron and hole wavefunctions and the selection rules of the transitions.
Defects	In general, defects of any kind represent traps and non-radiative recombination centres that reduce the PL intensity. In this way, the crystal quality of a sample *compared to another one* can be assessed, assuming that the other factors have a similar contribution.
Temperature	Carriers not only can emit phonons to relax into the nanostructures, but they can also absorb them and jump to an excited state or back to the surrounding matrix (4 and 5 in Figure 3.2). This process is governed by temperature and eventually quenches completely the PL.
Electric field	In some devices, nanostructures are in the presence of an electric field that might produce the tunnel of carriers out of them. Large electric fields increase the tunnel probability.

Table 3.2: Characteristics of the lasers used in this work. For the pulsed laser, P_{max} is the maximum average power at maximum repetition rate.

Brand/Model	λ (nm)	Type	P_{max} (mW)	Rate (MHz)
Alphalas, LDF1-808-3	808	CW	3000	-
SDL-537-LN-1000-T	532	CW	1000	-
PicoQuant, LDH-P-C-405	405	P	4	10-80

3.1.1 Time resolved photoluminescence (TRPL)

Conventional PL measurements give information about the properties of the sample averaged over time. However it can be desirable to study the dynamics of the carriers from the moment they are photogenerated, the thermalization process, the capture by the confined levels and the final

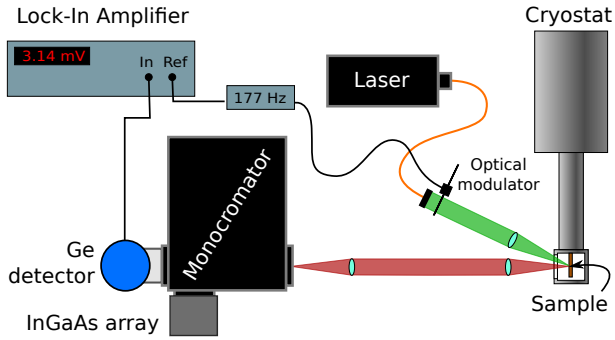

Figure 3.3: Schematic representation of the PL setup at IMM.

recombination by the emission of a photon. That information, essentially the values of the characteristic rates, can be accessed by means of time resolved PL measurements.

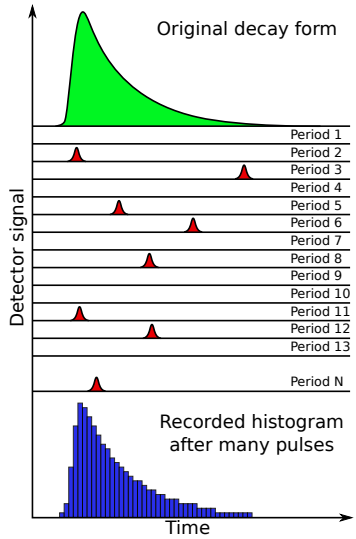

Figure 3.4: Illustration of the working principles of the TCSPC technique.[1]

In this kind of measurements, a pulsed laser with short pulse widths and high repetition rate (from 10 to 80 MHz in our case) is used as an excitation source and the photoluminescence is recorded with a fast

response photodetector (the PMT). Since typical rise and decay times in III-V semiconductor nanostructures are very fast, on the order of picoseconds and nanoseconds respectively, the full curve can not be measured at once by the detector, whose typical transit time spread is around 0.3 ns. A technique to overcome this limitation is the so called time correlated single photon counting (TCSPC).[1]

In this technique, only one (or none) photon is detected on each laser pulse repetition period (see Figure 3.4). The arrival time of the photon is recorded with a time resolution of ∼25 ps and the resulting data is stored as a histogram of photons *vs* the time delay relative to excitation.

Apart from the laser and the detector explained above, this technique also needs a correlation board that synchronizes the pulses of the laser and the photon counting detector, making the histogram in real time. We use a computer board Becker & Hickl SPC-130/134 and the SPCM software package, of the same company, for the data acquisition.

This data is not the real PL decay but it is actually convoluted with the temporal response of the experimental set-up $IRF(x)$, which includes its finite temporal resolution, the effect of lenses and gratings, laser afterpulses and any other effect not related with the carrier recombination process in the sample. The IRF is measured by directly recording the laser light dispersed in the copper holder inside the crysostat, next to the samples, to ensure that the optical path is the same in both cases. This light needs to be strongly attenuated to prevent damaging the detector. The relationship between the measured PL decay $I_{PL,exp}$ and the real PL decay I_{PL} is given by:

$$I_{PL,exp}(t) = \int_0^t IRF(x) I_{PL}(x)\,\mathrm{d}x \tag{3.1}$$

In order to get information about the decay times of the relevant processes, it is thus necessary to obtain I_{PL}, a deconvolution process that has been performed with a custom software named "Osgiliath".

Osgiliath: Photoluminescence time resolved analysis software

Osgiliath software has been developed using Matlab®.[1] The motivation was to create a standalone, easy-to-use, friendly and robust tool to perform the analysis of the PL decay curves measured in a TRPL experiment. Special attention has been paid to simplifying the visualization and deconvolution of series of measurements (TRPL *vs* temperature, wavelength...).

The program has been designed to work with the spectra provided by the SPCM software which includes the need for some extra information, such as the scale factor (SF) of each spectrum (SPCM normalizes the experimental signal to 32000 counts, providing externally the resulting scale factor) and the experimental window of measurement.

In Figure 3.5a we show the main window of the program. Roughly, it can be divided into eight parts (labelled A-H). In part A, there can be found buttons to load the TRPL spectra, the instrumental response (IRF) and the signal background, as well as global parameters that affect the fitting (background and IRF SFs, the color shift (CS) and measurements window width). In part B, there is a table that contains the loaded experimental spectra, the SF of each of them (introduced by hand) and a multiple choice list that allows to chose between two different decay models:

- **Multiexponential**: The PL intensity decay is defined by a sum of N exponentials with different characteristic times (τ_i) and prefactors (A_i).

$$I_{PL} = \sum_{i=1}^{N} A_i e^{-\frac{t}{\tau_i}} \tag{3.2}$$

- **Stretch exponential**: In this case, the PL intensity decay is defined by a continuous distribution of decay times, rather than few discrete values. The resulting decay has the following form:

$$I_{PL} = A e^{-\left(\frac{t}{\tau}\right)^{\beta}} \tag{3.3}$$

[1] "Osgiliath" comes from the name of the old capital of Gondor, in the imaginary universe created by J.R.R. Tolkien in "The Lord of the Rings" and related books.

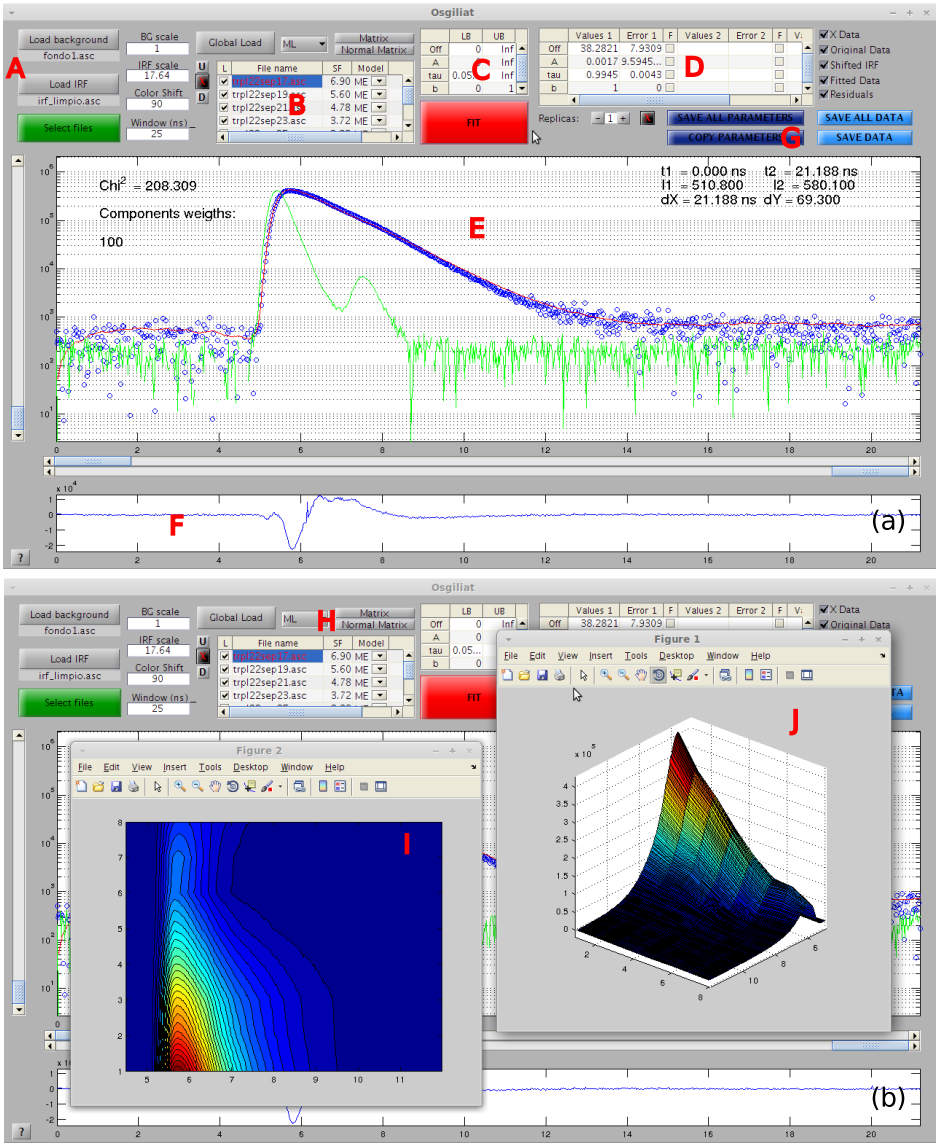

Figure 3.5: (a) Main window of the Osgiliat software. (b) Pop-up windows showing the 3D view of the TRPL series in contour and surface plot modes.

where τ is the most probable decay time and β the stretching parameter. More information about the derivation of this formula as well as on other decay time distributions can be found in Ref. [2–4].

The possibility of using a stretch exponential fitting is a unique feature of Osgiliath.

Next part, C, includes the upper and lower bounds of the parameters of the fitting, and in part D there are the parameter list with their values and errors for all components considered. Osgiliath does not set a limit on the number of components that can be used, although one or two are enough in most cases.

The central part of the Osgiliath window (E) is filled with the plot of the experimental data (blue, empty circles), the IRF (green line) and the fitted curve using the chosen model and conditions (red line). In the top left corner there is the value of χ^2 for the current fitting and the weight of each component, if more than one is used, defined as:

$$W_i = \frac{A_i \tau_i}{\sum_{j=1}^{N} A_j \tau_j} \times 100 \tag{3.4}$$

In the top right corner, there are the current marker positions which allow to restrict the fitting to a particular region of the curve. They can be modified with the horizontal sliders just below the plot. This is very useful in the case of having spikes or noise that affect the fitting without the need of modifying the data itself. The residual of the fitting is plotted in the lower part of the window (F), which allow to identify the regions that are not correctly reproduced by the fitted curve. The fitted curve and the resulting parameters, either of each individual spectrum or the whole series, can be saved using the settings and buttons of part G.

Finally, in Figure 3.5b we highlight two buttons in the upper part of the main window, H, labelled "Matrix" and "Normal Matrix". When pressed, they allow to visualise the whole series of data in a 3D plot (contour plot, I, or surface plot, J). The "Matrix" button plots the raw data whereas the "Normal Matrix" button normalise the spectra to unity before plotting them. The latter option is very useful to have, in a first sight, a qualitative idea of the evolution of the PL decay with the variation of a given parameter (for example, sample temperature).

The fitting of each spectrum typically completes in only a few seconds, with good accuracy and reproducibility. The structure of the program allows the fitted parameters of a spectrum to be inherited by the next one of the series, ensuring that there is not artificial dispersion of data by using initial values close to the optimum. Nevertheless, the result of the fit is barely sensitive to the initial values, which indicates good robustness of the algorithm.

Among the features that are planned to be incorporated before releasing the first stable version are:

- Including a filtering step for the input files, allowing the use of data recorded with a program different that SPCM.
- Improving the import of SPCM data and the dealing of trailing zeros in the spectrum.
- Including the possibility of using other decay models, apart from multiexponential and stretch exponential.
- Including the possibility of plotting the parameter resulting from the fitting.
- Including the option of global fit of the series, keeping some common parameters for all spectra and others varying in each of them.

3.2 Electroluminescence spectroscopy (EL)

Electroluminescence spectroscopy consist of injecting carriers from the electric contacts in a device (electrons from the n-region and holes from the p-region, if we consider a PN or PiN diode) and analysing the light emitted by the sample with a spectrometer. It shares most of the experimental set-up with PL but the carriers that recombine are not photogenerated with a laser but rather electrically injected by applying a bias to the sample. As it can be seen, to perform these measurements, the sample must be processed first in the form of a device and the cryostat must count with wall bushings for the electric contacts.

The information that can be extracted from the sample with this technique is very similar to that of PL, with some differences:

recombination takes places only in the semi-insulating region (the space charge region in a PN junction) where QDs are normally placed, thus avoiding parasitic signals coming from other parts of the structure.

The working principles of this technique are identical to those of the light emitting diodes (LEDs), which transform an electric current in usually monochromatic light due to recombination in the active region of the structure. It is also the starting point to design laser structures, where the spontaneous emission of LEDs becomes coherent and amplified within the material, giving rise to stimulated emission.

3.3 Photocurrent spectroscopy (PC)

Photocurrent spectroscopy is a characterization technique that consist on measuring the electric current produced in a device as a function of the wavelength of the incoming radiation. This radiation, if energetic enough, can promote electrons from the valence band to the conduction band, leaving a hole in the valence band. Contrary to PL measurements where we are interested in those carriers that recombine within the material, in this case we record the current generated by carriers that are able to reach the electric contacts of the device. Therefore, the information obtained with this technique is a combination of the absorption properties of the material and the transport capabilities of the device, from the point where carriers are generated to the contacts.

If the energy of the light is smaller than the energy gap of the barrier material it is possible to get photocurrent from transitions inside the nanostructures present in the sample (quantum dots, wells...). In general, this photocurrent is much smaller than the one produced in the bulk. The PC technique is very useful to study the excited energy levels of the nanostructures, normally not observed in PL measurements unless a very intense excitation source is used.

In general, all the phenomena described in the PL section are applicable here, although now we are interested in those processes that enhance the scape of carriers from the nanostructures. Referring to Figure 3.2, the PC recorded from the nanostructures will be larger if process 4 is more efficient that carrier trapping (1 and 2) and recombination (3 and 6).

At the IMM, the photocurrent system consist on a white light source

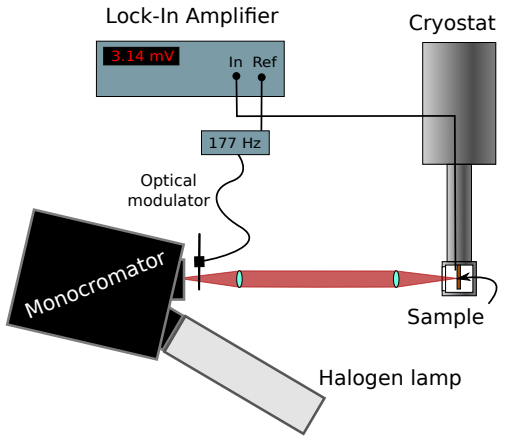

Figure 3.6: Schematic representation of the PC setup at IMM.

(100 W halogen lamp) connected to a 0.27 m SPEX 270M monocromator to select the wavelength of the incident radiation (Figure 3.6). This light is optically modulated and focused into the samples to a spot of around 400 μm in diameter. The samples are mounted in a close cycle helium cryostat that allows to vary the temperature in the 20 K to 300 K range (APD Cryogenic Displex DE-201). The cryostat counts with wall bushings to collect the photogenerated current and send it to a lock-In amplifier. To perform this kind of measurements, the samples need to be processed in the form of devices (pn, p-i-n or Schottky diodes). Normally each sample contains several devices although only one of them can be illuminated at a time.

3.4 Atomic force microscopy (AFM)

Atomic force microscopy is based in the interactions between a very sharp tip ($\sim$10 nm) and the surface of interest when the distance between them is on the order of nanometres. The relationship between the tip-surface distance and the interaction forces (electrostatic, Van der Waals, formation and braking of bonds between tip and surface, etc) can be used to get the topography of the samples. It is possible to obtain high resolution images of many materials (conductors, isolators,

semiconductors, polymers, biological...) with AFM without the need of any previous treatment. During the scanning time of the surface, an electronic feedback system records the bending of the small lever where the tip is place (cantilever). This bending can be measured from the reflection of a laser beam at the end of the cantilever, collected with a photodiode divided in four segments.

An AFM generally has two working modes: contact and dynamic (or tapping). In the former, also termed "static", the tip is in contact with the surface at all times. Assuming that the cantilever follows the Hooke's law ($F = -kx$), we can know the force experienced by the lever (F) from its bending (x) and the force contact (k). In contact mode, k must be in the interval 0.01-1 N/m in order to be flexible enough to give a measurable signal at the same time that its frequency of resonance is compatible with the typical scanning frequencies (1-5 Hz). A commonly used material of cantilevers that fulfil this condition is silicon.[5]

The dynamic mode reduces the friction force between the surface and the tip, which can be useful in soft samples. In this mode, a sinusoidal force with a frequency close to its first harmonic is applied to the cantilever with a piezoelectric transducer, producing its oscillation. When cantilever and surface get closer, the interaction between both changes the resonance frequency, affecting the amplitude and phase of the force oscillations. The comparison between these magnitudes before and after the interaction give the information about the sample. Cantilevers commonly used with this mode are tougher than those of constant mode. In the dynamic mode it is possible to work with modulated frequency and with modulated amplitude.[6, 7]

In this work we have used a Nanotec Cervantes AFM system, using both the contact mode and the modulated amplitude mode (see Figure 3.7). It has three main elements: the AFM head, the piezoelectric actuator and the electronic feedback system. The AFM head contains the laser, several lenses to adjust the laser beam direction, a holder for the cantilever and an small piezoelectric transducer in its base to excite the resonance frequency between 1 Hz and 2 MHz. The piezoelectric actuator allows to control the relative distance between the surface and the tip. The scanning range goes from 1 to 100 μm in the plane and from 3 to 5 μm in the vertical direction. The electronic feedback is controlled by a freeware

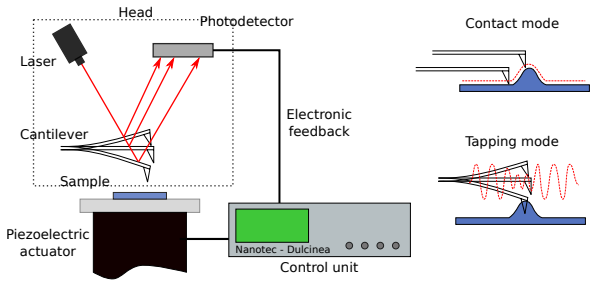

Figure 3.7: Schematic representation of the AFM setup. To the right, there is a detail of the path followed by the tip (red,dashed line) in contact and tapping modes (top and bottom, respectively). Figure taken and modified from Ref. [8].

software package, WSxM.[9] This same software, together with another freeware package, Gwyddion, have been used to process and analyse the data.[10]

3.5 Transmission electron microscopy (TEM)

Note: All TEM related micrographs and measurements have been performed by Prof. Sergio Molina's group, in the Departamento de Ciencia de los Materiales e Ing. Metalúrgica y Q. I. Universidad de Cádiz, Campus Universitario de Puerto Real, 11510 Puerto Real, Cádiz, Spain. (UCA)

From its development in 1932, electron microscopy has caused a large impact in a wide variety of fields, from biology to material analysis.[11–13] The main characteristic of transmission electron microscopy is the high resolution of the obtained images. It can be evaluated using the Reyleigh criterion for conventional microscopy that relates the smallest resolved distance (δ) with the wavelength of the radiation used as probe (λ).

$$\delta = \frac{0.61\lambda}{n\sin(\beta)} \tag{3.5}$$

where n is the refraction index of the medium and β the half collection angle of the magnifying lens. Since this angle is usually very small and the medium is air (n$\sim$1), in a TEM it is common to approximate Equation 3.5 by $\delta = 0.61\lambda/\beta$.[13] The electron wavelength can be related with its energy

by (ignoring relativistic effects):

$$\lambda \sim 1.22E^{-1/2} \tag{3.6}$$

As electrons are accelerated by an electrostatic potential, their energy is increased with the resulting reduction of the associated wavelength. A 100 keV electron beam would have an associated wavelength of $\lambda = 4$ pm, much smaller than the diameter of a atom. The real resolution of a TEM, however, is limited by many other factors, such as the ability of focused the e-beam. Despite this limitation, it is relatively easy to get high resolution images ($\sim$1 Å) at large magnification ($\sim 10^6\times$).

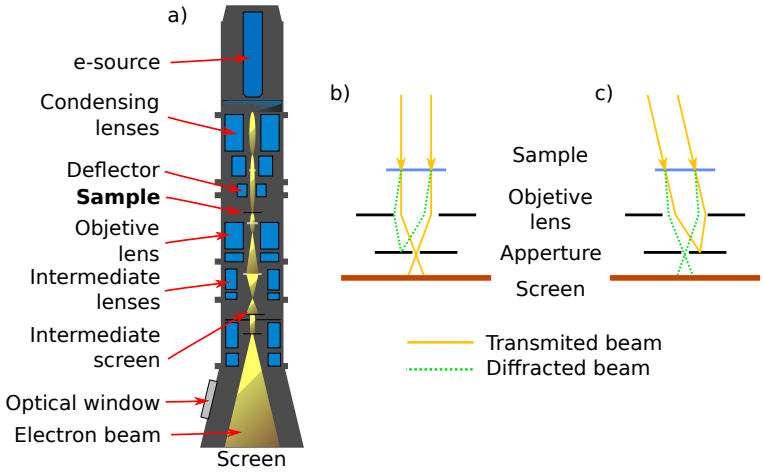

Figure 3.8: a) Schematic representation of a TEM microscope. b) Bright and c) dark field modes selected by the choice of the beam that forms the image. Figure adapted from Ref. [14]

Figure 3.8a shows a schematic representation of a TEM microscope. The beam is generated by a field emission or thermionic filament and accelerated along the microscope column by an electric potential of several hundreds kV. This beam is controlled by a series of magnetic lenses until it reaches the sample under study. After the sample, the objective lens form the final image.[12, 13]

In conventional TEM, only the transmitted beam or one of the diffracted beams (to form images in diffracted contrast mode) are used. To

select between one or the other working mode, an aperture is introduced between the objective lens and the screen: in bright field images the transmitted beam is selected (Figure 3.8b); in dark field images the diffracted beam is selected (Figure 3.8c).

It is possible to increase the resolution of TEM images by working in phase contrast mode. In this case, the magnitude of interest is the phase change produced in the electronic waves when they cross the thin sample. The image is formed with the interference of more than one beam in such a way that both, phase and amplitude, of the diffracted beams contribute to the image contrast.

The thinning process of the sample is critical and is divided into different stages: fracture of the crystal, thinning by mechanical polishing and thinning by focused ion beam until it is partly transparent to electrons. The thinning technology allows to take images in sections parallel and perpendicular to the growth front (planar TEM and cross section TEM, respectively).

Although this description has covered only the basic TEM functionality, more advanced TEM-based techniques are often found in the study of semiconductor nanostructures, such as high-resolution TEM (HRTEM), electron tomography or compositional analysis by Z-contrast imaging or energy dispersive x-ray spectroscopy (EDX).[15–18]

The cross-section TEM (XTEM) images shown in this thesis have been taken with a JEOL JEM-1200EX transmission electron microscope at the University of Cádiz, operated at 120 kV. Planar view images have been taken with a field emission JEOL 2010F transmission electron microscope, also at the University of Cádiz, at 200 kV. For the high angle annular dark field scanning TEM images (HAADF-STEM) it has been used an aberration-corrected NION ULTRASTEM at the Oak Ridge National Laboratory, TN, USA, operated at 100 kV.

3.6 X-ray diffraction measurements (XRD)

X-ray diffraction measurement is a common technique whose primary use (among many others) is to evaluate the structural quality of a crystalline structure. The basic working principles are as follows:[19]

When an X-ray beam reaches the sample surface it is reflected by the

crystal planes. The reflected beams can then interfere giving maximum values at well defined angles θ_c which are given by Bragg's Law:

$$n\lambda = 2d \sin\theta_c \tag{3.7}$$

where d is the distance between atomic planes, λ is the wavelength of the x-ray beam, n is an integer and θ the angle between the incident beam and the atomic planes (Figure 3.9a). Therefore, it is possible to measure the distance between atomic planes by measuring the position of the maximum of intensity, information that can be related with the material composition. In Figure 3.9a it can be seen the parameters that appear in Equation 3.7 and also ω which is the angle between the incident beam and the sample surface. If the atomic planes under study are parallel to the sample surface, $\omega = \theta$ and we talk about a symmetric reflection. Otherwise, $\omega \neq \theta$ and they are asymmetric reflections.

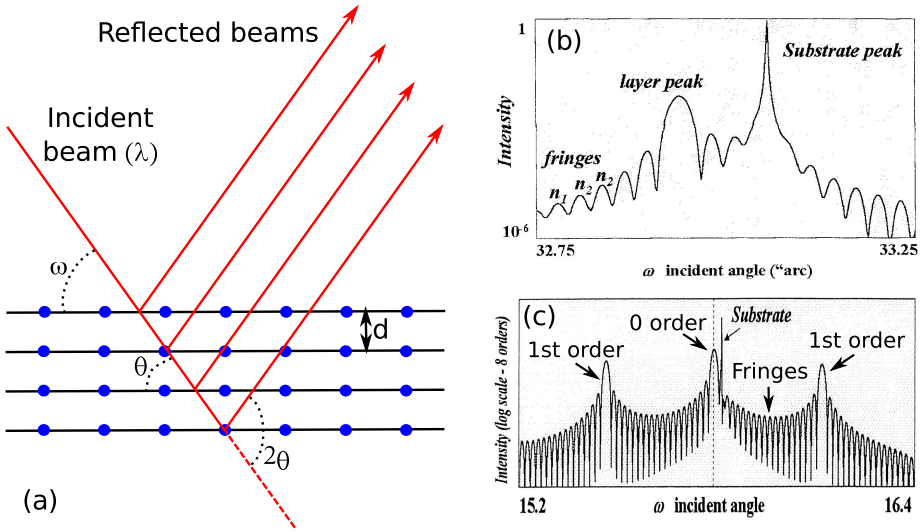

Figure 3.9: (a) Schematic representation of the x-ray reflection by different atomic layers which leads to the interference pattern. (b) Portion of a XRD spectrum of a single crystalline strained layer on a substrate. (c) Portion of a XRD spectrum of a multilayer structure. Spectra adapted from Ref. [19]

In semiconductor epitaxial heterostructures one often has a combination of lattice mismatch materials, the substrate material and the

layer material. If the lattice mismatch is small and the layer is strained on the substrate, it gives rise to an additional peak in the diffraction pattern close to the substrate peaks (Figure 3.9b). Assuming a symmetric reflection, it can be seen that the average out-of-plane strain $\langle\epsilon_\perp\rangle$ of the layer with respect to the substrate is given by:

$$\langle\epsilon_\perp\rangle = \frac{\sin\theta_{cL} - \sin\theta_{cS}}{\sin\theta_{cL}} \tag{3.8}$$

This perpendicular strain can be related with the in-plane strain and the lattice parameter of the layer a_L using a modified Poisson's ratio $\nu = -2C_{12}/C_{11}$, with C_{ij} the layer stiffness constants, leading to:[20]

$$\langle\epsilon_\perp\rangle = \nu\left\langle\epsilon_\parallel\right\rangle = \nu\frac{a_L - a_S}{a_L}. \tag{3.9}$$

It should be noted that the stiffness constants and the lattice parameter of the layer are composition dependent, so assuming a certain dependence of that composition on constituent materials (typically Vergard's law) it is possible to estimate the average composition of the layer.

Around the layer peaks, there will be a collection of small peaks (or fringes) due to multiple reflections of the beam within the layer. If the position of the layer peak gives information of the atomic planes spacing within the layer (hence on the strain and the layer composition), the separation of two fringes gives information about its thickness L from:

$$L = \frac{(n_1 - n_2)\lambda}{2(\sin\omega_1 - \sin\omega_2)} \tag{3.10}$$

where n_1 and n_2 are the fringes index (integer) and ω_1 and ω_2 their corresponding angular positions, respectively.[2]

Likewise, if a combination of layers is repeated several times we have a multilayer structure. In this case, there will be the substrate peak, the first order satellite peak (related with the average strain of the multilayer), several other satellite peaks representing the reflection within the multilayer (the separation between these peaks gives the multilayer thickness) and, again, a collection of fringes that are related with the individual layer thicknesses within the periodic structure (Figure 3.9c).

[2]This equation is valid only for scattering from planes parallel to the sample surface.

This simple picture is normally strongly influence by many factors such as partial relaxation of the layers, not-abrupt interfaces, tilting of the atomic planes, thermal vibrations, defects of any kind and the instrument resolution, itself. In general, in order to reproduce the XRD spectra, simulations that use a more complex general x-ray scattering theory by real crystals need to be used which, in addition, often incorporate some of the aforementioned factors.

We use a Phillips X'Pert system, using the Cu Kα line and a 4-crystal Ge (220) monochromator to increase the collimation and monochromaticity of the beam. High resolution is achieved by including a triple-axis crystal analyser in the output beam. The spectra analysis and simulation is done by the PANalytical X'Pert Epitaxy Software.

3.7 Fourier transform infrared spectroscopy (FTIR)

This spectroscopy allows to measure the absorption spectrum of a sample in the mid-infrared range (2-15 μm).[21] Contrary to the PC spectroscopy, in which the sample is illuminated with a single wavelength at a time, in FTIR the sample is illuminated with a broadband spectrum containing many wavelenghts, and the measurement is performed many times with a slightly different spectrum. The spectra used to illuminate the sample are created from an incandescent element at around 3000 K (close to an ideal black body) and a Michelson-type interferometer which allows to vary the wavelength composition of each spectrum. In Figure 3.10a we show a schema of the set-up.

The light created by the element is divided in the beam splitter into two perpendicular beams of equal intensity. This beams reflect in the corresponding mirrors and return to the beam splitter where they interfere. For each wavelength there is constructive interference at optical path differences given by $x = n\lambda$, with n an integer, whereas there is destructive interference at $x = (2n-1)\lambda/2$. Thus varying the position of the mobile arm of the interferometer, there is a different wavelength composition of the spectrum that finally reaches the sample and we can get its absorption spectrum as a function of the optical path difference, that is, the interferogram (Figure 3.10b). In order to have the absorption as a function

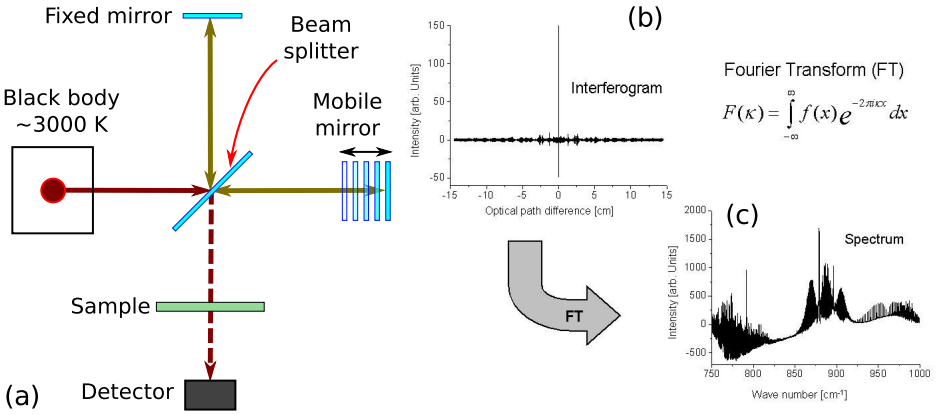

Figure 3.10: (a) Schematic representation of the FTIR set-up. (b) Interferogram and (c) spectrum of a sample after fourier transform the interferogram. Images (c) and (d) are reproduced from [22].

of wavenumber $(1/\lambda)$, wavelength or energy, which are more intuitive unities, it is necessary to apply a Fourier transform to this interferograms, leading to the resulting absorption spectrum (Figure 3.10c).

Apart from light absorbed in the sample, which is the magnitude of interest, there might be light reflected or scattered by the sample surface, intensity inhomogeneities for different waveleghts, artefacts of the set-up, spurious absorption due to the components of the air or the optical windows... For all this reasons, the measured spectra are always normalized by the spectrum measured in the absence of a sample and, typically, also normalised by the spectrum of a reference sample without the absorbers of interest but with similar based material, thickness and treatment. In order to reduce surface scattering, samples have to be mirror-polished using sub-micron polishing plaste.

The equipment used to perform these experiments is a Jasco FTIR 460 Plus system belonging to the Quantum Optics group (Experimental Solid State Physics), lead by Prof. Chris Phillips, at Imperial College London.

Bibliography

[1] W. Becker, *The bh TCSPC Handbook (4th Edition)*. Becker & Hickl GmbH, 2010.

[2] M. Berberansantos, E. Bodunov, and B. Valeur, "Mathematical functions for the analysis of luminescence decays with underlying distributions 1. Kohlrausch decay function (stretched exponential)," *Chemical Physics*, vol. 315, pp. 171–182, Aug. 2005.

[3] A. van Driel, I. Nikolaev, P. Vergeer, P. Lodahl, D. Vanmaekelbergh, and W. Vos, "Statistical analysis of time-resolved emission from ensembles of semiconductor quantum dots: Interpretation of exponential decay models," *Physical Review B*, vol. 75, pp. 1–8, Jan. 2007.

[4] M. N. Berberan-Santos, "A luminescence decay function encompassing the stretched exponential and the compressed hyperbola," *Chemical Physics Letters*, vol. 460, pp. 146–150, July 2008.

[5] T. Albrecht, S. Akamine, T. Carver, and C. Quate, "Microfabrication of cantilever styli for the atomic force microscope," *Journal of Vacuum Science & Technology A: Vacuum, Surfaces, and Films*, vol. 8, no. 4, pp. 3386–3396, 1990.

[6] T. Albrecht, P. Grutter, D. Horne, and D. Rugar, "Frequency modulation detection using high-Q cantilevers for enhanced force microscope sensitivity," *Journal of Applied Physics*, vol. 69, no. 2, pp. 668–673, 1991.

[7] Y. Martin, C. Williams, and H. Wickramasinghe, "Atomic force microscope–force mapping and profiling on a sub 100-Å scale," *Journal of Applied Physics*, vol. 61, no. 10, pp. 4723–4729, 1987.

[8] A. G. Taboada, A. M. Sánchez, A. M. Beltrán, M. Bozkurt, D. Alonso-Álvarez, B. Alén, A. Rivera, J. M. Ripalda, J. M. Llorens, J. Martín-Sánchez, Y. González, J. M. Ulloa, J. M. García, S. I. Molina, and P. M. Koenraad, "Structural and optical changes induced by incorporation of antimony into InAs/GaAs(001) quantum dots," *Phys. Rev. B*, vol. 82, p. 235316, Dec 2010.

[9] I. Horcas, R. Fernandez, J. Gomez-Rodriguez, J. Colchero, J. Gómez-Herrero, and A. Baro, "WSxM: A software for scanning probe microscopy and a tool for nanotechnology," *Review of Scientific Instruments*, vol. 78, p. 013705, 2007.

[10] "Gwyddion web page:." `http://gwyddion.net`.

[11] M. Knoll and E. Ruska, "Das elektronenmikroskop," *Zeitschrift f ″ur Physik A Hadrons and Nuclei*, vol. 78, no. 5, pp. 318–339, 1932.

[12] L. Reimer and H. Kohl, *Transmission electron microscopy: physics of image formation*, vol. 36. Springer Verlag, 2008.

[13] D. Williams and C. Carter, "The transmission electron microscope," *Transmission Electron Microscopy*, pp. 3–22, 2009.

[14] A. M. Beltrán, *Efecto de la incorporación de antimonio sobre la nanoestructura de puntos cuánticos III-V/III-V*. PhD thesis, Universidad de Cádiz, 2009.

[15] D. J. Smith, "The realization of atomic resolution with the electron microscope," *Reports on Progress in Physics*, vol. 60, no. 12, p. 1513, 1997.

[16] J. Frank, *Electron tomography: Three-dimensional imaging with the transmission electron microscope*. Plenum Pub Corp, 1992.

[17] S. Molina, D. Sales, P. Galindo, D. Fuster, Y. González, B. Alén, L. González, M. Varela, and S. Pennycook, "Column-by-column compositional mapping by z-contrast imaging," *Ultramicroscopy*, vol. 109, no. 2, pp. 172–176, 2009.

[18] D. Zhi, H. Davock, R. Murray, C. Roberts, T. Jones, D. Pashley, P. Goodhew, and B. Joyce, "Quantitative compositional analysis of InAs/GaAs quantum dots by scanning transmission electron microscopy," *Journal of Applied Physics*, vol. 89, p. 2079, 2001.

[19] P. Fewster, *X-ray Scattering from Semiconductors*. Imperial College Press, 2000.

[20] N. Ekins-Daukes, K. Kawaguchi, and J. Zhang, "Strain-balanced criteria for multiple quantum well structures and its signature in x-ray rocking curves," *Crystal Growth & Design*, vol. 2, no. 4, pp. 287–292, 2002.

[21] P. Griffiths and J. Haseth, *Fourier transform infrared spectrometry*. Chemical analysis, Wiley-Interscience, 2007.

[22] "Institute for Meteorology and Climate Research - Atmospheric Trace Gases and Remote Sensing (IMK-ASF):." `http://www.imk-asf.kit.edu/english/450.php`.

Chapter 4

Accumulated stress measurements

In this chapter we introduce the fundamentals of the mechano-optical stress sensor technique, that will be used in the following chapters to characterise and optimise the fabrication of strain balanced QDs and QPs structures. We begin the chapter with an historical introduction to the technique, its fundamentals and its current implementation at the IMM (Section 4.1). Then, we apply this technique to the characterization of single InAs/GaAs QDs layers (Section 4.2), performing later a series of studies about the In migration and segregation processes (Sections 4.3 and 4.4). The chapter ends with the characterization and calibration of the growth of GaAsP layers that will be used as strain compensating material (Section 4.5).

Contents

4.1 Mechano-optical stress sensor: theory

4.1.1 Fundamentals of the technique

Despite it was introduced back in the early 90's by Schell-Sorokin and Tromp, the mechano-optical stress sensor (MOSS) technique has never been a very extended characterization method in MBE systems.[1] The kind of information that can be extracted with this technique is very broad and ranges from the anisotropic strength of the surface reconstructions, [2] the study of QDs, QWRs and quantum rings formation,[3, 4] the formation and evolution of dislocations and plastic deformation processes,[5, 6] material amorphization during ion bombardment [7] or thermal expansion processes in thin films [8]. The information recorded with MOSS is directly related with the morphology of the deposited layers and hence is very valuable for being *in-situ* and, above all, in real time.[1]

The MOSS technique consist on measuring the variations in the stress of a sample during the epitaxial growth by monitoring the changes in its curvature. This is probed by measuring the sample bending using to that purpose the deflection of a laser beam on its surface. This

[1]Part of the fundamentals of the MOSS technique that follows has been adapted from Dr. M. Ujué González's thesis, with permission from the author.[9]

method is easy to implement inside a MBE reactor since all the optics and detection apparatus are outside the vacuum chamber. The sample has to be lever-shaped and fixed from one of its ends to a special sample holder. An aperture of enough size made on the center of the holder allows the lever to bend freely (Figure 4.1a). This particular requirements of the holder and the sample itself is probably what prevents a general implantation of the technique in commercial MBE reactors.

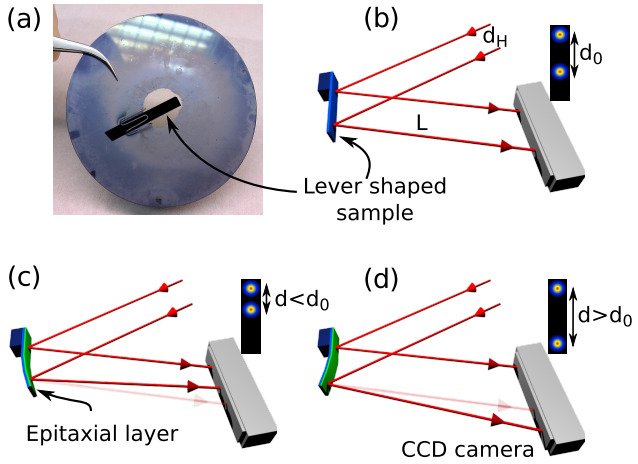

Figure 4.1: (a) Special sample holder for the MOSS technique, with an aperture in the center and the sample fixed by one end with a tungsten clip. Relationship between the material growth an the position of the reflected spots. The separation of the reflected spots is (b) constant (no stress accumulates), (c) becomes smaller closer (tensile stress) and (d) becomes larger (compressive stress)

More commonly, two parallel laser beams hit the sample in a direction perpendicular to the surface, one on the fix end and the other on the free one (Figure 4.1b). If substrate bends, we can measure the deflection of the beam that hits the free end with respect to the fix one. Using two beams reduces the noise associated with mechanical vibrations and small temperature variations. The deflection can be recorded collecting the reflected laser beams with a large area CCD camera. The substrate

curvature can then be calculated as (Stoney's equation):[10]

$$\Delta\left(\frac{1}{R}\right) = \frac{(d - d_0)\cos\alpha}{d_H 2L} \tag{4.1}$$

where d is the distance between the spots in the CCD camera, d_0 the initial distance between spots, d_H is the separation between the laser beams, L the sample-detector distance, α is the incidence angle and $\Delta 1/R$ is the substrate curvature variation. If the deposited layer material has a lattice parameter smaller than the substrate, then it suffers a tensile stress and the substrate bends, acquiring a concave curvature ($\Delta 1/R < 0$) (Figure 4.1c). On the contrary, if the lattice parameter of the deposited layer is larger than the substrate, the strain is compressive and the substrate becomes convex ($\Delta 1/R > 0$) (Figure 4.1d).

Before the plastic limit, where the sample suffers from partial relief of accumulated stress through the formation of dislocations, changes in the substrate curvature and the accumulated stress can be related by means of a modified version of the Stoney's equation, to include the biaxial character of the stress in the thin layers:[11]

$$\left(\frac{1}{R}\right) = -\frac{6(1 - \upsilon_S)\sigma h}{Y_s h_S^2} = -\frac{6 M_S \sigma h}{h_S^2} \tag{4.2}$$

where R is the curvature radius, h is the thickness of the deposited layer, h_S is the substrate thickness, σ the stress in the layer and $M_S{=}(1{-}\upsilon_S)/Y_S$ the biaxial modulus that relates the Young modulus Y_S and the Poisson modulus υ_S. This equation is valid only under the following conditions:[12, 13]

1. The thickness of the deposited layer and the substrate are much smaller than their lateral dimensions.

2. The thickness of the deposited layer is much smaller than the substrate.

3. The stress induced by the layer does not have a component in the direction normal to the sample surface.

4. Substrate material is linearly elastic, homogeneous and isotropic. The deposited layer must also be isotropic.

5. Edge effects are negligible and physical properties are homogeneous in planes perpendicular to the interface.

6. The strain and shear deformations are negligible, in such a way that layer and substrate are within the elastic limit at all times.

7. Substrate has no constraints to bend in neither of the two directions.

Not all of these conditions are satisfied in typical MOSS set-ups but there are approximately fulfilled under some conditions. For instance, the last condition is no fully satisfied in the set-up used at the IMM. As we use lever shaped substrates with one end fixed to the holder, we constrain the bending along the short side. However, if the lever satisfies $b > 3a$, with b and a the dimensions of the long and short sides, respectively, then the deformation in the transverse direction will not influence the bending along the long axis.[12, 14]

On the other hand, the crystal structure of the materials used in this work do not allow to fulfil the condition of isotropy (condition 4). Equation 4.2 is not valid and it must be adjusted to the experimental conditions, taking into account the crystal orientation of the interface and the elastic constants of the material in the direction along which the curvature is measured. In this way, the biaxial modulus becomes:

$$\frac{1-\upsilon_S}{Y_s} \equiv M_S = c_{11} + c_{12} + 2\frac{c_{12}^2}{c_{11}} \tag{4.3}$$

where c_{ij} are the substrate elastic constants. Rearranging Equation 4.2 for uniaxial stress along the [110] and [1-10] directions:

$$\left(\frac{1}{R}\right) = -\frac{6\sigma h}{h_S^2}\frac{M_S + 2c_{44}}{4M_S c_{44}} \tag{4.4}$$

The value of c_{44} is approximately $M_S/2$ so the error introduced by using Equation 4.2 instead of 4.4 is less than 2%.

Until now, we have considered the accumulated stress introduced by a layer in a static situation. However during a MBE growth the stress variation might be due to changes in the deposited layer thickness, changes in its stress or even the surface reconstruction. If the thickness of a layer

changes dh in a time $t + dt$, we can use a differential form of equation 4.2:

$$\frac{M_S h_S^2}{6} \frac{d\,(1/R)}{dt} = \sigma(z = h, t)\frac{dh}{dt} + \int_0^h \frac{d\sigma}{dt} dz + [\Delta\tau_S] \tag{4.5}$$

The right hand side of this equation has three terms. The first one describes changes in stress associated to an increase of thickness dh in a time interval $[t, t+dt]$. The second term accounts for relaxation processes in the already deposited layer at the time t. Finally, the third term is related with changes in the surface stress. We can define the accumulated stress at the time t as:

$$\Sigma\sigma[h(t)] = \sigma(z = h, t)\frac{dh}{dt} + \int_0^h \frac{d\sigma}{dt} dz = \int_0^{h(t)} \sigma(z) dz \tag{4.6}$$

Substituting Equation 4.6 in 4.5 we obtain:

$$\frac{M_S h_S^2}{6} \frac{d\,(1/R)}{dt} = \Sigma\sigma[h(t)] + [\Delta\tau_S] \tag{4.7}$$

As it can be seen, the magnitude measured in this experiments is the sum of the accumulated stress and the stress associated to changes in the surface reconstruction. Finally, combining Eq. 4.1 and 4.7 with $\alpha \simeq 0$, we obtain:

$$\Sigma\sigma(t) = \Sigma\sigma[h(t)] + [\Delta\tau_S] = \frac{M_S h_S^2}{6} \frac{(d - d_0)}{d_H 2L} \tag{4.8}$$

4.1.2 MOSS set-up at the IMM

The most common method used in the past to measure the deflection is to record the reflected laser beams with two segmented detectors.[2–6] However, as mentioned before, in this work we use a large area, high resolution, CCD camera to record directly the two reflected lasers beams, which has several advantages over the one based on segmented detectors. On the one hand, the optical alignment is considerably easier since there is only one detector to be put in place to record both beams. On the other hand, it has larger dynamical range, as the reflected spots are recorded at all times regardless of their separation and exact positions (within a reasonable range). Finally, it has larger resolution without the need of low noise amplifiers or other extra equipment.

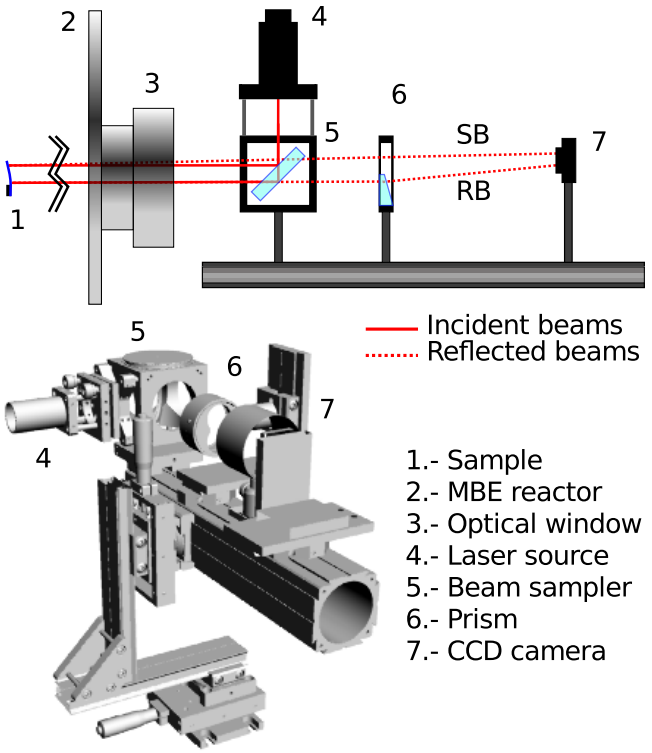

Figure 4.2: Schematic representation of the MOSS set-up, indicating the different parts of the system.

Figure 4.2 shows a detailed schema of the MOSS system available at the Instituto de Microelectrónica de Madrid (IMM). The laser source (608 nm) produces an intense beam that hits a beam sampler whose thickness determine the separation between two perfectly parallel beams of similar intensity. The beams cross the optical window of the MBE reactor and reach the sample perpendicularly to its surface. The reference beam (RB), hits the fix end of the sample so its reflection is not disturbed by the growth process. The signal beam (SB), on the other hand, hits the free end and its reflection is affected by the bending of the sample and hence by the stress accumulated during growth. The measurement of the reflected beams is performed in a backscattering geometry, minimizing the error introduced by the approximation made in Equation 4.8. The lever is fixed to the

holder by means of a tungsten clip, previously baked to remove as much impurities and physisorbed atoms as possible.

The SB reaches directly the CCD whereas the RB crosses a prism to change its trajectory and send it to the camera. This prism is of capital importance in the set-up and allows the use of a CCD camera instead of the segmented detectors. Even in the case of the beams been reflected perfectly parallel, the distances between the spots would be of around 1 cm. In a more realistic case, where the beams diverge due to the deflection of the lever, the separation at a reasonable distance from the sample surface ($\sim$1 m in our case) could be of several cm, too large for most CCDs. Since the accumulated stress measurements depends only on the distance difference between the spots and not on their absolute value, this approach does not have any effect in the results.

We use a SpotOn CCD camera of Duma Optronics Ltd. and their acquisition software to get a beam positioning with sub-micron resolution. The distance between spots is sent to a custom software that converts it into accumulated stress, in real time, by means of Equation 4.8.[2] This software also records the opening and closing of the effusion cell shutters, giving an exact match between the accumulated stress evolution and the materials growth. With this information, and assuming a typical distance of L = 975 mm between sample and detector, d_H = 8 mm as the initial separation of the laser beams, and using the parameters characteristic of our substrates (GaAs, thickness h_S=100 μm, M_S = 124 GPa), we obtain a maximum resolution of 0.02 N/m. This high resolution is normally not attainable due to vibrations and noise in the environment. Mechanical vacuum pumps, either from the MBE reactor or from nearby equipments, have the most detrimental effect and must be disconnected in order to perform high quality measurements. The real resolution in our system is normally between 0.05 and 0.1 N/m.

[2]This software was developed by Dr. A. Rivera de Mena, former member of the MBE group at the IMM.

4.1.3 Limitations of the technique

Thermal homogeneity along the lever

One of the main drawbacks of this technique is the remote thermal anchoring of the samples, which are in contact with the sample holder only by one of its ends. If thermal coupling between sample and holder is not good, the temperature of the former will not correctly follow the changes induced by the heater, even though part of the sample heating is by direct radiation from the tungsten filament. Moreover, there will be a thermal gradient along the sample thus changing the properties of the growth material in different positions of the lever. Since the MOSS technique averages the stress that accumulates along the lever, it is important to keep the physical properties as homogeneous as possible in order to have representative values of the growth conditions.

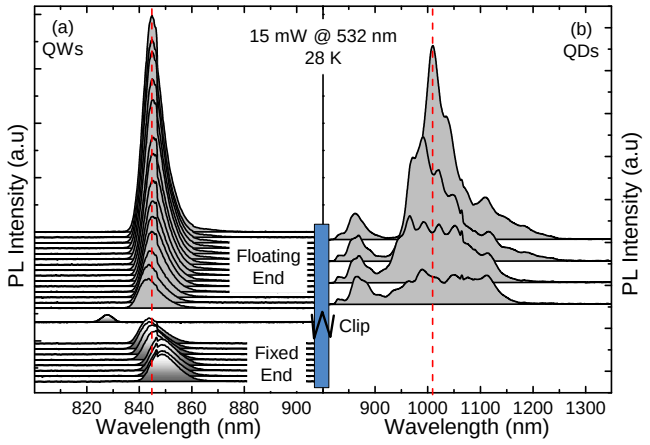

Figure 4.3: PL spectra recorded at different points of a lever in a (a) QW stack and (b) QDs stack.

To illustrate the effect of a poor thermal coupling, in Figure 4.3 we show the PL signal recorded at different points of the lever in two samples where we have fabricated a stack of QWs and of QDs. For the QWs (Figure 4.3a), it can be observed a reduction of the PL intensity as we approach the tungsten clip and, when we are really close, also a blue-shift in the peak position. The blue-shift can indeed be attributed to the

temperature gradient, although the reduction of the PL intensity is more probably related with contamination of the sample with impurities coming from the clip. In the QDs sample, the effect is more prominent. The PL first broadens and then splits into a collection of many Gaussian peaks with wavelengths ranging from 950 nm to 1150 nm. The integrated PL intensity also reduces.

The strong impact into the QDs optical properties is understandable since QDs structural properties (size, shape and composition) depends critically on the growth temperature. Having a dispersion of the substrate temperature will also lead to a large QDs inhomogeneity within the same layer and among different layers of the stack and thus the observed optical properties.

In order to increase the homogeneity of the temperature along the sample, it is convenient to have as much lever in contact with the holder as free. In addition, it helps to keep the free end as short as possible, within the previous stated requirement of $b > 3a$. Nevertheless, some inhomogeneity is inevitable and it is a good practice to check with RHEED the surface reconstruction of the sample in order to asses its extent.

A typical temperature difference between the clip and the free end of the lever is around 20 K.

Precision of geometrical parameters

Another source of errors in the MOSS technique is the precision of the geometrical and material values that enter into Equation 4.8. The biaxial modulus M_S has a generally accepted value that is tabulated so it is error free, in principle. The separation of the spots in the CCD camera $d - d_0$ is measured with submicron resolution so it can also be considered exact. The separation between the lever and the camera L is typically of around 1 m with a precision of millimetres, which introduces a relative error $<1\%$. Finally, we are left with the initial separation of the spots and the substrate thickness.

The former has typical values of 8-10 mm and is measured with a ruler (absolute error = ± 0.5 mm), so the relative error it introduces in the MOSS signal is around 6%. Substrates we use are nominally 100 μm thick, but the dispersion around this value according to the manufacturer specifications is ± 25 μm. Given that substrate thickness is squared in Equation 4.8, the

relative error of the measured accumulated stress, assuming a 25% error in the substrate thickness, is of 50%.

In order to circumvent this problem, the thickness of each lever used in this work has been measured after the growth with a precision of about 1 μm and the MOSS data corrected in consequence. This reduces its impact into the data precision to bout 1%, which is reasonable.

After all this considerations, the relative error due to the uncertainty in the geometrical parameters is typically of 8%.

4.2 Calibration of the accumulated stress by a QD layer

In order to use MOSS to study and optimize the strain balanced quantum dots, it is necessary first to calibrate the stress that introduces a single QDs layer. In this section we study this topic and the dependence of the accumulated stress on the growth conditions and parameters, such as substrate temperature or In coverage.

4.2.1 Temperature dependence

The substrate temperature plays a major role in the kinematics of QDs formation, In migration and desorption. Within a relatively narrow temperature range, it is possible to move from large, sparse QDs at high T_S to tiny but very dense QDs at low T_S or even to the complete suppression of its formation at even higher or lower values. It is thus expected that the substrate temperature had an important impact into the stress accumulated in the lever and recorded by MOSS.

In Figure 4.4 we show the evolution of the total accumulated stress as we grow an InAs QD layer for different substrate temperatures (2 ML of InAs). As it was found by Silveira *et al*, four regions can be distinguished:[3] Region I: InAs begins to grow layer by layer, increasing the compressive stress smoothly; Region II: just at the critical thickness, surface relaxes and QDs nucleate (monitored by RHEED). The remaining deposited In keeps floating on the surface or incorporates to the existing islands but without increasing the stress; Region III: during capping this remaining In incorporates, suddenly increasing the accumulated stress; and

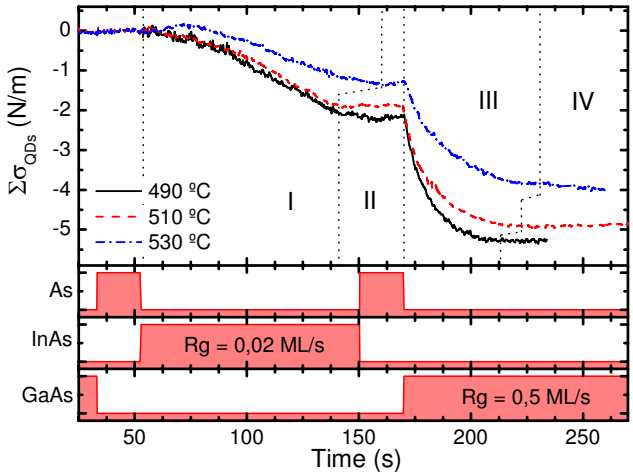

Figure 4.4: Stress accumulated during the formation of QDs after 2 ML of InAs. The lower part of the figure shows the materials that are growing at each time.

Region IV: when In is exhausted, GaAs grows without any further change in the stress.

Several things can be observed in these curves. Firstly, it can be seen that for the largest temperature (530 °C), QDs nucleation does not occur during InAs growth but rather during the short pause under As flux, being the stress that is accumulated at that point much smaller than for lower temperatures (∼1.4 N/m *vs* 1.9-2.2 N/m). Secondly, the final stress that the 2 ML of InAs accumulate after capping also differs, being again smaller for the largest temperature.

This dependence of the stress with temperature suggests two different phenomena. On the one hand, it is known that at these temperatures In atoms desorb from the sample surface, reducing thus the total amount of In that is incorporated to the crystal. According to Heyn *et al.*, InAs QDs are stable for over 5-10 minutes at low temperatures (<520 °C), but that around 535 °C the desorption rate of In from QDs is strongly accelerated, leading to their disappearance in few tenths of seconds. This cut-off temperature and the desorption time was found to be also dependent on the As pressure, being much faster (<10 s) in the absence of As even at 490 °C.[15, 16]

Martin-Sánchez studied this topic in his thesis and found that even

though the QDs disappear following a similar law to that found by Heyn, the complete removal of all deposited In incorporated in the form of a 2D layer (the WL) was slower.[17] According to his experiments, the desorption rate of In in the case of a 2D layer was 0.0006, 0.0012 and 0.0027 ML/s for the temperatures 490 °C, 510 °C and 530 °C respectively.

Following this reasoning, it is clear that the stress that nominally 2 ML of InAs accumulate should be temperature dependent, since the amount of In that really incorporates to the sample is smaller at high temperatures, either by a slow desorption of the WL or a faster desorption from the QDs or, possibly, the floating In. As an example of the lower limit of this desorption, lets estimate the amount of In that the sample loses during the InAs growth and the 20 s pause interruption under As flux (assuming that incorporation and desorption are independent processes). Using the values found by Martin-Sánchez for the desorption from a 2D layer, we obtain an In reduction of 0.066 ML (3.3%), 0.132 ML (6.6%) and 0.297 ML (14.8%), respectively for the three temperatures considered.

On the other hand, a second factor that might influence the accumulated stress is the position of In atoms in the crystal lattice or, similarly, the dilution of the In atoms in the GaAs matrix. During growth of an InAs layer, the real composition of the alloy is far from being of pure InAs. There is strong Ga-In intermixing with the substrate, with the capping, QDs formation for thick enough layers... Depending on where this In incorporates, the stress it introduces to the matrix is also different.

In order to illustrate this effect, lets consider the stress that introduces a perfectly 2D InGaAs layer that contains a fixed amount of InAs but with different In dilutions. In order to keep the amount of In constant, dilute $In_xGa_{1-x}As$ layers should be thicker. The relationship between the thickness of the layer and its In concentration is simply given by:

$$t_L(x) = \frac{t_{InAs}}{x} \tag{4.9}$$

Now we can estimate the stress of this layer by using:

$$\Sigma\sigma_L(x) = M_L(x)\epsilon_L(x)t_L(x) \tag{4.10}$$

where M_L and $\epsilon_L(x) = (a_{subs} - a_L(x))/a_L(x)$ are the layer biaxial modulus (given by Equation 4.3) and the lattice mismatch between the layer and the

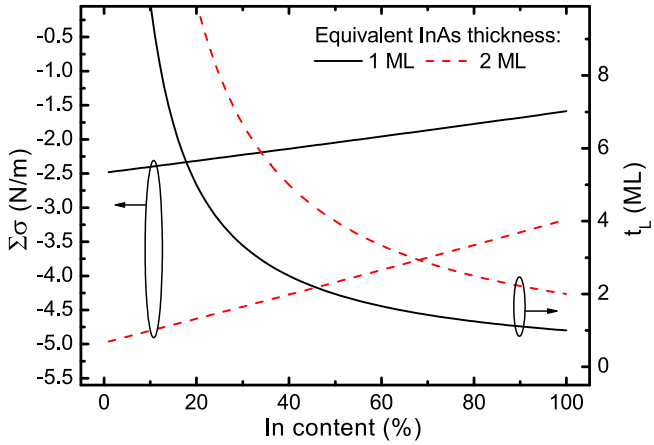

Figure 4.5: Evolution of the accumulated stress as a function of the In composition for a given total In amount. Right scale shows the corresponding layer thickness.

substrate, respectively. This equation was indirectly used in Chapter 1 to describe the modified thickness weighted (MTW) strain balanced criterion (Equation 1.8). Vegard's law is used to calculate the biaxial modulus and the lattice constant of the alloy.

The result of this calculation is shown in Figure 4.5. As it can be seen, even though the total amount of In is the same, dilute alloys introduce larger stress in the sample than a pure InAs layer. This increase might reach a 50% of the nominal value. A direct consequence of the segregation and intermixing phenomena typically observed in this system is thus an important increase in the stress accumulated by the QDs layer.

In principle, larger intermixing is related with high temperatures and high growth rates.[18, 19] However, we have shown previously that at high temperatures the stress that a QDs sample accumulates is smaller. The conclusion is that there is a trade off between these two factors: In desorption is dominant at high temperatures whereas the In intermixing is more important at medium ones. Although it has not been measured, it is expected that at very low temperatures ($<340\,^{\circ}$C), when intermixing should be minimum and the InGaAs layer closer to its nominal composition of pure InAs, the accumulated stress that introduces 2 MLs of InAs would be closer to the predicted 3.3 N/m.[18, 20]

From the point of view of the strain balanced process, the effects described in the previous paragraphs have a capital importance. The strain balanced criteria explained in Chapter 1 relied on the nominal values for the In(Ga)As thickness and composition. However, we have shown that during growth of InAs/GaAs quantum dots, these values are not valid, either because of In desorption or intermixing. As a consequence, in order to achieve a perfect strain balancing of QDs it is necessary to consider the real stress they introduce in the sample and not just the nominal calculated value.

4.2.2 InAs thickness dependence

Another important parameter is the InAs thickness used to grow the QDs, which is normally found to have a large impact into their size, shape and optical properties.[21] To study its effect into the accumulated stress we have performed MOSS measurements for nominal InAs thicknesses ranging from 1.8 to 2.4 ML.

In Figure 4.6 we compare the stress accumulated before and after the beginning of the capping for various values of the InAs thickness. As it can be seen, before capping the accumulated stress remains rather constant in the whole range, reaching values around 1.8±0.1 N/m in all cases. This indicates that InAs content of the sample has very little effect in the stress incorporated before capping (Figure 4.6a). The reason is that once the WL grows and QDs are nucleated, the extra In do not really incorporates to the crystal structure but it rather keeps floating in a liquid-like state or increases the height of the QDs, where the stress it introduces is minimum.

In Figure 4.6b we compare the experimental values of the accumulated stress after capping with the calculated ones using Eq 4.10. As it was explained in the previous section, the theoretical values are systematically smaller than in the experiment given the alloying effect, but the trends are the same in both cases: the accumulated stress monotonously increases with the deposited InAs thickness, from 4.1 N/m at 1.8 ML to 5.2 at 2.4 ML. Below 2 ML the stress increases faster and then it does so slower possibly indicating a saturation of the alloying effect. The explanation of this dependence during capping is that all liquid-like In that remains in the surface is incorporated to the sample and so the resulting accumulated stress should then be proportional to the original InAs thickness.[3]

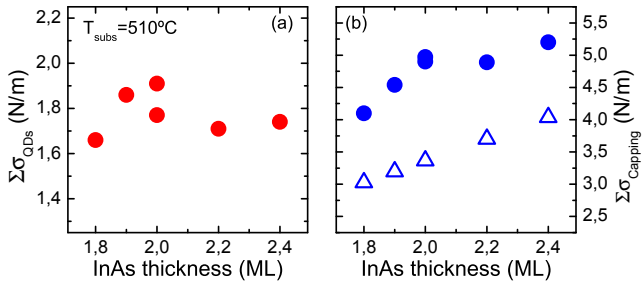

Figure 4.6: Accumulated stress per QD as a function of the InAs thickness (a) before and (b) after capping. Filled symbols represent the experimental data and empty ones the result of applying Equation 4.10 to the nominal InAs thickness.

4.3 Accumulated stress simulation of InAs QDs

As it has been shown in the previous sections, In segregation, intermixing and desorption has a strong effect on the stress accumulated after the growth of a QDs layer. Although the information we have obtained until now is very valuable, it will be interesting to quantify the extent of the observed segregation and intermixing. To this end, we have developed a simulation protocol with the aim of calculating the accumulated stress of a sample (the MOSS curve) given a physically reasonable structure for the WL, the QDs and the capping.

4.3.1 Simulation methodology

To calculate the accumulated stress, we have used the Nextnano++ software package combined with a custom code.[22, 23] Nextnano is a finite element simulation software that allows to calculate, among other things, the six components of the strain in a QD and the surrounding matrix by minimizing the elastic energy density in the simulation grid. The in-house code takes that strain calculated at each grid point and obtain the corresponding stress in the same region. The accumulated stress is then calculated by integrating the stress components up to the defined growth front position. In the following paragraphs we explain the process in greater detail.

Nextnano uses a fixed structure with well determined composition,

thicknesses and size of the QDs. However, the MOSS curve represents a dynamic situation with all these values dependent on time. In order to emulate this evolution with time, the simulation of the MOSS curve actually consists in a set of many simulations (around 200), each of them representing the structure of interest at a different stage of the growth. In Figure 4.7 there are several examples of the simulated structure. The WL is made of several steps, each of them increasing its thickness by 0.1 nm (Figure 4.7a). Once the WL growth is finished, the growth of the QDs begins, increasing its height by 0.1 nm in each simulation step. The material above the growth front, and around the QDs is simulated as an imaginary grid in vacuum, which does not introduce any stress in the sample, given the low values of the stiffness constants ($\sim$0 GPa) (Figure 4.7b and c). The capping proceeds in the same way, increasing its thickness in steps of 0.1 nm (Figure 4.7d). At certain point the QDs are completely covered (Figure 4.7e) and then buried until the capping is completed (Figure 4.7f).

From the strain components ϵ_{kl} calculated in the above structures, we have obtained the corresponding stress components σ_{ij} using the continuum elasticity theory:

$$\sigma_{ij} = C_{ijkl}\epsilon_{kl} \tag{4.11}$$

where C_{ijkl} are the stiffness coefficients. In cubic materials, only 3 of the 81 coefficients are independent, leading to the already presented constants:

$$\begin{aligned} C_{11} &\equiv C_{1111} = C_{2222} = C_{3333} \\ C_{12} &\equiv C_{1122} = C_{1133} = C_{2233} \ldots \\ C_{44} &\equiv C_{1212} = C_{1313} = C_{2323} \ldots \end{aligned} \tag{4.12}$$

The in-plain stress $\sigma_{in-plane}$ is calculated as the average of $\sigma_x = \sigma_{11}$ and $\sigma_y = \sigma_{22}$ components, integrated on the whole plane at a position z in the growth direction. Finally, the accumulated stress at a position h (the growth front) can be obtained by integrating the in-plane stress from the substrate to $z = h$.

To correctly compare with the experimental data, the resulting curve $\Sigma\sigma$ vs h has been weighted by the growth rates used in the experiment, leading to a curve $\Sigma\sigma$ vs growth time. This weighting is specially important for the QDs growth, when the MOSS measurement proceeds but there is

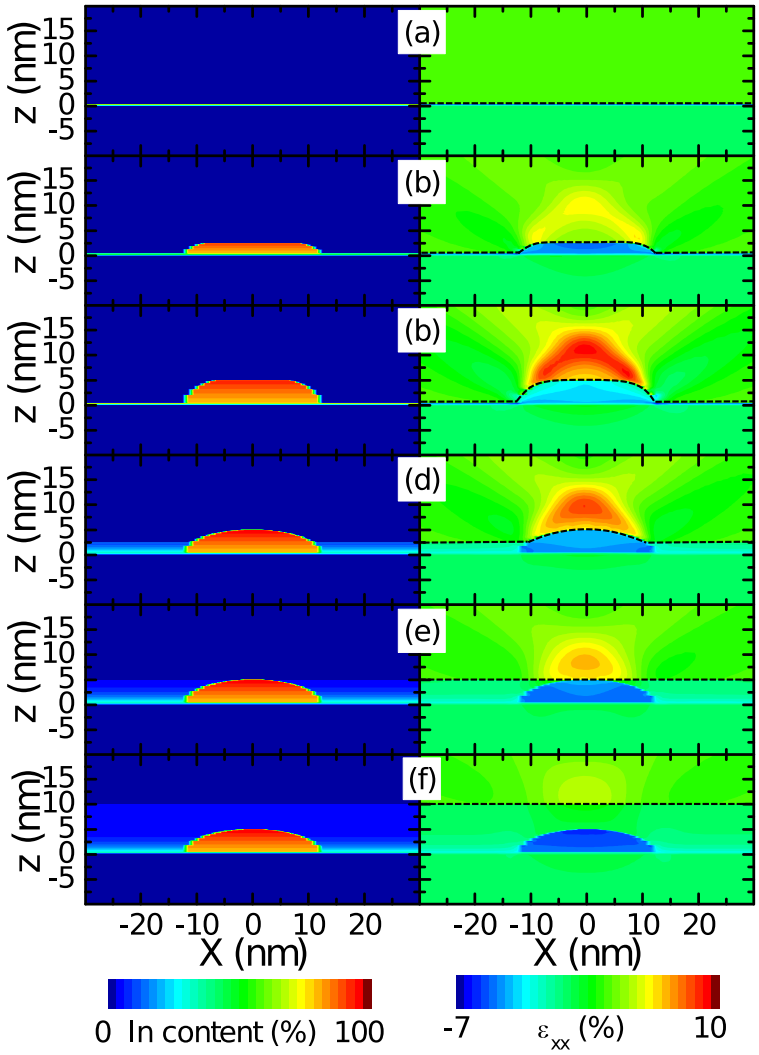

Figure 4.7: Examples of different stages of the simulation process: (a) the WL; (b), (c) the QD; (d) to (f) the capping. In the left column we show a cross-section of the In content in the structure and in the right column the ϵ_{xx} component of the strain. The dashed lines on the right column are the frontier between vacuum and the semiconductor. The apparent strain in the vacuum region is just a result of the calculation but without physical meaning.

not variation of the position of the growth front. In this case, the thickness considered is also weighted by the surface fraction of a "slice" of the QD at that position.

4.3.2 Single InAs QD layer

Three elements must be described in the simulation structure: the WL, the QDs and the capping. Given that segregation seem to be a key point in the accumulated stress, we will model the WL and the capping using one of the several models that for this purpose have been proposed in the literature.[24–27] To restrict the degrees of freedom, in this work we have only considered segregation profiles which can be described by the Muraki's model.[26] Namely, if x_0 is the nominal In composition of an $In_{x_0}Ga_{1-x_0}As$ layer of nominal thickness N monolayers, the actual composition of the nth monolayer will be given according with this model by:

$$x(n) = \begin{cases} 0 & \text{if } n < 0 \quad \text{(Below the WL)} \\ x_0(1-R^n) & \text{if } 0 \leq n \leq N \quad \text{(In the WL)} \\ x_0(1-R^N)R^{n-N} & \text{if } N < n \quad \text{(Above the WL)} \end{cases} \tag{4.13}$$

where R is the segregation coefficient which defines the probability of In atoms to be displaced from their nominal position at the WL.

In Figure 4.8 we show some examples of the profiles that result from Equation 4.13 for several values of the parameters. Except for $R = 0$ when the profile is the nominal one, the In is always diluted in an InGaAs alloy, either because of Ga-In exchange with the substrate or with the capping. In content increases until the nominal thickness for the WL is reached. From that point, In content in the InGaAs alloy reduces as we get farther from the interface. As it can be seen, large values of R give the most spread indium whereas small values lead to profiles closer to the nominal. Conversely, the larger the value of N, the smaller is the fraction of In displaced from its nominal place, although its absolute value increases with N.

We will apply the above In profile to our case of QDs grown after the deposition of 2 ML of InAs at a substrate temperature of 510 °C and whose accumulated stress evolution with time was already discussed above (Section 4.2.1).

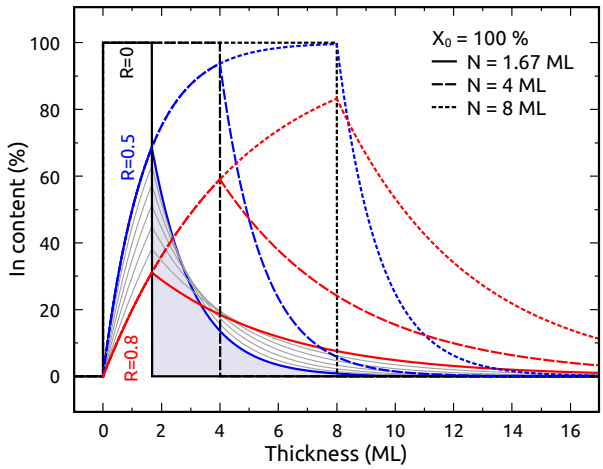

Figure 4.8: Several examples of Muraki's In profiles as a function of nominal thickness N and segregation coefficient R.

We can describe accurately the sublinear evolution of the accumulated stress curve that we observe during the WL growth introducing $x_0 = 1$, $N = 1.67$ MLs and $R = 0.5$ in Equation 4.13 for $n < N$ (region I in Figure 4.9a and Figure 4.9b). Here it is implicit an important intermixing between the incoming In atoms and Ga atoms from the substrate leading to a WL made of InGaAs of varying composition. In agreement with the observations made by García *et al.* less than 50% (about 40%, actually) of the deposited In effectively contributes to the accumulated stress in such region.[28]

Above the critical thickness ($N = 1.67$ MLs), the QDs begin to nucleate and the remaining 0.33 MLs, up to complete the deposited InAs thickness (2 MLs), are used to form the QDs during the elastic relaxation and ripening processes (region II in Figure 4.9a and Figures 4.9c-d). With such constraint, the formed QDs are simulated as InGaAs lens-shaped structures with a maximum height of 4.5 nm and a diameter of 24 nm. We consider a linear In gradient from 80% in the base to 100% in the apex, as this is a usual profile observed by cross sectional scanning tunnelling microscopy.[29] The simulation domain size (100×100 nm) is chosen to reproduce the typical areal density of this type of nanostructures

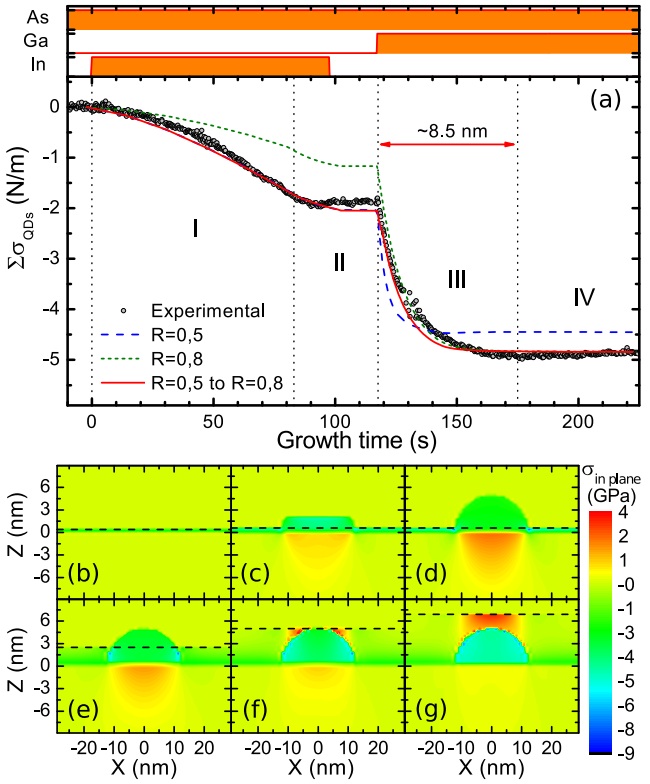

Figure 4.9: (a) Experimental and simulated accumulated stress curves for the QDs growth. The inset shows a detail of region II.(b)-(g) Cross section of the simulated in-plane stress at different stages of the growth. The thick dashed lines represent the position of the growth front.

(10^{10}cm^{-2}). The resulting accumulated stress after the QDs growth reaches -2 N/m, in reasonable agreement with the experimental value.

The In not incorporated to the WL or the QDs is available for the capping once the Ga cell is opened (region III in Figure 4.9a and Figure 4.9e-g). Experimentally, we observe that In is exhausted after growing $\sim$ 8.5 nm of GaAs, as it was mentioned before. In the simulation, keeping $R = 0.5$, the available In is incorporated to the bulk in just 2.5 nm (dashed curve in Figure 4.9a) and do not reach the experimental accumulated stress of -4.85 N/m. Better results in the capping region

are obtained increasing R to 0.8 (dotted curve), although this clearly underestimates the stress introduced in region I and II.

This result is not surprising since Muraki's model was developed to fit the In profiles of layers completely buried and not its dynamic coverage. In that sense, it is interesting to note that the value of R which fits better the final accumulated stress, when Muraki's model really applies, is $R = 0.8$, which is in good agreement with the typical values found in the literature for buried WLs ($R = 0.7 - 0.86$).[30–32]

The amount of In segregated from the WL can be calculated simply by integrating Equation 4.13 between N and ∞, which leads to:

$$S = \frac{x_0}{ln(R)} \left(R^N - 1\right) \tag{4.14}$$

in MLs of InAs. Regions I and II are correctly fitted with $R = 0.5$, which indicates that indium that segregates to the surface is $\sim$0.98 ML of InAs. However, the In segregated once the WL and the QD are capped is much higher, around $\sim$1.39 ML, since the stress is correctly fitted with $R = 0.8$. Even if the QD is completely dissolved and its In (0.33 MLs) incorporated to the capping, it will not be enough to make compatible both results.

On the one hand, this apparent contradiction suggest that at some point during capping, the WL might loose part of its In which will also segregate and incorporate to the upper layers. On the other hand, since there is no reduction in the accumulated stress during capping according to the MOSS measurements, that suggest that the In lost by the WL is not detached from the crystal matrix, but it rather segregates in a solid solution. This In (called hereafter "crystallized" indium) will thus differ from the In that can be found in a liquid-like state at the surface and that does not introduce any stress in the sample.

This picture allows to envisage the following growth kinematics: during the first stages of GaAs deposition ($\lesssim$1 ML), there is an important Ga-In exchange that reduces the In contained in the WL and creates an In rich InGaAs layer at the surface. As the GaAs deposition proceeds, this Ga-In exchange continues in such a way that the crystal growth takes place beneath the topmost InGaAs layer. The In of the layers that are growing comes in part from the surface InGaAs and in part from the liquid In. Eventually, In atoms (either crystallized or liquid) exhaust and

the resulting In profile is that predicted by Muraki, even though in the intermediate stages the profile was different.

Experimental evidence of this solid solution segregation process have not been reported, although some indirect observations can be found in the literature. For example, Yakimov showed a slight rise in the In related Auger signal just at the beginning of capping of 1 ML of InAs, suggesting an increase of the In content at the surface.[31] Likewise, In profiles of buried WLs are normally fitted with large values for the segregation coefficient R, of 0.7 to 0.86 depending on temperature, which is incompatible with the existence of the In-rich WL needed to achieve the observed stress before QDs nucleation.[30–32]

We can modify Equation 4.13 above in order to include the In rich growth front and incorporate this process to the simulation. We assume that Ga-In exchange takes place in the first monolayer of capping which approximately corresponds to 3 simulation steps (0.3 nm). In each of these steps the value of R in the WL is increased by 0.1 until it reaches 0.8 in the third step, which is the value in the capping:

$$R_{wl}(k) = \begin{cases} 0.5 & \text{if } k \leq N \\ 0.5 + 0.3(k - N) & \text{if } N < k \leq N + 1 \\ 0.8 & \text{if } N + 1 < k \end{cases} \tag{4.15}$$

where k is the position of the growth front in ML. The In expelled by the WL because of the R increase (A$\simeq$0.137 ML of InAs in each step) incorporates immediately in the corresponding step of the capping, increasing its In content accordingly:

$$\Delta x = A \frac{\text{Simulation step} = 0.1nm}{\text{Monolayer thickness} \approx 0.3nm} \approx 41\% \text{ of In} \tag{4.16}$$

The rate at which this crystallized In disappear from the top layer and incorporates to the layers underneath is somewhat arbitrary since during capping there are other processes that we are not taking into account, such as QDs crumbling or in-plane diffusion.[28] In order to minimize the degrees of freedom, we choose as the segregation probability of In atoms the same that for the liquid In, that is R. With all this information we can add a fourth line to the Muraki's equation to include this extra In that is kept at the growth front:

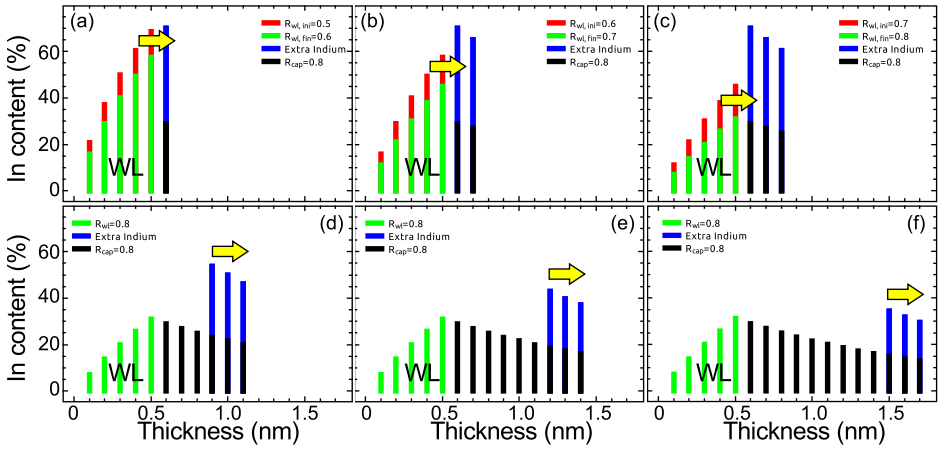

Figure 4.10: Bar plot of the In profile in the sample (excluding QDs) during the first stages of capping. (a) to (c) In the first ML of capping the WL looses part of its In, which incorporates in the surface layer. (d) to (f) As growth proceeds, the InGaAs layer at the surface keeps at the growth front, loosing In progressively.

$$x(n) = \begin{cases} 0 & \text{if } n < 0 \\ x_0(1 - R^n) & \text{if } 0 \leq n \leq N \\ x_0(1 - R^N)R^{n-N} & \text{if } N < n \leq k - 1 \\ x_0(1 - R^N)R^{n-N} + \Delta x R^{n-N-1/3} & \text{if } N, k - 1 < n \leq k \end{cases} \tag{4.17}$$

The In content of each simulation step during the first stages of capping according to the previous Equation is shown in Figure 4.10. Figure 4.10a to c represent the period in which the In in the WL is being expelled to the surface due to Ga-In exchange. They correspond to values of k=N+1/3, k=N+2/3 and k=N+1, respectively. The other plots of the panel represent more advanced positions of the capping growth, when k=N+2, k=N+3 and k=N+4, respectively. As it can be seen, the In-rich top monolayer (3 simulation steps) is always at the growth front and looses In progressively.

Using this schema in the simulation results in the last curve shown in Figure 4.9a (continuous red line). As it can be seen, in Regions I and II this curve is identical to that of $R = 0.5$ since the In profile is also identical. Once the capping begins, Ga-In exchange promotes part of the In of the

WL to the growth front and also part of the liquid In incorporates to the sample. The simulated accumulated stress in region III closely follows the experimental results and approaches rapidly the curve of $R = 0.8$, which is reached only when the capping is completed.

The implications of this results are very relevant. On the one hand, our findings support the limited incorporation of In to the WL leading to the *segregation* of the remaining In in the form of a liquid-like phase, result already suggested by Silveira *et al.* and also supported by the thermodynamic calculations made by Bottomley.[33, 34] On the other hand, they also support the existence of a strong *Ga-In exchange* during the WL capping that reduces its In content. The combination of both processes is responsible for the In profiles observed typically by TEM or X-STM and the low content WLs usually observed.

4.4 Strain driven In migration

Until now, in order to keep the interpretation and the simulations as simple as possible, we have not considered the migration of atoms from the QDs to the WL or *viceversa*, only including the vertical movement of In from the WL to the capping (process 1 in Figure 4.11).

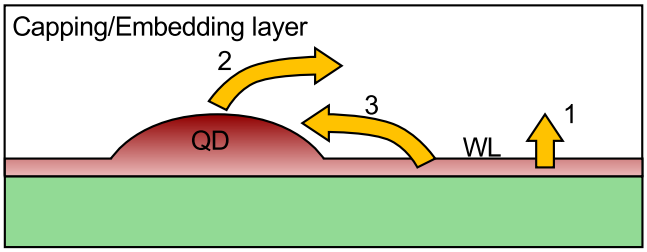

Figure 4.11: The different routes that In atoms already incorporated in the sample can follow (excluding In desorption).

The migration of In from the QDs to the WL (or more correctly, the embedding layer) is generally observed during their capping (process 2 in Figure 4.11). InAs QDs studied by AFM are typically 7-9 nm high whereas buried QDs are normally smaller, 3-5 nm high. Depending of the capping protocol, the extra material accumulates around de QDs in a

preferential direction, around their base or creates exotic nanostructures, such as quantum rings or quantum camels.[35, 36] As it was mentioned above, this process will have its main impact into the shape of the MOSS curve during the first stages of the capping, having very little effect in the total accumulated stress. For this reason, we have preferred to omit it in the simulations and to give the QDs their final size, directly including all extra In in the liquid phase.

However, the extent of the In migration from the WL to the QDs is still a matter of debate (process 3 in Figure 4.11). Joyce *et al.* made a study varying the InAs growth rate which suggested that, given enough time, the WL→QDs route would take place enhanced by the strain field gradients.[19] From their work, they also concluded that slow growth rates should enhance the unmixing of In and Ga species while fast growth rates would enhance their intermixing, not allowing the system to reach a thermodynamical equilibrium. Additionally, Bottomley suggested that this In transfer from the WL might be favoured by the existence of liquid phases at the surface.[34] A direct experimental demonstration for such mechanisms could not be given at that moment, though.

In theory, this migration of In atoms from one place to another could be observed with the MOSS technique as long as the stress difference between the initial and final state was important. For example, the migration of atoms from the liquid In phase to the top of the QDs is unlikely to produce any measurable response since in both states In atoms introduce very little stress, if any. This is confirmed by the experimental results shown in Section 4.2.2 and Figure 4.6a, where the accumulated stress before capping is independent on InAs coverage. On the contrary, the migration of In atoms from the WL to the liquid phase or the QDs should give a measurable signal in the MOSS curve since in the WL they introduce a larger stress than in an In rich QD.

In the following section we study two systems in which the strong strain fields present around the nanostrucures favour the WL→QDs In migration.

4.4.1 Stacked InAs QDs

It is widely accepted that the spatial correlation observed in vertically coupled quantum dots is driven by the inhomogeneous strain fields leading to the accumulation of In adatoms on top of buried QDs and the diffusion

of Ga adatoms in the opposite direction.[37, 38] It is very clear that four-fold coordinated atoms in the crystal do not significantly diffuse at the temperatures and times scales relevant for crystal MBE growth. What it is not so clear is if this diffusion only affects to not incorporated adatoms or might also happen in the atoms incorporated in the crystal lattice at the surface (process 3 in Figure 4.11) which have only two bonds to break. Additionally, due to surface roughness and the fast movement of atomic steps, buried atoms might become surface atoms without the need to diffuse.

To test the existence of the latter process, we have measured the MOSS curve in a stack of partly strain balanced QDs. The QDs are grown after the deposition of 2 MLs of InAs. The spacer between layers is 15 nm thick and is made of GaAs (first 8 nm of capping), $GaAs_{0.82}P_{0.18}$ (next 3 nm) and GaAs (final 4 nm). Substrate temperature and As BEP are kept constant at 510 °C and 1.5×10^{-6} mbar, respectively, during the growth of the stacks. P BEP is 8.5×10^{-7} mbar. In and Ga growth rates are 0.02 and 0.5 ML/s respectively. This sample will be studied in more detail in the next chapter (Sample QDs-D).

The MOSS curve of the first 10 periods is shown in Figure 4.12a. As it can be seen, during growth of InAs and the following GaAs capping, stress accumulates in each period and when GaAsP grows, it is partly compensated, giving to the MOSS curve that oscillating shape. In Figure 4.12b we show the same result but with the part of the curve corresponding to each period overlapped and vertically shifted for easier comparison. The shape of the curve in this case is similar to that discussed before but with the addition of the compensating layer which, as it can be seen, reduces the accumulated stress in each period for about a 60%.[3]

The most relevant part of these curves, in the discussion of In migration, is related with the evolution of the stress during the 20 s As pause after the InAs growth. As it can be seen, as the number of periods is increased, the accumulated stress in this region changes from being constant to being decreasing, with the MOSS curve turning upwards. The

[3]The large accumulated stress before and after the GaAs capping on each period (3.5 and 5.7 N/m, respectively) suggests that the substrate temperature for this sample is, on average, too low, well below the nominal 510 °C. However, it will serve for the purpose of this section which is to illustrate strain driven In migration.

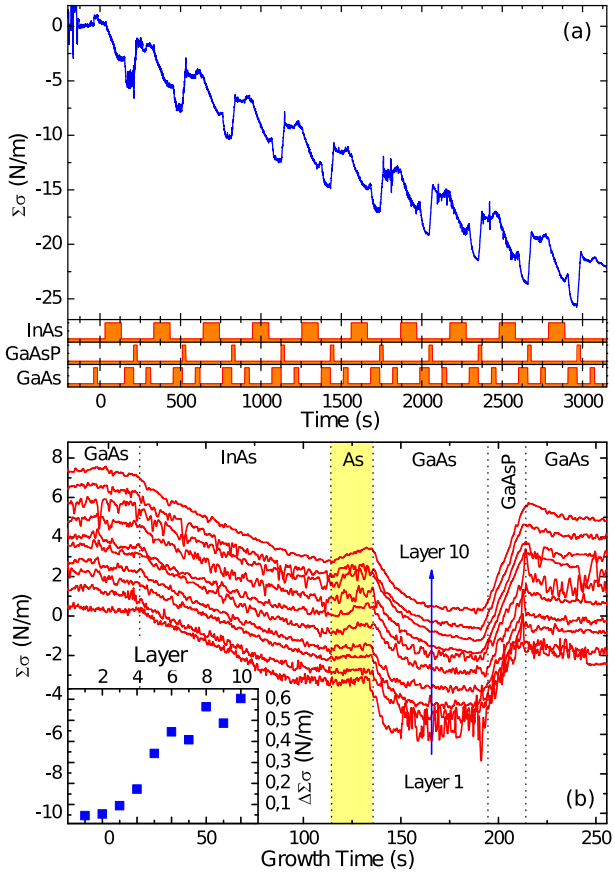

Figure 4.12: (a) MOSS curve of the first 10 periods of a partly strain balanced QDs stack. (b) The curve corresponding to each period overlapped and vertically offset, for clarity. The inset shows the accumulated stress difference between the beginning and the end of the As pause (yellow area in the main figure).

effect can be better appreciated in the inset of Figure 4.12b where we plot the accumulated stress difference between the beginning and the end of the As pause, being in the limit of the instrumental resolution in the first layer and up to 0.6 N/m in the tenth layer.

Between one layer and the following the only variable that is changing is the strain situation of the sample due to the already buried nanostructures.

Our hypothesis is that, during the As pause, those strain fields enhance the migration of In incorporated in the WL to the QDs, thus reducing the average stress in the sample. The strain fields piles up from layer to layer, leading to a more efficient process in the top layers than in the bottom ones and therefore the observed behavior of the inset of Figure 4.12b.

This result is thus an experimental demonstration of Joyce hypothesis about the activation of the WL→QDs migration route if enough time or strain fields are given.[19] Likewise, although we have not real proof of it, this migration might be assisted by the liquid-like In phase at the surface which will favour the migration if a driving force (the strain fields) are present, as suggested by Bottomley.[34]

4.4.2 Accumulated stress of QPs

A final study about In migration is related with the fabrication of quantum posts, which were briefly introduced in Chapter 1 and will be further discussed in the framework of strain balanced nanostructures in Chapter 6

The QPs we consider here are formed by deposition of a short period superlattice directly on top of a QD seed layer, which is fabricated with the deposition of 2 ML of InAs. In our case, we cycle 20 periods of 2.2 Å of InAs and 8.5 Å of GaAs to form the quantum posts while monitoring the accumulated stress. Substrate temperature and As BEP are kept constant at 510 °C and 1.5×10^{-6} mbar, respectively, during the growth of the QPs. The optical properties of this sample will be analysed in Chapter 6 using to that purpose an identical structure grown on a normal GaAs (001) substrate (Sample QPs-D).

We have applied the same stress measurement and modelling described above to the growth of InAs/GaAs QPs. Figure 4.13a shows the accumulated stress curve recorded over time for the QPs sample (small circles). The beginning of the curve is the seed QDs layer and the evolution is identical to regions I and II in Figure 4.9a. During the first periods of the superlattice, growing Ga increases the accumulated stress by the incorporation of the liquid In at the surface, as it is observed in the QDs sample, and similar behaviour is found when growing In, also as expected. It can be seen in those first periods that during the growth pause under As flux, the accumulated stress decreases slightly (∼0.1 N/m per period). In principle, this small change, also observed in the QDs growth, might be

attributed to several factors such as a change in the surface reconstruction or to a small cooling of the sample when the In effusion cell is closed. However, it might also correspond to the detachment of In atoms from the WL and their migration to the sample surface or the QDs, has it has been shown in the QDs stack sample.

The interpretation of such feature becomes clearer if we consider the following periods of the superlattice. From the 4^{th} period and ahead, it is evident that the reduction of the accumulated stress is taking place also when In atoms are reaching the sample. This behaviour is rather counter-intuitive since In growth should increase the stress accumulated in the sample. The reduction becomes larger as the growth proceeds and, conversely, the stress increase during the GaAs capping becomes smaller (inset of Figure 4.13a). The latter effect suggest that each period there is less free In to be incorporated to the sample during GaAs capping, whereas the former indicates that the In detachment process is enhanced during the QPs growth. The combination of both processes points out an augmented efficiency of the migration of In atoms towards places where they introduce less stress, which are the In rich columns that form the QPs.

More insight on the processes that are taking place can be obtained by the simulation of the QPs structure. For simplicity, we assume that a steady state has been reached with a constant amount of In segregating from layer to layer. The presence of the seed is neglected. The QPs are simulated as a stack of lens shaped QDs, 24 nm wide, 2 nm high, separated 1 nm from each other. This implies an overlap of consecutive QD layers, therefore the formation of the QPs. A homogeneous InGaAs alloy is assumed for the QPs (63% In). The surrounding matrix is modeled as a 1 nm thick InGaAs layer with 24% In that progressively reduces to 17% during the growth of the next InAs layer. For simplicity, we consider in the simulation a homogeneous InGaAs alloy although a more complex profile, similar to Muraki's model, would be more realistic. Each period of this structure (QD + capping) has an In content equivalent to 0.2 nm of InAs once buried, similar to the nominal values used in the experiment. 0.06 nm of InAs segregates from layer to layer. The accumulated stress that results from this simulation is also depicted in Figure 4.13a. As it can be seen, even with this idealized sequence, we can correctly reproduce the oscillations of the experimental curve.

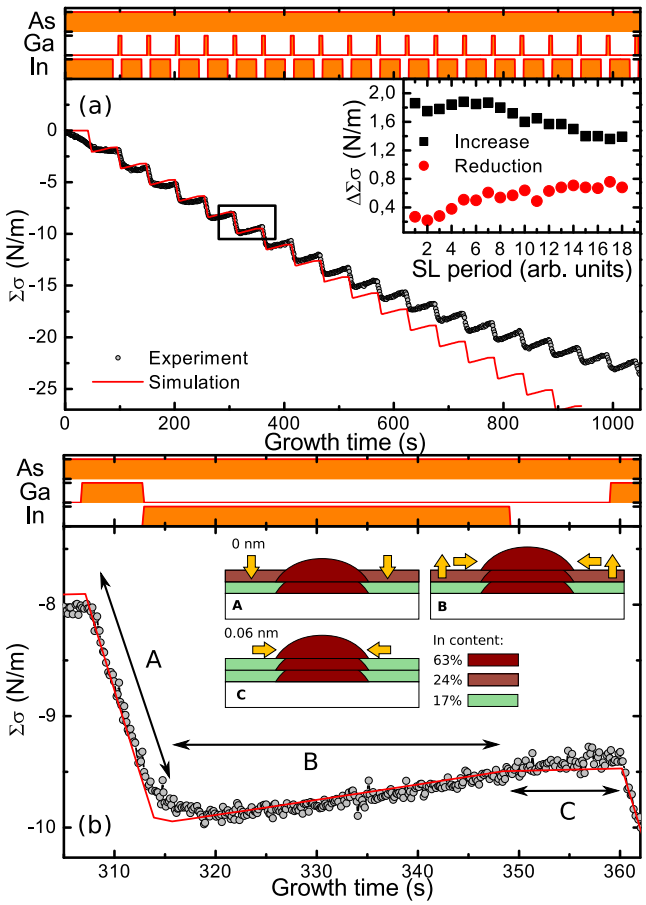

Figure 4.13: (a) Experimental and simulated accumulated stress curves of QPs. The inset shows the amplitude of the increase and the reduction of the accumulated stress as a function of the period number. (b) Detail of one period of the QPs growth. The inset shows the different stages of the process, with the amount of segregated In indicated in equivalent InAs thickness. Different colors indicate the In fraction and the arrows the In atoms route: A - Incorporation of In to the sample; B - segregation and migration of In incorporated in the last MLs; growth of the QPs; C - A certain amount of In keeps as a liquid phase in the surface.

Figure 4.13b shows a detail of the curve corresponding to a single period of the deposited InAs/GaAs superlattice (indicated by a rectangle in Figure 4.13a) The opening/closing sequence of As, Ga and In effusion cells are indicated. During region A in Figure 4.13b, GaAs is growing and it incorporates most of the liquid-like In at the surface. In region B, InAs grows very slowly. At the beginning, the stress accumulates slightly and then it diminishes. This reduction is more prominent for the last periods of the structure. We believe that at the beginning of the In growth, the stress increases due to a strong In-Ga intermixing and this intermixing leads to the partial melting of the surface, according to the thermo-piezochemistry calculations made by Bottomley.[34] In general, the presence of In-As bonds at the surface enhances the diffusion process given that they are weaker than Ga-As bonds and therefore easier to break, in terms of energy.[39] In this situation, the strong strain fields due to the buried QDs will favour the migration of this liquid-like In towards them to form the QPs. This migration is indirectly incorporated in the simulation by assuming that part of the In deposited during region B keeps in a liquid-like solution and part lead to the formation of a new, very shallow QD, as explained in the previous paragraph. Since in the simulation the fraction of In that incorporates to the QPs is constant, the curve do not completely reproduce the experimental results shown Figure 4.13a which is an evidence of the enhancement of the In migration with the number of periods.

In summary, the results presented in this part of the work demonstrate that there is an important loss of In from the WL during capping of the QDs (as found in Section 4.3.2). This In redistribution is also present during growth of QDs stacks, where the WL→QDs route is activated due to the strain field of buried nanostructures and during QPs growth, where the strong Ga-In intermixing, surface melting and strain fields enhance In migration across the liquid-like surface to the QPs and leads to the observed inversion of the accumulated stress curves. Our results give an experimental demonstration of the processes suggested by Joyce and Bottomley, shedding light on the different processes occurring during the growth of InAs/GaAs based quantum nanostructures.

4.5 Calibration of the accumulated stress by a GaAsP layer

A final issue to be addressed in this chapter in order to fabricate perfectly strain balanced quantum dots is the calibration of the accumulated stress by a GaAsP layer.

4.5.1 Stress *vs* pressure

The variable of interest in the case of GaAsP growth will be the phosphorus BEP, given that the As BEP is kept constant and equal to 1.5×10^{-6} mbar. The stress accumulated by a GaAsP layer at a substrate temperature of 510 °C and a growth rate of $R_g = 0.5$ ML/s is shown in Figure 4.14 for various P pressures as a function of time. The As/P BEP ratio is also indicated. As it is expected, the accumulated stress is tensile, owing that the lattice parameter of GaAsP is smaller than that of GaAs. In all curves, stress accumulates following a linear tendency. High P BEPs give curves with a larger slope, indicating higher P content in the layer.

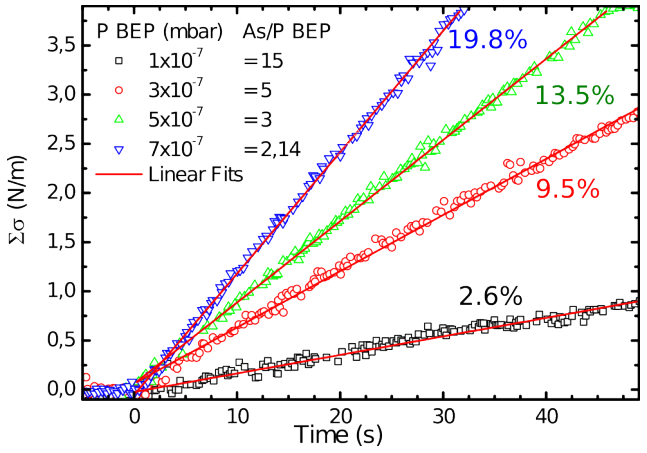

Figure 4.14: Accumulated stress as a function of the P BEP.

In order to use this results to fabricate strain balanced nanostructures, it is important to know the rate at which tensile stress increases as a function of the P BEP, that is, the slopes of the plots in Figure 4.14. In

Figure 4.15a we show those slopes, measured in $\mathrm{Nm^{-1}ML^{-1}}$, assuming the typical growth rate we use of 0.5 ML/s. The data includes not only the results shown above but also those of samples that will be presented and discussed in the next chapter, in order to increase the data statistics.

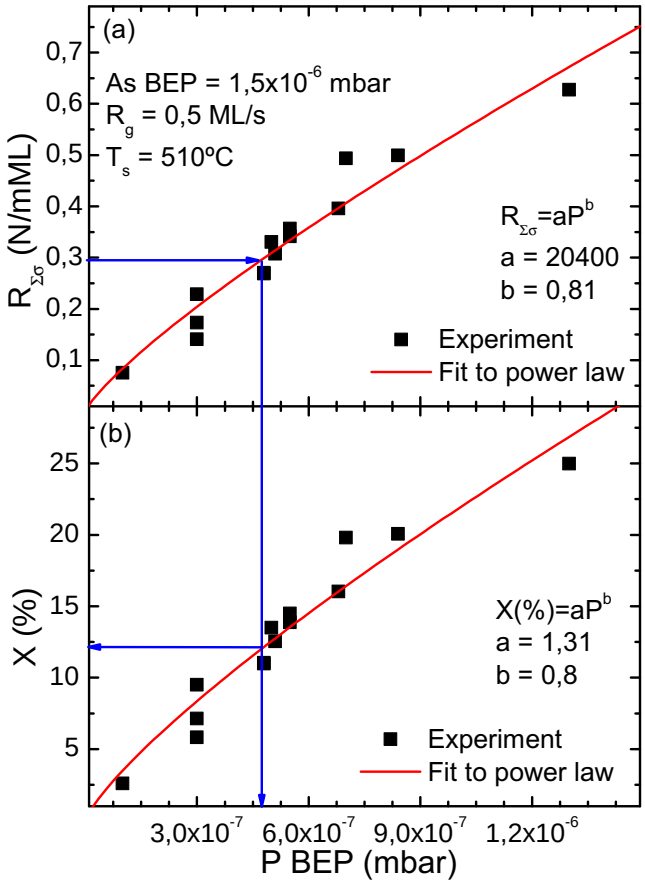

Figure 4.15: (a) Accumulated stress rate and (b) P composition in a GaAsP layer as a function of P BEP.

As it can be seen, the stress rate increases monotonously with increasing P BEP following a sublinear dependence. A fit of the data to a power law, $R_{\Sigma\sigma} = aP^b$, gives $a = 20400$ and $b = 0.81$. The reciprocal of this law, without physical meaning in principle, $P = (R_{\Sigma\sigma}/a)^{1/b}$ will

be used in the following to calculate the P BEP needed to have a given stress rate. This stress rate will depend, in turn, in the compressive stress to compensate $\Sigma\sigma_{compresive}$ and in the thickness to be used for the compensation $t_L(ML)$:

$$R_{\Sigma\sigma} = \frac{\Sigma\sigma_{compresive}}{t_L(ML)} \tag{4.18}$$

4.5.2 Composition *vs* pressure

Although it is not needed to achieve a correct compensation, it is interesting to estimate the P composition of the layers as a function of its BEP. If the accumulated stress is introduced by a flat, strained $GaAs_{1-x}P_x$ layer, assumed homogeneous, then we can use Equation 4.10 but written as a function of time:

$$\Sigma\sigma_L(x) = M_L(x)\epsilon_L(x)a_L(x)R_g t \tag{4.19}$$

From each slope obtained in the previous section we can get the value of x by numerically solving Equation 4.19. In Figure 4.15b we show the P content of the GaAsP layers extracted following the above method for various P pressures. As it can be seen, the P content of the GaAsP layer follows also a sublinear evolution with the P BEP with a dependence very similar to that of the accumulated stress rate. This sublinear dependence with P BEP (or As/P BEP ratio) is often found in the literature.[40, 41] This result suggests that achieving layers with high P content might be difficult without reducing the competing As BEP.

With all this information now it is straight forward to calculate the P BEP needed and an estimation of its content in the GaAsP layer, as illustrated by the blue arrows in Figure 4.15.

4.5.3 Comment on the dependence with temperature and growth rate

Although we have not performed MOSS measurements of the stress accumulated by GaAsP layers as a function of temperature, it is interesting to briefly review the available literature to have an idea of the effect that this parameter might have on the process of strain compensation.

According to Liang *et al.*, P incorporation in a GaAsP layer grown on GaAs (001) remains constant until 520 °C when the incorporation efficiency increases, leading to P-richer alloys.[40] In their experimental conditions, the P content of the GaAsP layer doubles, from 20% to 40%, when temperature is rose from 500 to 600 °C.

Nomura *et al.* found a similar dependence, with larger P content at high temperatures, observing also a strong influence of the growth rate.[41] Using slow growth rates led to P-richer alloys. In their experimental conditions of As/P BEP = 45, they get a P content as high as 70% when growing at 0.2 μm/h ($\sim$0.2 ML/s) and 525 °C.

In general, these studies suggest that increasing the temperature favours the desorption of As from the sample surface so high temperatures are actually equivalent to reduced As/P BEP ratio.

In summary, the calibration described above is valid for the low temperature range, being expected an important increase of the P content in the layer if the growth is performed at higher temperatures while keeping other conditions constant.

4.6 Conclusions

In conclusion, in this chapter we have introduced the fundamentals of the MOSS technique and its current implementation at the Insituto de Microelectrónica de Madrid.

We have used this technique to study the dependence of the stress accumulated by an InAs QDs layer as a function of temperature and InAs thickness. Our results indicate that the total accumulated stress is determined by a trade-off between the degree of In desorption, which increases with temperature, and the degree of alloying, being this factor dominant at the typical growth temperature for the QDs of 510 °C.

In combination with finite element simulations, we have identified several processes that produce an important loss of In from the WL. At the first stages of QDs capping we observe that Ga-In exchange with the WL creates an In rich InGaAs layer that keeps at the growth front and incorporates progressively during the rest of the capping. Contrary to the liquid In phase, which is stress-free, this InGaAs layer is strained and hence it incorporates the corresponding stress to the sample.

In QDs stacks we have shown that the intense strain fields might also be responsible from the migration of In atoms from the WL to the QDs. This observation confirms the hypothesis made by Joyce *et al.* one decade ago of In detachment from the WL and reincorporation in the QDs if time or other process such as strain fields exist.

A third phenomena was described in the growth of QPs. In these nanostructures it was observed and modelled that during the InAs growth period of the superlattice, the stress was reduced rather than increased. This counter-intuitive process was explained by the Ga-In exchange and subsequent melting of the top layers. Once melted, the strong strain fields that are responsible for the QPs formation would promote the migration of In atoms from the WL to the growing QPs.

As a final step towards the complete control of the strain balanced process by the MOSS technique was the characterization of the GaAsP layer. In this line, we have calibrated the accumulated stress rate and the layer composition as a function of the P BEP in the chamber, vital information that will be extensively used in the following chapters.

Bibliography

[1] A. J. Schell-Sorokin and R. M. Tromp, "Mechanical stresses in (sub)monolayer epitaxial films," *Phys. Rev. Lett.*, vol. 64, pp. 1039–1042, Feb 1990.

[2] D. Fuster, M. U. González, Y. González, and L. González, "In situ measurements of InAs and InP (0 0 1) surface stress changes induced by surface reconstruction transitions," *Surface Science*, vol. 600, no. 1, pp. 23–32, 2006.

[3] J. Silveira, J. Garcia, and F. Briones, "Surface stress effects during MBE growth of III-V semiconductor nanostructures," *Journal of Crystal Growth*, vol. 227, pp. 995–999, 2001.

[4] D. Fuster, M. Ujúe González, L. González, Y. González, T. Ben, A. Ponce, and S. I. Molina, "Stacking of InAs/InP(001) quantum wires studied by in situ stress measurements: Role of inhomogeneous stress fields," *Applied Physics Letters*, vol. 84, no. 23, p. 4723, 2004.

[5] M. González, Y. González, and L. González, "In situ detection of an initial elastic relaxation stage during growth of $In_{0.2}Ga_{0.8}As$ on GaAs(0 0 1)," *Applied Surface Science*, vol. 188, no. 1-2, pp. 128–133, 2002.

[6] M. U. González, Y. González, and L. González, "Study of the relaxation process during InGaAs/GaAs (001) growth from in situ real-time stress measurements," *Applied Physics Letters*, vol. 81, no. 22, pp. 4162–4164, 2002.

[7] C. A. Volkert, "Stress and plastic flow in silicon during amorphization by ion bombardment," *Journal of Applied Physics*, vol. 70, no. 7, pp. 3521–3527, 1991.

[8] P. Flinn, D. Gardner, and W. Nix, "Measurement and interpretation of stress in aluminum-based metallization as a function of thermal history," *Electron Devices, IEEE Transactions on*, vol. 34, no. 3, pp. 689–699, 1987.

[9] M. U. González, *Growth and characterization of III-V semiconductor nanostructures for advanced optical devices.* PhD thesis, Universidad Complutense de Madrid, 2002.

[10] G. G. Stoney, "The tension of metallic films deposited by electrolysis," *Proceedings of the Royal Society of London. Series A*, vol. 82, no. 553, pp. 172–175, 1909.

[11] K. Roll, "Analysis of stress and strain distribution in thin films and substrates," *Journal of Applied Physics*, vol. 47, no. 7, pp. 3224–3229, 1976.

[12] F. J. von Preissig, "Applicability of the classical curvature-stress relation for thin films on plate substrates," vol. 66, no. 9, pp. 4262–4268, 1989.

[13] L. Freund, J. Floro, and E. Chason, "Extensions of the stoney formula for substrate curvature to configurations with thin substrates or large deformations," *Applied Physics Letters*, vol. 74, p. 1987, 1999.

[14] H. Ibach, "Erratum to:"the role of surface stress in reconstruction, epitaxial growth and stabilization of mesoscopic structures"[surf. sci. rep. 29 (1997) 193]," *Surface Science Reports*, vol. 35, pp. 71–73, 1999.

[15] C. Heyn, "Formation and dissolution of InAs quantum dots on GaAs," *Journal of Crystal Growth*, vol. 210, pp. 421–428, Mar. 2000.

[16] C. Heyn, "Desorption of InAs quantum dots," *Journal of Crystal Growth*, vol. 251, pp. 218–222, Apr. 2003.

[17] J. M. Sánchez, *Selective growth of InAs on GaAs(001) substrates patterned by local oxydation nanolithographyJavier Martín Sánchez.* PhD thesis, Instituto de Microelectrónica de Madrid, may 2009.

[18] P. B. Joyce, T. J. Krzyzewski, and T. S. Jones, "Composition of InAs quantum dots on GaAs(001): Direct evidence for (In,Ga)As alloying," *Physical Review B*, vol. 58, pp. R15981–R15984, Dec. 1998.

[19] P. Joyce, T. Krzyzewski, G. Bell, T. Jones, S. Malik, D. Childs, and R. Murray, "Effect of growth rate on the size, composition, and optical properties of InAs/GaAs quantum dots grown by molecular-beam epitaxy," *Physical Review B*, vol. 62, no. 16, p. 10891, 2000.

[20] A. Bosacchi, "Indium surface segregation in InGaAs-based structures prepared by molecular beam epitaxy and atomic layer molecular beam epitaxy," *Journal of Crystal Growth*, vol. 150, pp. 185–189, May 1995.

[21] D. Bimberg, M. Grundmann, and N. N. Ledentsov, *Quantum dot heterostructures*. Wiley, 1998.

[22] "Nextnano++ Software Package." `http://www.wsi.tum.de/nextnanoplus`, 2011.

[23] S. Birner, S. Hackenbuchner, M. Sabathil, G. Zandler, J. Majewski, T. Andlauer, T. Zibold, R. Morschl, A. Trellakis, and P. Vogl, "Modeling of semiconductor nanostructures with nextnano3," *Acta Physica Polonica Series A*, vol. 110, no. 2, p. 111, 2006.

[24] J. Moison, C. Guille, F. Houzay, F. Barthe, and M. Van Rompay, "Surface segregation of third-column atoms in group III-V arsenide compounds: Ternary alloys and heterostructures," *Physical Review B*, vol. 40, no. 9, p. 6149, 1989.

[25] N. Grandjean, J. Massies, and M. Leroux, "Monte Carlo simulation of In surface segregation during the growth of $In_xGa_{1-x}As$ on GaAs (001)," *Physical Review B*, vol. 53, no. 3, p. 998, 1996.

[26] K. Muraki, S. Fukatsu, Y. Shiraki, and R. Ito, "Surface segregation of In atoms during molecular beam epitaxy and its influence on the energy levels in InGaAs/GaAs quantum wells," *Applied Physics Letters*, vol. 61, no. 5, pp. 557–559, 1992.

[27] O. Dehaese, X. Wallart, and F. Mollot, "Kinetic model of element III segregation during molecular beam epitaxy of III-V semiconductor compounds," *Applied physics letters*, vol. 66, no. 1, pp. 52–54, 1995.

[28] J. García, J. Silveira, and F. Briones, "Strain relaxation and segregation effects during self-assembled InAs quantum dots formation on GaAs (001)," *Applied Physics Letters*, vol. 77, p. 409, 2000.

[29] A. G. Taboada, A. M. Sánchez, A. M. Beltrán, M. Bozkurt, D. Alonso-Álvarez, B. Alén, A. Rivera, J. M. Ripalda, J. M. Llorens, J. Martín-Sánchez, Y. González, J. M. Ulloa, J. M. García, S. I. Molina, and P. M. Koenraad, "Structural and optical changes induced by incorporation of antimony into InAs/GaAs(001) quantum dots," *Phys. Rev. B*, vol. 82, p. 235316, Dec 2010.

[30] P. Offermans, P. M. Koenraad, R. Nötzel, J. H. Wolter, and K. Pierz, "Formation of InAs wetting layers studied by cross-sectional scanning tunneling microscopy," *Applied Physics Letters*, vol. 87, no. 11, p. 111903, 2005.

[31] M. Yakimov, V. Tokranov, G. Agnello, J. van Eisden, and S. Oktyabrsky, "In situ monitoring of formation of InAs quantum dots and overgrowth by GaAs or AlAs," *Journal of Vacuum Science & Technology B: Microelectronics and Nanometer Structures*, vol. 23, p. 1221, 2005.

[32] D. Gerthsen, H. Blank, D. Litvinov, R. Schneider, a Rosenauer, T. Passow, a Grau, P. Feinäugle, H. Kalt, C. Klingshirn, and M. Hetterich, "On the incorporation of indium in InAs-based quantum structures," *Journal of Physics: Conference Series*, vol. 209, p. 012006, 2010.

[33] J. Silveira, J. García, and F. Briones, "Limited In incorporation during pseudomorphic InAs/GaAs growth and quantum dot formation observed by in situ stress measurements," *Applied Surface Science*, vol. 188, pp. 75–79, Mar. 2002.

[34] D. J. Bottomley, "Thermo-piezochemistry of InAs on GaAs(001)," *Applied Physics Letters*, vol. 80, no. 25, pp. 4747–4749, 2002.

[35] D. Granados and J. García, "In (Ga) As self-assembled quantum ring formation by molecular beam epitaxy," *Applied physics letters*, vol. 82, p. 2401, 2003.

[36] G. Costantini, A. Rastelli, C. Manzano, R. Songmuang, G. Katsaros, O. G. Schmidt, and K. Kern, "Interplay between Thermodynamics and Kinetics in the Capping of InAs/GaAs(001)Quantum Dots," *Physical Review Letters*, no. 96, p. 226106, 2006.

[37] Q. Xie, A. Madhukar, P. Chen, and N. Kobayashi, "Vertically self-organized InAs quantum box islands on GaAs (100)," *Physical review letters*, vol. 75, no. 13, pp. 2542–2545, 1995.

[38] J. Tersoff, C. Teichert, and M. Lagally, "Self-organization in growth of quantum dot superlattices," *Physical review letters*, vol. 76, no. 10, pp. 1675–1678, 1996.

[39] K. Shiramine, T. Itoh, and S. Muto, "Critical cluster size of InAs quantum dots formed by Stranski?Krastanow mode," vol. 22, no. 2, pp. 642–646, 2004.

[40] B. W. Liang and C. W. Tu, "A kinetic model for As and P incorporation behaviors in GaAsP grown by gas-source molecular beam epitaxy," *Journal of Applied Physics*, vol. 74, no. 1, p. 255, 1993.

[41] T. Nomura, H. Ogasawara, M. Miyao, and M. Hagino, "Composition control of GaAsP grown by molecular beam epitaxy," *Journal of Crystal Growth*, vol. 111, pp. 61–64, May 1991.

Chapter 5

Strain balanced InAs quantum dots stacks

In this chapter we apply the MOSS monitoring of QDs growth to the design and fabrication of strain balanced QDs stacks. After a short introduction on strain balanced QDs (5.1), we analyse the effect that the compensating layer has into the QDs size, shape and density (5.2). Then we enter into the stack design, exploiting the MOSS technique for strain balancing optimization and studying the properties of the resulting structures from the structural and optoelectronic points of view (5.3 and 5.4). These experiments will yield the formulation of some hypothesis regarding the detrimental effect of the QDs strain fields on the strain compensating layer formation and the conditions in which this effect might be prevented (5.5). We finalize the chapter with a new design of strain balanced stacks in which we circumvent the aforementioned limitations and fabricate a 50-folder stacked QDs solar cell (5.6 and 5.7).

Contents

5.1 Strain balanced QDs: general overview

The quantum dots generally represent a small fraction of the total volume in a monolithic semiconductor device. A single InAs QD layer has typically a total InAs coverage of 2 monolayers (MLs) and a spacer thickness

between QD layers of many tens of MLs. In most applications it is thus necessary to stack multiple QD layers to increase the number of photons emitted/absorbed per unit area at the QD energy levels. The number and density of those layers depends on the particular use. In lasers, for example, it is common practice to stack only three to ten QD layers to increase the modal gain and prevent gain saturation without impairing the laser threshold and modulation bandwidth. Quantum dot infrared photodetectors and solar cells, on the other hand, need tens if not hundreds of QD layers in order to have an appreciable absorption at long wavelengths. In these cases it is also interesting to stack them with thin spacer layers to increase the volume fraction corresponding to the QDs.

Due to the larger covalent radius of the atomic species forming the QDs, increasing the number and stack density of QDs layers inevitably leads to an increase of the the strain fields created by the nanostructures, as illustrated in Figure 5.1. For simplicity, QDs are described as a 4.5 nm high, 24 nm wide, lens-shaped nanostructures with a homogeneous composition of $In_{0.8}Ga_{0.2}As$ on top of a 0.5 nm thick WL of the same composition, which is typical of experimental InAs/GaAs QD samples. The strain field is calculated by minimizing the elastic energy according to continuum mechanical elastic theory using Nextnano++.[1]

In Figure 5.1a there are only three well separated QD layers. The layers are almost independent and the strain they introduce essentially dilutes in the thick spacer. As layers become closer, QDs have a tendency to align vertically due to the interacting inhomogeneous strain fields (Figure 5.1b), leading to vertically coupled quantum dots (VCQDs). If the interaction is small, Tersoff *et al.* predicted a narrowing of the QD size and inter-QD distance distribution.[2] While such beneficial effect is generally observed in VCQDs and quantum wires, it should be noted that if such interaction is strong, QDs become larger with each layer until their formation is inhibited by dislocation nucleation. The threshold between both regimes depends on the spacer thickness but also on the growth conditions (substrate temperature, orientation, growth rate, elements flux...). For thin spacers (Figure 5.1c), the VCQDs not only grow vertically aligned due to the strain fields, but also the electronic structure of the stack is modified due to electron tunneling between layers. Finally, in the limit of such small spacer that VCQDs completely overlap, each QD on the first layer becomes

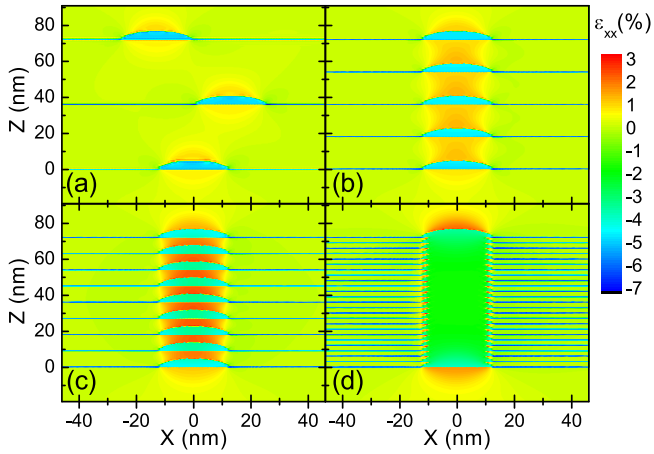

Figure 5.1: Color map showing the strain field (ϵ_{xx} component) of uncoupled (a) and vertically coupled (b,c) InAs/GaAs QDs stacks with decreasing spacer thickness and increasing number of layers and of a InAs/GaAs QP (d)

a monolithic vertical nanostructure of large aspect ratio (height/width) with new electronic properties, a quantum post (QP) (Figure 5.1d), that will be discussed in detail in the next chapter.

QD layers can be stacked only up to a point where the energy cost of bond breaking and dislocation nucleation is offset by the elastic energy due to the accumulated stress. At that point, it is energetically favourable for the structure to plastically relax and relieve the energy in excess in the form of dislocation. Their nucleation can be prevented to some degree by compensating the accumulated stress with the incorporation of a smaller atom in the crystal, typically by substituting As for P or N. Such substitution does not in fact reduce the total elastic energy, but much to the contrary increases it, as elastic energy increases quadratically with both negative and positive local strain. The real benefit of strain compensation is thus that the *average strain* of the structure is reduced and thus the nucleation of a dislocation no longer sufficiently reduces the total elastic energy.[3, 4]

Several groups have implemented their own combinations of materials in an attempt to stack many layers of QDs, either using P or N compounds, for photovoltaic applications. Nuntawong *et al.* demonstrated improved

optical quality in a stack of InAs QDs on GaAs using Ga(In)P as compensating layer (CL) for laser applications.[5] Bailey *et al.* used pure GaP as CL in a 10-folded stack of InAs QDs and Popescu *et al.* preferred GaAsP, stacking up to 50 InGaAs QDs layers on a GaAs (113) substrate.[6, 7] Finally, Oshima *et al.* used Ga(N)As very successfully as CL, in spite of the problem of reducing the bandgap of the host material.[8] In all cases, they found improved crystal quality and optical properties although the overall performance of the devices as solar cells were not as good as a reference solar cell without QDs.

Despite these promising results, it is still the open question whether the criteria used to estimate the optimum layer structure in quantum wells, as described in Section 1.5, are also valid in quantum dots and what is the actual effect of the QDs in the CL.

As pointed out by Tatebayash *et al.*, the strain field in QDs samples has two components, one homogeneous and another one inhomogeneous.[9] The former is due to the wetting layer (WL) and it can be compensated as in the case of quantum wells. The inhomogeneous strain field created by the 3D shape of the QDs, on the other hand, only can be partly relieved by the usage of strain balanced techniques. In their case, the only criterion to assess the optimum strain compensation condition for the InAs/GaP system was the QDs photoluminescence intensity. X-ray diffraction measurements of their samples showed that the zero order satellite peak was not coincident with the substrate peak, result in agreement with the prediction of the zero stress (ZS) criterion explained before.

Bailey *et al.* suggested a modification to the zero in-plane stress criterion by considering an effective thickness for the QDs layer.[6] In their approach, they weighted the WL thickness and the QDs height by the surface fraction they fill, respectively, using the resulting effective thickness as the input of the zero in-plane stress equations. Contrary to Tatebayashi *et al.*, they found an almost perfect match of the zero order satellite peak and the substrate peak at the optimum calculated conditions, also for the InAs/GaP combination.

Finally, Popescu *et al.* used an atomistic approach to obtain the strain balance condition in an InGaAs/GaAsP system.[7] They minimized the total elastic strain energy within the framework of a generalized valence

force field model. They found that only at a particular P composition in the GaAsP strain CL, the predictions of the zero in-plain stress and the atomistic criteria were coincident, largely differing for other values. Precisely at that P concentration in the barrier, optimized for a quantum well, they obtained the maximum photoluminescence intensity for the InGaAs/GaAsP strain balanced QDs system with the same nominal In content, thus concluding that the conditions were also optimal for QDs.

In this Chapter we address the strain compensation process of QDs and its optimization by using the MOSS technique, as a novel approach to evaluate the stress situation of the sample.

5.2 The QDs and the GaAsP layer

One question to be addressed before entering into the stacking of strain balanced QDs is the effect that the CL might have into the QDs morphology. In other words, whether the presence of the CL affects the size, shape and density of the QDs.

We consider three general configurations: placing the CL far from the QDs, growing the QDs directly on top of the CL and growing the CL directly on top of the QDs. A fourth possibility, embedding the QDs inside the CL, should gather the effects related with the two latter possibilities.

Following the previous reasoning, we have grown four samples. The first sample (S-A) is simply a reference sample where the QDs are fabricated at the standard conditions used along this thesis work (Figure 5.2a): 2 ML of InAs grown at T_s=510 °C, As BEP = 2×10^{-6} mbar, R_g(Ga)=0.5 ML/s and R_g(In)=0.02 ML/s. A 10 s growth pause under As flux is inserted before and after the InAs growth. This QDs layer is buried to perform PL measurements. The QDs are capped with GaAs at T_s=510 °C during the first 32 nm and then the temperature is rose to T_s=590 °C to complete 100 nm. A second QDs layer is grown on top at the same conditions to perform AFM measurements. This sample represent the situation when the QDs and the CL are very separated and there is no interaction between them. The second sample (S-B) have the same general structure but with a GaAsP layer 5.4 nm thick directly beneath the QDs layer (Figure 5.2b). It has a nominal P content of 5%, being its BEP during growth 2.4×10^{-7} mbar. A third sample (S-C) contains also

a 5.4 nm thick GaAsP layer identical to that of S-B but directly on top of the QDs (Figure 5.2c). In this case, the top AFM layer is capped with 1 nm thick GaAsP layer of the same composition to study the effect of P in the QDs size and shape. In order to compare with this one, a fourth sample (S-Acap) is fabricated with 1 nm of GaAs capping on top of the AFM QDs layer (Figure 5.2d).

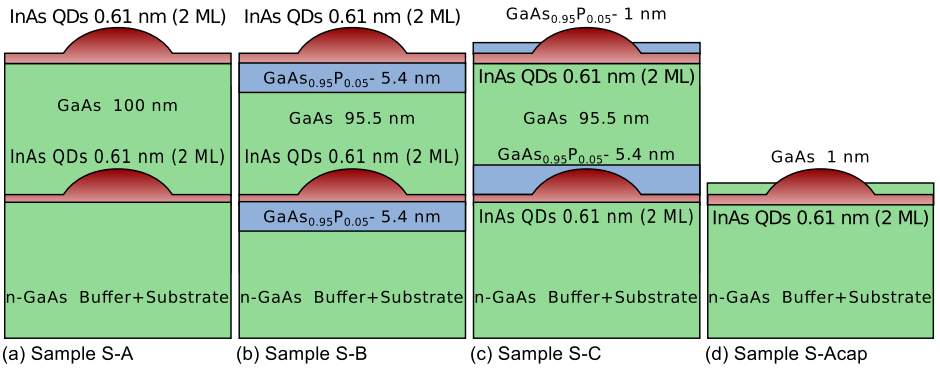

Figure 5.2: Schema of the structure of samples (a) S-A, (b) S-B, (c) S-C and (d) S-Acap.

5.2.1 AFM analysis

GaAsP beneath the QDs

To study the effect of P on the QDs properties we first compare the surface of samples S-A and S-B with AFM. The results are shown in Figure 5.3. As it can be seen, in both cases we obtain a bimodal distribution of QDs, one around 9-9.5 nm high and the other 6.5-7 nm high, labelled as large and small family respectively. The surface density is also comparable ($\sim 1.5 \times 10^{10}$ cm^{-2}). The main difference is in the contribution to that density of each family and the shape of the QDs. In S-B, the QDs have a round base and the small height family is dominant with 64% of the QDs. As it can be seen, this family has a larger dispersion of sizes, as deduced from the gaussian fits of Figure 5.3c and d. In the reference sample S-A the dominant family is the large one, with 78% of the total QDs. They have a larger base and show a slightly elongated shape in

the [1-10] direction, which is commonly observed in InAs/GaAs QDs. In general, QDs in sample S-B have less volume than in S-A indicating that part of the deposited In has not been incorporated to the nanostructures.

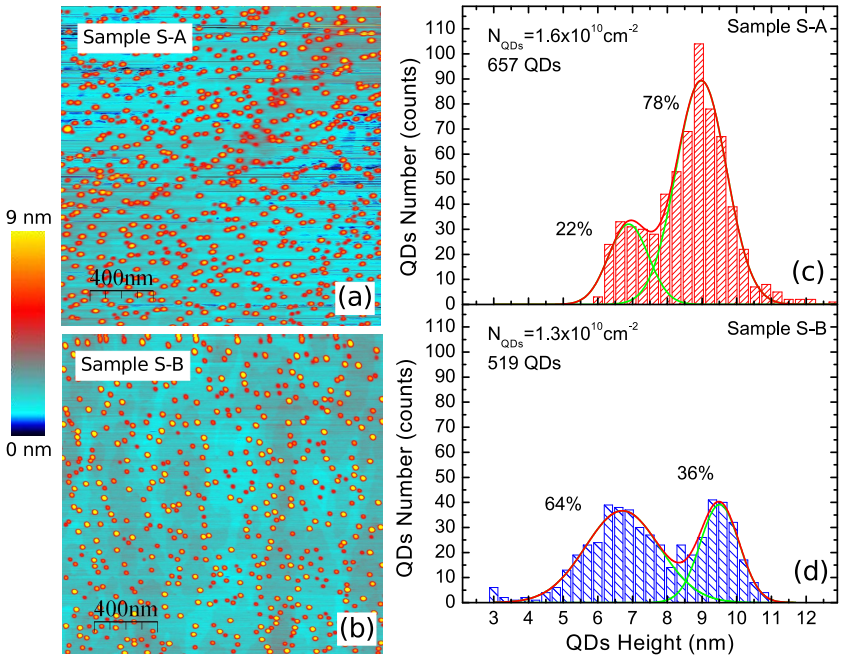

Figure 5.3: AFM images of samples (a) S-A and (b) S-B. (c) and (d) shows the corresponding height histograms of the two samples and gaussian fits.

These results are in good agreement with the findings of Kim *et al.* and Lever *et al.* who observed a reduction of the QDs size when they are nucleated on GaAsP and GaP layers, respectively.[10, 11] The main reason for this reduction is suggested to be an enhanced interdifusion of group III and V atoms between the underlying GaAsP layer and the WL/QDs, leading to layers less strained and hence to smaller QDs.

GaAsP over the QDs

The effect of the GaAsP when it is grown on top of the QDs is studied through AFM imaging of samples S-C and S-Acap (Figure 5.4a and b). As it can be seen, after 1 nm of capping the QDs heights are severely

reduced (Figure 5.4c), far more than the corresponding 1 nm, and they become elongated in the [1-10] direction in both cases (Figure 5.4d and e). The increased asymmetric lateral extension of the QDs is generally observed in this nanostructrues. It the result of the migration of In atoms from the apex of the QDs to the edges, where they can alloy with Ga and lead to a energetically more favourable situation, as it has been studied in detail by Costantini *et al.* and by Granados *et al.* at different growth conditions.[12, 13]

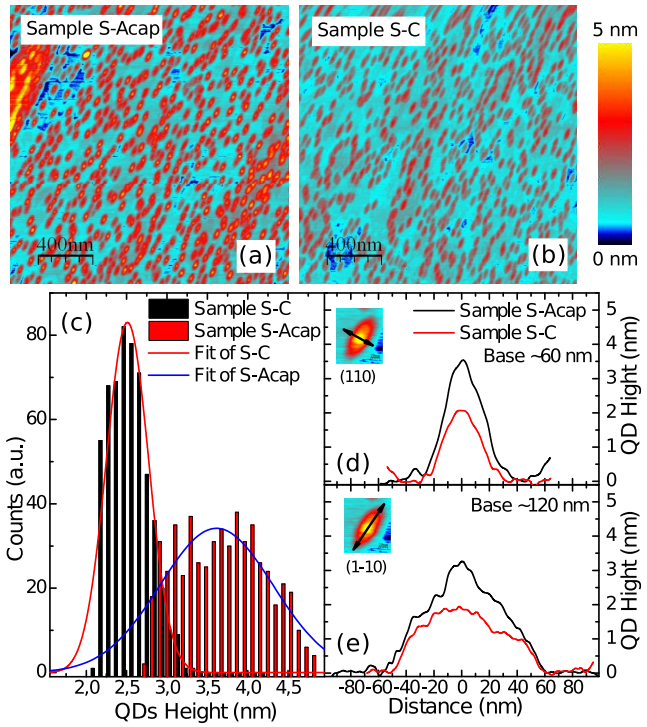

Figure 5.4: AFM images of samples (a) S-Acap and (b) S-C. (c) Histogram of QDs height for the two samples. Heights profile of typical QDs in the two samples along the (c) [110] and (d) [1-10] directions.

The heights distribution that results after analysing the images in Figure 5.4a and b is centred at 3.6 nm in the case of GaAs capping and it is further reduced to 2.5 nm in the case of GaAsP capping. Given that the initial QDs population is the same in the two samples (the one shown

in Figure 5.3c) and that the capping thickness is nominally identical (1 nm) the larger height reduction in sample S-C must be attributed to the presence of P. As shown in Figure 5.3d and e, where there is a height profile of characteristics QDs, the lateral dimensions of the partly buried QDs are the same in the two samples. This would suggest that the extra material removed from the top does not simply accumulates around the QDs in sample S-C, as explained above, but it rather spreads in the interdot space. The reason for this behaviour is probably the reduced strain of this alloyed In removed from the QDs apex due to the presence of P atoms which makes favourable the formation of a 2D layer instead of clustering around the QDs.

5.2.2 Optical characterization

The PL measurements performed at low temperature in samples S-A, S-B and S-C can be seen in Figure 5.5. As it can be observed, the resulting emission bands obtained for the three samples completely mirror the trends depicted after the AFM measurements.

Sample S-A shows an intense emission band centred at 1.116 eV and a secondary, less intense band at 1.157 eV (Figure 5.5a). They correspond to the large and small QDs families observed by AFM, respectively, being their contribution to the total PL in good agreement with the fraction of the QDs of each family. Likewise, in sample S-B two contributions are also observed. The band centred at 1.124 eV is related with the large QDs family, slightly blue-shifted with respect to its equivalent in S-A probably due to P incorporation to the QDs or the effect of the larger confinement barrier (Figure 5.5b). The broad band at 1.174 eV should be fitted with two Gaussian components and it gathers the contribution from the smaller QDs. The relative weight of each band also corresponds pretty well with the fraction of QDs of each family. It should be noted that the integrated PL intensity of the whole emission band in samples S-A and S-B is almost identical.

In sample S-C the effect of the GaAsP layer is more evident (Figure 5.5c). The PL emission band is strongly blue-shifted (56 meV) and the integrated intensity is half the value observed for sample S-A. This behaviour is in good agreement with the reduced QDs size observed by AFM after 1 nm of capping which is maintained once the dots are

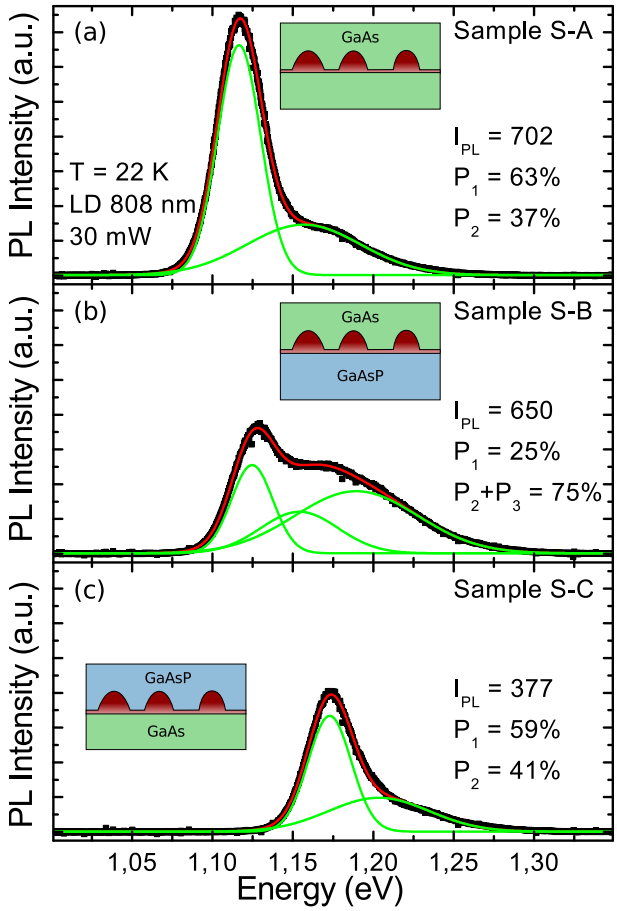

Figure 5.5: PL emission of samples (a) S-A, (b) S-B and (c) S-C. Red lines are gaussian fits of the experimental data (Squares) and green lines the different components of the fit, from P_1 (low energy) to P_3 (high energy).

completely buried. This size reduction might completely dissolve the smaller QDs which justify the small integrated PL.

5.2.3 Summary of results

In summary, this experiments indicate that the main effect of placing the CL adjacent to the QDs is a reduction of their size. This effect is small in

the case of QDs being on top of the CL but very important in the opposite situation. In the latter case, the emission properties of the QDs are strongly influence by the presence of the CL, which might be undesirable if the QDs should have low emission energies, as it is often the case.

In conclusion, in order to preserve the QDs size and separate the tuning of their properties from the strain balanced process, the CL should be placed as far from the QDs as possible, being preferable placing it beneath them than above. In this case, a thin GaAs layer between the CL and the QDs would probably completely suppress the P intermixing and the CL influence on the QDs properties.

5.3 Full strain balanced stacks: calculation of optimum conditions

5.3.1 Empirical strain balancing with MOSS and comparison with other criteria

Apart from the *ad-hoc* criteria presented in Section 1.5 which are derived for QWs, there are other two criteria with an empirical or semi-empirical origin specific for QDs: Bailey criterion and MOSS criterion.

Bailey criterion

A semi-empirical criterion, midway between the *ad-hoc* criteria presented in Section 1.5 and the experimental approximation shown below, is the modification introduced by Bailey *et al.* of the zero-stress criterion (Equation 1.14).[6] This modification considers an effective thickness that takes into account the QD density and size as well as the WL thickness. Using the zero-stress criterion (Equation 1.14), they calculate separately the optimum thickness to compensate the WL, on the one hand, and to compensate a layer with the same thickness that the QDs height, on the other hand (t_{cl}^{WL} and t_{cl}^{QDs} respectively). The resulting effective thickness of the CL t_{cl}^{eff} is obtained by weighting the QDs and the WL values by their corresponding areal fraction (d and $1-d$, respectively):

$$t_{cl}^{eff} = dt_{cl}^{QDs} + (1-d)t_{cl}^{WL} \tag{5.1}$$

This modification gives more accurate values for the CL parameters but it assumes a certain composition for the QDs and a thickness for the WL, information that is not usually known unless cross section techniques sensitive to composition were used. Additionally, QDs are usually smaller and wider once they are capped compared with the information taken from atomic force microscopy images (AFM) which introduce another source of error (see Section 5.2, for example). Nevertheless, Equation 1.14 combined with Equation 5.1 in principle constitute a better starting point to further refine the optimum parameters of the CL than the *ad-hoc* criteria.

MOSS criterion

One of the contributions of this thesis work is the introduction of the MOSS technique to evaluate the strain balancing state of the sample. MOSS is sensitive to In segregation, the real P incorporation and the presence of the QDs, so it presents several advantages over other strain balanced criteria. With MOSS, the criterion for a perfectly balanced QDs sample consists simply in reaching a situation where the accumulated stress per period is zero:

$$\Sigma\sigma_{compressive} + \Sigma\sigma_{tensile} = 0 \tag{5.2}$$

In Chapter 4, we showed that the compressive stress accumulated by the QDs, $\Sigma\sigma_{QDs}$, has a rather complex dependence on the growth rate, substrate temperature and As BEP. The tensile stress $\Sigma\sigma_{tensile}$, on the other hand, in principle can be assumed to correspond to a perfectly flat layer of homogeneous composition in which case it can be described by Equation 4.10. This assumption serves only to have an idea on the P composition of the layer given that the real variable that will be used is the P BEP, as shown in Figures 4.14 and 4.15. The resulting criterion results in:

$$\Sigma\sigma_{QDs} + M_{cl}\epsilon_{cl}t_{cl} = 0 \tag{5.3}$$

where M_{cl} , ϵ_{cl} and t_{cl} are the biaxial modulus, the lattice mismatch and the thickness of the CL, respectively. It should be noted that in the limiting case of a flat, homogeneous compressive layer with the nominal composition and thickness, $\Sigma\sigma_{QDs}$ will also be given by Equation 4.10 and this criterion

Table 5.1: Different criteria used to evaluate the strain balanced condition. In Bailey's criterion, we show the equation that estimates the effective thickness of the CL (Equation 5.1). Only the last two are specific to QDs.

Criterion	**Equation**	**Ref.**
Average Lattice (AL)	$t_{cl}a_{cl} - t_{QW}a_{QW} = (t_{cl} + t_{QW})a_{subs}$	[14]
Thickness Weighted (TW)	$t_{cl}\epsilon_{cl} + t_{QW}\epsilon_{QW} = 0$	[15]
Modified TW (MTW)	$A_{cl}t_{cl}\epsilon_{cl} + A_{QW}t_{QW}\epsilon_{QW} = 0$	[4]
Zero Stress (ZS)	$A_{cl}\epsilon_{cl}t_{cl}a_{QW} + A_{QW}\epsilon_{QW}t_{QW}a_{cl} = 0$	[4]
Bailey	$t_{cl}^{eff} = dt_{cl}^{QDs} + (1-d)t_{cl}^{WL}$	[6]
MOSS	$\Sigma\sigma_{QDs} + M_{cl}\epsilon_{cl}t_{cl} = 0$	[16]

would be identical to the MTW shown in Table 1.1. Nevertheless, there is no real need of representing the MOSS criterion in the form given in Equation 5.3 since its empirical form shown in Equation 5.2 is more general and do not assumes any condition for the CL.

Criteria comparison

Before entering into the strain compensation of stacks of QDs, it is interesting to compare the strain balanced criteria used in the literature with the experimental approach used here. In Table 5.1 we reproduce the equations that allows to estimate the appropriate strain balanced conditions (composition and thicknesses) according to the various *ad-hoc* criteria reported to date and discussed in Section 1.5, namely the average lattice (AL), thickness weighted (TW), modified thickness weighted (MTW) and zero stress (ZS), the semi-empirical approach introduced by Bailey and the MOSS empirical strain balanced criterion presented here.

In order to compare the criteria, we have calculated the thickness of the CL needed to balance the stress introduced by 2 ML InAs. The barrier material is GaAsP of various compositions, from very dilute alloys to pure GaP layers. For MOSS, we apply Equation 5.3 using the experimental accumulated stress shown in Figure 4.4. For Bailey's criterion, we use the parameters obtained from an atomic force microscopy image of an uncapped QDs layer grown in the same conditions explained above at 510 °C (t_{QD} = 5 nm and d = 0.13) and a WL thickness of t_{WL} = 0.5

nm. In this case, we consider that the QDs and WL compositions are pure InAs.

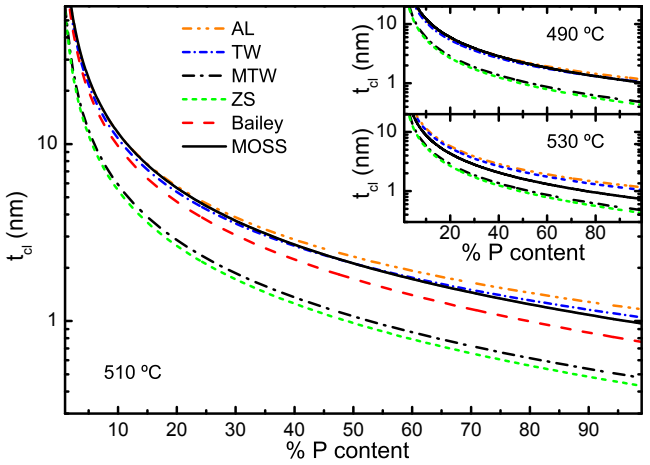

Figure 5.6: Comparison of the main strain balanced criteria.

The result of such calculations are shown in Figure 5.6. As it can be seen, in all criteria the CL thickness rapidly reduces as the P content of the layer is increased, as expected. The predicted optimum CL thickness according to our approach is very similar to the predictions of the AL or TW criterion. Conversely, our predicted values are almost double of those deduced from the MTW or the ZS criteria, which is a direct consequence of the larger stress accumulated by the 2 ML of InAs compared to the theory, as shown before (see Section 4.2). In the case of Bailey's criterion, the values obtained are also larger than the MTW and the ZS, but still smaller than our results or the AL/TW criterion.

In the light of the previous analysis, it might be concluded that MOSS and AL criteria are essentially equal, however, the differences become clearer when the same comparison is made for other substrate temperatures, shown in the insets of Figure 5.6. Although for the 490 °C our approach is identical to the AL, for 530 °C it is very different, predicting values midway between the AL/TW and the MTW/ZS criteria. The explanation is that the theoretical criteria do not take into account the variations in the accumulated stress due to the growth parameters, such as the substrate temperature, As BEP or growth rates, something that MOSS

criterion does. As a consequence, the coincidence between the MOSS predictions and other criteria's is only by chance and not a fingerprint of a fundamental relationship between them.

Our analysis also explain why two very similar strain balanced structures, as those shown by Tatebayashi *et al.* and Bailey *et al.*, can give different results when they are analysed with XRD. From a theoretical point of view, only a structure grown following the AL criterion should give an exact match of the first order satellite peak and the substrate peak, as shown by Ekins-Daukes *et al.*[4] However, according to our results, that is the situation only for certain growth conditions, namely low growth temperature in this case. Using other conditions will result in a sample with different In segregation and, hence, with different stress, even for the same nominal structure. In principle this is a general conclusion also valid for strain balanced QWs.

From this results we conclude that a match of the satellite and substrate peaks can not be used in general as a fingerprint of a correct strain balanced structure and that perfectly compensated stacks can give a wide variety of XRD patterns.

5.3.2 Design and growth of the stacks

After this preliminary analysis, we designed two strain balanced QDs stacks (QDs-A and QDs-B) aiming to a 100% of strain compensation according to the MOSS criterion. In both cases we use 2 ML of InAs for the QDs and a total spacer between layers of 15 nm. Substrate temperature and As BEP are kept constant at 510 °C and 1.5×10^{-6} mbar, respectively, during the growth of the stacks. As usual, the substrate is GaAs (001) cantilever shaped with a thickness of 100 μm.

The only difference between the samples is the CL layer thickness and composition. In sample QDs-A we use a 13 nm thick layer with a P BEP of 2×10^{-7} mbar after 1 nm of GaAs capping, whereas in sample QDs-B we use a layer 5 nm thick and a P BEP of 8.5×10^{-7} mbar after 8 nm of GaAs capping. These pressures corresponds, approximately with 4.3% and 18% of phosphorus content, respectively, according to the previous calibration (Section 4.5). The structure of both samples can be seen in Figure 5.7.

The MOSS curve recorded during the fabrication of both stacks can be seen in Figure 5.8a and b together with the opening/closing sequence of

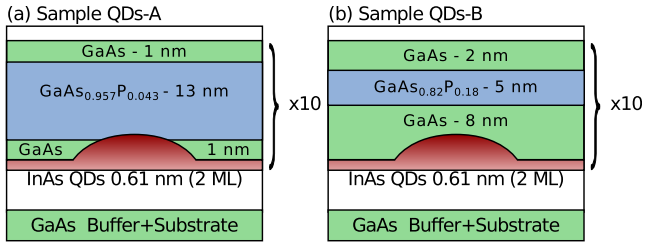

Figure 5.7: Schema of the structure of samples (a) QDs-A and (b) QDs-B.

the effusion cells.

As it can be seen, both curves show an oscillating behaviour result of the sequence of compressive/tensile stress introduced by the InAs and GaAsP layers, respectively. The stress has been successfully balanced in both cases since the accumulated stress after several periods is close to zero. Assuming that each QD layer introduces a stress of -5 N/m, we obtain an average strain compensation of 95% for sample QDs-A and 105% for sample QDs-B. Using Equation 4.19, we can estimate the P content from a linear fit of the accumulated stress in the GaAsP region (dashed red lines), leading to 3.8% and 20.6%, respectively. These values are slightly different but still within reasonable agreement to the nominal values.[1] The oscillations corresponding to the compressive/tensile stress sequence are damped in sample QDs-A. This is due to the InAs and GaAsP intermixing and was expected given the small GaAs capping on top of QDs. The formation of quaternary InGaAsP compounds introduces a stress (compressive or tensile) smaller than the corresponding InAs or GaAsP alloys separately thus, although the strain is balanced on average, the stoichiometry of the stack is uncontrolled. This intermixing has an impact on the optical properties of the QDs and must be taken into account when placing the strain CL too close to the QDs, as it was discussed in Section 5.2.

It should be noticed that the results presented here are only an example of perfectly balanced stacks using the MOSS technique. Other combinations of strain CL composition and thickness are possible, such as using pure GaP layers, GaInP or dilute nitrides, having optical or electrical

[1]These two values were also used in Section 4.5 to increase the statistics of the study of accumulated stress *vs* P BEP.

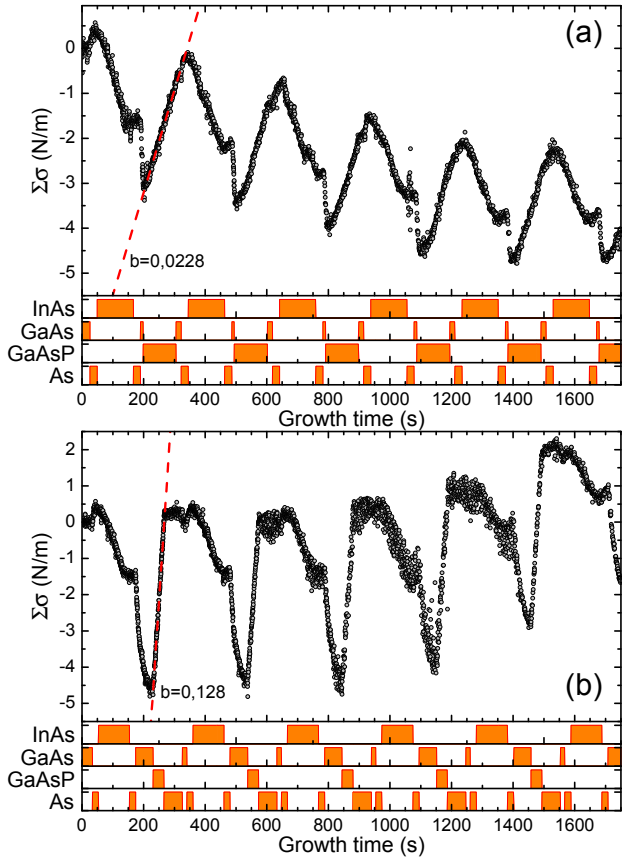

Figure 5.8: Accumulated stress of samples a) QDs-A and b) QDs-B.

properties more suitable for a particular application.

5.3.3 Structural characterization

Modeling of the MOSS curve

We can get an insight into the composition of these two samples by simulating the MOSS curve, the same way we did in Section 4.3 with a regular InAs QD.

In the case of sample QDs-B, no intermixing between the strain CL

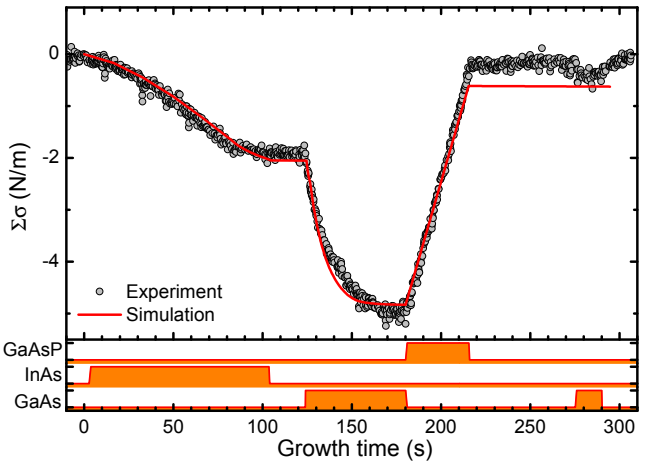

Figure 5.9: Experimental and simulated accumulated stress curves of one period of Sample QDs-B.

and the segregating In is expected as most of it is already incorporated to the sample. In this case, the CL is modelled as a homogeneous GaAsP alloy 5 nm thick and with 20.6% of P, as deduced from the fit of the curve made before. In Figure 5.9 the result of the simulation is plotted as a continuous line together with the experimental data corresponding to the first period shown in Figure 5.8b. As it can be seen, the schema used in the simulation closely follows the experimental results, both in the QDs and first stages of capping and in the compensation region. In the latter, the simulated curve shows a slightly smaller slope than in the experiment, giving a degree of compensation of 88%, close but smaller than the 105% found experimentally.

For sample QDs-A, on the contrary, the reduced separation between the InAs and the GaAsP suggests a large degree of intermixing during capping. In this case we have used an InGaAsP layer with a homogeneous P content of 3.8% and the same In profile used in Section 4.3 for the GaAs capping. The simulation, shown in Figure 5.10, continuous, red line, clearly deviates from the experiment, both from a qualitative and quantitative points of view. The curve exhibits a transition region at the beginning of the InGaAsP layer, from increasing to reducing the accumulated stress, which is not present in the experimental results. In addition, the final

accumulated stress is -2.62 N/m giving a degree of compensation of only 48%.

This disagreement between experiment and simulation seems to indicate the existence of an additional mechanism regarding the In incorporation and segregation in the presence of P. Such mechanism might be either an increased segregation efficiency or even evaporation of In adatoms back to the chamber in the presence of P or an enhancement of the P incorporation to the sample, any of them leading to the formation of a quaternary InGaAsP alloy with larger P content than expected. In both situations, we can try to model the CL as an homogeneous GaAsP alloy, that is In-free, using the P content deduced before (3.8%). The In that is not incorporated to the sample after 1 nm of GaAs capping is omitted. The In-rich growth front is frozen at its position when the GaAsP growth begins. The result of that simulation is shown as a dashed, blue line in Figure 5.10. As it can be seen, the simulation mimic more precisely the experimental results, although it is still visible a certain curvature related with the coverage of the QDs. The agreement in the final accumulated stress is not complete due, again, to the smaller slope of the GaAsP region in the simulation than in the experiment, leading to a degree of compensation of 72%.

Despite the small disagreement in the slopes, these results suggest that the incorporation of In and P are strongly interdependent. Apart from the quaternary alloy used in the calculations, the In segregation or its desorption, the formation of complex binary or ternary compound regions due to composition modulation is also probable, as it is often observed in InGaP based alloys where a spinodal decomposition in GaP and InP is energetically favorable.[17] As a consequence, the accumulated stress in a structure where the strain CL is grown very close to the InAs layer can not be anticipated from the simple simulations made before.

RHEED and AFM

Although the stress balancing process was perfect according to the MOSS measurements, the above structures presented the fundamental drawback of lack of QDs formation beyond the seventh QDs layer.

During growth of these stacks, the whole process is monitored with RHEED which allows to asses the planarity of the sample surface or

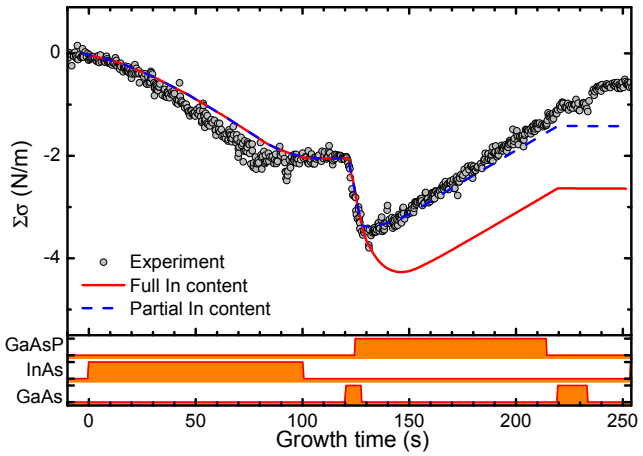

Figure 5.10: Experimental and simulated accumulated stress curves of one period of Sample QDs-A. Continuous curve assumes an In distribution similar to that used in non-strain balanced samples (R=0.5→R=0.8 during capping). Dashed curve assumes that all In not incorporated in the first 1 nm of capping is lost.

the nucleation of QDs, among other things, as discussed in Chapter 2. During the fabrication of these two samples, the RHEED intensity faded progressively with the number of layers until no QDs formation were observed after the 7^{th} layer.

To discard any influence of the experimental set-up and/or the growth conditions, we performed a series of tests that allow us to evaluate the problem.

As mentioned before, growing on a lever might present the problem of temperature inhomogeneity along the cantilever due to a distant thermal anchoring. Therefore, in order to remove any effect related with the particular growth conditions, the same sequences were repeated on normal GaAs (001) substrates 500 μm thick sticked to a Si wafer with indium, which is our standard sample holding method. The other growth parameters (substrate temperature, P and As BEP...) were kept unchanged. As it happened before, under these conditions, we get the same progressive blurring of the RHEED image which allows discarding the lever set-up as a source of errors.

Secondly, a new stack following the sequence of sample QDs-B was

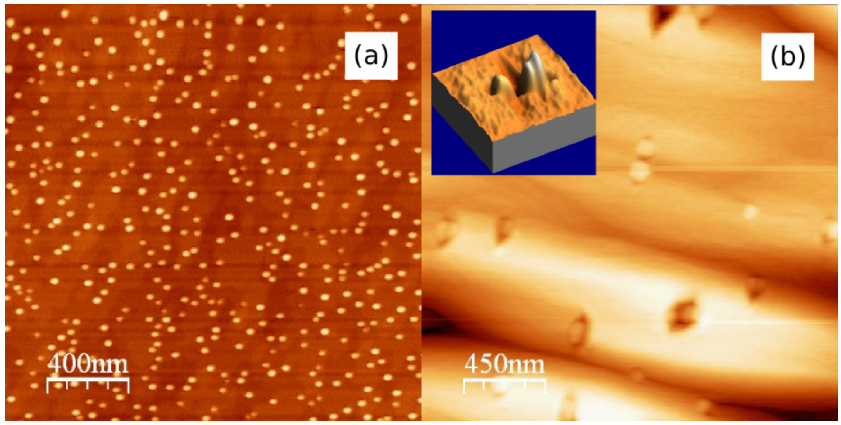

Figure 5.11: (a) Typical QD layer grown at 510 °C after 2 ML of InAs. The QD density is 10^{10} cm^{-2} and their height and diameter 5 and 40 nm respectively. (b) Surface of the 7^{th} QDs layer. The inset shows a detail of one QD representative of this layer with a very large size (>10 nm height and 100 nm in diameter) and inside holes or ridges.

grown leaving the 7^{th} layer uncapped to perform AFM measurements. In Figure 5.11, there is a comparison of a typical layer of QDs grown at 510 °C after the deposition of 2 InAs ML and the uncapped 7^{th} layer of the stack grown at the same conditions. As it is evident in Figure 5.11b, the formation of QDs is almost completely inhibited. Sample surface presents important undulations and only a few large QDs inside holes.

Finally, we check the quality of other samples fabricated on this MBE system in order to discard a possible contamination or related problem on the reactor. None of the other samples considered (including QPs samples that will be discussed in Chapter 6) presented any anomalous behaviour that could be related with this.

5.4 Partly strain balanced stacks

To fully discard the possibility of an overcompensation we decided to fabricate new QDs stacks by using more conservative conditions than those predicted by the MOSS technique. For this reason, we have designed and grow two new stacks of QDs aiming, in this case, only to a 60% of

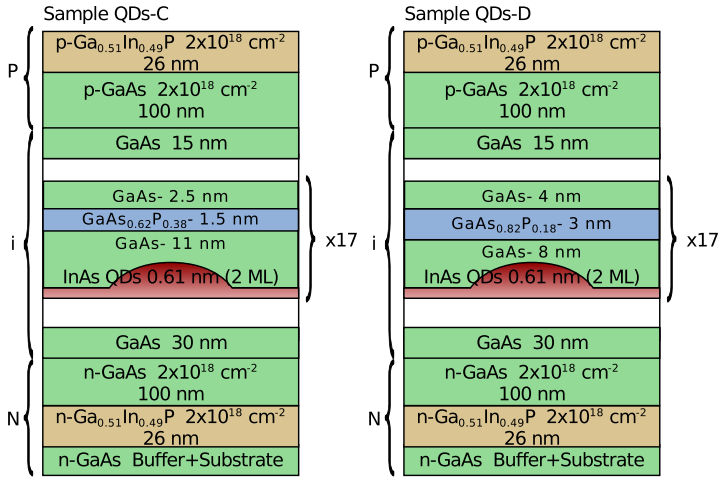

Figure 5.12: Schema of the structure of samples (a) QDs-C and (b) QDs-D.

strain balancing. A 60% of compensation according to MOSS criterion is, roughly, a 130% of compensation according to the ZS criterion. These partly strain balanced samples are then characterized from structural and optical points of view in order to get an insight into the properties of these stacks.

5.4.1 Design and growth of the stacks

The two structures were first fabricated in thin substrates to perform a MOSS analysis and then repeated in normal n-type GaAs substrates in the form of PiN diodes in order to study their optical and electrical properties. We will use the subscript m to indicate that we are talking about the structures grown for MOSS measurements.

In both samples we use 2 ML of InAs for the QDs and a total spacer between layers of 15 nm. Substrate temperature and As BEP are kept constant at 510 °C and 1.5×10^{-6} mbar, respectively, during the growth of the stacks. As with samples QDs-A and QDs-B, the only difference between these structures is the strain balancing layer thickness and composition. In sample QDs-C we use a 1.5 nm thick layer with a P BEP of 1.85×10^{-6} mbar after 11 nm of GaAs capping, whereas in sample QDs-D we use a layer 3 nm thick and a P BEP of 8.5×10^{-7} mbar after 8 nm

of GaAs capping (Figure 5.12). These pressures correspond, approximately with 38% and 18% of phosphorus content, respectively, according to the previous calibration (Section 4.5).

Both QDs sequences are repeated 17 times and embedded in the seminsulating region of a PiN diode, with 30 nm of GaAs below and 15 nm above them. The full structure and growth sequence of the PiN diodes can be found in Figure 5.12 and are as follows: After a n-GaAs (Si:10^{18} cm^{-2}) buffer layer, we grow a n-$Ga_{0.51}In_{0.49}P$ (Si:2x10^{18} cm^{-2}) 26 nm thick back surface field layer, 100 nm of n-GaAs (Si:2x10^{18} cm^{-2}), the seminsulating region around 310 nm thick that contains the QDs, 100 nm of p-GaAs (Be:2x10^{18} cm^{-2}), 26 nm of p:$Ga_{0.51}In_{0.49}P$ (Be:2x10^{18} cm^{-2}) and a thin p-GaAs (Be:2x10^{18} cm^{-2}) layer to serve as contact layer.

Standard optical lithography and wet etching techniques were used to define mesas and metal ohmic contacts following schema number 1 (Section 2.2.1).

5.4.2 Structural characterization

MOSS measurements

The evolution of stress during the growth of both stacks can be seen in Figure 5.13. In sample QDs-C_m, the stress accumulates during QDs growth and the initial stages of capping following a similar behaviour already discussed in samples QDs-A and B, and also in the previous chapter. Once In is exhausted, the GaAsP layer grows, rapidly compensating the compressive stress. The compensation degree found for this sample is around 50% and the estimated P content of the GaAsP layer obtained after a linear fit and using Equation 4.19 is 29%.

This compensation and the P content are below the nominal values (60% and 38%, respectively), suggesting that achieving high P content GaAsP layers might require larger P BEP that predicted or even to reduce the As BEP to mitigate the competition between both species.

The results shown for sample QDs-D, on the other hand, have some distinctive features compared to sample QDs-C. Whereas the latter accumulates around -2 N/m during the InAs growth, the same that the other samples considered so far, sample QDs-D_m accumulates around -3.5 N/m. In addition, the stress accumulates linearly, without the smooth

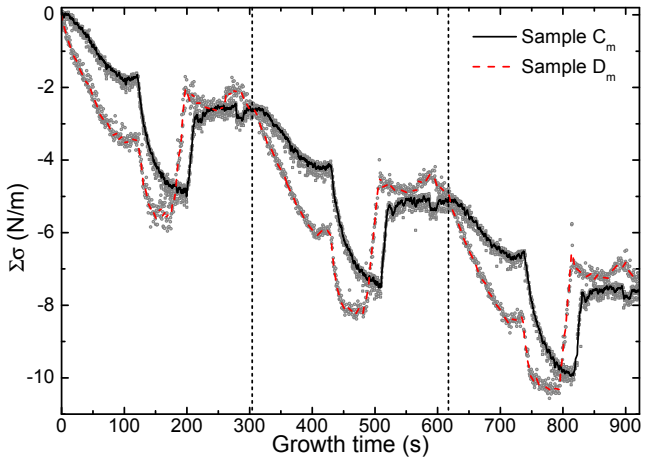

Figure 5.13: Accumulated stress of samples QDs-C$_m$ and QDs-D$_m$. Vertical dashed lines indicate the different periods.

curvature typically observed. Finally, during GaAs capping the stress accumulates very fast and In seems to be exhausted in only 4 nm. All of this characteristics suggest that the substrate temperature during growth of sample QDs-D$_m$ was, on average, too low, well below the nominal 510 °C and hence the accumulated stress curve presented for sample QDs-D$_m$ is not truly representative of the strain balanced structure grown in sample QDs-D and that will be considered next.

RHEED analysis

Even thought the compensation in these two samples was close to the calculated value (at least in the case of sample QDs-C), the RHEED monitoring again indicated that there was no QD formation beyond the 6-7th layer of the stack, as it was also observed in the full compensated samples. This happens in the lever structures and in the PiN diode structures.

In Figure 5.14 we compare the critical thickness of all samples grown so far within this chapter (samples QDs-A to QDs-D). The first thing to be noted is that θ_c decreases in all cases for the layers following the first one (layers 2 to 4, depending on the sample). This reduction of the critical

thickness has been reported before and, considering the spacer between layers, it must be attributed to the presence of the strain fields of buried nanostructures which ease the formation of the QDs.[18]

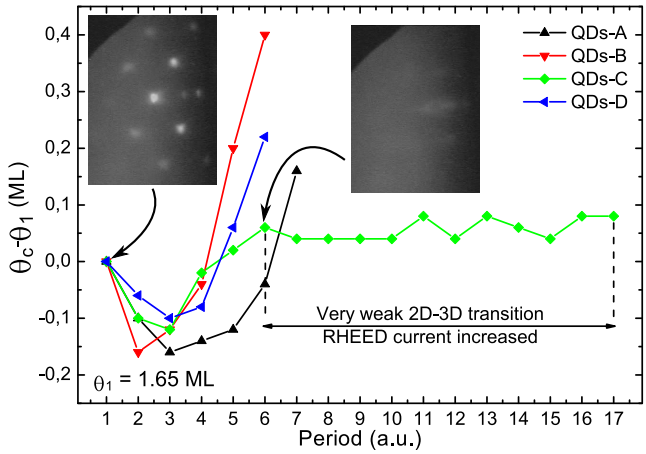

Figure 5.14: Comparison of the critical thickness evolution as a function of the period number for samples QDs-A to QDs-D. The insets show the recorded RHEED pattern after QDs nucleation of the first and sixth layer of samples QDs-C.

After those first layers, θ_c increases again, becoming larger with each QDs layer. Samples QDs-A and QDs-B, as explained above, do not show the 2D→3D transition beyond the 7^{th} layer, not even a slight hint of QDs formation with increased RHEED intensity. In sample QDs-D, on the contrary, the beginning of the transition is apparent beyond the sixth layer although the critical thickness is hard to measure even with increased RHEED current, given that the pattern is blurred. Similarly, in sample QDs-C, the critical thickness is barely measurable and the RHEED signal becomes weaker with each layer. In this case, although a value for the critical thickness is given, it has a large uncertainty.

In summary, the analysis of the critical thickness for QDs nucleation suggest that the mechanism responsible for the stack degradation is not directly related with an overcompensation of the QDs layers, given that very similar results are obtained in both, 100% and 50-60%, compensated samples.

TEM imaging of the stacks

Further structural characterization has been performed in sample QDs-C by transmission electron microscopy (TEM). In Figure 5.15a we show a low magnification high angle annular dark field scanning TEM image (HAADF-STEM) of the QDs stack. The seventeen InAs layers are clearly seen as bright horizontal stripes whereas the GaAsP layers are seen as darker stripes above the clearer ones.

In the lower layers, it can be seen the formation of QDs which appear vertically aligned, as it is commonly observed in stacks with small spacers. Although it is generally observed that VCQDs become wider with the number of layers due to the increased strain fields and lower lattice mismatch on a local scale, in our case this QDs evoulution leads to their disappearance at a certain point. The image reveals that there is no QDs formation beyond the seventh layer, leading to homogeneous, flat structures with no distinct characteristics at this magnification.

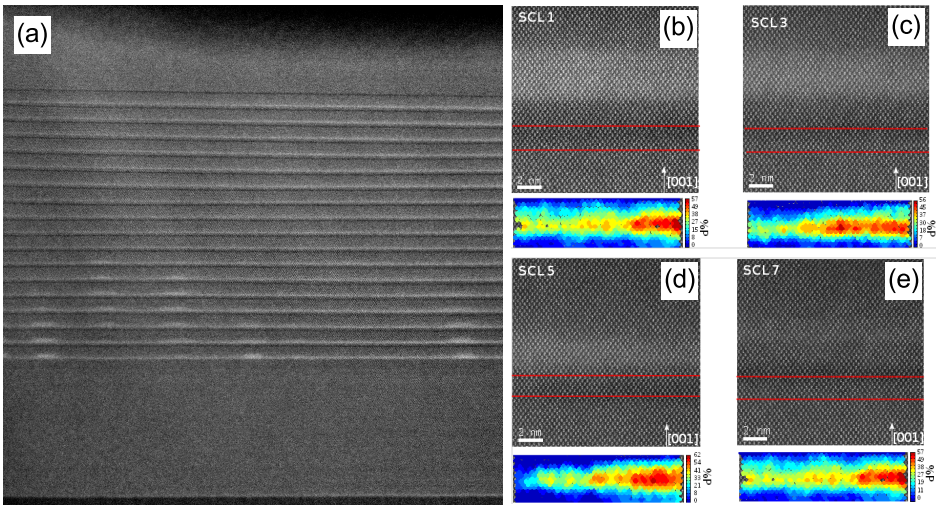

Figure 5.15: (a) Low magnification HAADF-STEM image of sample QDs-E. (b) to (e) HAADF-STEM images of 1^{st}, 3^{rd}, 5^{th} and 7^{th} CLs, respectively, and the corresponding P compositional maps. STEM Images taken by Dr. Manuel A. Roldán and analysed at UCA.

Quantitative information about the composition of the CLs can be

extracted with the aid of Z-contrast HAADF images by comparing simulated and experimental images.[19] In Figure 5.15b to e we show the resulting composition maps of P in layers 1^{st}, 3^{red}, 5^{th} and 7^{th} approximately above a QD. As it can be seen, the P composition along the layer in this region is highly inhomogeneous, even in the first layer, with values ranging from 8% to 60% of P. No clear evolution is observed with the layer number.

This result is in agreement with the observation of no QDs formation beyond certain layer observed by RHEED and indicates that, far from the assumptions made in the strain balanced criteria, the CL can not be considered a 2D layer with homogeneous composition. Much to the contrary, it presents large deviations from its nominal content (as large as ±30% of P in the previous case) that leads to severe over and sub compensated regions on a local scale.

5.4.3 Optoelectronic characterization

Despite the inhomogeneity observed before, we have study the optical and optoelectronic properties of these QDs stacks by means of photoluminescence, electroluminescence and photocurrent spectroscopy. This experiments will allow to depict the band diagram of the samples and have a better idea on the properties of these strain balanced QDs.

First, we have measured the PL of samples QDs-C and QDs-D. Being the epitaxy relatively thin and the substrate n-type GaAs, we have used a short wavelength laser (532 nm) to avoid spurious contribution to the PL signal of the later.

As it can be seen in Figure 5.16, the low temperature PL of these two samples is characterized by the presence of several emission bands between 1.1 and 1.5 eV. In sample QDs-C, we identify up to five Gaussian contributions at 1.14, 1.18, 1.24, 1.31 and 1.37 eV, in addition to the higher energy bands that we will discuss later. The inhomogeneous broadening of these bands ranges from 40 to 60 meV. Similar trends are observed in sample QDs-D, with bands centred at 1.12, 1.18, 1.25 and 1.31 eV and broadenings also ranging from 40 to 60 meV. As it can be seen, the different contributions observed for both samples are very similar, suggesting that they have the same origin.

As it was discussed in Section 5.2.2, a sample with a single layer of QDs

grown in our typical conditions shows the ground state emission band of the dominant QDs family at 1.12 eV. On the other hand, the TEM characterization made before suggest that QDs become shallower with the number of layers until they disappear. As a consequence, we believe that each band observed in Figure 5.16 is related with the emission from a QDs family placed in a different layer. The lowest energy band at 1.12-1.14 eV would correspond to the first QDs layer and the higher energy bands to the QDs in the successive layers.

The highest energy peaks (at 1.45, 1.478 and 1.50 eV in sample QDs-C; 1.44, 1.472 and 1.497 eV in sample QDs-D) have their origin in optical transitions associated to the substrate and doped layers (CB-acceptor and its LO phonon replica mainly). The WL is expected at 1.42 eV although is barely visible in the PL spectrum due to the high QD density of these samples. Its contribution will be more important in EL as shown below.

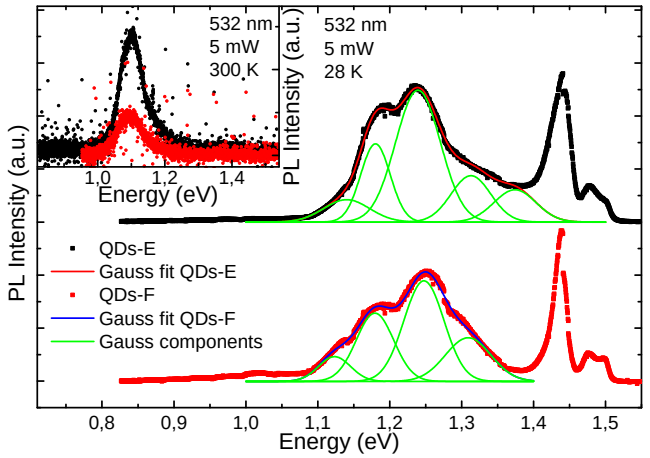

Figure 5.16: Low temperature PL emission of samples QDs-C and QDs-D together with a Gaussian fit. The inset shows the PL at room temperature.

PL *vs* temperature

Further information about the QDs can be obtained by performing PL measurements as a function of temperature. In Figure 5.17a we show the resulting measurements for sample QDs-D. As it can be seen, with

increasing temperature the high energy contributions tend to disappear whereas the lower energy ones become more relevant. Coloured arrows show the position of the bands described previously for this sample. In general it can be seen that the whole band looses intensity and shifts to lower energies as a result of the bandgap reduction at higher temperatures.

We can fit the temperature series to four Gaussian contributions in order to study the thermal scape properties separately of each band. The resulting Arrhenius plots of the four bands are shown in Figure 5.17b. The bands disappear sequentially from the higher energy (peak 4) to the lower energy (peak 1). Simultaneous to the quenching of peaks 4 and 3 there is an appreciable increase in the corresponding emission of peak 2. Conversely, when this one looses intensity, peak 1 becomes more intense. This link between the reduction of a family contribution and the increase of a less energetic one suggest a charge transfer from small QDs to larger ones.

Fitting the high temperature range of peaks 2-4 to a straight line we can obtain the corresponding thermal activation energies of each family. The result of such fitting is plotted as dashed lines in Figure 5.17b. For peak 4 we find a thermal activation energy of 145 meV, compatible with excitonic scape of carriers from the QDs to the WL (assumed at 1.44 eV). For peak 3 we find 187 meV, which suggest the same excitonic scape mechanism. Finally, for peak 2 we obtain an activation energy of only 167 meV which is too low to correspond to excitonic scape given the observed transition energy at 1.18 eV. In this case, the unipolar scape either of electrons or holes is probably the dominant quenching mechanism.

PL *vs* applied voltage

To get further insight into the nature of the transitions observed in PL, we have taken advantage of the PiN diode structure of these samples and performed PL measurements for varying applied voltage. A positive voltage has been applied until electrical injection of carriers begins to produce electroluminescence (which we study later). The negative bias is applied until no significant variation is observed in the PL signal or the current flowing through the device reaches 1 mA. The results of these measurements for sample QDs-D are shown in Figure 5.18.

As it can be seen, the PL signal slightly differs from the one shown

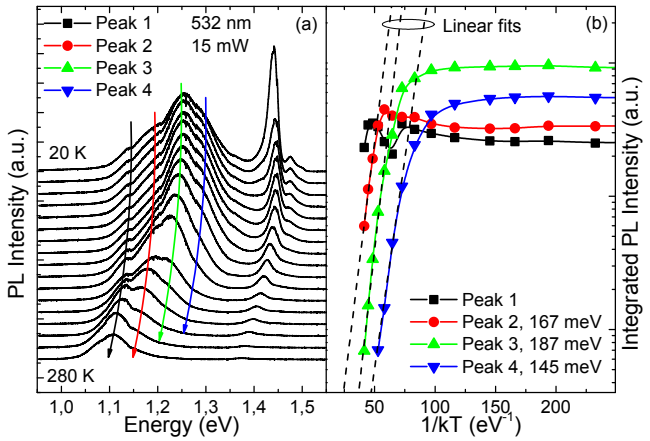

Figure 5.17: (a) PL intensity as a function of temperature for sample QDs-D. (b) Arrhenius plots of the corresponding Gaussian components.

before, showing only three well resolved Gaussian contributions at 1.125, 1.2 and 1.298 eV with widths ranging from 40 to 63 meV. The reason for this discrepancy is that the device was processed in a part of the wafer close to its edge, which is known to have smaller temperature during MBE growth.

In Figure 5.18a it can be seen the sequential disappearing of the emission bands, from the low energy to the high, until only the peaks associated to bulk transitions from the doped layers remain (they are not affected by the electric field). We can extract the band position and the integrated PL intensity as a function of the applied voltage by fitting the series to three Gaussian components (Figure 5.18b). To perform this fitting, the spectrum at -3 V has been subtracted from the others to leave only the part of the signal that varies with voltage.

The integrated PL intensity (Figure 5.18c) shows that the low energy band disappears slowly up to -0.7 V, then it begins to quench faster. Similar trends can be observed for peaks 2 and 3, with cut-off voltages of -1.6 and -2.6 V approximately. In each case, the quenching acceleration is accompanied by a red-shifts of the peaks (Figure 5.18d). This shift is consistent with existence of the quantum confined Stark effect (QCSE) often observed in this kind of nanostructures.[20]

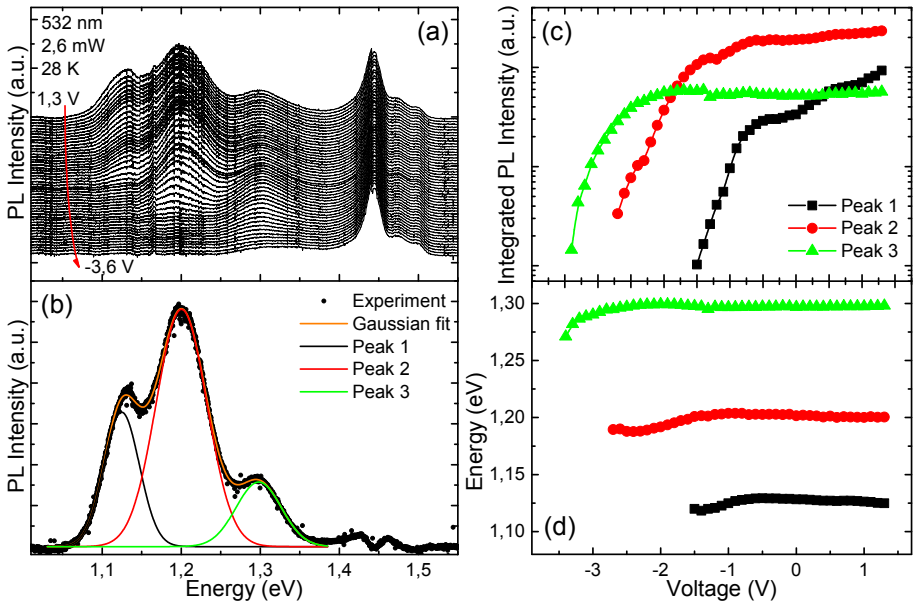

Figure 5.18: (a) PL emission as a function of voltage. (b) Gaussian fit of the highest voltage spectrum, showing the components that are used to fit the whole series. (c) Integrated intensity and (d) energy position of the Gaussian components as a function of voltage.

Although the disappearance of the PL bands is expected, the observed sequence is not the usual one. Since less confined carriers should be able to scape before most confined ones, if the electric field is constant within the intrinsic region, the peaks at higher energy should disappear before the low energy ones irrespectively of their spatial origin within the QD stack. The spectra shown in Figure 5.18a follow the opposite sequence with the quenching proceeding from low to higher energies with increasing reverse voltage. This can be explained if the electric field along the vertical QD stack is not constant.

The main mechanism that might produce a varying dropping of the electric field in the structure is the presence of unintentional residual doping in the materials.

In Figure 5.19 we show a comparison of the calculated band diagrams using Nextnano in a PiN structure containing 17 $In_{0.8}Ga_{0.2}As$ QWs 0.5

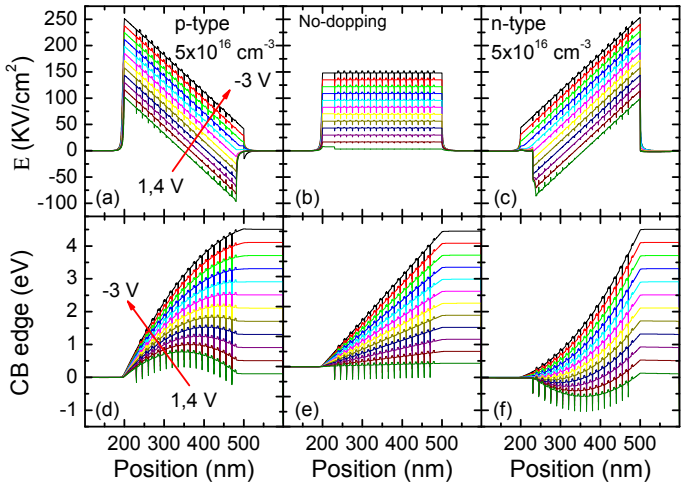

Figure 5.19: Calculated electric field (top row) and CB edge (bottom row) for a background doping in the semi-insulating region: (a)(d) p-type, (b)(e) no-doping and (c)(f) n-type.

nm thick, a spacer of 15 nm and $GaAs_{0.82}P_{0.18}$ barriers 3 nm thick for various residual doping levels in the spacers and applied voltages. The bottom/top GaAs regions have a thickness of 300 nm each and a doping level of 2×10^{18} cm^{-3}. Ohmic contacts are assumed. As it can be seen, if no doping is present (true semi-insulating layer, Figure 5.19b and e) the voltage drops homogeneously in the structure and the electric field is constant. On the other hand, in the case of n-type doping the voltage drops nearer the top p-region and the electric field is therefore more intense in the last layers (Figure 5.19c and f). Finally, if residual doping is p-type, voltage drops near the bottom n-region where the electric field is more intense (Figure 5.19a and d).

As we saw in Section 5.2.2 (Figure 5.5), an InAs QDs layer grown at the typical conditions we use has the main PL emission band centred at 1.12 eV. In these stacks, those conditions can only be found in the first layer given that the others have the influence of the strain fields created by the deeper ones. On the other hand, as we see in the TEM image of the stack (Figure 5.15), from the second layer QDs seem to become wider and shallower until they are indistinguishable from thin quantum

wells. This change of their shape would shift their emission to higher energies. For these two reasons, we believe that the lower energy band found in this sample should correspond to the emission from the first QDs layer and the additional bands to emission from the successive layers. The observed sequential disappearance of the bands, from low to high energy, suggests that the electric field that results from the application of an external voltage is not homogeneous in the semi-insulating region but larger in the region of the first QDs layer. Given discussion of the previous paragraph, we conclude that the situation that gives a better explanation of the experimental results is that of a p-type residual doping in the structure.

Electroluminescence

If the positive bias is increased beyond that considered in the previous paragraphs, the sample begins to emit light due to the injection of carriers from the electric contacts. The resulting electroluminescence (EL) can be seen in Figure 5.20.

In Figure 5.20a it can be seen a photograph of the sample in the visible range, where the mesas, metallic contacts and gold wires bonded to the contacts can be appreciated. Figure 5.20b, on the other hand, shows a photograph taken with an infra-red camera during an EL experiment. As it can be seen, the device under test emits light whereas the rest of the sample remains in the dark. The light comes out of the device by the circular top window but also by the edge of the mesas, illuminating the nearby devices (bright square around the opaque metallization).

The EL spectra as a function of the applied voltage are shown in Figure 5.20c in log scale. EL starts at around 1.27 V and increases exponentially with applied bias. This can be better appreciated in Figure 5.20d and e, where we show the IV curve and the dependence of the EL with the current, respectively. In this last case, it can also be seen that the dependence is slightly superlinear. The spectra shows two main bands. The lower energy band consist in an intense peak at 1.11 eV and a weaker contribution at around 1.18 eV. No dependence on the energy position of the peaks are appreciable. We attribute these two peaks to the emission from the first and second QDs families, given the observed energies and the explanation given in the previous section.

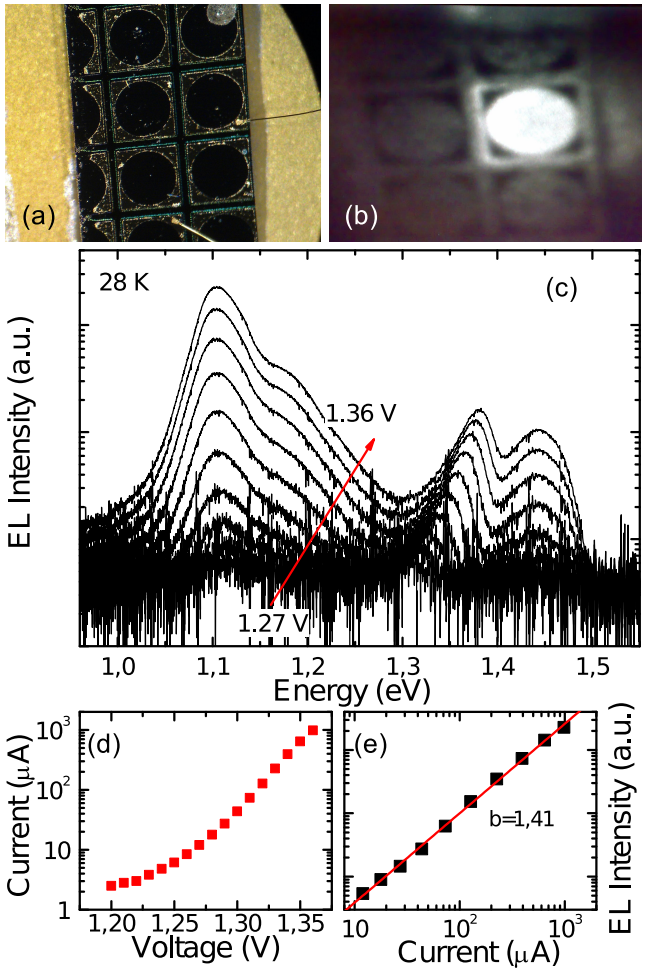

Figure 5.20: Photograph of the sample (a) in the visible range and (b) in the infra-red range under current injection, showing the EL emitted by the device under test. (c) EL intensity as a function of the applied voltage for sample QDs-D.

A secondary emission band appears at the high energy side of the spectra, also with two contributions. One of them is fixed at 1.44 eV and its position does not show any dependence on the applied voltage. The other appears at 1.31 eV but rapidly increases its intensity and the maximum

blue-shifts up to 1.38 eV. The high energy peak can be assigned to emission from the WLs of the first QDs layers, given its energy and evolution with voltage. The other band, on the other hand, might correspond to emission from the InAs QWs of the top layers that did not evolved in QDs+WLs. In that sense, the less energetic contribution, visible at the lowest injection, would be related with the last InAs layer, shifting the emission to higher energies as more layers (with less In due to some QDs formation and hence less deep QWs) begin to emit. In the limit of very deep layers, this emission will be coincident with that of the WL and it will have associated a QDs emission at lower energies.

This explanation is in agreement with the PL experiments made before and the band diagram depicted in the previous section for the case of p-type background doping.

Photocurrent spectroscopy

Finally we study the photocurrent properties of theses structures, focusing our attention again in sample QDs-D.

In Figure 5.21a we show the resulting PC spectra for increasing temperature. As it can be seen, including InAs QDs in the intrinsic region of the diode extends the absorption edge of GaAs from 1.52 eV at 20 K to 1.07 eV, as it is usually observed in this kind of structures. In this sub-bandgap photocurrent, four contributions can be identified, at least. The most intense can be found around 1.44 eV, being a factor of 2 weaker than the signal at the GaAs edge. It is directly related with the absorption in the InAs WL and QWs. At lower energies, we can observe well resolved bands at 1.1 and 1.18 eV which can be associated with absorption in the first QDs layers. A broader band can be seen around 1.28 eV which we associate with transitions in the following QDs layers.

When we rise the temperature of the sample, the whole spectrum red-shifts, as expected, and increases its intensity as a result of enhanced thermal scape from the nanostructures. However, this enhancement is not homogeneous. The lowest energy contribution shifts to 1.02 eV when temperature is rose to 320 K, increasing its contribution from 0.29 to 0.34 nA, only a 17% of enhancement due to thermal scape. On the contrary, the contribution from the WL-related band shifts from 1.44 to 1.35 eV, with an intensity variation from 10 to 23 nA (123% of enhancement).

The larger impact on the temperature in the high energy transition is reasonable, given the smaller confinement energy of carriers in the levels involved in those transitions. However, the small absolute PC enhancement suggest that the dominant mechanism of carrier extraction from the nanostructures is not thermal scape. Given that at the level of illumination used in PC experiments, around 1 μW between 1 to 1.5 eV, carrier photogeneration is small and the bands are similar to those found in the dark, the most probable scape mechanism becomes tunnelling through a potential barrier to the GaAs matrix or an adjacent layer of nanostructures.

We can asses this hypothesis by performing PC measurements as a function of the voltage applied to the sample. In Figure 5.21b we show the PC of sample QDs-D for voltages ranging from 1 V to -3 V. Reducing the reverse bias (applying a less negative or positive voltage) causes the reduction of the tunneling rate up to the point where it becomes slower than the relaxation and radiative rates. Therefore as we apply a positive voltage to the sample (blue curves) the PC below the GaAs edge strongly reduces. The first to disappear are the low energy peaks and then the WL/QW related band at 1.44 eV which is not completely quenched due to the acceptor-CB contribution at similar energies.

Reverse biasing the sample leads to a general enhancement of the PC in the whole energy range. At the lowest energy side there is a remarkable increase in the PC below the QDs-related feature at 1.1 eV which might be related with free carrier absorption.[21, 22] If that contribution is subtracted from the curves (using an exponential fit to that tail and extrapolating to higher energies), it can be seen that the PC coming from the peak at 1.1 eV saturates at -0.2 V and then begins to decrease (Figure 5.22). The PC coming from the peak at 1.18 eV, in turn, saturates at -2 V although no reduction is visible afterwards. In both cases, the saturation and subsequent reduction is accompanied by an important red-shift of the peaks which amounts to $\sim$20 and $\sim$40 meV, respectively. No saturation or shift is observed in the rest of the curve. This shift, also present in the PL *vs* voltage experiments (Figure 5.18d), was attributed the quantum confined Stark effect and, in this experiments, it is also accompanied by the expected signal shrink due to the decreased electron-hole overlap and thus the transition probability.[20]

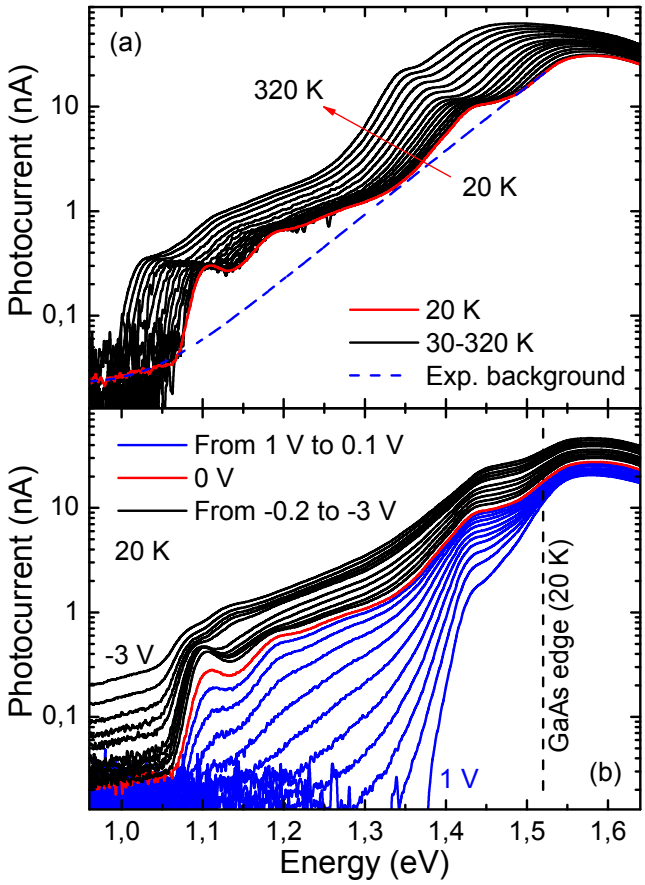

Figure 5.21: Photocurrent of sample QDs-D (a) as a function of temperature at 0 V and (b) as a function of voltage at 20 K.

The saturation of the lowest energy peak before the rest of the curve again supports the inhomogeneous voltage dropping in the structure and the origin of the emission/absorption bands observed in these curves.

Summary of the optical properties

In summary, the important inhomogeneity of the QDs layers in these samples suggested by RHEED and TEM micrographs produces a wide range of emission bands, each of them corresponding to emitters in different

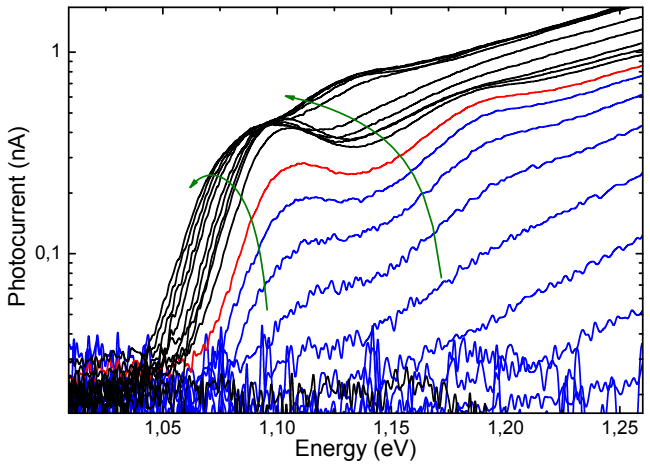

Figure 5.22: Detail of the low energy photocurrent of sample QDs-D after background subtraction.

layer of the stack and hence giving information about a different region of the structure. In Figure 5.23 we summarize these results by comparing the PL, EL and PC spectra of sample QDs-D. For the PC we have used the 20 K signal recorded at 0 V after the subtraction of an exponential background (shown as a dashed blue line in Figure 5.21a). For EL we have used the 1.36 V spectrum. To make the comparison easier, the three signals have been normalized to unity using, as reference, the most intense peak in the QDs region (1.1 to 1.35 eV).

In the figure we highlight the contribution of each part of the spectrum and we relate them to the parts of the stack where the emission comes from. The four regions that can be distinguished are: Region I: the emission comes from the first QD layer, which is the only one that really have the nominal properties of an isolated QD layer under our growth conditions. It is clearly visible in EL and PC experiments although in PL only appears as a small hump. Region II contains the emission of the intermediate layers which have well developed QDs structures. They appear in PC experiments and are the main contribution to the PL signal. Depending on the material quality, the contribution of the QDs families can be more or less resolved. Emission from this region is not visible in EL experiments since injected carriers only reach the outermost part of the stack. Region

III represents the contribution of the upper parts of the stack which does not contain well developed QDs. They are thin InGaAs QWs of diverse composition depending on the layer. It also contains the contribution from the normal WL associated to the QDs of the lower layers. They are visible in PL experiments as a tail in the emission band and in EL as a well resolved peak, possibly because it corresponds only to the last few layers of the stack. In PC measurements it is the most intense contribution below the GaAs absorption edge. The final region, Region IV, overlaps with the previous one and contains the emission due to transitions from the CB to acceptor levels.

5.4.4 Summary of results

Although it is clear that this is not the result we expected after optimization of the strain balanced conditions using MOSS, the QDs evolution and the existence of a range of emitting families might be interesting for its application in QDs infrared photodetectors and intermediate band solar cells, for example. In these devices, it is generally interesting to have a wide band intraband photoresponse, something that is not the case if all the QDs in the active region are perfectly homogeneous. Obviously, the appearance of defects and dislocations due to this dispersion in sizes would be detrimental and hence should be avoided by all means.

5.5 Role of the inhomogeneous strain fields

Once any influence of the experimental set-up and the possibility of over compensation on the stack degradation have been discarded, and after analysing in detail the properties of this kind of stacks, our conclusion is that the inhibition of the QDs nucleation is something intrinsic to these samples, direct consequence of their structure, the growth conditions or a combination of both. We suggest as the most plausible explanation for the degradation of the QDs stack the inhomogeneous strain fields that the 3D nanostructures create around them and its impact into the CL.

The strain field that QDs and QWRs generate has been studied by several authors and their effect has been often observed in stacks of many nanostructures.[23, 24] If the layers are close enough, the strain field

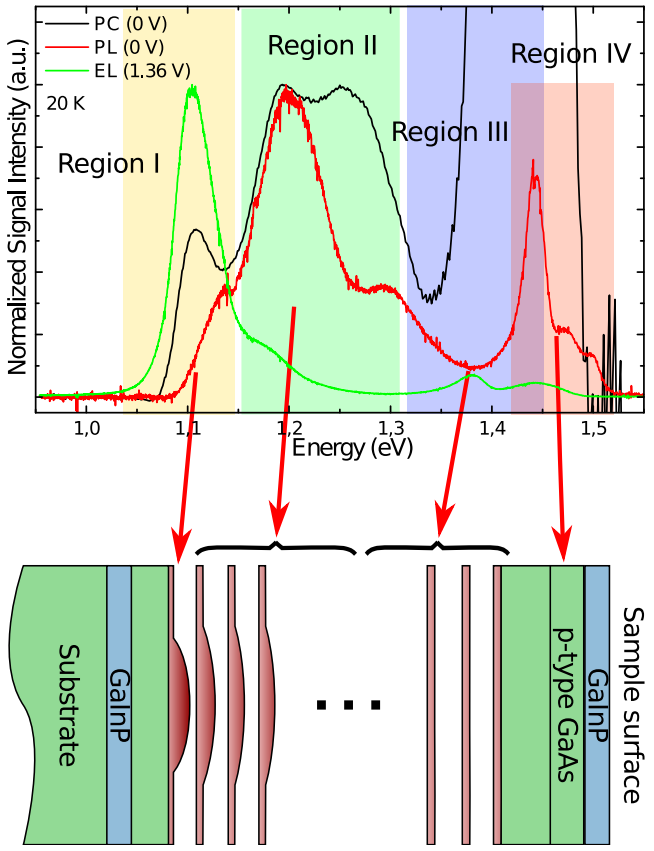

Figure 5.23: Normalized PC, PL and EL emission of sample QDs-F.

favours the vertical correlation of nanostructures and can eventually induce both lateral and vertical ordering.[2] In the context of strain compensation, the inhomogeneous strain fields have been studied by Tatebayashi *et al.*[9] They separated the strain introduced by QDs into homogeneous and inhomogeneous and found that the CL could only suppress the former and partly relieve the latter.

In all calculations performed so far, the CL is assumed to be 2D for all growth conditions and compositions. However, as it has been shown in the previous section, this is not always true. In the same way the

inhomogeneous strain fields of a given layer have an effect in the layer of nanostructures grown on top of it, they might have an impact in the CL shape as well. In principle, the top of a QD is the less favourable place for the growth of a GaAsP alloy. In such a place, the in plane strain is highly tensile and the tendency of P adatoms will be to migrate to compressive regions around the QDs where the in plane lattice parameter is smaller, in agreement with the inhomogeneity observed in Figure 5.15.

5.5.1 Factors that influence QDs strain balancing

Based on this principle, our experimental results described in the previous sections and the available literature, in the following paragraphs we discuss the impact of different growth parameters in the compensating process, in order to achieve a better understanding of the characteristics required by an optimum strain CL, namely: QDs size and composition, barrier composition, barrier position, substrate orientation and separation of the QDs layers.

QD size and composition

Being responsible for the strain field in the surrounding matrix, the properties of the QDs will have a major impact on the final result. We performed several simulations of the strain field generated by lens shaped InGaAs QDs of different compositions and sizes using the Nextnano++ software package.[1, 25] A schema of the simulation region can be seen in Figure 5.24a. Bottom surface is assumed to be an infinite GaAs substrate; top surface is in contact with air so it is free to relax and periodic boundary conditions are set for the lateral faces. The maximum in-plane strain ($(\epsilon_{xx}+\epsilon_{yy})/2$) at the top surface occurs exactly above the tip of the buried QD (point A in Figure 5.24a).

As it can be seen in Figure 5.24b, strain increases rapidly with the QD height but decreases with the QD base diameter beyond certain value. This is expected since an infinitely wide QD, a QW, should have an in-plane strain equal to zero outside the QW itself. The dependence on the QD composition is strictly linear as illustrated in Figure 5.24c.

In general, this calculations indicate that shallow QDs of wide base made of InGaAs will be preferable as they introduce less intense strain

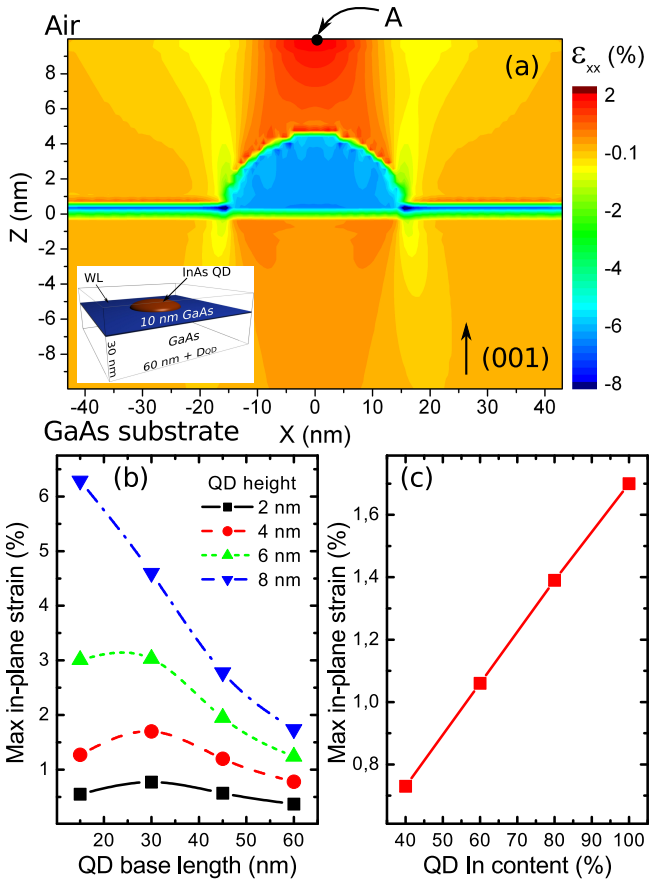

Figure 5.24: (a) Color map of the strain field (ϵ_{xx} component) created by the InAs QDs in a GaAs matrix (QDs 4 nm high, 30 nm wide). The inset shows a schema of the simulation region. D_{QDs} is the base length of the QDs. (b) Maximum in-plane strain 10 nm above the WL for different InAs QDs sizes (point label A in (a) subfigure). (c) Maximum in-plane strain as a function of In content for QDs 4 nm high, 30 nm wide. The WL thickness is of pure InAs and 0.5 nm thick in all cases.

fields at a given distance above the wetting layer and hence their impact into an eventual CL grown at that position will be smaller too.

CL material

There are several materials that can be used to compensate the compressive strain of InAs QDs grown on GaAs.[5–8] From all of them, the only binary compound is GaP. GaAsN and GaAsP are ternary alloys that can suffer from composition modulation which means that anything that locally changes the chemical potential (strain fields or atomic steps, for example) will induce the formation of a non-homogeneous alloy.

In particular, in the case of a GaAsP barrier, P adatoms will migrate away from the top of buried QDs giving a phosphor-poor alloy in such places. As a side effect, this process will produce alternate overcompensated and undercompensated regions, which in turn leads to a surface with large in-plane strain inhomogeneity.

CL position

As explained in Section 5.2, essentially there are three options for the CL: placing it directly on top of the QDs, directly below or at a certain distance above them. In the formers, there will be a large intermixing between the QDs and barrier materials, as shown before. From the point of view of strain, the fields will be less intense and the QDs will be able to relax, thanks to the InAs/GaAsP intermixing, and reduce their height. However, this method would have a larger impact in the optical and electrical properties of the QDs and their emission would be blue shifted depending on the barrier composition.

The last option gives, in principle, more homogeneous materials, separating the properties of the barrier and the QDs. However, in this case the QDs will accumulate the whole strain of the available In leading to a more extreme strain situation, as illustrated in Figure 5.9 and Figure 5.10. In addition, if the barrier is a ternary alloy, it could eventually exhibit composition modulation.

Substrate orientation

The substrate orientation has an important effect on the QD growth characteristics. [26–28] It involves actually two different aspects: (i) the intensity and propagation of the strain fields, and (ii) the surface reconstruction. In general, high index substrates show better QDs

lateral ordering and marked QDs columns tilted from the growth surface normal.[26] Additionally the growth front is usually rougher which might prevent the diffusion of barrier adatoms to energetically more favourable positions and, hence, reducing the CL strain inhomogeneity.[29]

Separation of the QDs layers

In principle, if QD layers are enough separated, the strain field will fade into the spacer and it will have little effect in the upper layers (as shown in Figure 5.1a).[30] The drawback of this approach is that the volumetric density of the QDs will be small and it will influence also any property that depends on it (absorption coefficient, emission intensity...). Reducing the spacer thickness to increase the QDs density is a requirement of many applications, such as solar cells or infrared photodetectors, and therefore the necessity of strain balanced techniques to reduce the spacer thickness while keeping good material quality.

5.5.2 Summary of conditions

Taking all this information into account, we must conclude that the QDs strain fields might affect the formation of the CL as much as they affect the formation of the next QDs layer. This is of particular relevance when using a compensating ternary alloy as presented here, where severe composition modulation is expected. Since a binary alloy can not suffer from composition modulation, using nominally pure GaP layers might give better results to fabricate large QDs stacks. The use of off-cut or high index substrates might be also beneficial since the propagation of strain fields are distorted reducing their average magnitude at a certain distance over the dot, although this approach has not been tested in this work.

In general these studies indicate that, contrary to strain balanced QWs, in QDs it is not enough to achieve a zero stress condition on average. Other factors, such as the CL composition (binary or ternary alloy) and its position inside the spacer, critically affect the final material quality.

5.6 Digital strain balanced QDs with GaP monolayers

All the previous studies lead to the conclusion that strain balancing of QDs is not a straight forward process and that the inhomogeneous strain fields affect the formation of the strain CL as much as they affect the formation of the following QDs layer. Summarizing this results suggest as the optimum structure one that uses pure GaP barriers for compensation placed as far as possible from the QDs to prevent any kind of composition modulation. In this section we address the design and characterization of a sample containing such structure.

5.6.1 Design and growth of the stacks

Depending on the strain balanced criteria chosen, the InAs/GaP thickness ratio to achieve a correct compensation differs. The GaP thickness needed to compensate 2 ML of InAs ranges from 1.55 ML in the case of the ZS criterion to 4 ML of GaP if AL criterion is used. Assuming that QDs accumulate a stress of around -5 N/m , the MOSS criterion needs 3.55 ML of GaP (see Figure 5.6).

In this case we have chosen to use 2 ML of nominal pure GaP as CL. In this conditions, the degree of compensation would be 50% for the AL, 60% according to MOSS, and around 130% according to ZS criterion. This allows to compare the results of this approach and those of the previous samples since the nominal degree of compensation is the same in both cases.

Two samples with ten QDs layers each were grown with and without GaP stress CLs. In the first sample (sample QDs-E), 2 ML of GaP are introduced in the GaAs spacer by each QDs layer grown, 1 ML of GaP placed 1.53 nm below the QDs and a second GaP ML, placed 12.6 nm above them. Due to the large bandgap energy of GaP, we used 1 ML + 1 ML of GaP instead of just 2 ML of GaP to keep the barriers as thin as possible and facilitate the tunneling of carriers through them. The second sample (sample QDs-F) was grown without GaP monolayers as a reference. The spacer layer thickness between QD was 18 nm in both samples, 3 nm more than the samples considered so far. In Figure 5.25 it can be seen the complete structure of both samples. This sequence was repeated ten times

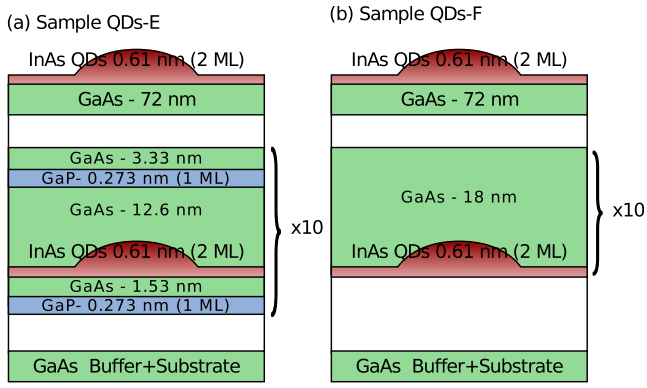

Figure 5.25: Schema of the structure of samples (a) QDs-E and (b) QDs-F.

and buried under 72 nm thick GaAs barrier. An AFM layer was grown on top to study the surface quality. All layers were grown at a substrate temperature T_s of 510 °C and an As BEP = 2×10^{-6} mbar was employed for the growth of GaAs and InAs layers. For QDs formation, 2 ML of InAs were deposited at 0.02 ML/s.

With the aim of controlling the amount of strain compensation, we began each GaP monolayer by first depositing 1.2 ML of Ga on the (2x4) As rich reconstruction with the As cell fully closed and then opening the P cell at a P BEP = 2.3×10^{-7} Torr for 2.7 s. Before and after the GaP monolayers growth all shutter cells were closed during 25 and 30 s respectively to pump out the excess of the group V element for avoiding the formation of the undesirable ternary alloys.

5.6.2 Structural characterization

RHEED and AFM

Sample growth of these samples was monitored by RHEED and the critical thickness analysed. The 2D→3D transition related with the QDs formation was not observed in sample QDs-F beyond the 4^{th} deposited layer, indicating excessive defect formation due to the accumulated strain, increased surface roughness and the resulting blurred of the RHEED signal.[31] This result is identical to that found for samples QDs-A to D, suggesting that, despite the strain compensation, the degradation

mechanism might be similar.

In sample QDs-E, on the other hand, we observed the 2D→3D transition on the ten layers. After a small reduction in the second layer, the critical thickness remains constant for the rest of the stack, suggesting well controlled In migration during growth and proper stress compensation.

This good results are supported by AFM measurements performed on the top layer which also indicates an improved structural quality of the sample QDs-E (Figure 5.26a), with very uniform QDs size (9 nm high, 50 nm in diameter) and distribution (1.7×10^{10} cm^{-2}). Figure 5.26b corresponds to sample QDs-F and shows large surface undulation, QDs clusters and dark spots. Ng *et al* reported the formation of large "volcano-like" defects in this system that would concentrate most of the In adatoms and prevent the formation of normal size QDs.[32] This kind of defects, nucleated in the stack and extending to the surface might be related with the dark spots observed in the AFM image.

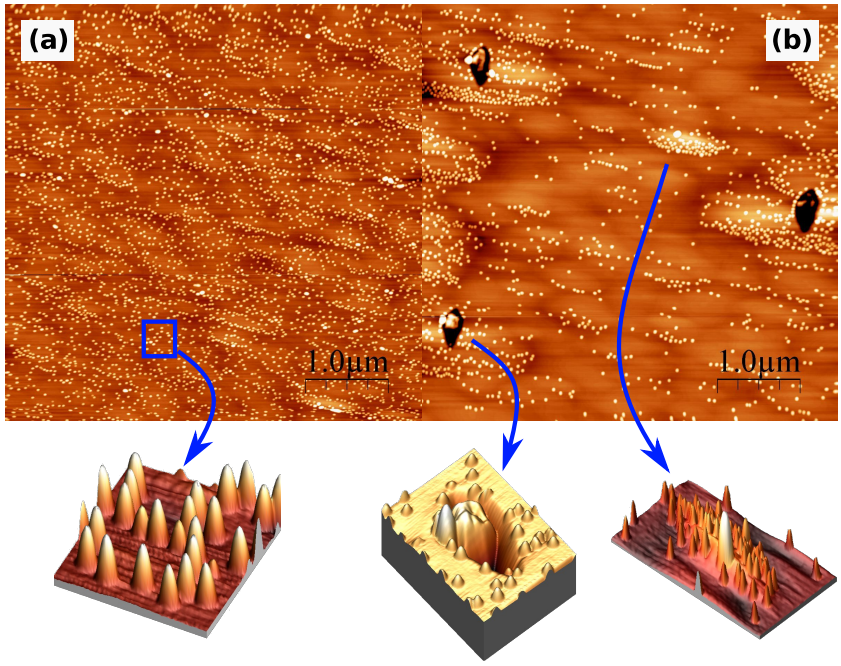

Figure 5.26: AFM image of the top layers of samples (a) QDs-E and (b) QDs-F.

XRD

X-ray diffraction (XRD) measurements around the (004) symmetric reflection in $\omega/2\theta$ geometry are used to quantitatively analyse the strain balancing effect on the strain accumulation and lattice distortion of samples QDs-E and QDs-F. As it was discussed in Section 5.3.1, XRD is not a good characterization technique to asses the compensation degree of a sample given that several identical nominal structures produce a range of XRD patterns depending on the In segregation and migration processes. However, it will serve us to compare the results against the predictions of the theoretical models and with MOSS.

The experimental XRD spectra are shown in Figure 5.27, together with a simulated spectra for the nominal structure of sample QDs-E. No influence of the QDs is taken into account in the simulation. The perpendicular average strain, which is the magnitude probed with this kind of XRD measurements, can be determined by (Equation 3.8):

$$\langle \epsilon_{\perp} \rangle = \frac{\sin\theta_{cL} - \sin\theta_{cS}}{\sin\theta_{cL}} \tag{5.4}$$

where θ_{cL} and θ_{cS} are the Bragg angle of the zero order satellite peak and GaAs substrate peak, respectively. The relative strain reduction is defined as:

$$SR = \frac{\langle \epsilon_{\perp} \rangle_{ref} - \langle \epsilon_{\perp} \rangle_{sb}}{\langle \epsilon_{\perp} \rangle_{ref}} \tag{5.5}$$

where ref stands for the strain of the reference sample (QDs-F) and sb for the strain of the strain balanced sample or simulation. In turn, the compensation degree achieved by a given criterion according to this results will be given by:

$$CD = \frac{SR_{exp}}{SR_{sim}} \times CF \tag{5.6}$$

where CF is the compensation factor, which is simply the expected compensation degree according to the nominal, simulated structure. In this case, assuming the ZS criterion, the CF=1.3. The results are summarized in Table 5.2 .

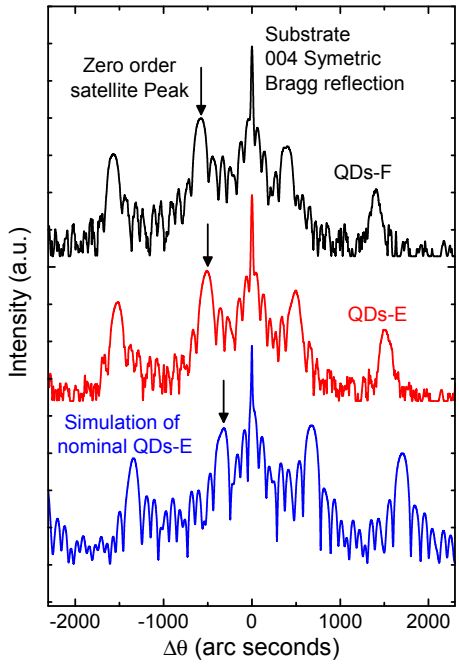

Figure 5.27: Comparison of the XRD spectra of the reference sample (QDs-F) the strain balanced sample (QDs-E) and the simulation of the nominal strain balanced structure.

Table 5.2: XRD data for the (004) symmetric reflection, including the zero order peak position $\Delta\theta$, the average perpendicular strain $\langle\epsilon_\perp\rangle$, the relative strain reduction and the stress compensation degree.

	QDs-F	QDs-E	Simulation
$\Delta\theta$ (arcs)	581	491	309
$\langle\epsilon_\perp\rangle$	0.004368	0.003679	0.002403
SR (%)	0	16	45
CD (ZS) (%)	0	46	130

A 16% of relative strain reduction with respect to the reference sample (Sample QDs-F) has been achieved in sample QDs-E as a consequence of the introduction of GaP stress CLs. This reduction does not reach the expected value according to the simulated spectrum of the nominal

structure, which would lead to a 45% of relative strain reduction. This result might indicate that the GaP layer thicknesses or its P content is actually smaller than their nominal values, suggesting phosphorus incorporation into the sample during growth lower than the expected.

According to the ZS criterion, only 46% of compensation degree has been achieved, which implies that the compensation degree according to MOSS must be lower. However, this low values seems to be enough to allow the growth of ten QDs layers keeping good structural quality. This situation strongly contrast with the results obtained so far, in which the stack degraded and QDs formation was inhibited.

MOSS measurement of the "digital" strain balanced sample

It is interesting to understand the reason for achieving such reduced compensation degree in sample QDs-E. To this end, we use the MOSS technique to monitor the stress accumulated in that structure. The result of measuring two periods of such structure can be seen in Figure 5.28.

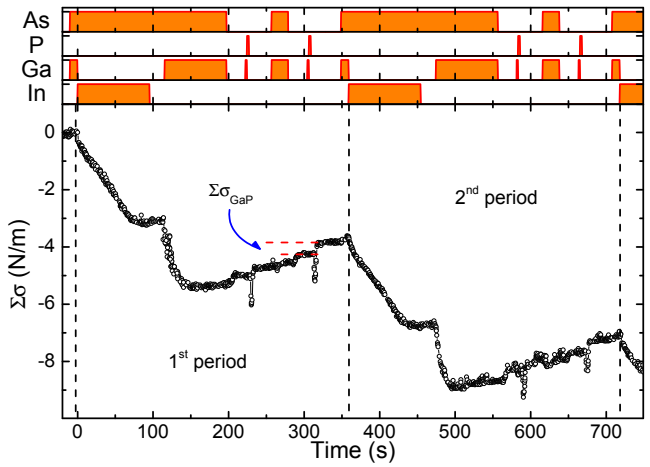

Figure 5.28: MOSS measurements of the structure of sample QDs-E.

As it can be seen, the figure exhibit the oscillating behaviour already observed in strain balanced samples, with stress accumulating during the InAs growth and capping and being compensated in other parts of the structure. We will discuss when it is the stress compensated later. The

resulting compensation degree achieved when growing this sequence is 32%, about half of what it was expected.

As it can be seen, just when the GaP layer is grown, there is a sudden overshoot of the accumulated stress. This behaviour is due to the opening of the Ga effusion cell in the absence of a group V element that momentarily saturates the sample surface with Ga atoms and changes the reconstruction.

In general, two main reasons are identified as responsible for the observed compensation degree of 32% rather than the predicted 60%:

1. *Low P incorporation*: As stated in the sample design, P incorporation into a GaAs matrix is not an efficient process. Although the growth sequence for the GaP layers was designed to enhance P incorporation by saturating the surface with Ga atoms, the incorporation rate of the former was not enough. From Figure 5.28 we find that the average tensile stress that incorporates each GaP monolayer is $\Sigma\sigma_{GaP}$= 0.4 N/m at most, whereas the predicted value is around 1.7 N/m according to Equation 4.10. This leads to a P content of the layer of only ∼24%.

2. *Incorporation of background P*: With only the above phenomenon, the compensation degree should be around 16%, not 34% as we have found.[2] The P needed to achieve the observed compensation is probably incorporated from the background pressure in the MBE reactor along the whole sample growth. This means that phosphor atoms are incorporated at all times during the fabrication of the QDs stack leading to a very dilute ternary or quaternary alloy. The net effect of the incorporation of this background phosphor is clearly visible in the MOSS measurements once the In is exhausted during capping. In this region, the general behaviour of the curve is to decrease the accumulated stress even without intentional strain compensation.

Other features observable in the curve of Figure 5.28 are related with surface reconstruction changes during growth interruptions, similar

[2] 0.4 N/m per nominal GaP ML × 2 ML and divided by ∼5 N/m introduced by the InAs QDs layer gives a compensation degree of around 16%.

to the Ga-related overshoot. Nevertheless, due to its nature, surface reconstruction changes are reversible process so they do not have a net effect on the accumulated stress once a full period of the stack is considered.

In general, this results suggest that P incorporation to the sample, at least in the form of pure GaP, was not achieved. The observed accumulated stress is more compatible with very thin GaAsP layers, with around 20-25% of P each and a very dilute P background that incorporates along the whole structure. The key differences with previous results might be the growth sequence use to grow the GaP layers and their reduced thickness. Since in this case only P cell was open, the competition with As to incorporate to the lattice was suppressed and hence the homogeneity of the layer might have been enhanced.

5.6.3 Optical characterization

Figure 5.29a shows the photoluminescence spectra recorded at low temperature of samples QDs-E and QDs-F. Up to four Gaussian contributions can be observed in sample QDs-F, at 1.12 eV, 1.17 eV, 1.22 eV and a tail at 1.28 eV. This contributions are very close to those observed in samples QDs-C and QDs-D, studied above and hence each of them must be associated to QDs of different average size contained in a different layer. This result is supported by the evolution with excitation power shown in Figure 5.29b together with the Gaussian fit of the lowest power spectrum. As it can be seen, with increasing power, the different components first exhibit an apparent blue-shift due to the increase of the contribution of the excited states and then suffer a red-shift as a consequence of the sample heating.

On the other hand, a very good optical quality is observed in sample QDs-E, with a much narrower peak centred at 1.13 eV (full width at half maximum of 61 meV). The peak bandwidth and its evolution with the excitation power (Figure 5.29c) suggest the existence of two distinct QDs families very close in size, given their similar emission energy. Although the full width at half maximum of 61 meV is still too large to consider a monomodal distribution in all layers, our results clearly demonstrate the improvement of the material quality and a considerable suppression of the QD size inhomogeneity as a consequence of the introduction of GaP layers.

Room temperature photoluminescence (Figure 5.30a) shows that the

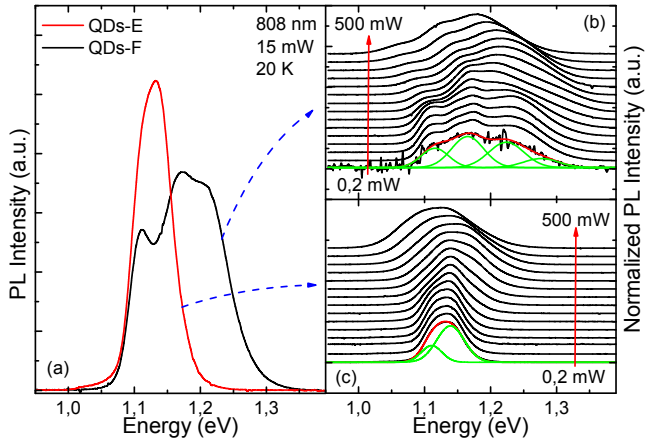

Figure 5.29: a) Low temperature PL of samples QDs-E and QDs-F. Evolution of the PL intensity with excitation power of b) sample QDs-F and c) sample QDs-E.

PL intensity of sample QDs-E is increased by a factor of 2.4 compared to sample QD-F. Moreover, the temperature dependence of the emission spectrum reveals an additional consequence of the strain compensation process. As shown in Figure 5.30b, an Arrhenius-type plot of the integrated PL intensity yields a carrier thermal activation energy for sample QDs-E of 431 meV, double than that obtained for standard InAs/GaAs QDs or the samples of the previous sections.[33] This energy might be compatible with ambipolar scape of carriers to the matrix, rather than scape of electrons and holes separately.

5.7 Fifty layers sample: the QDs solar cell

Following the studies of the previous section about strain balancing with GaP, a third sample was grown to test the strain balanced method in a device with a large stack of QDs. This sample, QDs-G, contains 50 strain balanced InAs QDs layers grown following the sequence of sample QDs-E. The device was designed to test, in addition, the quantum dot IBSC principles that we introduce next.[34]

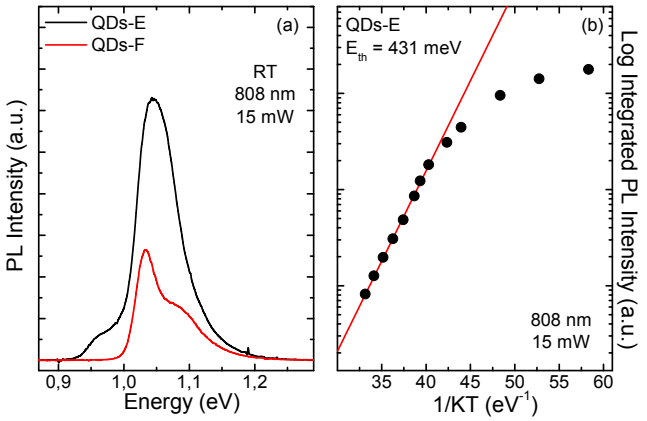

Figure 5.30: (a) Room temperature PL at 808 nm.(b) Arrhenius plot sample QDs-E.

5.7.1 Introduction to the intermediate band solar cell

One of the most intense research field of strain balanced QDs is that of the intermediate band solar cell. For this reason, prior to the application of the previously studied structures in a full solar cell structure with a large QDs stack, in this section we briefly introduce fundamental concepts related to its design from a theoretical point of view, the characteristics of the intermediate band material and the assumptions made for it to work.

Introduction

The intermediate band solar cell (IBSC) concept was originally introduced by Wolf in the early 60's but it gained its current importance only after the work of Luque and Martí in 1997 that updated the concept in terms of detailed balance calculations. [35, 36]

The IBSC is based on the existence of a band partly filled with electrons inside the bandgap of a host material which can absorb low energy photons that otherwise would be lost. Figure 5.31a summarizes the process. The absorption of photons with energies above the bandgap of the host material is mostly due to the interband transitions (A), from the valence band to the conduction band (VB→CB). Transition B takes place between the valence band and empty states in the intermediate band (VB→IB). Finally, transition C promotes an electron in the intermediate band to the

conduction band (IB→CB).

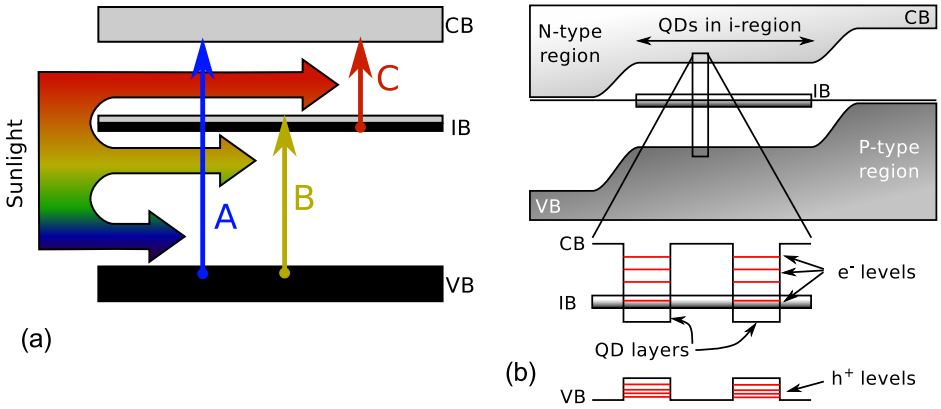

Figure 5.31: (a) Intermediate band material and the electronic transitions involved in the generation of two electron-hole pairs. (b) PiN diode structure including QDs in the intrinsic region and a detail of the QDs levels from which arises the IB.

According to the calculations, an IBSC optimally designed can achieve conversion efficiencies that exceed the Shockley-Queisser limit for an ideal single gap solar cell and is near to the efficiency of an ideal series connected 3J cell under full concentration.[37] The advantage of this technology is that it can be used as a supplement in a multijunction device, giving an overall efficiency larger than that of a 3J or an IBSC separately.

There are several material systems that can, in principle, form the intermediate band in a semiconductor. For example, there are studies that predict the formation of this band in a Si crystal highly doped with Ti, and chalcopyrite compounds and thiospinels partially substituted with transition metals can also lead to the same kind of intermediate band.[38–40] However, the approach that has received more attention is using nanotechnology to create the intermediate band, in particular, the confined electron levels in QDs.

IBSC fundamentals

In the original work by Luque and Martí they established several conditions that the intermediate band solar cell must fulfil, which can be summarized

in the following [36, 41]:

1. Only optical transitions are permitted between the three bands depicted in Figure 5.31: non-radiative processes must be avoided (thermal or tunnel escape, phonon emission and absorption, Auger processes...).

2. The optical transitions must be allowed and be efficient.

3. There should be no overlap between the absorption coefficients, which means that if a photon can produce the transition A or B, it will not be efficient in producing the transition B or C, respectively.

4. The position of the IB inside the bandgap, and the bandgap itself, should be such that the energies of transitions A (E_A), B (E_B) and C (E_C) approach the optimum calculated values for the ideal case: E_A ∼2.1 eV, E_B ∼1.2 eV and E_C ∼0.7 eV. This configuration gives the highest efficiency.

The first condition avoids the drop in the open circuit voltage (voltage preservation principle) and implies the existence of three independent quasi-Fermi levels. The other three conditions maximize the photocurrent produced by the solar cell.

Under the previous assumptions, the conversion efficiency limit of an IBSC simulating the Sun as a black body at 6000 K and full concentration (x46050) is 63.2%. As a comparison, the efficiency limit in the same conditions of a single, double and a triple junction solar cells are 40.8%, 55.7% and 63.8% respectively.[37]

The QDs and the IB

In its simplest form, a QD-IBSC is a P-i-N diode with several layers of QDs placed in the intrinsic region (i), as it can be seen in Figure 5.31b.[34] The IB material is limited to only one region, electrically isolated from the N and P contacts.

In this configuration, the IB arises from the confined electron energy levels in the QDs which, due to the 3D confinement, are isolated between them and with the conduction band (Figure 5.31b). This is one of

the reasons that makes QDs preferable to QWs and QWRs: in these nanostructures there is no isolation between the confined levels and the conduction band, but a continuum of states, as it was shown in Figure 1.1. In this situation, a fast thermal relaxation and excitation between the CB and the confined levels would take place, violating the condition 1 set in the previous paragraphs.

In order to work as an IB and to have strong transitions B and C, the ground level have to be half filled with electrons so, in general, the intrinsic region is lightly doped to reach the required carrier concentration. This is a second reason why QWs are not good candidates to form the intermediate band: transition C is forbidden for incident light perpendicular to the QW plane, as it was introduced in Chapter 1, regardless of the doping level, so condition 2 would never be fulfiled.[42]

In general condition 3 is always satisfied since the transition probability depends on the density of states and the wavefunction overlap of the initial and final states, which have the appropriate dependency with the photon energy.

Finally, the degree of fulfilment of condition 4 is limited by the range of materials available and the possibility of making QDs with them. There are several works that predict the optimum materials to achieve this goal, but, as a matter of fact, most groups work with the system InAs/GaAs: there is a long tradition of growing InAs QDs on GaAs substrates and there are many experimental and theoretical studies about its properties.[20]

5.7.2 Design and growth of the sample

After this review, we enter into the design of the large stacked QDs sample. Its structure can be seen in Figure 5.32a and includes an AlGaAs top layer and a back surface field layer to prevent minority carrier recombination in the top and bottom interfaces respectively. A field damping layer has been inserted between the emitter and the intrinsic region, which contains the dots, to screen the electric field generated by the former and to keep all the QDs layers partly filled with electrons. These electrons are supply by the n-type δ-doping introduced between the two GaP monolayers.

In Figure 5.32b we also show a cross-section TEM image of the QDs stack and the upper part of the device. In this general image, it can already be seen the formation of the QDs in the 50 layers, contrary to what was

observed in sample QDs-C. The AlGaAs window is clearly visible as a bright, thin stripe on top. We will further discuss the structural properties of the sample below.

Standard optical lithography and wet etching techniques were used to define mesas and metal ohmic contacts following schema number 2 (Section 2.2.1).

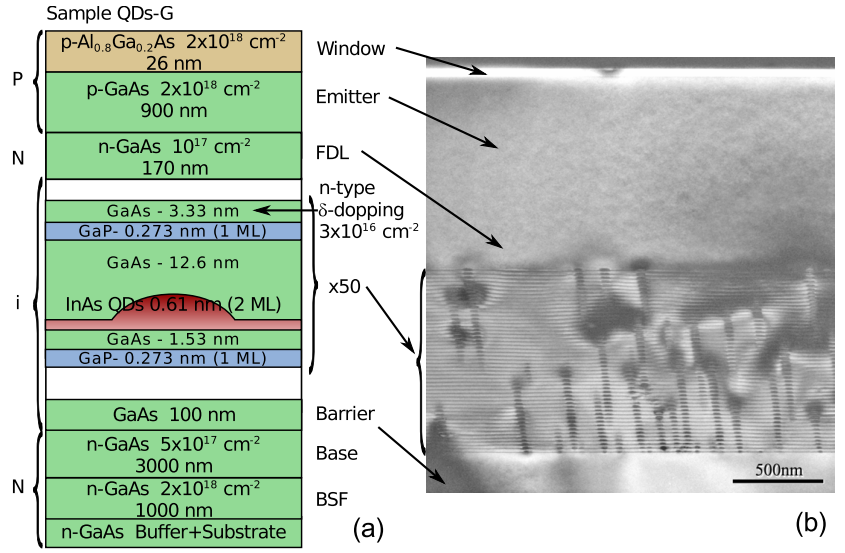

Figure 5.32: a) Structure of sample QDs-G. b) Cross-section TEM image of the 50 stacked QDs layers and the upper part of the structure. TEM image taken by Dr. Ana M. Sánchez (UCA).

5.7.3 Structural characterization

RHEED

During growth, the sample was monitored with RHEED, as usual, and the critical thickness for QDs nucleation analysed along the stack. In Figure 5.33 we show an histogram with the resulting critical thicknesses measured for the 50 layers. As it can be seen, the distribution of thicknesses is quite homogeneous and slightly asymmetric towards smaller values. A Gaussian fit indicates that the average critical thickness is 1.62 ML and

the dispersion ±0.04 ML. Given that typical thickness of an isolated QDs layer is around 1.65 ML, this result indicates that there is an excellent QDs homogeneity along the whole stack, being attributed the generally observed smaller values to the effect of the strain fields.[18]

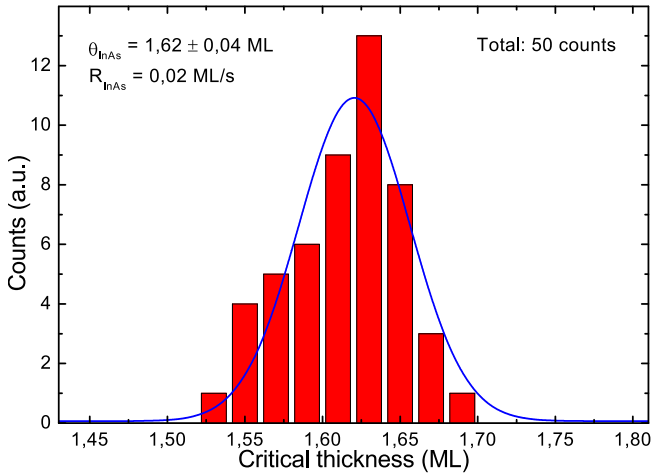

Figure 5.33: Critical thickness of the 50 QDs layers of sample QDs-G as deduced from the 2D→3D transition in the RHEED pattern.

TEM

A representative cross-section TEM image is shown in Figure 5.34a. The image reveals the QDs formation in all layers of the stack, leading to columnar structures often found in this kind of closely spaced QDs layers.[30] This kind of growth is in agreement with the existence of strain around the nanostructures that propagates to the following layer, creating spots of increased nucleation probability. As mentioned before, this vertical correlation among QDs layers can not be avoided through strain balanced techniques.[9]

The QDs columns appear titled 7° from the growth direction (001) (Figure 5.34b). It has been reported that a certain asymmetry in the composition of the stacked nanostructures leads to an associated asymmetry in the strain fields and hence to the tilting of the columns.[43, 44] Most of the QDs columns seem to appear at a certain layer, then widen

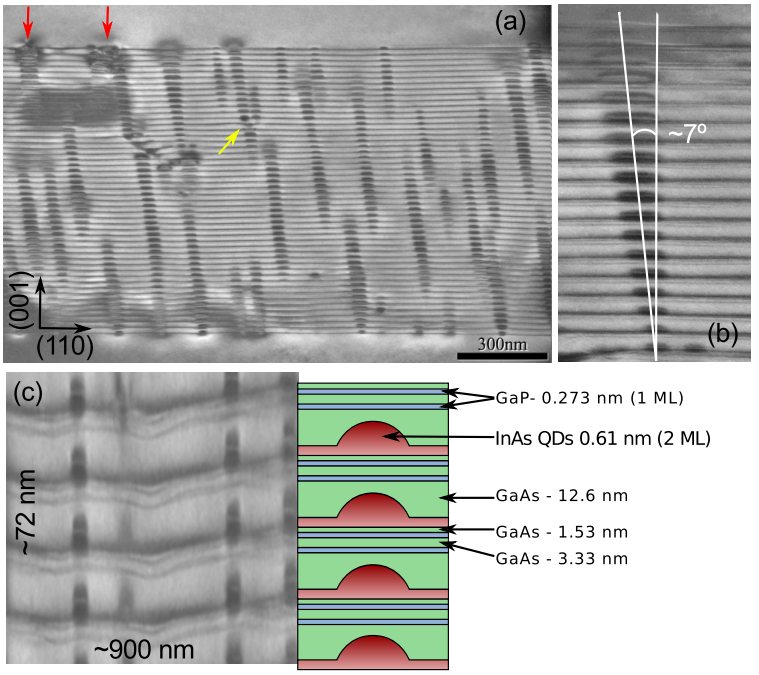

Figure 5.34: (a) TEM image of the QDs stack in sample QDs-G. Red arrows indicate defects and the yellow arrow a QDs column split. (b) Detail of vertically coupled QDs showing a tilt of around 7°. (c) Horizontally compressed image of part of the stack, showing the different layers, and a schema of the structure. TEM images taken by Dr. Ana M. Sánchez (UCA).

and then disappear again. This striking behaviour is consequence of an additional tilting of the columns in a direction normal to the image plane. As a consequence of this tilting, the columns first enter in to the image plane, QDs appear wider when the plane cuts the column by the middle and finally the column gets farther from the plane and the QDs are no longer shown.

In Figure 5.34c we show a compressed image of part of the QDs stack, around 900 nm wide and 72 nm high. In this conditions, the layers of the structure are more clearly seen and compared to the cartoon. The image shows QDs as black rounded regions, the WL as thick dark stripes and reveals the formation of the Ga(As)P layers as thin dark stripes. As it is more evident in this representation, the layer structure is not flat but,

most to the contrary, it is rather undulated.

In general, the structure shows only some defects in the very last few layers (indicated by red arrows in the image). These defects seem to be produced by the interaction of very close or especially large QDs and not as a consequence of a generalized excessive stress accumulation.[45]

5.7.4 Optoelectronic characterization

Photoluminescence spectroscopy

PL measurements of this sample have been performed as a function of power and temperature. As it can be seen in Figure 5.35a, the spectrum has an intense emission band centred at 1.16 eV, with an inhomogeneous broadening of 73 meV and asymmetric towards the high energy side. A secondary emission band, less intense and narrower (∼23 meV) can be found at 1.49 eV. The former is attributed to the emission of the QDs of the stack, being remarkable the relative small broadening after growing such large number of layers. This emission is blue-shifted around 40 meV compared to that of sample QDs-E, which have the same nominal structure in the stack, discrepancy that we analyse below. The weaker band corresponds to the CB to acceptor levels transition and will not be considered further.

As it can be seen in Figure 5.35b, at very low excitation powers the PL band is symmetric and it becomes asymmetric as we increase the power. No extra bands associated to emission from excited states are resolved in the spectra even at the highest powers. The inset shows in log-log scale the peak intensity as a function of power. The dependence is strictly linear for over three orders of magnitude indicating that ground state emission does not saturates. This result is in agreement with the large amount of QDs present in the sample.

In Figure 5.36a we show the evolution with temperature of the PL emission of sample QDs-G. As it can be seen, the main band observed in the spectrum progressively disappear as temperature is increased. Simultaneous to this quenching there is a red-shift of the emission consequence of the bandgap reduction with temperature. The Arrhenius plot of the signal is shown in Figure 5.36b. A linear fit of the high temperature range results in an activation energy of 332 meV, larger than

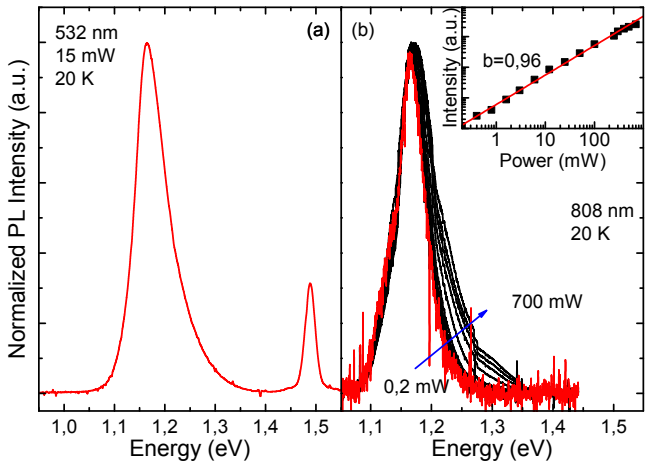

Figure 5.35: (a) Low temperature PL signal of sample QDs-G. (b) Normalized PL intensity of sample QPs-G as a function of excitation power. The inset shows the peak intensity as a function of power in log-log scale and a linear fit.

that typically observed in InAs QDs but smaller that the one found for sample QDs-E, despite having the same nominal structure.

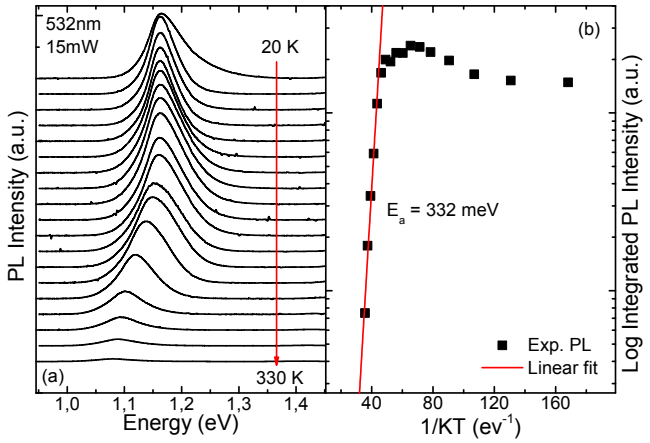

Figure 5.36: (a) PL signal of sample QDs-G as a function of temperature. (b) Integrated PL intensity of the emission band as a function of temperature together with the linear fit of the high temperature range.

This discrepancy might be related with the difference in the PL emission energy already mentioned. We believe that these two effects are due to the unintentional sample annealing during the growth of the thick emitter at 580°C. It is well known that thermal annealing of QDs favours the In-Ga interdifussion between the dots and the matrix increasing the PL emission energy, as observed.[46] To asses this hypothesis, we have annealed sample QDs-E at 580°C for 1 hour. The sample surface was covered with SiO_2 to prevent As lost. In Figure 5.37a we show the PL spectrum of sample QDs-E before and after annealing and we compare it with sample QDs-G spectrum. As it can be seen, after annealing the peak blue-shifts around 35 meV and slightly narrows (ΔFWHM = 6 meV). The integrated PL intensity, on the other hand, remains almost constant which suggest that the effect of annealing is actually to reduce the size and/or In content of the larger QDs and increase the homogeneity of the sample. The spectrum of the annealed sample compares very well with that of sample QDs-G, supporting the hypothesis of the unintentional annealing.

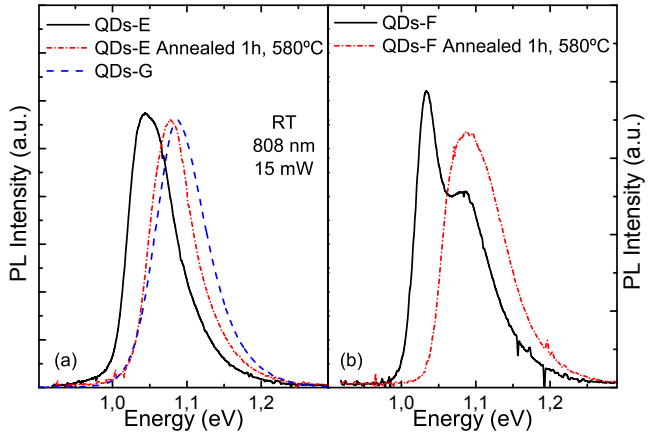

Figure 5.37: (a) Room temperature PL of sample QDs-E, before and after annealing, and QDs-G. The spectrum of the latter has been scaled for easy comparison. (b) (a) Room temperature PL of sample QDs-F, before and after annealing.

Identical annealing has been applied to sample QDs-F. The PL measurements of that sample are shown in Figure 5.37b. As it can be seen, after annealing there is only one band rather than the two overlapped

peaks visible before. This effect is accompanied by a blue shift of the whole band of around 54 meV and a small narrowing (∼3 meV). The integrated PL intensity is barely affected by the annealing . As with sample QDs-E, the result of the annealing is a homogenisation of the QDs distribution by the reduction of the size and/or In content of the larger QDs.

Photocurrent spectroscopy

We study next the optoelectronic properties of sample QDs-G by measuring its photocurrent (PC). In Figure 5.38 we show the room temperature photocurrent of this sample recorded with no applied voltage. As it can be seen, the curve exhibits intense PC below the GaAs absorption edge (∼1.42 eV), down to 1.05 eV. In this region, the are two contributions: the shoulder at 1.36 eV corresponds to carriers photogenerated in the WL whereas the broad absorption between 1.33 and 1.05 eV corresponds to the QDs, including ground and excited states. In this low energy region, some humps can be appreciated that might be related with the individual transitions. In the framework of the IBSC, the absorption found above the GaAs absorption edge is the transition labelled A in Figure 5.31a whereas the absorption in the QDs/WL would be, in principle, that labelled B.

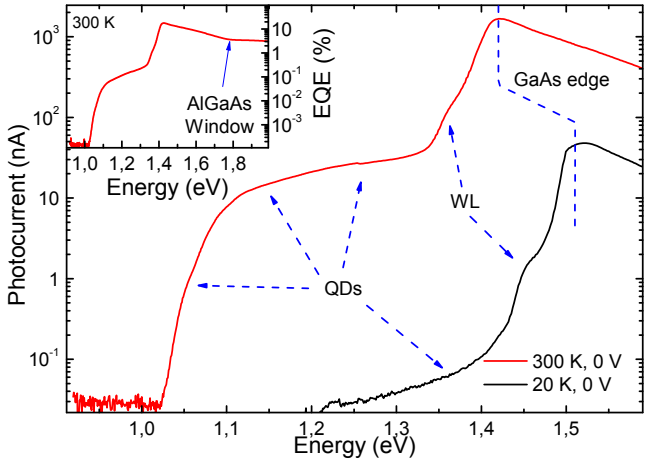

Figure 5.38: Room and low temperature photocurrent of sample QDs-G. The inset shows the external quantum efficiency at room temperature, where we indicate the energy position of the AlGaAs window.

For comparison, we include the low temperature PC spectrum, recorded also at zero bias. As it can be seen, the GaAs absorption edge is blue-shifted to ∼1.51 eV, as expected due to the bandgap increase with decreasing temperature. In this spectrum, it can also be seen the WL related signal at 1.445 eV and a very weak low energy tail. At this temperature, the QDs contribution is about three orders of magnitude smaller, given that photogenerated carriers in the nanostructures have a much smaller probability to scape from the confined levels to the GaAs matrix than to radiatively recombine (PL emission). As temperature is rose, the scape probability increases until the PC from the QDs reaches the observed contribution at RT.

From the point of view of the IBSC concept, this highly efficient thermally activated scape of carriers from the QDs represent an important limitation. [47] As it was explained in Section 5.7.1, one of the conditions for the succeeding of the concept is that only photonic coupling must exist between the IB and the other two. If the CB and the IB are in thermal equilibrium, as it is the case, the IB→CB route takes place with the absorption of phonons and the electron quasi-fermi level pins inside the GaAs bandgap. In other words, transition C in Figure 5.31a would not be needed to produce an electron-hole pair. In this conditions, although more photocurrent will be obtained from the cell, it will be so in the detriment of the open circuit voltage of the device.[47, 48] Current state of the art quantum dot solar cells exploit this absorption edge tailoring of the host material rather that the IBSC concept, accepting a small reduction of the open circuit voltage of the device.[49–51]

In Figure 5.39 we show the low temperature PC recorded at different applied voltages, from 0 V to -7 V. As it was described above, at 0 V the sample shows very little PC below the GaAs absorption edge at 1.51 eV, being the most intense contribution that of the WL at 1.445 eV.

As we rise the applied voltage, the PC increases in the whole curve. In particular, in the QDs region (from 1.15 to 1.4 eV) the obtained PC is about two orders of magnitude larger as a consequence of enhanced carrier scape with the aid of the extra electric field. No saturation of the curve is apparent in this region, indicating that, in principle, more current might be expected at higher voltages. Identical linear dependence with voltage is found in the WL, as it can be seen in the inset of Figure 5.39.

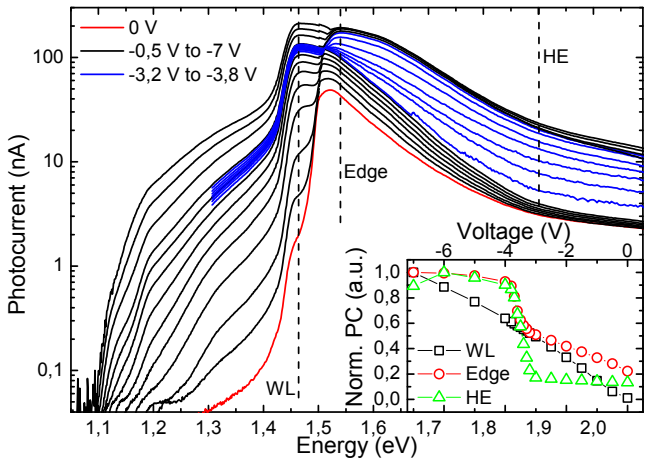

Figure 5.39: Low temperature photocurrent of sample QDs-G as a function of the applied bias. The inset shows the normalized PC at three different energies, indicated by dashed lines in the figure.

Above the GaAs absorption edge, on the contrary, the behaviour of the PC with the applied bias is very different. Three voltage regions can be distinguished. From 0 to -3 V, current increases linearly, being the dependence larger for energies near the absorption edge. Between -3 and -4 V, the current above the edge suffers an abrupt increase, being the maximum of the curve in this region also blue-shifted, from 1.51 to 1.54 eV. We have measure more in detail the PC as a function of voltage in this region to highlight and correctly characterized the abrupt current increase (blue curves in Figure 5.39). From -4 to -7 V, the curves lever again and the PC becomes almost independent of voltage. The three regions can be identified in the inset of Figure 5.39, where we represent a current profile at 1.54 eV (next to the absorption edge) and at 1.9 eV.

The explanation of this behaviour can be found in the dependence of the PC at different points above the edge and the knowledge of the absorption place of the light depending of its energy. Given that the absorption coefficient for GaAs increases with increasing energy, high energy radiation is absorbed closer to the sample surface (in the emitter/FDL regions) that the lower energy one, which has larger penetration depth and is absorbed in the whole PiN structure.

This has two consequences. Firstly, it is know that the blue response of the sample might be greatly affected by recombination of carriers at the top surface of the structure, as it is often observed in solar cells. Passivation treatments and thin GaInP or AlGaAs windows are commonly used to reduce the recombination rate and to keep the electrons away from the surface. In the design of this sample we chose AlGaAs as the window material, but its tendency to oxidation, especially in Al rich alloys, may have cancelled its benefits. This would explain the low current observed in the high energy side even at room temperature (inset of Figure 5.38).

Second, although the TEM image and PL measurements indicate good structural quality, defects present in the last few layers of QDs, in the FDL and in the emitter region may act as non radiative recombination centres and traps for electrons.[45] An increase of the electric field allows the ionization of deep level centres contained in the FDL until the signal saturates when all available traps are ionized.[52] Light with a wavelength below the GaAs edge and absorbed in the QDs region is not affected by this phenomenon, as observed in Figure 5.39. This process will be revealed as an abrupt increase of the PC at the electric field where the ionization of traps takes place.

Infrarred spectroscopy

We finally characterize the absorption capabilities of this sample in the mid infra-red range, which is of particular interest to asses the intermediate band solar cell concept and evaluate the existence of transition C in Figure 5.31a. To this end, we have used a Fourier transform infra-red spectroscopy (FTIR) using a semi-insulating (SI) and n-type GaAs substrates with the same processing that sample QDs-G as reference (see Section 3.7). We have chosen not to normalize QDs-G transmission spectrum to that of the n-type GaAs substrate given that this one actually corresponds to a different wafer of a different brand and, hence, it might contain slightly different properties.

In Figure 5.40 we show the resulting absorbance of the samples. As it can be seen, sample QDs-G presents two clear regions: between 125 and 300 meV the sample shows a broad absorption band centred at 165 meV; above 300 meV the absorbance becomes constant and about four times smaller than at the maximum. N-type reference, in turn, also presents

this flat absorbance region from 150 meV, and an increased absorption in the very low energy region. Finally, the SI reference does not show any distinct feature, having a low, flat absorbance in the whole range.

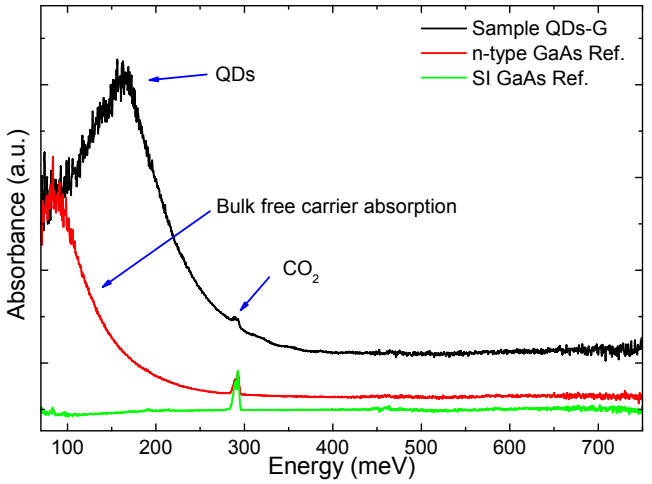

Figure 5.40: Room temperature FTIR spectra of sample QDs-G and of a reference SI and n-type GaAs substrates.

The flat region absorption in the three samples contains a wide range of contributions, including impurity scattering and absorption in the substrate and scattering in the hand-polished back surface. In this sense, no contribution from the epitaxy or the QDs is expected. Likewise, the sharp peak at 290 meV is related with the absorption of CO_2 typically quimisorbed in the sample surface.[53]

The low energy absorption present in the n-type sample, on the other hand, can be attributed to free carrier absorption which, in doped samples represents an important contribution, as it can be seen when it is compared with the SI sample spectrum. This contribution is also present in sample QDs-G but, in this case, overlapped with the band at 165 meV. This band corresponds to light absorption by electrons contained in the QDs confined levels, possibly including ground and excited states. It should be noted that this absorption takes place in the 50 QDs layers, which represent a very small fraction of the whole sample thickness ($\sim$500 μm). Similar energy position and width of the absorption band has been observed at

room temperature in single InAs QDs layers when using a waveguide configuration to enhance the QDs related signal.[54, 55]

In general, this result suggest both an efficient charge transfer from the δ-doping layer to the QDs and high oscillator strength for the intraband transition which, given the temperature, might be aided by the phonon interaction. In principle, this result agrees with the desired behaviour in an IBSC structure and demonstrates the existence of transition C in Figure 5.31a. Nevertheless, the lack of absorption in the 300-900 meV range indicates that a wide range of photons will be lost. The same trends have been observed in QDIPs, where the intraband absorption is found in a narrow energy range around 50-400 meV, at most.[56–58]

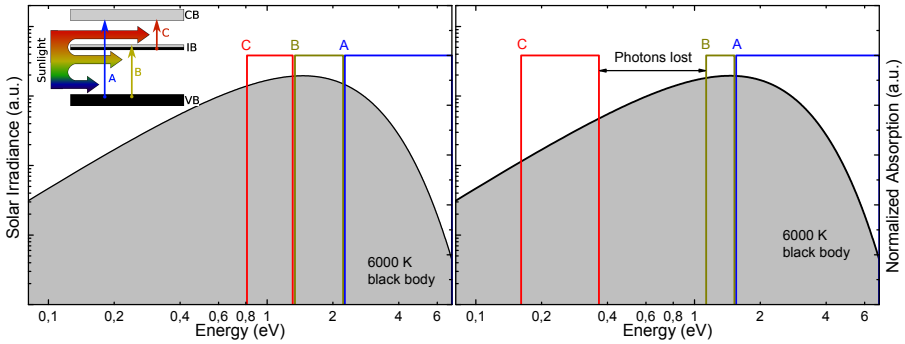

Figure 5.41: Solar irradiance with the absorption bands (a) in the ideal IBSC and (b) found experimentally.

To illustrate the situation, in Figure 5.41 we show ideal and realistic absorption bands in an IBSC according to the theory and our results in PC and FTIR experiments, respectively. As it can be seen, in the ideal situation derived from the IBSC theory, the three transitions (A to C) have adjacent absorption bands that map the region of maximum intensity of the solar spectrum (modelled as a black body at 6000 K). On the contrary, the absorption regions of the three transitions identified in our experiments clearly differs from the ideal case. Even though transitions A and B are adjacent and their energy positions might be acceptable, transition C edge is far in the infrared region, where the solar spectrum has very small irradiance, and it is not continuous to the next edge (region B). Without this absorption, the IBSC principles stated above will not be fulfilled and

no efficiency enhancement can be expected in the InAs/GaAs QDs system exploiting this effect.[7]

This lack of spectral matching is a severe limitation and something intrinsic to the InAs/GaAs system so there are a number of theoretical works suggesting alternatives of QDs/barrier combination with better properties.[59, 60] Very little experimental results in this line can be found, yet.

5.7.5 Summary of results

In this part of the work we have demonstrated the feasibility of the strain compensation with GaP monolayes to fabricate very large stacks of QDs. We have shown that even a small fraction of the full compensation degree (32% according to MOSS) is enough to keep good structural and optical quality in the device, with intense and relatively narrow PL, PC and mid-infrared absorption. The homogeneity of the QDs along the whole stack indicates that the compensation procedure, despite being partial, prevents the detrimental effects related to the CL composition modulation observed in previous sections. The device presented poor response in the high energy region, attributed to certain degradation of the upper part of the device. This suggest that the results we have obtained might be further improved increasing the compensation degree and changing the device design.

In reference to the IBSC behaviour, we have assessed in our strain balanced sample the existence of the three transitions needed for the succeeding of the concept, although some parasitic effects, such as carrier extraction by thermal promotion and the lack of spectral matching in the InAs/GaAs system, have been identified, in agreement with other authors results.

5.8 Conclusions

Along this chapter we have analysed in detail the design and fabrication of strain balanced materials from a fundamental point of view. Beginning with some basic experiments with single QDs layers, we have studied the impact on the CL (GaAsP in this case) on the properties of the QDs. This

results show that in order to keep separated the properties of the QDs an those of the whole structure it is necessary to maintain the CL as far from the QDs as possible, to avoid interaction. Placing the CL adjacent to the QDs leads to smaller sizes and strong blueshift of the emission.

Using the MOSS technique we introduced an additional strain balanced criterion, based on the in-situ monitoring of the accumulated stress and used the resulting knowledge to fabricate perfectly balanced QDs structures under different conditions. This experiments demonstrated the difference among the perfect strain balancing of QDs and QWs and the reasons why the traditional criteria can not be used directly in QDs. We highlight the effect of In segregation in the strain balancing process and concluded that XRD can not be used a a fingerprint of correctly balanced nanostructures (including QWs).

The fabrication of perfectly strain balanced QDs also highlighted another effect that had been disregarded until now. In a similar way that buried QDs affect the formation of the following QDs layers, they have also an effect on the strain CL. This effect, that includes composition modulation, surface undulation and the inhibition of QDs formation, is enhanced for dilute P alloys separated from the QDs. From our experiments we conclude that in QDs it is important to consider the effect of the inhomogeneous train fields on the formation of the CL, being the most favourable situation the use of a binary alloy, such as GaP, well separated from the QDs.

We have analysed the optical properties of several strain balanced structures where this composition modulation and stack degradation takes place. In these samples we find broadband emission due to the overlapping of the individual emission of the QDs in different layers of the stack. The results are in agreement with the degradation picture presented before.

We have finalised the chapter by fabricating a IBSC with 50 stacked QDs layers compensated with nominally pure GaP monolayers, where the composition modulation aforementioned does not occur. Our results show that P incorporation was smaller than expected and only a fraction of the aimed compensation was achieved. Nevertheless, they also suggest that high QDs homogeneity can be achieved under these conditions of only a 32% of strain compensation degree according to MOSS.

In general, we have demonstrated, using the MOSS technique as a novel

tool to characterize strain balanced materials, the strong interdependence between the QDs and the CL, highlighting the fundamental processes such as In migration and composition modulation, that can lead to the degradation of perfectly balanced stacks.

Bibliography

[1] "Nextnano++ Software Package." `http://www.wsi.tum.de/nextnanoplus`, 2011.

[2] J. Tersoff, C. Teichert, and M. Lagally, "Self-organization in growth of quantum dot superlattices," *Physical review letters*, vol. 76, no. 10, pp. 1675–1678, 1996.

[3] E. Fitzgerald, "Dislocations in strained-layer epitaxy: theory, experiment, and applications," *Materials Science Reports*, vol. 7, pp. 87–142, Nov. 1991.

[4] N. Ekins-Daukes, K. Kawaguchi, and J. Zhang, "Strain-Balanced Criteria for Multiple Quantum Well Structures and Its Signature in X-ray Rocking Curves," *Crystal Growth & Design*, vol. 2, no. 4, pp. 287–292, 2002.

[5] N. Nuntawong, S. Birudavolu, C. Hains, S. Huang, H. Xu, and D. Huffaker, "Effect of strain-compensation in stacked 1.3 μm InAs/ GaAs quantum dot active regions grown by metalorganic chemical vapor deposition," *Appl. Phys. Lett.*, vol. 85, p. 3050, 2004.

[6] C. G. Bailey, S. M. Hubbard, D. V. Forbes, and R. P. Raffaelle, "Evaluation of strain balancing layer thickness for InAs/GaAs quantum dot arrays using high resolution x-ray diffraction and photoluminescence," *Applied Physics Letters*, vol. 95, no. 20, p. 203110, 2009.

[7] V. Popescu, G. Bester, M. Hanna, A. Norman, and A. Zunger, "Theoretical and experimental examination of the intermediate-band concept for strain-balanced (In, Ga) As/Ga (As, P) quantum dot solar cells," *Physical Review B*, vol. 78, p. 205321, Nov. 2008.

[8] R. Oshima, A. Takata, and Y. Okada, "Strain-compensated InAs/GaNAs quantum dots for use in high-efficiency solar cells," *Applied Physics Letters*, vol. 93, no. 8, p. 083111, 2008.

[9] J. Tatebayashi, N. Nuntawong, P. S. Wong, Y.-C. Xin, L. F. Lester, and D. L. Huffaker, "Strain compensation technique in self-assembled InAs/GaAs quantum dots for applications to photonic devices," *Journal of Physics D: Applied Physics*, vol. 42, p. 073002, Apr. 2009.

[10] N. H. Kim, P. Ramamurthy, L. J. Mawst, T. F. Kuech, P. Modak, T. J. Goodnough, D. V. Forbes, and M. Kanskar, "Characteristics of InGaAs quantum dots grown

on tensile-strained GaAs(1-x)P(x)," *Journal of Applied Physics*, vol. 97, no. 9, p. 093518, 2005.

[11] P. Lever, "InGaAs quantum dots grown with GaP strain compensation layers," *Journal of Applied Physics*, vol. 95, no. 10, p. 5710, 2004.

[12] G. Costantini, A. Rastelli, C. Manzano, R. Songmuang, G. Katsaros, O. G. Schmidt, and K. Kern, "Interplay between Thermodynamics and Kinetics in the Capping of InAs/GaAs(001)Quantum Dots," *Physical Review Letters*, no. 96, p. 226106, 2006.

[13] D. Granados and J. M. García, "Customized nanostructures MBE growth: from quantum dots to quantum rings," *Journal of Crystal Growth*, vol. 251, no. 1-4, pp. 213–217, 2003.

[14] N. J. Ekins-Daukes, K. W. J. Barnham, J. P. Connolly, J. S. Roberts, J. C. Clark, G. Hill, and M. Mazzer, "Strain-balanced GaAsP/InGaAs quantum well solar cells," *Applied Physics Letters*, vol. 75, no. 26, p. 4195, 1999.

[15] N. Dutta, W. Hobson, D. Vakhshoori, H. Han, P. Freeman, J. de Jong, and J. Lopata, "Strain compensated InGaAs-GaAsP-InGaP laser," *IEEE Photonics Technology Letters*, vol. 8, pp. 852–854, July 1996.

[16] D. Alonso-Álvarez, B. Alén, J. M. Ripalda, A. Rivera, A. G. Taboada, J. M. Llorens, Y. González, L. González, and F. Briones, "In-situ accumulated stress measurements: application to strain balanced quantum dots and quantum posts." 2011.

[17] R. Hong-Wen, M. Sugisaki, S. Sugou, K. Nishi, A. Gomyo, and Y. Masumoto, "Lateral composition modulation induced optical anisotropy in InP/GaInP quantum dot system," *Japanese Journal of Applied Physics*, vol. 38, no. 4, pp. 2438–2441, 1999.

[18] P. Howe, E. Le Ru, E. Clarke, R. Murray, and T. Jones, "Quantification of segregation and strain effects in InAs/ GaAs quantum dot growth," *Journal of applied physics*, vol. 98, p. 113511, 2005.

[19] S. Molina, D. Sales, P. Galindo, D. Fuster, Y. González, B. Alén, L. González, M. Varela, and S. Pennycook, "Column-by-column compositional mapping by Z-contrast imaging," *Ultramicroscopy*, vol. 109, no. 2, pp. 172–176, 2009.

[20] D. Bimberg, M. Grundmann, and N. N. Ledentsov, *Quantum dot heterostructures*. Wiley, 1998.

[21] W. Spitzer and J. Whelan, "Infrared absorption and electron effective mass in n-type gallium arsenide," *Physical Review*, vol. 114, no. 1, p. 59, 1959.

[22] E. Haga and H. Kimura, "Free-Carrier Infrared Absorption in III-V Semiconductors III. GaAs, InP, GaP and GaSb," *Journal op the Physical Society of Japan*, vol. 19, no. 5, 1964.

[23] D. Fuster, M. Ujúe González, L. González, Y. González, T. Ben, A. Ponce, and S. I. Molina, "Stacking of InAs/InP(001) quantum wires studied by in situ stress measurements: Role of inhomogeneous stress fields," *Applied Physics Letters*, vol. 84, no. 23, p. 4723, 2004.

[24] D. Alonso-Álvarez, A. Taboada, J. Ripalda, B. Alen, Y. González, L. González, J. García, F. Briones, A. Martí, A. Luque, and Others, "Carrier recombination effects in strain compensated quantum dot stacks embedded in solar cells," *Applied Physics Letters*, vol. 93, no. 12, p. 123114, 2008.

[25] S. Birner, S. Hackenbuchner, M. Sabathil, G. Zandler, J. Majewski, T. Andlauer, T. Zibold, R. Morschl, A. Trellakis, and P. Vogl, "Modeling of semiconductor nanostructures with nextnano3," *Acta Physica Polonica Series A*, vol. 110, no. 2, p. 111, 2006.

[26] M. Schmidbauer, S. Seydmohamadi, D. Grigoriev, Z. M. Wang, Y. I. Mazur, P. Schäfer, M. Hanke, R. Köhler, and G. J. Salamo, "Controlling Planar and Vertical Ordering in Three-Dimensional (In,Ga)As Quantum Dot Lattices by GaAs Surface Orientation," *Phys. Rev. Lett.*, vol. 96, p. 066108, Feb 2006.

[27] B. L. Liang, Z. M. Wang, Y. I. Mazur, V. V. Strelchuck, K. Holmes, J. H. Lee, and G. J. Salamo, "InGaAs quantum dots grown on B-type high index GaAs substrates: surface morphologies and optical properties," *Nanotechnology*, vol. 17, pp. 2736–2740, June 2006.

[28] Z. M. Wang, S. Seydmohamadi, J. H. Lee, and G. J. Salamo, "Surface ordering of (In,Ga)As quantum dots controlled by GaAs substrate indexes," *Applied Physics Letters*, vol. 85, no. 21, p. 5031, 2004.

[29] R. Nötzel, L. Däweritz, and K. Ploog, "Topography of high- and low-index GaAs surfaces," *Phys. Rev. B*, vol. 46, pp. 4736–4743, Aug 1992.

[30] Q. Xie, A. Madhukar, P. Chen, and N. Kobayashi, "Vertically self-organized InAs quantum box islands on GaAs (100)," *Physical review letters*, vol. 75, no. 13, pp. 2542–2545, 1995.

[31] K. Koike, S. Shuwei, and M. Yano, "Molecular Beam Epitaxial Growth and Characterization of the Vertically Aligned InAs Quantum Dots Embedded in $Al_0.5Ga_0.5As$," *Jpn. J. Appl. Phys.*, vol. 39, p. 1622, 2000.

[32] J. T. Ng, U. Bangert, and M. Missous, "Formation and role of defects in stacked large binary InAs/GaAs quantum dot structures," *emicond. Sci. Technol.*, vol. 22, no. 2, pp. 80–85, 2007.

[33] J. M. Ripalda, D. Alonso-Álvarez, B. Alén, A. G. Taboada, J. M. García, Y. González, and L. González, "Enhancement of the room temperature luminescence of InAs quantum dots by GaSb capping," *Applied Physics Letters*, vol. 91, no. 1, p. 012111, 2007.

[34] A. Marti, N. Lopez, E. Antolin, E. Canovas, C. Stanley, C. Farmer, L. Cuadra, and A. Luque, "Novel semiconductor solar cell structures: The quantum dot intermediate band solar cell," *Thin Solid Films*, vol. 511-512, pp. 638–644, 2006.

[35] M. Wolf, "Limitations and Possibilities for Improvement of Photovoltaic Solar Energy Converters: Part I: Considerations for Earth's Surface Operation," *Proceedings of the IRE*, vol. 48, no. 7, pp. 1246–1263, 1960.

[36] A. Luque and A. Martí, "Increasing the efficiency of ideal solar cells by photon induced transitions at intermediate levels," *Physical Review Letters*, vol. 78, pp. 5014–5017, Jun 1997.

[37] A. Martí and A. Luque, *Next generation photovoltaics: high efficiency through full spectrum utilization*. No. 1, Taylor & Francis, 2004.

[38] G. González-Díaz, J. Olea, I. Mártil, D. Pastor, A. Martí, E. Antolín, and A. Luque, "Intermediate band mobility in heavily titanium-doped silicon layers," *Solar Energy Materials and Solar Cells*, vol. 93, no. 9, pp. 1668–1673, 2009.

[39] P. Palacios, I. Aguilera, K. Sánchez, J. Conesa, and P. Wahnón, "Transition-metal-substituted indium thiospinels as novel intermediate-band materials: Prediction and understanding of their electronic properties," *Physical Review Letters*, vol. 101, pp. 2–5, July 2008.

[40] P. Palacios, K. Sánchez, J. Conesa, J. Fernández, and P. Wahnón, "Theoretical modelling of intermediate band solar cell materials based on metal-doped chalcopyrite compounds," *Thin Solid Films*, vol. 515, pp. 6280–6284, May 2007.

[41] A. Zunger, A. Franceschetti, J.-W. Luo, and V. Popescu, "Understanding the physics of carrier-multiplication and intermediate-band solar cells based on nanostructures - what is going on?," *Proceedings 34th IEEE Photovoltaic Specialists Conference*, 2009.

[42] J. Singh, *Electronic and optoelectronic properties of semiconductor structures*. Cambridge University Press, 2003.

[43] B. Alén, J. Martínez-Pastor, L. González, J. García, S. Molina, A. Ponce, and R. García, "Size-filtering effects by stacking InAs/InP (001) self-assembled quantum wires into multilayers," *Physical Review B*, vol. 65, no. 24, pp. 1–4, 2002.

[44] S. I. Molina, T. Ben, D. L. Sales, J. Pizarro, P. Galindo, M. Varela, S. Pennycook, D. Fuster, Y. González, and L. González, "Determination of the strain generated in

InAs/InP quantum wires: prediction of nucleation sites," *Nanotechnology*, vol. 17, no. 22, pp. 5652–5658, 2006.

[45] A. Martí, N. López, E. Antolín, E. Cánovas, a. Luque, C. R. Stanley, C. D. Farmer, and P. Díaz, "Emitter degradation in quantum dot intermediate band solar cells," *Applied Physics Letters*, vol. 90, no. 23, p. 233510, 2007.

[46] J. Tatebayashi, Y. Arakawa, N. Hatori, H. Ebe, M. Sugawara, H. Sudo, and A. Kuramata, "InAs/GaAs self-assembled quantum-dot lasers grown by metalorganic chemical vapor deposition—Effects of postgrowth annealing on stacked InAs quantum dots," *Appl. Phys. Lett.*, vol. 85, no. 6, pp. 1024–1026, 2004.

[47] E. Antolín, A. Martí, C. D. Farmer, P. G. Linares, E. Hernández, A. M. Sánchez, T. Ben, S. I. Molina, C. R. Stanley, and A. Luque, "Reducing carrier escape in the InAs/GaAs quantum dot intermediate band solar cell," *Journal of Applied Physics*, vol. 108, no. 6, p. 064513, 2010.

[48] A. Luque, P. G. Linares, E. Antolín, E. Cánovas, C. D. Farmer, C. R. Stanley, and A. Martí, "Multiple levels in intermediate band solar cells," *Applied Physics Letters*, vol. 96, no. 1, p. 013501, 2010.

[49] S. A. Blokhin, A. V. Sakharov, A. M. Nadtochy, A. S. Pauysov, M. V. Maximov, N. N. Ledentsov, A. R. Kovsh, S. S. Mikhrin, V. M. Lantratov, and S. A. Mintairov, "AlGaAs/GaAs photovoltaic cells with an array of InGaAs QDs," *Semiconductors*, vol. 43, no. 4, pp. 514–518, 2009.

[50] D. Guimard, R. Morihara, D. Bordel, K. Tanabe, Y. Wakayama, M. Nishioka, and Y. Arakawa, "Fabrication of InAs/GaAs quantum dot solar cells with enhanced photocurrent and without degradation of open circuit voltage," *Applied Physics Letters*, vol. 96, no. 20, p. 203507, 2010.

[51] S. M. Hubbard, C. G. Bailey, R. Aguinaldo, S. Polly, D. V. Forbes, and R. P. Raffaelle, "Characterization of quantum dot enhanced solar cells for concentrator PV," in *Proceedings 34th IEEE Photovoltaic Specialists Conference*, vol. 1, pp. 1–6, 2009.

[52] P. Rodin and I. Grekhov, "Dynamic avalanche breakdown of a p-n junction: Deterministic triggering of a plane streamer front," *Appl. Phys. Lett.*, vol. 86, no. 24, p. 243504, 2005.

[53] Z. Zhao, C. Yi, a Stiffroberts, a Hoffman, D. Wasserman, and C. Gmachl, "Probing dopant incorporation in InAs/GaAs QDIPs by polarization-dependent Fourier transform infrared spectroscopy," *Infrared Physics & Technology*, vol. 51, pp. 131–135, Oct. 2007.

[54] S. Sauvage, P. Boucaud, F. H. Julien, J.-M. Gérard, and V. Thierry-Mieg, "Intraband absorption in n-doped InAs/GaAs quantum dots," vol. 71, no. 19, pp. 2785–2787, 1997.

[55] S. Sauvage, P. Boucaud, T. Brunhes, V. Immer, E. Finkman, and J.-M. Gérard, "Midinfrared absorption and photocurrent spectroscopy of InAs/GaAs self-assembled quantum dots," *Applied Physics Letters*, vol. 78, no. 16, p. 2327, 2001.

[56] N. Vukmirović, Ž Gačević, Z. Ikonić, D. Indjin, P. Harrison, and V. Milanović, "Intraband absorption in inas/gaas quantum dot infrared photodetectors-effective mass versus kp modelling," *Semiconductor Science and Technology*, vol. 21, pp. 1098–1104, Aug. 2006.

[57] Y. H. Kang, J. Park, U. H. Lee, and S. Hong, "Effect of the dot size distribution on quantum dot infrared photoresponse and temperature-dependent dark current," *Applied Physics Letters*, vol. 82, no. 7, p. 1099, 2003.

[58] W.-H. Lin, C.-C. Tseng, K.-P. Chao, S.-Y. Kung, S.-Y. Lin, and M.-C. Wu, "Broadband quantum-dot infrared photodetector," *IEEE Photonics Technology Letters*, vol. 22, pp. 963–965, July 2010.

[59] M. Y. Levy, C. Honsberg, A. Martí, and A. Luque, "Quantum dot intermediate band solar cell material systems with negligible valence band offsets," in *Proceedings 31st IEEE Photovoltaic Specialists Conference*, vol. 31, p. 90, 2005.

[60] P. Linares, C. Farmer, E. Antolín, S. Chakrabarti, a.M. Sánchez, T. Ben, S. Molina, C. Stanley, a. Martí, and a. Luque, "$In_x(Ga_yAl_{1-y})_{1-x}As$ quaternary alloys for quantum dot intermediate band solar cells," *Energy Procedia*, vol. 2, pp. 133–141, Aug. 2010.

Chapter 6

Strain balanced quantum posts

In this chapter we apply the strain balanced technique to the fabrication of quantum post with the aim of increasing their height while keeping good structural and optical properties. First we give a short introduction to this kind of nanostructures of relatively recent discovery and the main results available in the literature (Section 6.1). Then we apply the strain balanced technique to short quantum post fabrication to asses the effect of P in the growth process and the nanostructures properties (Section 6.2). Finally, we apply the technique to the fabrication of large nanostructures, studying their structural and optoelectronic properties (Section 6.3). In the last section, we study in further detail the polarization properties of the luminescence of this nanostructures, which is one of the most defining characteristics of quantum posts (Section 6.4).

Contents

6.1 Fundamentals and applications of QPs

As it has already been mentioned, if the spacer between QDs layers becomes very small, they can lead to the formation of QPs, which behave as individual vertical nanostructures and not as vertically coupled QDs. QPs present several unique properties, midway between those of QDs and nanowires. They are vertical structures whose height can be controlled by varying the number of stacked QDs or, more precisely, the number of periods of a short period superlattice. The limit to this approach is similar to QDs: an excessive accumulation of stress that can be partly relieved by using strain balanced techniques. Being self assembled and embedded in a semiconductor matrix, they can be doped at will to fabricate devices and are potentially free of detrimental surface recombination effects usually present in other types of vertical nanowires that are free standing.[1, 2] In addition, when embedded in a device, the fabrication processing follows the standard and mature techniques known for III-V semiconductor technology.

As it was briefly introduced in Chapter 4 (Section 4.4), these nanostructures form spontaneously when a very short period InAs/GaAs superlattice (SL) is grown on top of an InAs QDs seed layer. Due to the

strain field generated by the seed, the adatoms of the SL redistribute during growth producing In accumulation on top of QDs and Ga accumulation around them. As a result, In rich columns are created surrounded by a Ga rich matrix. The diameter of the columns can be controlled tailoring the size of the QD seeds and the height - the length of the QPs - by varying the number of periods of the SL. This is a desirable property since the aspect ratio (height/diameter) of standard self-assembled quantum dots can be hardly increased. Following the QP growth protocol, the diameter of the dot can be varied independently of its height. For example, it is possible to grow conical nanostructures, dots-in-a-rod or high aspect ratio QDs. Following this sequence, InGaAs/GaAs QPs of up to 40 nm high and 10-20 nm in diameter have been grown with excellent quality.[3–6]

QPs present a number of interesting properties with technological application. According to the calculations of the electronic structure of InAs/GaAs QPs (no SC) made by He *et al.*, electrons are delocalized along the whole length of the QPs whereas holes are confined in the strained-induced region at its bottom.[4] Large dipole moments can be induced in such situation by further separating electrons and holes with a longitudinal electric field. This results on exceedingly tunable exciton radiative lifetimes, from few ns to tenths of miliseconds at low temperatures. Such feature is of interest for different applications like quantum memories or highly non-linear electro-optical devices.[7] The possibility of controlling the height of the nanostructures with nanometer precision also makes QPs of interest in applications where the linear polarization of the absorbed/emitted light is a key issue. This is the case of semiconductor optical amplifiers (SOAs) where a polarization independent optical gain is desirable. QPs could be such material, combining the broadband amplification, high saturation output power, and ultrafast response expected for QDs SOAs with a control of the light polarization.[5, 8] Kita *et al.* demonstrated that eight alternating bilayers of InAs/GaAs are enough to produce QPs showing an inversion from transverse electric (TE) mode dominant emission to transverse magnetic (TM) mode dominant emission.[9] That means an aspect ratio (height/diameter) of about 0.8, very difficult, if not impossible, to achieve by self-assembling of a single QD layer. In quantum information technology applications, the requirements of the QPs might be even more demanding

and the QPs investigated by Krenner *et al.* had a height of 40 nm, with an aspect ratio of 2.[7] Meanwhile, Li *et al.* also reported QPs with 41 nm height but with an aspect ratio of 4, due to the smaller lateral size of their nanostructures.[10]

In summary, these nanostructures are very appealing and the application of the strain balanced technique to increase their length and improve their quality is thus an important step toward the realization of novel concept devices.

6.2 Strain balanced QPs: short nanostructures

Although the goal of this work is the fabrication of large QPs, we will first test the suitability of strain balanced QPs fabrication in shorter nanostructures. As it has been shown before, using phosphorus directly on top of the QDs have a major impact into their properties so it is expected that in short period superlattices of InAs/GaAsP and closely spaced QDs stacks, intermixing and shape modification of the nanostructures will rule the growth and greatly affect the QPs formation.

6.2.1 Sample fabrication

In order to study the fabrication of strain balanced QPs, we designed a set of three samples with different In and P content as well as total spacer thickness. The aim is to explore the effect of those parameters in the QPs properties, not to perform a systematic study.

Considering that the QPs are the limit of vertically coupled QDs when the spacer between layers is very small, we begin the QPs design with this idea in mind. The structures of the following samples can be found in Figure 6.1. Sample QPs-A consist on a stack of 11 QDs layers separated by 18 ML (∼5.2 nm) of GaAsP, which is of the same order than the QD height. P BEP is 5×10^{-7} mbar and its nominal content in the GaAsP layer is 13%. The first QDs layer is formed after growth of 2 ML of InAs whereas for the other ten, this is reduced to 1.8 ML. In sample QPs-B we reduce the spacer thickness to 10.7 ML and use nominally pure GaP layers 3.7 ML thick placed 3.5 ML above the InAs. P BEP is 5×10^{-7} mbar. Finally, Sample QPs-C is identical to Sample QPs-D described in detail in

Chapter 4 (page 111) but substituting the GaAs spacer by GaAsP with nominal P content of 13.5%. The P BEP is 6×10^{-7} mbar.

The GaAsP and GaP growth in these samples proceeds by opening simultaneously the corresponding effusion cells. All other growth conditions have the standard values used along this work, namely T_s = 510 °C, As BEP = 2×10^{-6}, R_g(Ga) = 0.5 ML/s and R_g(In) = 0.02 ML/s.

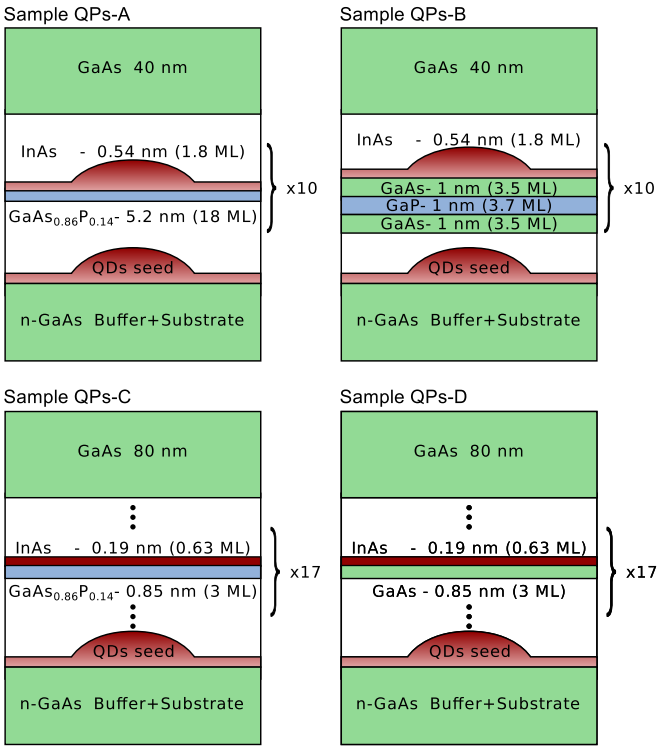

Figure 6.1: Schema of the layer structure of samples QPs-A to D. The InAs thickness to grow the seed layer is always 2 ML.

Table 6.1 and Figure 6.1 summarizes the sample structure for easy comparison. We include the information of sample QPs-D, that will be further analysed as representative of not strain balanced QPs.

Table 6.1: Sumary of QPs samples. t(tot), t(InAs) and t(CL) are the total spacer, the InAs and the compensating layer (CL) thicknesses. P(%) is the phosphorus content in the CL and z(CL) its position above the InAs layer. All thicknesses are in ML.

Sample	t(total)	t(InAs)	t(CL)	P(%)	z(CL)
QPs-A	18	1.8	18	13%	0
QPs-B	12	1.8	3.7	100%	3.5
QPs-C	3	0.63	3	13.5%	0
QPs-D	3	0.63	-	-	-

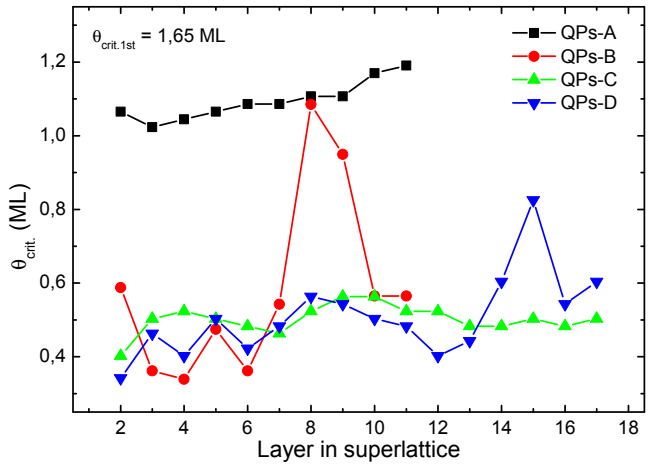

Figure 6.2: Critical thickness for the 2D→3D transition in samples QDs-A to QDs-D.

RHEED measurements

The first information we have on these samples is gathered during growth due to the RHEED monitoring of the critical thickness (Figure 6.2). In all cases, the streaky RHEED pattern disappears during the capping of the InAs and it appears again after a certain amount of In is deposited in the following layer. In sample QPs-A this amount of InAs is around 1 ML in the $2nd$ layer and slowly increases until reaching 1.2 ML in the $11th$ layer. For the other three samples, the amount of InAs needed is much smaller, between 0.3-0.5 ML in the first layers to 0.5-0.6 in the lasts ones.

As it was observed in the previous chapter for QDs stacks, the critical

thickness for QDs nucleation is greatly reduced after the first layer. Given the small spacers used in this samples, and following the analysis done by Howe *et al.*, the reduction in the critical thickness in this case is a combination of two effects: the strain fields created by the buried layers and In segregation.[11] Sample QDs-A have the largest spacer (∼5.2 nm) and thus the impact of these factors is smaller and the critical thickness is closer to that of the seed QDs layer. Samples QDs-C and D have the thinnest spacer and both effects probably have an important contribution, leading to very small critical thicknesses. Sample QDs-B, on the other hand, have a spacer 4 times thicker but it shows the same critical thickness values than samples QDs-C and D. This might be the result of the largest amount of In that it contains and hence the increased segregation from layer to layer.

No effects related with the presence of P in the spacer are apparent on these measurements, showing samples QDs-C and D, which have identical structure except for the presence of P in the former, a comparable behavior for the critical thickness with the number of layers.

AFM analysis

AFM measurements taken on the top surface of the samples are more revealing of the quality of the structures. As it can be seen in Figure 6.3, the surface roughness largely differ among the samples. Samples QDs-A and B have a RMS roughness of 1.69 and 6.75 nm, respectively, whereas in samples QDs-C and D it is 0.42 and 0.88 nm. The images of the former are clearly covered with holes and large mounds that are fingerprint of a degraded structure.

The RMS of the samples is directly related first with the InAs thickness used in the superlattice and secondly with the presence of P strongly interacting with the deposited In. Larger In content with such small spacers means that QDs might become very large within one period, with the aid of the segregating In and the strain fields. Those large QDs might dislocate when they are covered, dislocations that will propagate upwards to the surface. As shown in Section 5.2, using phosphorus directly on top of the QDs reduce their size and helps to avoid the In to introduce all its potential stress. In that case, the formation of large nanostructures will be partly inhibited.

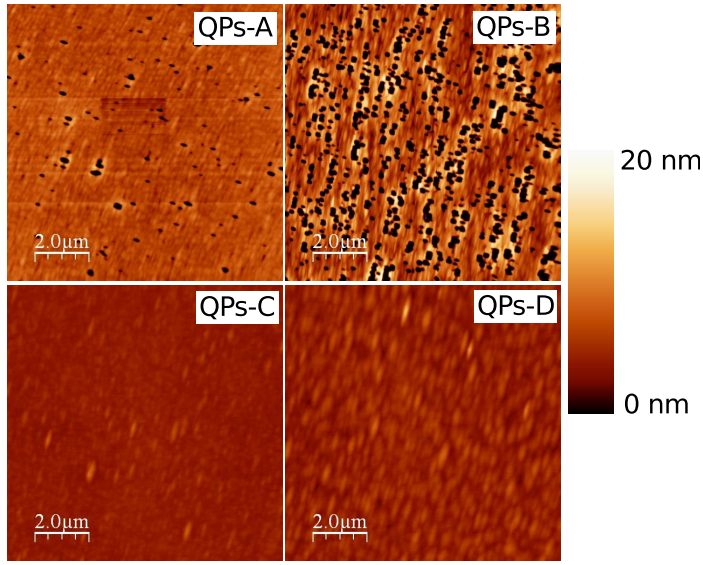

Figure 6.3: AFM analysis of samples QDs-A to QDs-D.

In the light of this interpretation, the surface covered with holes of sample QPs-B is expected, given its large In content and reduced spacer. Conversely, the smoother surface observed in sample QDs-C compared to QDs-D is also reasonable, as a result of the P effect.

In summary, in growing short period superlatices for QPs formation it is critical to avoid the appearance of large QDs due to the accumulation of too much In. This can be done by reducing the amount of In deposited per layer and relying into the strain fields of the buried layers to get the appropriate QDs formation.

6.2.2 Structural characterization

In Figure 6.4 we show the cros-sectional TEM images of samples QPs-C and QPs-D. Figure 6.4a, corresponding to sample QPs-C, clearly reveals the formation of small QPs, around 20 nm high and 20 wide. The QPs are embedded in a darker region corresponding to the InAs/GaAsP superlattice that did not developed QPs. A similar result is found for sample QPs-D (Figure 6.4b) It can be seen in sample QPs-C that the

QPs are tilted from the vertical direction and the presence of large surface undulations in the QPs region. This might be related with an inhomogeneous elastic relaxation processes via surface roughening which is often found in low strained materials, such as $In_{0.2}Ga_{0.8}As/GaAs$.[12] It is curious that, as revealed in the AFM images, this sample shows smoother surface after the GaAs capping than sample QPs-D which seem to contradict the flatter growth front just after QPs growth seen in its TEM image (Figure 6.4b). This might be consequence of the reduced stress introduced in the the former due to the presence of phosphorus.

MOSS measurements performed in this sample are shown in Figure 6.4b. The curve corresponding to sample QPs-D, discussed in Chapter 4, is also included for clarity.

As it can be seen, sample QPs-C accumulates less stress than sample QPs-D. The evolution of the accumulated stress in sample QPs-C is almost linear, which contrast with the bending observed for sample QPs-D and discussed before. This is reasonable in this case since the presence of P in the structure automatically reduces the strain and the effectiveness of the In migration processes. The strain balanced oscillations are barely visible which, as observed previously for QDs (Figure 5.8a), is directly related with the intermixing of the constituent materials. The degree of compensation in the superlattice (disregarding the QDs seed, that is common to both structures) can be estimated in 57%.

Assuming that we are growing a homogeneous quaternary alloy and that all In incorporates to the sample, we can estimate the P content from the slope of the curve. The resulting average In and P content of the alloy are around 20% and 30%, respectively (Figure 6.4b, green line) the latter calculated with Equation 4.19. It should be noted that assuming that all In is incorporated in a homogeneous alloy will overestimate the P content since it introduces more stress than the same In in a more concentrated, thinner layer, as it was demonstrated in Chapter 4. This calculation, thus, establishes just an upper limit for the P content of the sample. A lower limit can be found if all In is assumed to be incorporated in the form of InAsP 0.19 nm thick and the barrier is made of GaAsP 0.85 nm thick (the nominal thicknesses). In this case, the average P content that fits better the experimental results has to be obtained by performing several simulations of the accumulated stress, as it was done in Chapter 4. The

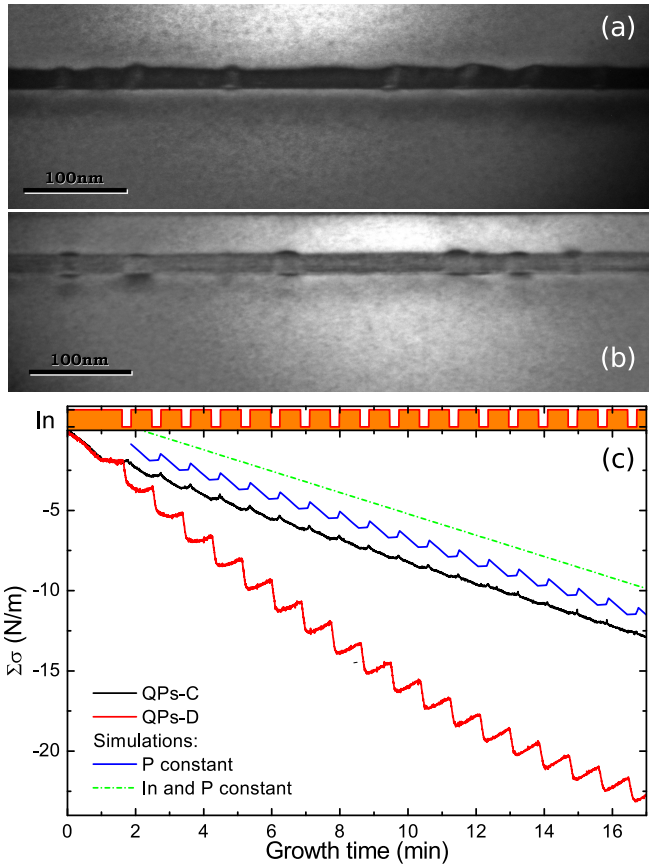

Figure 6.4: Cross-section TEM of samples a) QPs-C and b) QPs-D. MOSS analysis of both samples. TEM images taken by Dr. Ana M. Sánchez (UCA)

best result is obtained when the P content is 14% in both layers, equal to the nominal value (Figure 6.4b, blue line). Including P in the InAs layer is a reasonable hypothesis in a steady state situation where residual P in the chamber will, unavoidably, incorporate to the sample during the InAs growth.

The simulation of the accumulated stress of both limiting cases shown in Figure 6.4b have been shifted from the experimental curve for major clarity.

6.2.3 Optical properties

We finalize the study of these samples by analysing their optical properties by means of PL experiments.

Figure 6.5 shows a comparison of the PL emission of the four samples at low temperature.[1] Several features can be seen in these curves. First, sample QPs-A emission presents two bands, centered at 1.263 and 1.307 eV with a FWHM of ∼25 meV in both cases. The first peak is associated with the ground state emission whereas the second one is an excited stated. Sample QPs-B, on the contrary, shows a single, broad asymmetric emission band, centred at 1.153 eV and with a FWHM of 70 meV. No excited states are resolved. Samples QPs-C and D, in turn, have two emission bands each with emission energies of 1.239 and 1.275 eV the former, and 1.176 and 1.233 eV the latter. In this case, the high energy peaks are not excited states but a second emitter, possibly another QPs family with different size and/or composition or even a quantum well result of the coupling of the WLs in different layers. The FWHM of these peaks are 33, 18, 57, and 26 meV, respectively.

As it can be seen, the two samples where the GaAsP layer is grown directly on top of the QDs (QPs-A and QPs-C) have an emission blueshifted and narrower than those that use GaP or no compensation. The same trends can be found in the integrated PL intensity, which for samples QPs-B and QPs-D it is double that of the QDs-A and QPs-C. The reason is that when GaAsP is growth in close contact with the nanostructures their size is reduced and part of them might completely dissolve, leading to the blueshift and the reduction of the PL intensity, as it was discussed in Section 5.2.

PL experiments as a function of temperature can give more information about this issue. The results up to room temperature are shown in Figure 6.6.

As it can be seen, in all samples the PL signal is quenched below

[1] Part of the PL measurements of these samples were performed at Imperial College London (UK) during a short stay in Summer 2009. The equipment, belonging to Prof. Ray Murray's group, consisted in a Ti:Sapphire ultrafast pulsed laser, emitting 3 ps pulses at a wavelength of ∼790 nm. The PL signal was dispersed by a Spex 1404 double-monochromator to provide wavelength selectivity. We used a Ge detector, identical to that of our own setup for continuous wave experiments.

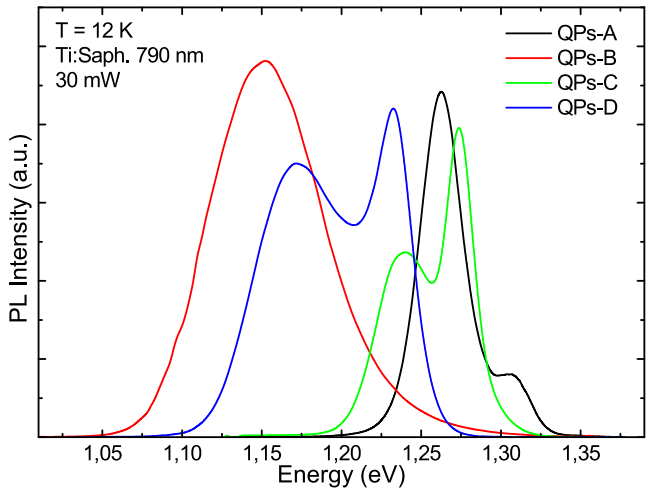

Figure 6.5: Low temperature PL measurements of samples QDs-A to QDs-D.

the room temperature. In samples QPs-A and C, it disappears at 220 K whereas in QPs-B and D it almost reaches 280 K. This is consistent with the larger emission energy of the latter which is related with larger confinement energies. These energies can be obtained from the Arrhenius plots included in each subfigure. Samples where the QDs/QPs are capped directly with GaAsP show thermal activation energies around 150 meV whereas those that use a GaAs capping (regardless if they are strain balanced or not) show higher values (200 meV). This result is consistent with the observed higher transition energies in the former, closer to the GaAs band edge. Given the energies of the emission peaks, these activation energies probably correspond to unipolar scape to the InAs WLs or to an alloyed GaInAsP matrix of varying composition surrounding the QPs.

A detailed analysis of the emission of samples QPs-C and D shows that, with increasing temperature, the intensity of the low energy band increases in the detriment of the high energy band. This suggest a charge transfer from small QPs to the bigger ones, as it is often observed in asymmetric QDs bilayers and QDs molecules.[13, 14]

The same feature can be seen in the emission of sample QPs-B and, less pronounce, also in sample QPs-A. However, in these cases we suggest that the extra carriers available with temperature might be actually being

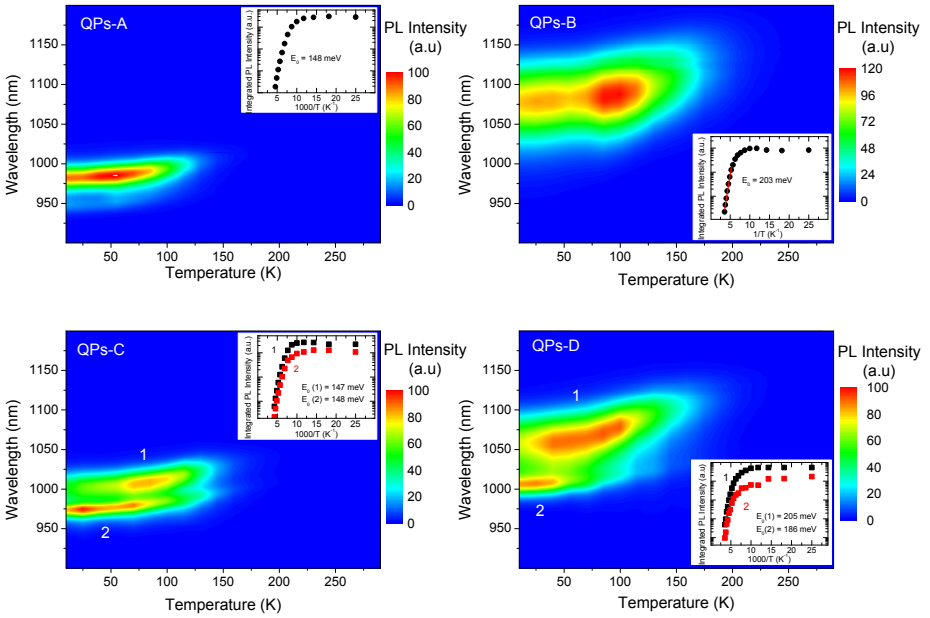

Figure 6.6: Color map showing the PL as a function of temperature for samples (a) QPs-A to (d) QPs-D. The corresponding insets include an Arrhenius plot of each of the observed emission bands.

released by traps and defects in the other parts of the structure.

6.2.4 Summary of results

From the results of QPs samples of small size, we can conclude that using P to fabricate QPs is a feasible process never attempted before that improves the material quality. The sample surface becomes smoother and the PL emission, although blueshifted, becomes narrower. We can also conclude that the amount of In in the structure plays a key role in the quality of the material. Even in the case of larger spacers, the quality of the QPs is severely degraded if excessive In is incorporated.

6.3 Strain balanced QPs: large nanostructures

Once we have shown that it is possible to fabricate strain balanced QP and having studied some of their properties, we now apply the technique to long strain balanced structures.

6.3.1 Sample fabrication

The protocol we use to fabricate long strain balanced QPs (sample QPs-E) is that of sample QPs-C, which included a seed QDs layer, grown after the deposition of 2 ML of InAs, and a short period superlattice of 0.63 ML (0.19 nm) of InAs and 3 ML (0.85 nm) of GaAsP (14% of P). In this case, the number of periods is increased to 100 which, with a simple rule of thumb, should correspond to a QPs height of 118 nm. A second sample with identical structure but containing 0.73 ML (0.22 nm) of InAs in the superlattice is also fabricated to continue testing the effect of the In content in the structure (sample QPs-F). As we will see below, this increase of 15% of the In content have a major impact into the QPs properties.

Both QPs structures are embedded in the seminsulating region of a PiN diode, with 110 nm of GaAs below and 20 nm above the nanostructures. The full structure and growth sequence of the PiN diodes can be found in Figure 6.7 and are as follows: After a n-GaAs (Si:10^{18} cm^{-2}) buffer layer, we grow a n-$Al_{0.75}Ga_{0.25}As$ (Si:3x10^{18} cm^{-2}) 20 nm thick back surface field layer, 20 nm of n-GaAs (Si:5x10^{18} cm^{-2}), the seminsulating region around 240 nm thick that contains the QPs, 50 nm of p-GaAs (Be:2x10^{18} cm^{-2}), 30 nm of p:$Al_{0.25}Ga_{0.75}As$ (Be:10^{19} cm^{-2}) and a thin p-GaAs (Be:5x10^{18} cm^{-2}) layer to avoid aluminum oxidation and as contact layer.

Standard optical lithography and wet etching techniques were used to define mesas and metal ohmic contacts following schema number 1 (Section 2.2.1).

6.3.2 Structural characterization

TEM characterization

Figure 6.8 shows bright field, cross-section TEM (XTEM) and planar view images of sample QPs-E. In Figure 6.8a, it is clearly visible the formation of continuous vertical contrasts crossing part of the intrinsic region of the

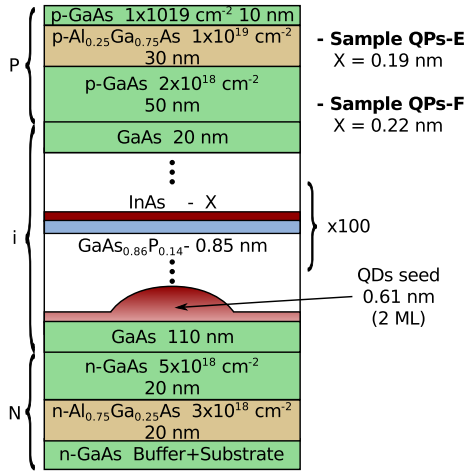

Figure 6.7: Schema of the layer structure of samples QPs-E and F.

device. These contrasts indicate the successful fabrication of the QPs, which have a height of ∼120 nm and and estimated diameter of around ∼13 nm. The diameter found in this image is underestimated, though. The planar view image of the same sample (Figure 6.8b) suggest that actual shape of the QPs deviates from perfectly cylindrical, being elongated in the $[1\bar{1}0]$ direction. The lateral size of the QPs is thus around 34×19 nm. The average dislocation density deduced from these images is of 10^7 cm^{-2}. It should be noted that although in the cross-section TEM images QPs appear as vertical columns, they might be actually tilted in the direction normal to the image plane, as it has been discussed before for sample QDs-G (Figure 5.34).

In both, cross-section and planar view images, the QPs seems to be surrounded by darker regions which might correspond either to the effect of the strain fields or even a fingerprint of a core-shell structure. Quantitative compositional studies on sample QPs-E are currently in progress in the University of Cádiz in order to clarify the In distribution in the QPs. To this purpose the two techniques that are being used are atom probe tomography (APT) and energy dispersive x-ray spectroscopy (EDX).

A comparison between samples QPs-E and F is shown in Figure 6.8c and d. The bright field <220> images of both samples shows the vertical

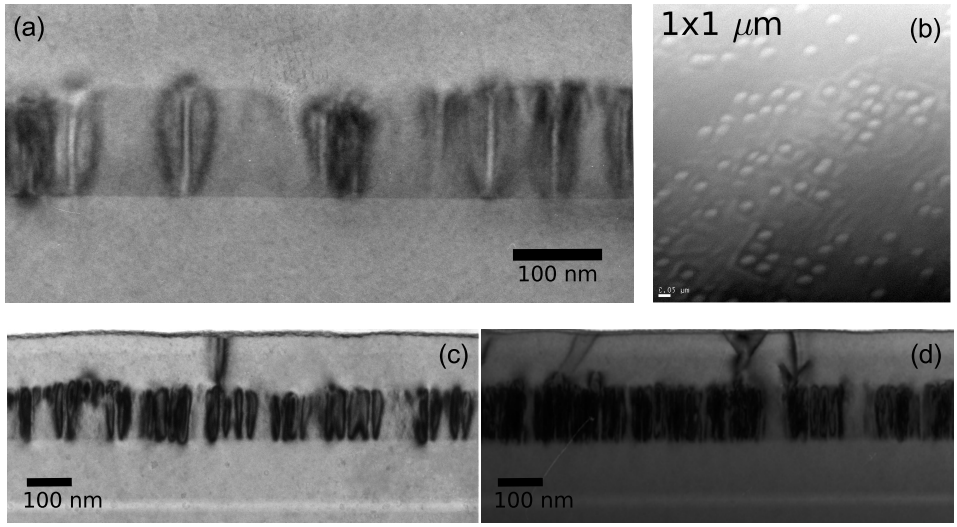

Figure 6.8: (a) Bright field XTEM image (zone axis <110>) and (b) planar view annular dark field (ADF) image of sample QPs-E. Bright field XTEM images around the <022> reflection of samples (c) QPs-E and (d) QPs-F. TEM images taken by Mr. David Hernández and Dr. Manuel A. Roldán (UCA).

contrast that we have attributed to the QPs. However, in this mode of measurement, defects and dislocations present in the structure are highlighted. As it can be seen, sample QPs-F shows higher dislocation density (∼5 times higher) than sample QPs-E, result that is confirmed after the analysis of several images taken in different regions.

The larger defect density is directly attributed to the larger In content of sample QPs-F (15% more), that increases the stress accumulation and leads to plastic relaxation of the structure. It is possible that this result could be prevented by increasing the P content of the sample to compensate the extra In, but we believe that it would not have avoided the formation of too large In clusters leading to material degradation.

XRD measurements

We have performed an XRD analysis on these samples to asses their crystal quality and get information about its composition. In Figure 6.9 it can be

seen the XRD spectra of samples QPs-E and QPs-F near the GaAs <004> symmetric reflection. As it can be seen, in both cases we have a very intense peak, ascribed to the substrate, and a weaker one at lower angles. This peak can be attributed to the diffraction by the thick embedding matrix that surrounds the QPs, as it was observed in TEM images, which resulted from the alloying of the InAs/GaAsP short period superlattice in between the QPs. The effect of the nanostructures (either QDs or QPs) can not be seen with this kind of measurement and would be revealed only as a broadening of the layer-related peaks due to the crystal lattice distortion.[15]

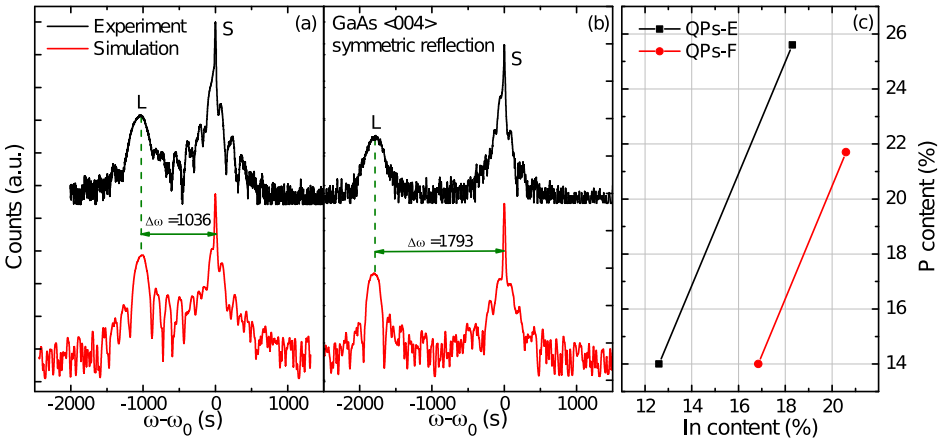

Figure 6.9: Experimental and simulated XRD patterns of samples (a) QPs-E and (b) QPs-F. (c) In and P composition ranges in the InGaAsP matrix that can lead to the observed diffraction patterns in both samples. Substrate peak scattering angle $\omega_0 = 33.02403°$.

From the position of the layer peak we can get information about the composition of the matrix layer. Assuming a homogeneous quaternary InGaAsP alloy for that layer, we can give a reasonable range of In and P compositions that can lead to these patterns within the nominal sample structure. We use as the upper limit that all deposited In is in the matrix (18.3% and 20.6% of In for samples QPs-E and QPs-F, respectively) and as the lower limit that the matrix has the nominal 14% of P content. Using X'Pert Epitaxy software, and simulating the sample as a 125 nm thick, strained InGaAsP layer embedded in GaAs, we find that the In and P

contents that can give the measured diffraction pattern are those shown in Figure 6.9c. As a comparison, typical In content on the matrix in not strain balanced QPs samples grown with a similar protocol are found to be between 14% and 16%, which is within the range for sample QPs-E but below that of sample QPs-F, something that can be attributed to the higher nominal In content of this sample.[10, 16]

In Figure 6.9a and b we show the simulated pattern using the highest In content, although the other In/P composition combinations shown before will lead to the same result. As it can be seen, the simulation correctly reproduce the layers peak position, being their experimental width larger than in the simulation due to the presence of nano structures distorting the lattice, as mentioned before.

It is interesting to estimate the expected critical thickness for plastic relaxation of an epitaxial layer under biaxial strain. From the angular separation $\Delta\omega$ between the layer and substrate peaks we can calculate the in-plane strain of the layer using Equations 3.8 and 3.9. The exact composition of the layer chosen to calculate the modified Possion's ratio has only a minor influence on the result. We find in-plain strains of $\sim$0.4% and $\sim$0.7% for samples QPs-E and QPs-F, respectively.

To calculate the critical thickness we use the Matthews and Blackeslee formalism, which is widely accepted and used in strained epitaxial systems, considering as the plastic relaxation mechanism the formation of 60° misfit dislocations.[17–20] The result of such calculation gives critical thicknesses of $h_c \sim 152$ nm for sample QPs-E and $h_c \sim 78$ nm for sample QPs-F.

Even though in this analysis we neglect the effect of the QPs, from this result it is clear that the thickness of the InGaAsP matrix in sample QPs-F is well above the critical thickness for plastic relaxation and thus higher defect density must be expected. In sample QPs-E, on the other hand, such thickness is larger than the growth structure and the formation of dislocations due to excessive strain accumulation should be prevented and lead to higher crystal quality and better optoelectronic properties.

Finally, it is convenient to mention that other authors suggest a more conservative critical thickness value, being a simple estimation of it $h_c = a_{sub}/2|\epsilon_\perp|$, with a_{sub} the substrate lattice constant and $\epsilon_\perp$ the in-plane strain.[21] If this criterion is chosen, the resulting critical thicknesses would be $h_c \sim 71$ nm for sample QPs-E and $h_c \sim 40$ nm for sample QPs-F. In

this case, both samples would be defective.

6.3.3 Electronic band structure and exciton recombination dynamics

The emission and carrier recombination processes in these samples have been assessed by means of PL and TRPL experiments. Unless otherwise indicated, the excitation source in this section is a pulsed laser at 405 nm with a repetition rate of 40 MHz since most experiments include both steady state under pulsed excitation and time resolved measurements.

Figure 6.10a shows the PL spectra recorded at low temperature of the two samples considered. They show relatively narrow peaks due to emission from the QPs, centered at 1.17 eV and 1.1 eV with an inhomogeneous broadening of 21 and 32 meV, respectively. Sample QPs-E shows an additional and very broad emission band centered at 1.28 eV that can be tentatively attributed to small QDs in the seed layer which either do not lead to QPs formation or lead to QPs with a lower In content (P2). Emission from sample QPs-E is shifted 71 meV to lower energies and the integrated PL intensity is four times smaller than sample QPs-F. Both effects are a direct consequence of the larger In content of sample QPs-F. On the one hand, more In increases the band offsets leading to increased localization of carriers; on the other hand, the strain energy introduced by the extra In might surpass a critical plastic deformation level of the system and generate a number of defects that act as non-radiative recombination centers, thus reducing the PL intensity.

The PL decay transients corresponding to the same excitation conditions are shown in Figure 6.10b. A preliminary analysis of these curves indicate that sample QPs-E can be deconvoluted with a simple monoexponential decay, giving a characteristic time of around 1 ns. This value is of the same order that those found by Li *et al.* in this kind of nanostructures.[10] Sample QPs-F, on the other hand, shows a more complex decay transient which can be described with two exponentials, indicating two different emitters very close in energy.[22, 23]

Using the geometry of the QPs obtained from the TEM images, the composition range of the matrix deduced from XRD and the energy position of the PL emission band, we can give an estimation of the

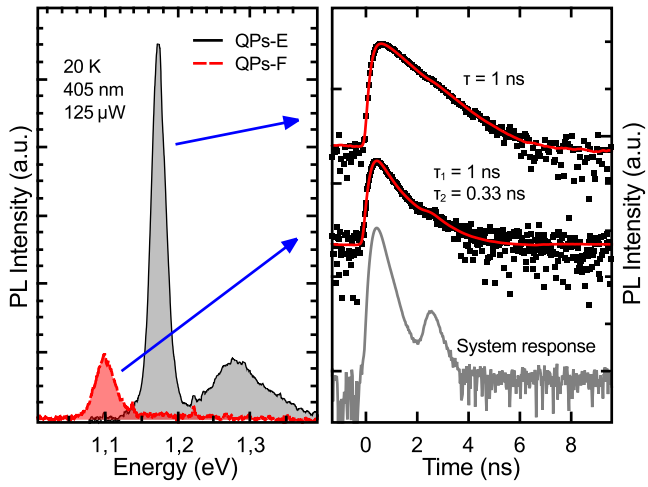

Figure 6.10: (a) PL emission of sample QPs-E and QPs-F. (b) The corresponding TRPL measurements deconvoluted with one and two exponentials, respectively. The system response is included as a reference.

composition of the QPs columns and the barriers.[2] In Figure 6.11 we show the calculated bandgap of a biaxially strained InGaAsP/GaAs alloy as a function of its composition around the values obtained by XRD. As it can be seen, the bangaps compatible with the XRD measurements are all above, but close, to the GaAs bandedge, being the most extreme possible value around 1.59 eV. To calculate the QPs transition energy we use a barrier made of $In_{0.15}Ga_{0.85}As_{0.82}P_{0.18}$ (black cross in Figure 6.11). The PL energy as a function of the QPs in-plane aspect ratio for a range of In and P contents is calculated using Nextnano and shown in Figure 6.12.

As it can be seen, the transition energy decreases for increasing In content in the QPs and in-plane aspect ratio a/b, whereas it increases for increasing P content. In order to have a ground state transition within reasonable agreement with the experiment (shaded rectangular area) it is necessary that the P inside the QPs was low (close to zero) and an In composition of around 70-75%.

[2]Theoretical calculations on the density of states and band structure that appear in this thesis have been carried out by Dr. Jose M. Llorens, a member of the MBE group at IMM.

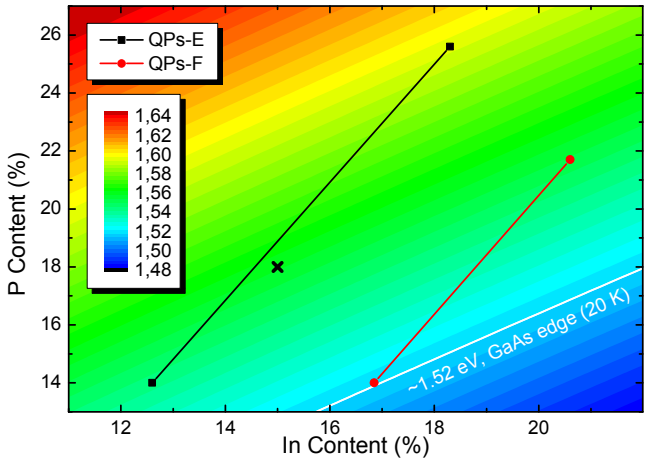

Figure 6.11: Colour map of the bandgap energy of the embedding InGaAsP barrier as a function of its composition. We include the composition ranges deduced from XRD (Figure 6.9c). Black cross indicates the barrier composition used in the calculations of the QPs ground state.

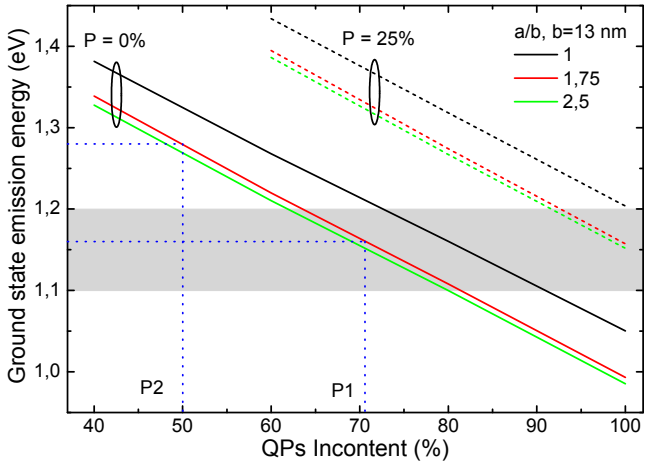

Figure 6.12: Calculated transition energy as a function of QPs indium and P content as well as of the in-plane aspect ratio. Calculations performed by Dr. José M. Llorens.

More insight into the electronic structure and carrier recombination dynamics in this samples can be extracted from the temperature and power

dependence of the decay times and the PL intensity which we discuss below separately for the two samples.

Sample QPs-E: Lower In content

We first analyze sample QPs-E as its monoexponential behavior suggest a simple, defect free electronic structure. In Figures 6.13 and 6.14 we show the PL and the TRPL evolution for increasing excitation power. As the laser intensity increases, the relatively small linewidth of the emission band allows the observation of an asymmetric broadening towards higher energies (Figure 6.13). At the maximum power, the asymmetric full width at half maximum reaches 58 meV. Yet, contrarily to QDs with similar inhomogeneous broadening, no additional bands are observed which could be associated to excited states emission.[24, 25]

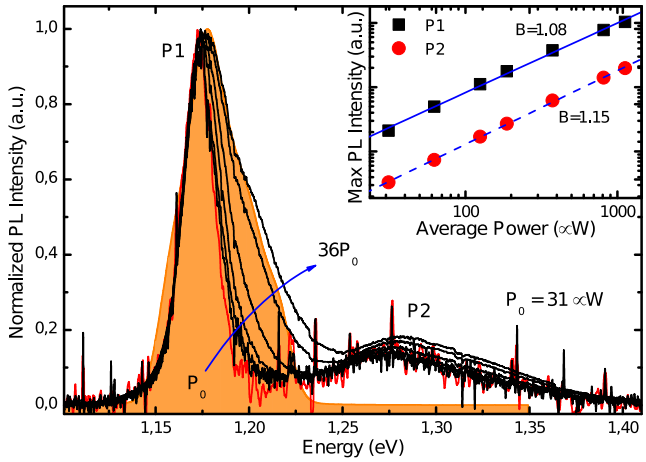

Figure 6.13: Evolution with the excitation power of the normalized PL. The inset shows the maximum PL intensity in log-log scale as a function of power for the two bands and the corresponding slope of a linear fit.

The asymmetric broadening can be explained if the QPs had a density of states midway between a quantum dot and a quantum wire. To this end, we have calculated the joint density of states (DOS) of a QP of the same average height and diameter.[26] The electronic structure has been calculated using the 8×8 $\boldsymbol{k} \cdot \boldsymbol{p}$ method together with a function expansion as in Ref. [27]. An homogeneously strained infinite cylinder has

been considered to include the elastic deformation effects.[28] To mimic the inhomogeneous broadening of the spectrum, the resulting joint DOS is artificially broadened with a 15-meV-broad Gaussian convolution and plotted as a shaded area behind the experimental curves in Figure 6.13a. To reproduce the experimental broadening at high power we just need to consider the first 12 conduction band states and an equivalent number of valence band states. They correspond to excited states of the vertical confinement potential in the first shell of the in-plane one. Our analysis thus reveals that these QPs have to be described as one-dimensional-like nanostructures, rather than elongated QDs.

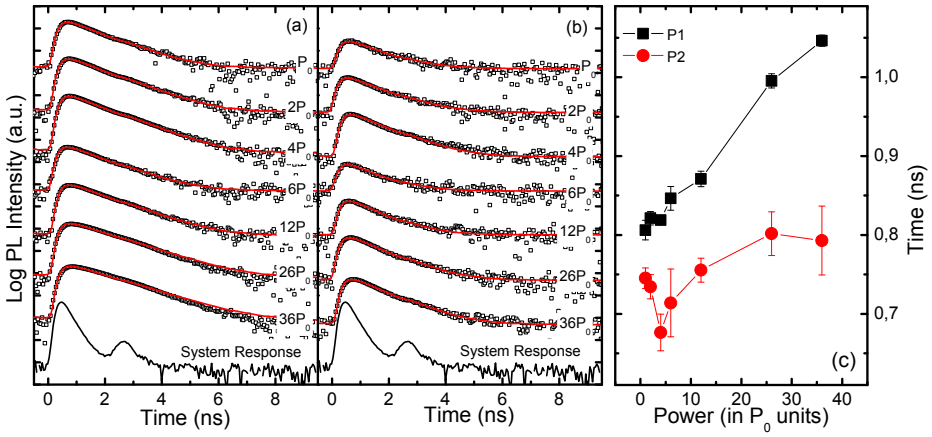

Figure 6.14: Monoexponential deconvolution of the TRPL decay curves as a function of excitation power for (a) P1 and (b) P2 bands in sample QPs-E. (c) Decay times deduced from such deconvolution.

In the inset of Figure 6.13, it can be seen that the PL intensity of the two emission bands (P1 and P2) follow a linear dependence with the excitation power in the whole measured range, indicating that there is neither saturation of electronic states nor the activation of non-radiative events.

The TRPL decay curves of both bands have been deconvoluted using a monoexponential dependence (Figure 6.14a and b). The resulting decay times are shown in Figure 6.14c. As it can be seen, the high energy band exhibits a decay time faster than the lower energy one in the whole power

range. Nevertheless, in both cases, the times keep a relatively constant value, increasing only slightly with power, which might be caused by carrier transfer between QPs at high powers but in general agrees with the lack of saturation of the PL signal deduced from the intensity behaviour.

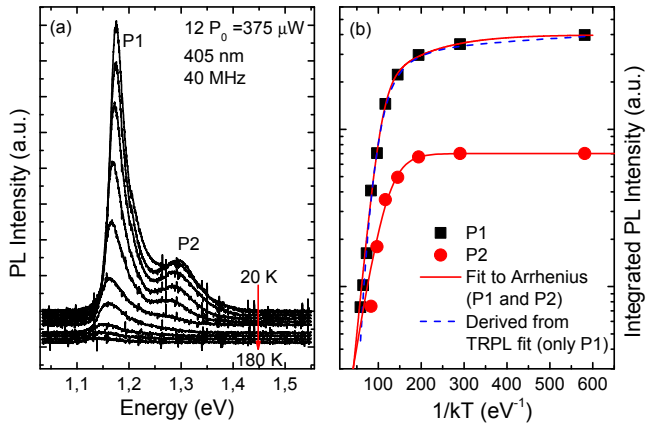

Figure 6.15: (a) Evolution with temperature of the PL and (b) the corresponding Arrhenius plot of the integrated PL intensity for sample QPs-E.

The PL and TRPL measurements as a function of temperature can be observed in Figure 6.15 and Figure 6.16, respectively. As the temperature increases, the PL intensity reduces, being such reduction faster for the high energy band. At 120 K, P2 completely disappears while P1 holds up to 180 K. The steady state behaviour, shown in Figure 6.15b can be fitted with an Arrhenius dependence with two activation energies:

$$I_{PL} = \frac{I_0}{1 + Ae^{\frac{-E_A}{kT}} + Be^{\frac{-E_B}{kT}}} \tag{6.1}$$

with $E_A = 10.2$ meV, $E_B = 65$ meV, $A = 2.6$ and $B = 2000$. In turn, the evolution of the secondary band can be fitted with only one activation energy, giving $E_A = 39$ meV and $A = 112$.

In these fits (continuous lines in Figure 6.15b) it is assumed that the radiative decay time, which enters into the constants A and B, is constant on the whole temperature range. However, it is known that the radiative time has a certain dependence with temperature that depends, among other factors, on the kind of nanostructure in which carriers recombine.

We can get further insight into this effect by analysing the decay time τ_d as deduced from a monoexponential deconvolution of TRPL curves shown in Figure 6.16a (only the main band P1 is analysed). As it can be seen, it presents a slight increase with temperature up to 60 K and then a progressive reduction, characteristic of the appearance of thermally activated scape paths (Figure 6.16b). Assuming that at 20 K the only loss mechanism is radiative recombination, the radiative τ_R and non-radiative τ_{NR} decay times can be extracted from:

$$\tau_R = \frac{I_0}{I_{PL}}\tau_d \tag{6.2}$$

and

$$\frac{1}{\tau_d} = \frac{1}{\tau_R} + \frac{1}{\tau_{NR}} \tag{6.3}$$

with I_0 and I_{PL} the PL intensity at 20 K and as a function of T, respectively. As it can be seen, τ_{NR} decreases with temperature as it is typically observed in thermally activated processes. τ_{NR} can actually be fitted with two components τ_1 and τ_2, of the form:

$$\frac{1}{\tau_{NR}} = \frac{1}{\tau_1} + \frac{1}{\tau_2} = \frac{1}{\tau_1^0}e^{\frac{-E_1}{kT}} + \frac{1}{\tau_2^0}e^{\frac{-E_2}{kT}} \tag{6.4}$$

with $E_1 = 6.4$ meV and $E_2 = 46$ meV the activation energies of the non-radiative processes characterized by time constants $\tau_1^0 = 1.31$ ns and $\tau_2^0 = 0.011$ ns, respectively. Conversely, τ_R increases exponentially with temperature:

$$\tau_R = \tau_R^0 + Ce^{\frac{T}{T_C}} \tag{6.5}$$

being $\tau_R^0 = 0.89$ ns, C=0.14 ns and $T_C = 46$ K. Combining Equation 6.2 to Equation 6.5 we can obtain an Arrhenius-like equation with an explicit dependence of the PL intensity on all the parameters derived from the TRPL analysis:

$$I_{PL} = \frac{I_0}{1 + (\tau_R^0 + Ce^{\frac{T}{T_C}})(\frac{1}{\tau_1^0}e^{-\frac{E_1}{kT}} + \frac{1}{\tau_2^0}e^{-\frac{E_2}{kT}})}. \tag{6.6}$$

As it can be seen in Figure 6.15b, both results are equally good in reproducing the experimental data in steady state conditions. However,

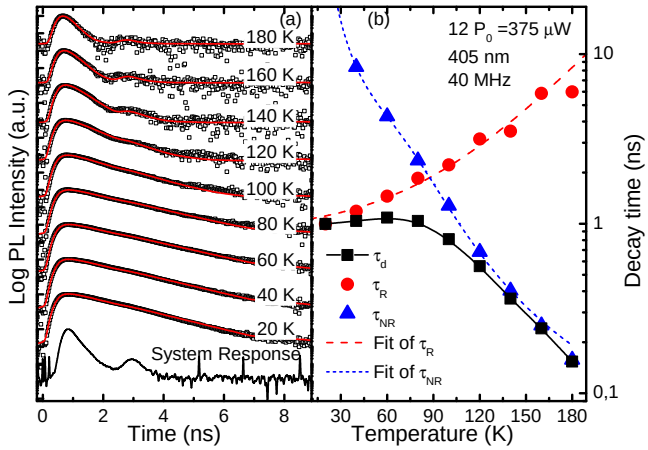

Figure 6.16: (a) Experimental TRPL as a function of temperature (squares) and its deconvolution (solid lines) at the maximum of band P1 in sample QPs-E. (b) Decay times as a function of temperature with the radiative and non-radiative components.

Equation 6.1 overestimates the activation energies as it does not take into account the dependence of the radiative time with temperature.

We now discuss the numerical results obtained in this analysis. On the one hand, the non radiative scape process with smaller activation energy is probably associated with trapping of carriers by impurities or defects in the surface of the QPs, as it has been reported before.[29] The other process is more intriguing as the activation energy, $E_2 = 46$ meV, is too small to correspond to unipolar scape of carriers from the QPs to the matrix. The most plausible explanation is that it corresponds to trapping by a kind of defects of a different nature than those at $E_1 = 6$ meV, given the large difference in characteristic time. This idea is supported by the fact that if a CW laser is used as excitation source, the temperature dependence of the PL is heavily altered. In Figure 6.17a we compare the integrated PL intensity of sample QPs-E using either a CW (10 mW, 532 nm) or a pulsed laser. Even though the low activation energy is the same in both cases, the high activation energy is increased up to 170 meV. This energy is now compatible with the unipolar escape of carriers from the nanostructures to the matrix.[29] To understand this difference, the defects that are apparent in pulsed experiments should be saturated with carriers and therefore not

act as efficient traps.

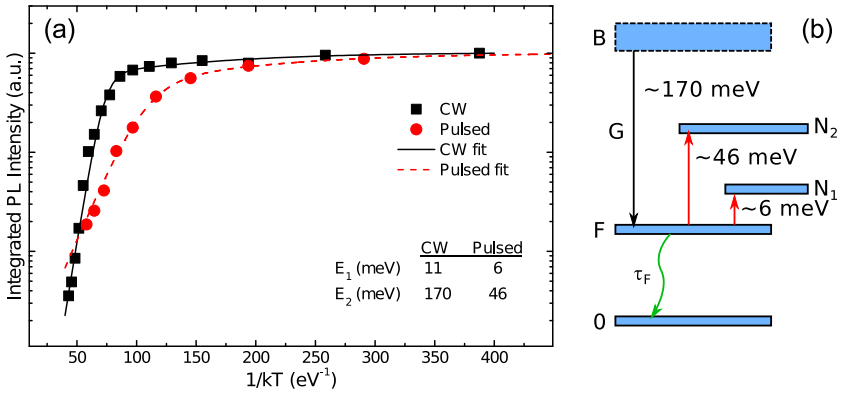

Figure 6.17: (a) Comparison of the integrated PL intensity of the P1 band and the corresponding fit of the measurements performed with a CW laser and a pulsed laser. (b) Levels involved in the exciton dynamics in sample QPs-E.

We have found a exponential increase of the radiative lifetime with increasing temperature in or QPs. If they were 1D-like nanostructures, as it is theoretically our case, the dependence should be with the square root of temperature, as it has been reported by Guillet *et al.*.[30] Nevertheless, this result relies on two assumptions: the existence of free excitons and a rapid thermalization of the exciton population. In the presence of disorder and taking into account exciton ionization, those assumptions are no longer valid and other functional dependences, result of the presence of localized excitons with larger radiative lifetimes, might be found.[31–33] That is the case of V-groove quantum wires where an exponential dependence of the radiative time with temperature has been observed.[31]

The previous analysis of sample QPs-E allows to draw a simple picture of the levels involved in the exciton dynamics, namely the recombining level F and the two trap levels N_1 and N_2 (Figure 6.17b). The recombining level can be considered of near free excitons since, as mentioned before, they suffer from the presence of alloy disorder and interface roughness but still keeping a characteristic 1D-like density of states.[30, 34] With pulsed excitation, the barrier level is energetically too far from the ground level to play any role in the dynamics apart from the initial injection of carriers into

the QPs, although with CW excitation it is the one that finally quenches the PL signal.

Sample QPs-F: Higher In content

A similar analysis of the exciton dynamics can be performed in sample QPs-F. Figures 6.18a and b shows the results of the PL measurements with increasing excitation power and temperature, respectively. As it can be seen, the PL band broadens towards the high energy side and the maximum intensity of the signal follows approximately a linear tendency with excitation power (Figure 6.18a, inset). This behaviour is identical to that observed in sample QPs-E which would indicate that sample B can also be described by a 1D-like density of states.

In turn, the dependence of the PL signal for increasing temperature indicates a quench of the the emission while the band red-shifts. The integrated PL intensity (Figure 6.18b, inset) can also be fitted with Equation 6.1, giving E_1 = 13 meV, E_2 = 49 meV, A=9.4 and B=1150. These values are of the same order than those found for sample QPs-E.

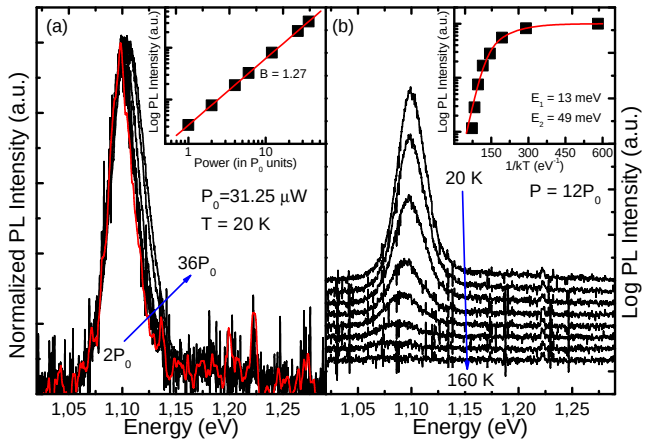

Figure 6.18: PL spectra of sample B as a function of (a) excitation power and (b) temperature. The insets show the maximum PL intensity in both series and a fit to a linear dependence and a two activation energy Arrhenius equation, respectively.

As mentioned before, the TRPL decay of this sample can be

deconvoluted with two exponentials. In Figure 6.19 we show the experimental and deconvoluted curves and the resulting decay times of the two components as a function of the excitation power. The fast component shows a decay time τ_F ranging from 0.15 to 0.55 ns whereas the slow component τ_S ranges from 0.7 to 1.5 ns (Figure 6.19b, filled symbols). In both cases, the decay is faster at low power, increasing slightly with the excitation intensity. The contribution of each component to the PL can be obtained by integrating the corresponding exponential decay in one period ($P = 25$ ns). If A_F and A_S are the prefactors of the fast and slow exponentials, respectively, their contribution to the overall PL signal are:

$$I_{PL}^{F(S)} = \int_0^P A_{F(S)} e^{-\frac{t}{\tau_{F(S)}}} dt \tag{6.7}$$

The results, shown in Figure 6.19c (filled symbols), indicate that both components have comparable contribution to the PL signal at low power but the fast component becomes more relevant when the excitation intensity is increased, given the smaller slope found for the former and its apparent saturation at high powers. At maximum power the decay is governed mainly by that fast component.

When we analyse the TRPL dependence with temperature, using again a two exponential deconvolution (Figure 6.20), we observe that the resulting decay times becomes smaller at high temperatures. Contrary to sample QPs-E, in this case the reduction of the decay times begins at the lowest temperatures, without a increasing or, at least, constant region at the beginning.

An analysis similar to that applied in sample QPs-E can be done using the contribution of each component to the integrated TRPL as a function of temperature. Figure 6.20c shows the temperature evolution of I_F and I_S, of their sum (I_F+I_S) and of the PL intensity as obtained with the CW detector. As in the power series, the slower component contribution becomes less important when temperature is increased, being clearly dominant the fast component at high temperatures. As expected, the results derived from the TRPL integration closely follow the PL intensity obtained with the CW detector, confirming that the latter can be derived from the former.

With this information, we can use Equation 6.2 to Equation 6.5 individually with each component to extract all the parameters that

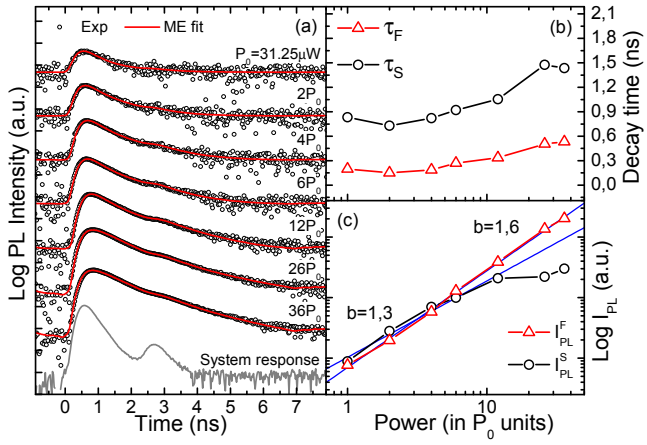

Figure 6.19: (a) TRPL measurements and their deconvolution using two exponentials as a function of excitation power. (b) The resulting decay times and (c) the associated PL intensity of each component found by integration of the exponential decays. The slope of each curve, result of a linear fit of the low power region, is indicated next to them.

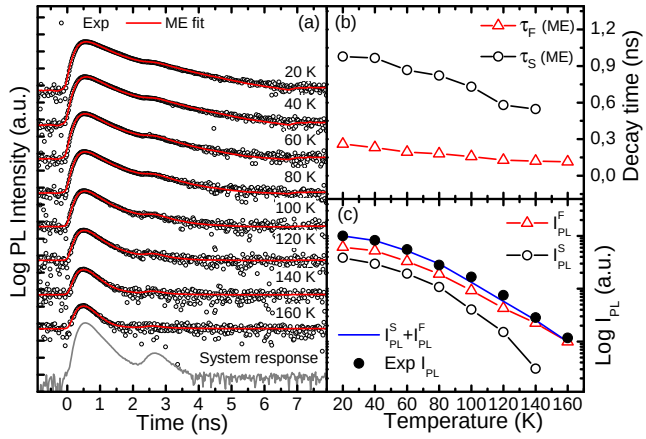

Figure 6.20: (a) TRPL measurements and their deconvolution using two exponentials as a function of temperature. (b) The resulting decay times and (c) the associated PL intensity of each component found by integration of the exponential decays. Squares represent the experimental total integrated PL intensity.

characterized the decay in these nanostructures. The slow component is reproduced straight forward, using the same assumptions than in sample QPs-E, namely pure radiative decay at low temperature and two thermally activated, non-radiative scape paths (Figure 6.21a). The behavior of the decay time of the fast component with temperature, on the other hand, suggests that there is a non-radiative contribution even at the lowest temperatures, which prevents using Equation 6.2 directly. To overcome this limitation, we assume that the radiative lifetime at 20 K is the same that for the slow component, $\tau_R^F(20\text{K})=\tau_R^S(20\text{K})$, and that a temperature independent, non-radiative decay τ_C is also present. This assumption will be justified later in the light of the results. The value of τ_C is then given by:

$$\frac{1}{\tau_C} = \frac{1}{\tau_F(20K)} - \frac{1}{\tau_R^F(20K)}, \tag{6.8}$$

leading to $\tau_C = 0.36$ ns. Since τ_C is temperature independent, now we can calculate the radiative lifetime τ_R^F of the fast component at any temperature using Equation 6.2 by replacing τ_d with τ_F and $1/\tau_R$ with $1/\tau_C+1/\tau_R^F$. The overall decay time as a function of temperature will be given by:

$$\frac{1}{\tau_F(T)} = \frac{1}{\tau_C} + \frac{1}{\tau_R^F(T)} + \frac{1}{\tau_{NR}^F(T)} \tag{6.9}$$

The result of this analysis can be seen in Figure 6.21b, together with a fitting of τ_{NR}^F to Equation 6.4 and of τ_R^F to Equation 6.5. The fitting parameters are compared with the slow component and with those obtained for QPs-E in Table 6.2.

As it can be seen, the parameters of the three components (one in sample QPs-E and two in sample QPs-F) are very similar indicating that we are working with the same kind of nanostructures. In all cases, we find a radiative time τ_R^0 of around 0.8-0.9 ns with an exponential increase with temperature, in agreement with reported results in quantum wire structures under the influence of disorder and inhomogeneities.[31] The thermally activated scape paths are also comparable, being the main difference the existence of a temperature independent, non-radiative scape in the fast component of sample QPs-F. These similarities justify the assumption made before of considering the radiative recombination at low temperature equal in both components. It implies that there are two

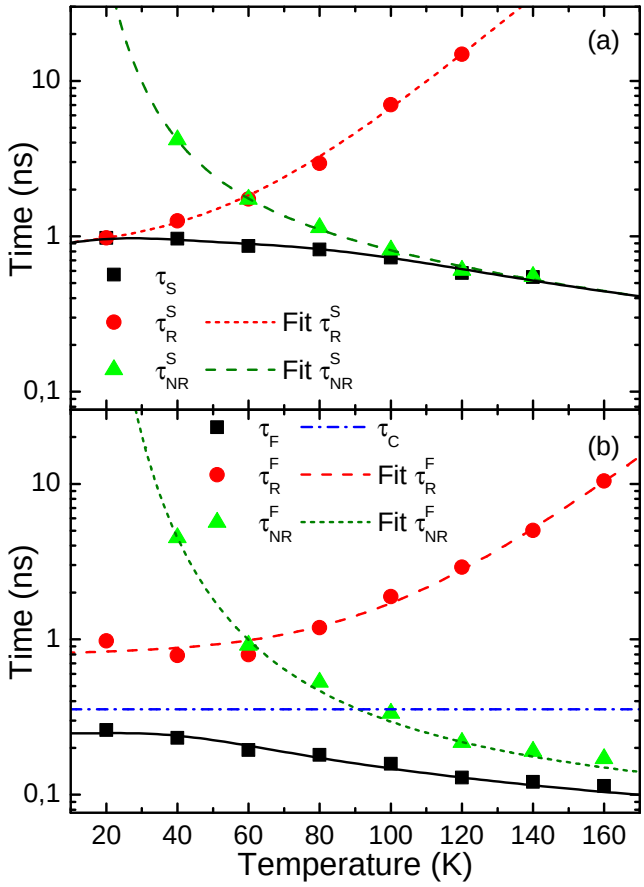

Figure 6.21: Experimental decay times (squares) and their fitting for the (a) slow and (b) fast component in sample QPs-F.

QPs families with similar optical properties but one of them, the most numerous, containing defects or dislocations inside the nanostructures that quenches the PL signal. This also explains the lower PL intensity observed of sample QPs-F compared to sample E.

A different interpretation compatible with the experimental results is that of free/localized excitons. In that picture, there are two excitonic levels. The first level corresponds to "near free" excitons and is extended in the whole length of the QPs; the second level is consequence of size or

Table 6.2: Values of the parameters used to fit the TRPL data of samples QPs-E and F.

Parameter	**QPs-E**	**QPs-F**	
		Slow	Fast
τ_R^0 (ns)	0.9 ± 0.3	0.8 ± 0.1	0.8 ± 0.1
C (ns)	0.14 ± 0.1	0.08 ± 0.02	0.018 ± 0.006
T_C (K)	46 ± 8	23 ± 1	26 ± 2
τ_1 (ns)	1.31 ± 0.06	0.31 ± 0.04	-
E_1 (meV)	6.4 ± 0.2	6.2 ± 0.3	-
τ_2 (ns)	0.011 ± 0.002	0.1 ± 0.1	0.048 ± 0.005
E_2 (meV)	46 ± 2	30 ± 20	15.6 ± 0.4
τ_C (ns)	-	-	0.36

composition modulations along the QPs that creates regions with smaller bandgap and, hence, few meV more confined that the former. Both levels are in thermal equilibrium and excitons tend to fall to the localized level or be thermally promoted to the free level if temperature permits. This picture has been used, for example, by Fuster *et al.* to explain the observed behavior of the TRPL in InAs/InP QWRs. If this were the case, the decay times and their contribution of each of the components to the PL as a function of power and temperature could be similar to that observed in our experiments.

In order to asses or discard this alternative interpretation, we have measured the TRPL decay transients at different energies across the PL band. As it can be seen in Figure 6.22b, the decay times of each component become longer in the low energy side of the peak and shorter in the high energy side compared to their values at the maximum. Meanwhile, the associated PL intensity calculated with Equation 6.7 shows that both components have similar contribution to the PL in the whole energy range with the maximum at the same energy (Figure 6.22a).

In the free/localized excitonic picture it would be expected for the slower component, associated to localized levels, to dominate the low energy tail of the emission band and the fast component the high energy side. The results shown in Figure 6.22a indicate that the ratio of both components does not change with the emission energy, thus supporting

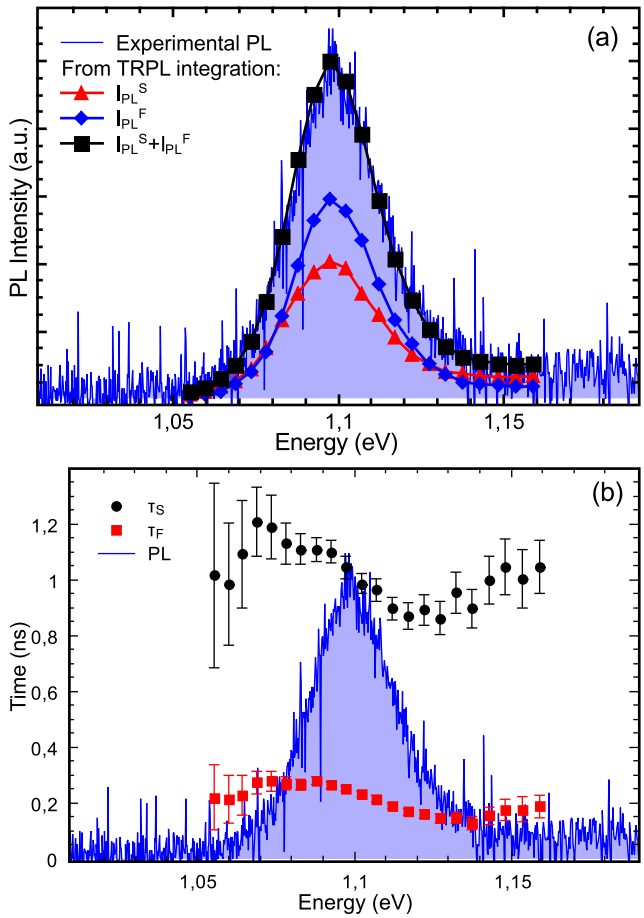

Figure 6.22: (a) Comparison of the experimental PL and the integrated TRPL of the two components as a function of the detection energy. (b) Decay times of the two components as a function of the detection energy.

their assignment to two QPs families with different non-radiative paths. The evolution of the decay times for each component as a function of the emission energy, in turn, supports that each of these families have their own "localized" and "free" excitons that produces the observed dependence on the energy and also the exponential increase of the radiative lifetimes..

Summary of results

In this section we have analysed in detail the optoelectronic properties of long strain balanced QPs. Our results indicate that the quality of these QPs is very sensitive to the In content in the superlattice, as it has been shown by TEM and the carrier recombination measurements. The interpretation of this data suggest that even in sample QPs-E, which has superior quality compared to sample QPs-F, defects play an important role in carrier dynamics.

In particular, we have seen that our QPs have a narrow photoluminescence whose asymmetric high energy broadening with increasing excitation power suggest the existence of a 1D-like density of states as a result of their elongated shape.

Time resolve experiments point to a radiative time at low temperature of around 1 ns, in agreement with other QPs structures, and have revealed the existence of non-radiative scape mechanisms related with the presence of defects in the structure which might be present even at low temperatures if an excessive amount of In is used in the superlattice.

6.3.4 PL and TRPL *vs* applied bias

Among the interests of QPs is the expected longer radiative lifetime but, as shown in the previous analysis, the values found are of the same order than those of normal QDs. One of the reasons for this discrepancy between the results expected and those obtained might be the presence of temperature independent non-radiative channels due to defects and inhomogeneities that lower the decay time of the PL and mask the real radiative lifetime, as it happened with the fast component of sample QPs-F. Another reason might be related with the presence of a tunneling component that reduces the decay time at low temperatures.

In order to study this second possibility we have performed PL and TRPL measurements on sample QPs-E as a function of the applied bias to the device. In Fig. 6.23 it can be seen the PL emission for bias voltages ranging from 1.4 V to -2 V. The main emission band monotonously quenches as reverse bias increases. The secondary band also becomes weaker but more slowly than the main band, resulting in emission only from the former at large negative voltages. We have fitted these spectra

with three Gaussian components of constant energy position (1.16, 1.19 and 1.28 eV) and width (28, 67 and 86 meV). The first two components intends to reproduce the main emission band, one the main peak and the other the asymmetry. No physical meaning is attributed to the latter, being just a mathematical tool. The third component fits the band at 1.28 eV. As it can be seen in the inset, the main band quenches faster than the second band, as pointed out before, also becoming the asymmetry smaller as we reduce the voltage. This behaviour of the asymmetry is the expected for excited states, where carriers can be more easily extracted by tunnelling. The small dependence on the voltage of the second, higher energy band suggest that its origin relies on QDs from the seed layer which are less polarizable by the electric field due to their more shallow height.

The energy position of the bands barely changes which, in principle, is surprising given the large polarizability expected in this kind of nanostructures. At a positive bias of 1.4 V, the PL signal overlaps with EL, indicating the beginning of the injection of carriers from the contacts.

The narrow high energy band does not change with the applied voltage. Given the energy position (1.54 eV) it can not correspond to conduction band to acceptor levels transitions, as we concluded in some samples of the previous chapter, but rather to recombination in the top/bottom AlGaAs/GaAs interfaces.

Time resolved decay transients are recorded at the maximum of the main emission band (1.16 eV) and shown in Figure 6.23b. The TRPL analysis reveals two components (Figure 6.24a). The first one is characterized by a time constant of around 1.15 ns that rapidly reduces to few hundred picoseconds with increasing reverse bias. The second component is slower and only visible for biases smaller than 0.6 V. Its time constant ranges from 2 ns to around 0.9 ns. As it can be seen in the figure, its evolution suggest that this component might also be present for voltages larger than 0.6 V but with a time constant too large to be revealed with the TRPL experimental conditions used. The contribution to the PL of each component can be obtained by integrating them in one period, as before. In Fig. 6.24b, it can be seen that the first component dominates the emission except for the lowest biases, when it becomes comparable to the second component. The experimental PL intensity and the integrated TRPL are in good agreement, with only small differences in the low bias

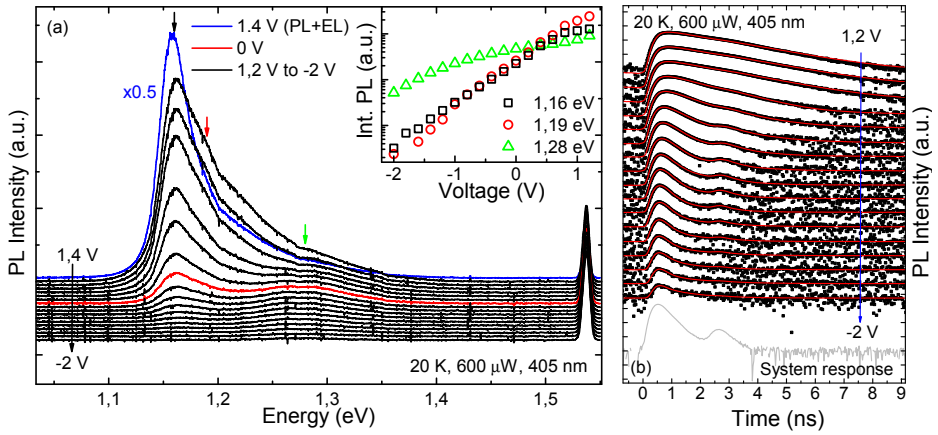

Figure 6.23: (a) PL spectra as a function of the applied voltage. The 1.4 V spectrum have contribution from the photoluminescence and the electroluminescence (EL). The inset shows the integrated Pl intensty of the three Gaussian components the spectra are fitted with. (b) TRPL decay curves (squares) and their deconvolution using one/two exponentials (red line).

range that might be attributed to the noise of the PL signal.

Assuming that at 1.2 V the PL decay is only due to radiative recombination, we can calculate the radiative τ_R and non-radiative τ_T lifetimes as a function of bias, in a similar way that has been done with the temperature. Only the first component is considered in this case. Both lifetimes are plotted in Figure 6.24c as a function of the electric field, assuming a built-in voltage of 1.51 V and a thickness for the neutral region of 237 nm (nominal value according to the structure). The radiative lifetime increases very slowly up to 100 KV/cm^2 and then the increase becomes much faster, reaching 18 ns at 148 KV/cm^2. The non-radiative lifetime, on the other hand, decreases with increasing electric field as one would expect for tunnel scape. Assuming a Fowler-Nordheim tunneling process, the experimental values can be fitted by:[7]

$$\tau_T = \frac{2m_e^* L^2}{\hbar\pi} exp\left[\frac{4}{3}\sqrt{\frac{2m_e^*}{\hbar^2}}\frac{E_{ion}^{3/2}}{eF}\right] \tag{6.10}$$

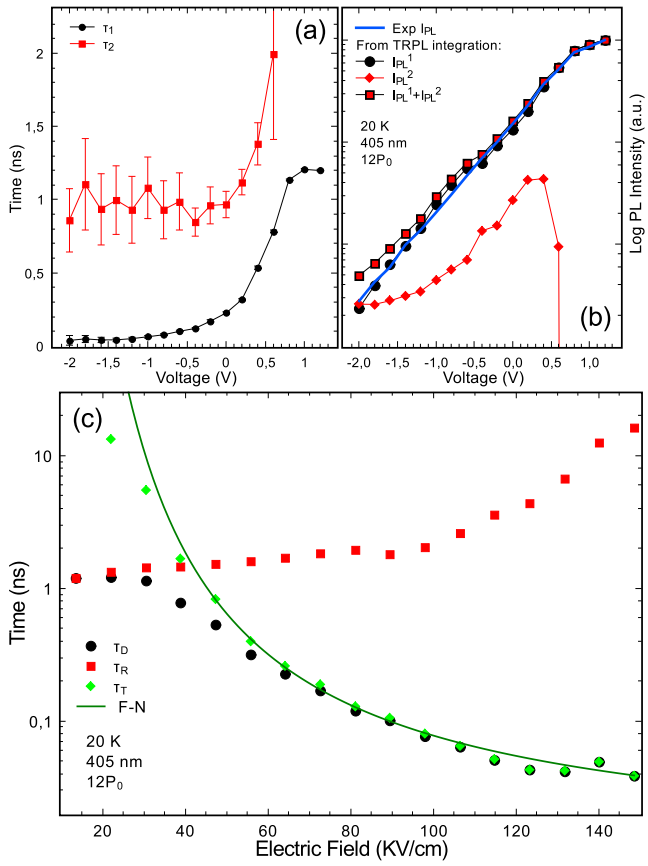

Figure 6.24: (a) Decay time as a function of voltage found for the main emission band. (b) Experimental PL and integrated TRPL of the two components. (c) Decomposition of the decay time (only fast component) in radiative and non-radiative (tunnel) components as a function of the electric field, together with a fit to the Fowler-Nordheim tunneling expression (Equation 6.10).

where m_e^*, L and E_{ion} are the electron effective mass, the length of the confining potential and the ionization energy, respectively. We consider that electrons are those that tunnel out of the nanostructures due to their smaller effective mass. If we take m_e^*=0.067m_0, from the fit of the experimental data we obtain L=159.7 nm and E_{ion}=52.2 meV. The value of L is in reasonable agreement with the observed length of the QPs

in transmission electron microscopy images (∼120 nm). The ionization energy, despite its small value, is also consistent with the activation energy found in the temperature analysis under pulsed excitation, where we obtained $E_2 = 46$ meV.

It is remarkable that if the effective mass used in the analysis is increased to m^*=$0.11m_0$ this match between parameters is even better (L=125 nm and E_{ion}=44 meV). This effective mass is accessible if we consider that holes are those that tunnel out of the nanostructures, instead of electrons. In particular, a combination of heavy and light holes with more contribution of the latter will easily lead to this effective mass. Since holes drift towards the upper part of the device due to the electric field, and given the small ionization energy, we believe that the scape might correspond to trap assisted tunnelling, and not direct tunnelling to the GaAs barrier (Figure 6.25). In that case, the energy barrier that carriers must surpass in order to scape from the QPs is smaller than in direct tunnelling and given by $E_b = E_0 - E_T$, where E_0 is the localization energy of carriers and E_T the energy of the trap levels below the band edge. This trap levels are very likely to be also responsible for the PL quenching with increasing temperature, as explained before.

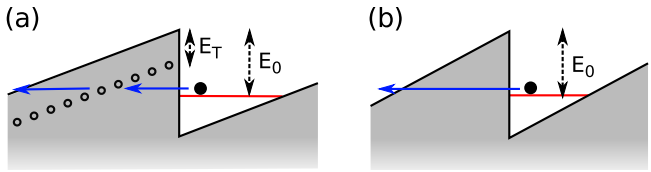

Figure 6.25: Schematic representation of the (a) trap assisted and (b) direct tunnelling processes.

The deduced radiative lifetime and the emission energy with the electric field do not show the large polarizability expected for a QP, larger in principle than in a QD where we have observed Stark shifts of 10-30 meV, as shown in Figure 5.18. We tentatively attribute the insensitivity to the electric field to the weak localization of carriers inside the post.

The second component follows the same functional dependence that the first one but with much larger radiative time. It is unclear within the present context whether this is a consequence of a larger localization of electron and hole in separated regions of the QPs or not. If this were the

case, the second component might be related with a family of QPs with better homogeneity and crystal quality in which the tunnelling through trap levels is thus suppressed.

6.3.5 Photocurrent spectroscopy

In order to asses the absorption capabilities of these QPs structures we have also performed photocurrent spectroscopy. In Figure 6.26 we show the resulting measurements for samples QPs-E y QPs-F at room and low temperatures. As it can be seen, both samples have intense PC below the GaAs absorption edge, indicating both efficient absorption of photons and collection of the photogenerated carriers by the electric contacts.

When we decrease the temperature, the curves blue-shift as expected due to the bandgap increase, but the contribution to the PC below the absorption edge is essentially the same. This means that the light absorption and carrier collection efficiency are the same at low temperature indicating that the process that dominates the latter is tunnel scape from the nanostructures, not thermal scape. The situation is comparable to that we found in sample QDs-D (Figure 5.21), where there was very little increase of the PC for increasing temperature, and opposite to that of sample QDs-G (Figure 5.38), where decreasing the temperature completely suppresses the PC from the QDs.

Below the GaAs edge, the low temperature curves show two clear humps, at 1.17 and 1.28 eV in sample QPs-E and at 1.1 and 1.23 eV in sample QPs-F. Those features also appear in the low temperature PL signal, as shown in the spectra included for reference in each case. In sample QPs-E, the higher energy contribution appears as a well resolved, separated band whereas in sample QPs-F it is only a tail much less intense than the main band. The low energy transition, corresponding to the main PL band in both samples, is related with the ground level absorption in the QPs, whereas the secondary band corresponds to the contribution to small QDs on the seed layer that did not evolve in the form of QPs, given the analysis we performed in Section 6.3.3.

It is remarkable that in these samples there is no contribution around 1.44 eV (at low T) that could be related with a WL absorption, in contrast to what was observed in QDs samples. This result supports the idea that the individual WL of the InAs/GaAsP superlattice actually mix, leading

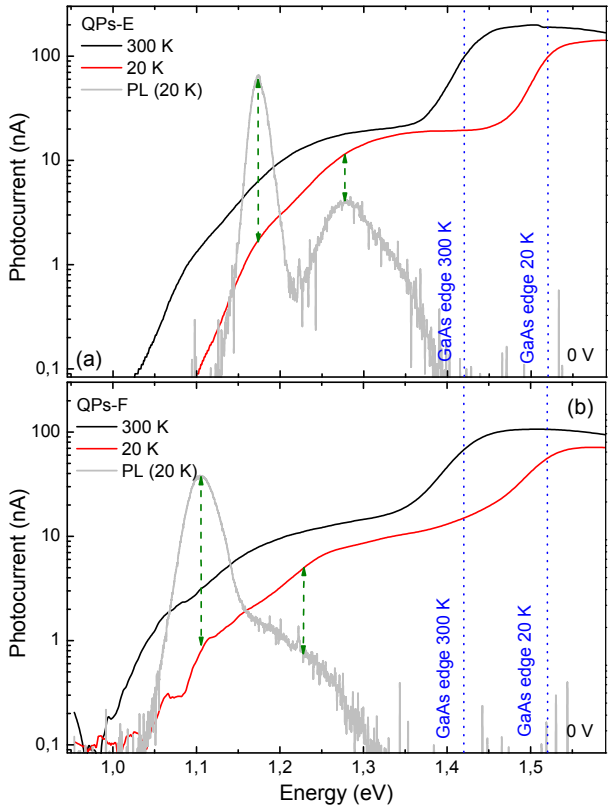

Figure 6.26: PC of samples (a) QPs-E and (b) QPs-F at room and low temperatures. Vertical dotted lines indicate the GaAs absorption edge at both temperatures. A PL spectrum is included in both cases as a reference.

to a more or less homogeneous alloy for the embedding matrix with an absorption edge very close or even above the GaAs edge, in agreement with the XRD analysis and the MOSS measurements.

We have performed PC measurements as a function of the applied bias in sample QPs-F in order to asses the scape mechanism from the nanostructures. In Figure 6.27 we show the resulting PC curves for voltages between 0.6 and -1 V. As it can be seen, as we apply a positive voltage, PC coming below the GaAs edge rapidly quenches, indicating a strong reduction of the scape probability from the nanostructures. The opposite

behaviour is found for negative biases, when the electric field is increased and the carriers that had not escaped from the QPs yet are finally collected.

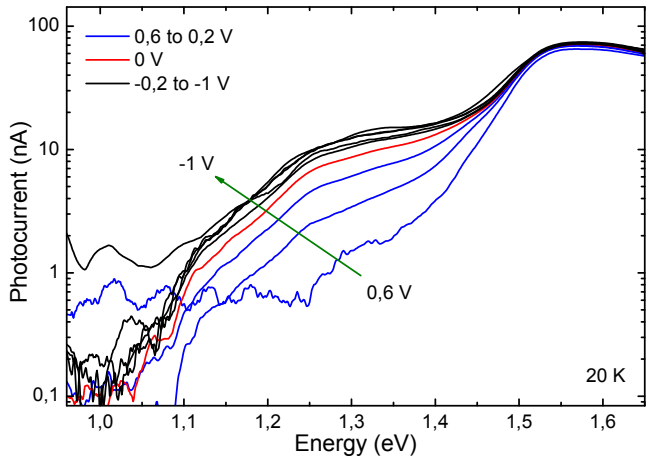

Figure 6.27: Low temperature PC as a function of applied bias of sample QPs-F.

The high dark current of these devices prevented the application of larger voltages, leading also to very noisy spectra, but from the curves shown in Figure 6.27 both limiting cases, saturation of the PC with negative bias and its quenching at positive ones, are clearly seen. This points out to the strong dependence of carrier extraction with electric field in these samples, which in turn might be related with the elongated shape of the nanostructures.

6.4 PL polarization anisotropy in strain balanced QPs

Most of the research performed so far on QPs is aimed to the development of polarization insensitive edge emitting or absorbing devices with a perfect balance between TE and TM components. Such feature is highly desirable for QD-Semiconductor Optical Amplifiers (QD-SOAs). In a seminal work, Kita *et al.* observed that the TE/TM ratio inverts in stacks comprising 8-9 QD layers.[9] Similar studies have been performed on InAs/InP columnar quantum dashes targeting at emission at the telecommunication windows

(1.3 and 1.5 um).[35, 36] It is worth noting the important role played by the strain fields in these developments, since the same inversion was obtained by Jayavel et al. by the deposition of a strain reducing layer on top of a single QD layer with no further stack.[37]

The change of the polarization from TE to TM mode has been carefully studied by Saito et al.[38] As the number of staking layers increases, the biaxial strain component at the centre of the QP changes sign, from a positive value to a negative one. Under these strain conditions, the valence band ground state acquires a light hole character instead of heavy hole one. As a results of this bulk band inversion, the light hole contribution to the hole states of the QPs is not negligible any longer and TM transitions might become dominant. On top of that, the compositions of the stack layers also plays an important role, being necessary a minimum compositional contrast between the QPs and the surrounding matrix to achieve the TE/TM inversion.[39] The relative weight between TE and TM emission results of a trade-off between the splitting of the heavy hole and light hole band edges and the relative contribution of each band to the hole ground state character. Such interplay can be engineered to obtain TE/TM polarization insensitive optoelectronic devices.[40]

In this section we thus analyse the polarization properties of strain balanced QPs. We will show only the experiments corresponding to sample QPs-E but sample QPs-F has also been measured with identical results.

6.4.1 Polarization set-up

The polarization characteristics of the light emitted by the QPs can be assessed by introducing a Glan-Thomson prism and a $\lambda/2$ wave-plate between the sample and the monochromator (Figure 6.28). When light coming from the sample reaches the wave-plate, the phase between the two perpendicular polarization components is shifted by $180\,^{\circ}$. As a result, the polarization state of the light on the other side of the wave-plate is rotated by a certain angle with respect its state at the beginning. This rotation angle is double the angle between the fast axis of the wave-plate and the polarization direction of the incoming light.

The Glan-Thomson prism serves to filter the rotated light in such a way that only the component parallel to the extraordinary axis crosses the prism and reaches the monochromator. By rotating the wave-plate

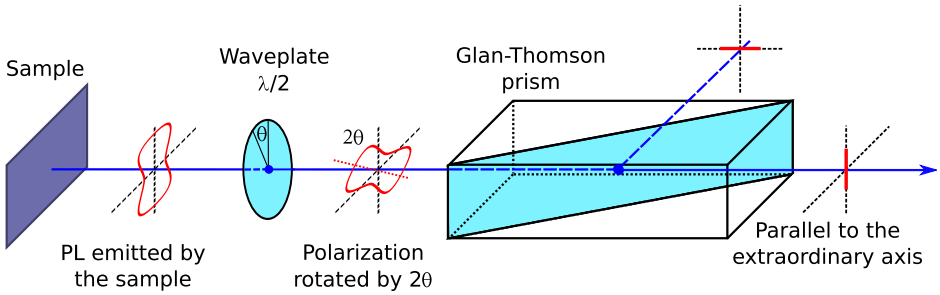

Figure 6.28: Schematic representation of the polarization setup which shows the wave-plate and the Glan-Thomson prism inserted between the sample and the monochromator.

between 0 and 180 ° we can measure the intensity of the light transmitted for linear polarization angles between 0 and 360Â° and thus the linear polarization anisotropy degree of the incoming light.

6.4.2 Experimental results

Depending on whether we consider the light emitted in the growth direction or though the cleaved edge of the sample, we introduce the following linear polarization anisotropy degrees:

$$P_{[001]} = \frac{I_{[1\bar{1}0]} - I_{[110]}}{I_{[1\bar{1}0]} + I_{[110]}} \quad \text{and} \quad P_{\text{edge}} = \frac{I_{\text{TE}} - I_{\text{TM}}}{I_{\text{TE}} + I_{\text{TM}}}, \tag{6.11}$$

respectively. For P[001] excitation and collection of the PL is perpendicular to the growth plane. For Pedge, the PL is excited through the growth plane near the sample edge and collected through the sample cleaved edge.

In Figure 6.29a, two PL spectra collected along the vertical axis of the QPs are shown with polarization vectors along the $[1\bar{1}0]$ and [110] crystal directions, respectively. The lower part of the figure shows the corresponding normalized polar diagram obtained varying the wave-plate angle in our sample and in a reference sample containing standard InAs QDs. The diagrams are fitted with:

$$I_{\text{PL}} = I_{0^\circ} \cos^2\theta + I_{90^\circ} \sin^2\theta \tag{6.12}$$

where I_{0° and I_{90° are the normalized PL intensities in the two perpendicular directions.

As it can be observed, the QPs luminescence emitted in the growth direction is strongly linearly polarized along the $[1\bar{1}0]$ direction, $P_{[001]}$ = 84%. The polarization anisotropy degree drops as we deviate from the main emission peak. For the secondary peak, although still noticeable, the anisotropy is half the value at the maximum. Similarly, in Figure 6.29b we show the polarization properties of light emitted through one of the sample edges, along the $[1\bar{1}0]$ direction. As it can be seen, the TM mode is dominant in the whole wavelength range, leading to a maximum P_{edge}=-63% in the QPs band which drops to -40% in the secondary band.

The axis of the QPs defines a preferential direction along which there is a greater polarizability of the electron-hole dipole.[7] Therefore, TM polarized emission can be expected for light emitted through the edge, as we observe experimentally along the $[1\bar{1}0]$ azimuth (P_{edge}=-63%).[9] This is the expected behaviour in QPs, which have a vertical, elongated shape and whose strain properties lead to a hole ground state with large light hole (LH) projection.[40]

Surprisingly, the prediction fails in the [110] azimuth where P_{edge} is 27% (Figure 6.29c), meaning that the TE component dominates over the TM component for light emitted through the edge in such direction.

The differences observed between both edges is in agreement with the large polarization anisotropy observed in the growth direction ($P_{[001]}$ = 84%). It is well known that InAs/GaAs QDs usually have an elongated shape in the $[1\bar{1}0]$ direction.[41] This anisotropy is also found in our QPs, with average shapes of 34×19 nm. Although there is no precedent in the literature for such an effect to produce an 84% percent degree of polarization by itself (commonly it is between 15% and 30% at most) it can account for the large $P_{[001]}$ found in our experiments, as it can be seen in Figure 6.30.[42, 43] In the figure we show the calculated polarization anisotropy degrees of an infinitely long QPs (a vertical quantum wire) in the three perpendicular directions for different in-plane anisotropies using the 8×8 $\boldsymbol{k}\cdot\boldsymbol{p}$ method. We use a QP with lateral dimensions around those found by planar TEM and made of $In_{0.75}Ga_{0.25}As$. The surrounding matrix is a homogeneous $In_{0.15}Ga_{0.85}As_{0.85}P_{0.15}$ alloy. Both compositions have been extracted from XRD, MOSS and the ground state energy observed in

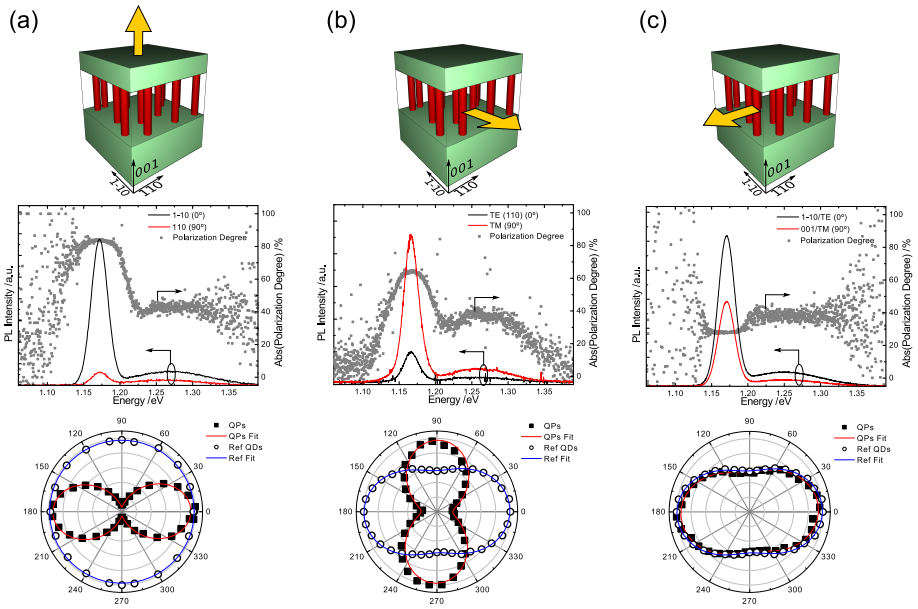

Figure 6.29: (a) PL spectra collected in the growth direction, (b) in one sample edge ($[1\bar{1}0]$ azimuth) and (c) in the other sample edge ([110] azimuth). Grey squares indicate the polarization anisotropy. The lower part of the figures show polar diagrams of the PL intensity for varying linear polarization angles in our sample (solid squares) and in a reference sample (hollow circles). The continuous lines are fits to a sinusoidal dependence.

PL. As it can be seen, the polarization anisotropy in the growth direction rapidly increases as the QP becomes elongated in the [1-10] direction, from unpolarized emission when the QP cross-section is perfectly circular to values as high as 80% for a a/b ratio of 2. This result would be in reasonable agreement with our experimental result of $P_{[001]} = 84\%$, given the experimental in-plane anisotropy of $a/b \sim 1.8$.

This calculations are not so good in predicting the polarization of light emitted through the edges of the sample, in which we find $P_{[1\text{-}10]} = -63\%$ and $P_{[110]} = 27\%$. In Figure 6.30, it can be seen that both polarizations are dominated by the TM component and equal to P= -83% if a circular section for the QPs is considered. However, as the in-plane anisotropy increases, $P_{[1\text{-}10]}$ becomes smaller (down to -94% at $a/b \sim 2$) whereas $P_{[110]}$ increases (up to -62% at $a/b \sim 2$). The trends of the curves suggest

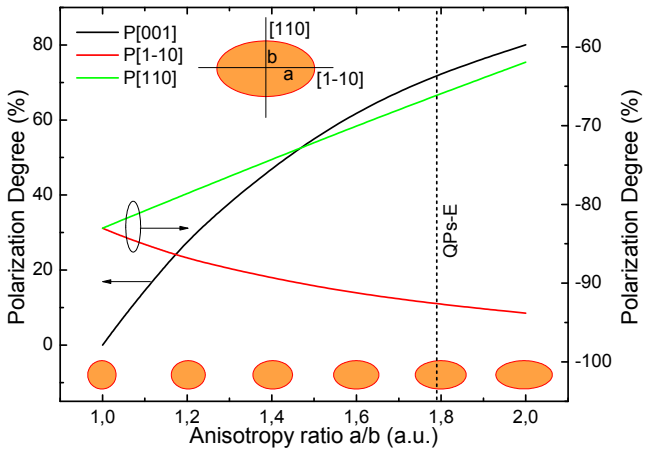

Figure 6.30: Calculated polarization degrees as a function of the in-plane anisotropy for the three perpendicular directions [001], [1-10] and [110] of the emitted light. The inset shows the cross-section of the QP, indicating the elongation direction and the axes. Calculations performed by Dr. José M. Llorens.

that eventually, for an anisotropic enough QPs, the latter component might become positive, indicating that the TM mode is no longer dominant over the TE mode. That would be the case in columnar quantum dashes studied by Sek.[43] Such intermediate situation, with TM dominant in one azimuth and TE dominant in the other, has also been found by Yu *et al.* in closely stacked QDs layers and also attributed to the elongation of the QDs in one direction.[44]

The effect in-plain anisotropy of the QPs we have just described is a factor that also influences the polarization properties of not strain balanced QPs. However, there is another contribution that becomes very relevant in strain balanced ones, namely the self-lateral ordering and composition fluctuations that take place in short period superlattices and some ternary compounds.[42, 45, 46] It is found that the strong anisotropic strain in these structures affects the valence bands mixing in QDs embedded in them, leading to a polarization anisotropy of up to 40% for light emitted in the growth direction, even with almost symmetric QDs.[42] It is clear that this band mixing will have also an effect on the polarization properties of the nanostructures for light emitted through the edges,

although no experimental or theoretical results of it have been reported. From qualitative considerations, and given the results of Hong-Wen *et al.*, it would be expected that light emitted in the [110] direction were more TE polarized that the one emitted in the [1-10]. Extrapolating the interpretation to our case, this would result in the theoretical $P_{[110]}$ increasing and even becoming positive, in closer agreement with our experimental values.

Finally, an important contribution might be related to the particular microscopic structure of the interfaces in the superlattice. It has been shown that the bonds present in no common atom interfaces (such as GaP/InAs or InAs/GaSb) lack of a rotoinversion fourfold symmetry axis. [47, 48] This property is behind the polarization anisotropy of up to 50% that is often observed for light emitted perpendicular to such interfaces in superlattices. This effect would scale with the number of interfaces and hence it might be of special relevance in our case.

6.4.3 Impact on the design of devices with polarization control

The polarization properties of our strain balanced QPs suggest their exploitation in several optoelectronic devices.

Polarization sensitive devices

The first application is related with the extraordinary polarization anisotropy in the growth direction, $P_{[001]}$=84%.

It is commonly found in vertical-cavity surface-emitting lasers (VCSELs) that the polarization of the emitted light is either unpolarized or linearly polarized but with a random orientation in the plane.[49–51] Polarization control in such devices is important because the systems in which they are used, such as magneto-optical disks or coherent detection systems, use polarization-sensitive elements such as beam splitters.

The desired polarization control has been achieved to date by artificially manipulating the optical gain or the field coupling between the laser cavity and the active media. Some approaches use anisotropic transverse cavity geometries, or the application of internal or external stress occurring from an elliptical hole etched in the substrate side to define

a preferred crystallographic polarization direction.[51, 52] Others directly use coatings with differential loss on the sides of the upper distributed Bragg reflector to maintain polarization in a given crystal direction.[50]

Using QPs similar to those presented in this work as the active media of the laser structure automatically produces light emitted in the vertical direction with a well defined polarization direction ([1-10]) thus allowing a simplification of the laser design. Additionally, using QPs would probably increase the performance of the laser and reduce the threshold current, as it has been observed in both edge and surface emitting nanostructure-based lasers.[53–56]

Polarization independent devices

Finally we address the impact that using phosphorus in QPs growth has in the design and fabrication of devices where a gain polarization independence is desirable, such as SOAs.

We have seen in the previous sections that the growth of very large QPs using the strain balanced technique is a feasible process that leads to characteristic carrier recombination and polarization properties. However, one often is interested in achieving a structure without polarization anisotropy and excellent optical and crystal quality, situation in which large QPs might not be necessary. As already mentioned, Kita *et al.* have found that 8-9 periods of the superlattice, and a resulting aspect ratio of around 1, could lead to a balance of the TM and TE components.[9] In turn, Ridha *et al.* concluded that the conditions for achieving such balance where dependent not only in the aspect ratio but also on the compositional contrast between the QP and the surrounding matrix.[39]

Following Ridha's argumentation, in this last section we study from a theoretical point of view the effect of including phosphorus into the matrix. In a very simplified situation, the condition for achieving the TM/TE balance is that the HH and LH band edges were degenerate at the centre of the QP, situation that is found if the axial strain in such a place cancels. Using linear elasticity theory it can be seen that the strain distribution due to the QP inside a well can be treated as the sum of the strain distribution due to an $In_{X_w}Ga_{1-X_w}As$ quantum well (the matrix) plus that due to an $In_{X_p}Ga_{1-X_p}As$ QP, each embedded in a GaAs matrix.[39] This situation is modified in our case by using for the quantum

well an $In_{X_w}Ga_{1-X_w}As_{1-Y}P_Y$ alloy. The in-plane strain of the matrix will be given by $\epsilon_{xx} = \epsilon_{yy} = (a_w - a_{GaAs})/a_{GaAs} \equiv \epsilon_w$, with a_w and a_{GaAs} the lattice parameters of the well and the GaAs substrate, respectively. Given the well composition, the former could be expressed as:

$$\begin{aligned} a_w = \quad & a_{InAs}X_w(1-Y) + a_{GaAs}(1-X_w)(1-Y) \\ & + a_{GaP}(1-X_w)Y + a_{InP}X_wY \end{aligned} \tag{6.13}$$

with the a_i the corresponding lattice parameters of the constituent binary materials. If the In and P contents of the well are small ($X_w, Y \ll 1$), we can approximate the previous equation by neglecting the terms that contain the X_wY product, leading to:

$$a_w \simeq X_w(a_{InAs} - a_{GaAs}) + Y(a_{GaP} - a_{GaAs}) + a_{GaAs} \tag{6.14}$$

The resulting in-plain strain of the matrix results in:

$$\epsilon_w = \frac{a_w - a_{GaAs}}{a_{GaAs}} \simeq X_w\epsilon_{InAs} + Y\epsilon_{GaP} \tag{6.15}$$

with $\epsilon_{InAs} = (a_{InAs} - a_{GaAs})/a_{GaAs}$ and $\epsilon_{GaP} = (a_{GaP} - a_{GaAs})/a_{GaAs}$. The strain along the z-direction is given by $\epsilon_{zz} = -2\sigma\epsilon_w/(1-\sigma)$, with σ the Poison's ratio. The axial strain due to the $In_{X_w}Ga_{1-X_w}As_{1-Y}P_Y$ well, is then given by:

$$\epsilon_{ax} = \epsilon_{zz} - \frac{1}{2}(\epsilon_{xx} + \epsilon_{yy}) = -\frac{1+\sigma}{1-\sigma}\epsilon_w \tag{6.16}$$

In order to have zero net axial strain at the centre of the QP we require that the axial strain there due to the QP is equal and opposite to that due to the strained well. Treating the QPs as a cuboid of height h and base $b \times b$ and assuming isotropic elastic constants, the strain distribution of the cuboid can be calculated analytically and leads for the axial strain to:[39]

$$\epsilon_{ax} = -(\epsilon_p - \epsilon_w)\frac{1+\sigma}{1-\sigma}\left[1 - \frac{6}{\pi}\arctan\left(\frac{h}{\sqrt{2b^2 - h^2}}\right)\right] \tag{6.17}$$

with $\epsilon_p = (a_{QPs} - a_{GaAs})/a_{GaAs} = X_p\epsilon_{InAs}$ the in-plane strain of the QPs. Finally, combining Equations 6.16 and 6.17 under the condition of zero net

axial strain, calling $A(h,b)$ the term in square brackets and rearranging the terms, we obtain:

$$\frac{X_p}{X_w} = \frac{A(h,b)-1}{A(h,b)}\left(1+\frac{Y\epsilon_{GaP}}{X_w\epsilon_{InAs}}\right) \tag{6.18}$$

In Figure 6.31 we show the dependence of the In compositional contrast between the QPs and the barrier as a function of the aspect ratio of the QPs for several values of Y/X_w. The black curve corresponds to $Y = 0$ and represents the situation described by Ridha *et al.* of regular, not strain balanced QPs. As it can be seen, they found that a minimum compositional contrast of 3 (green, dotted line) was necessary in order to achieve the TM/TE balance, and that only for infinitely large QPs. The inclusion of P in the matrix has the important consequence of relieving such requirement. With increasing Y/X_w ratio, the curves shifts downwards allowing more flexibility in the choice of the compositional contrast and aspect ratio. As an example, the above contrast of 3 can lead to the TM/TE balance with QPs having an aspect ratio of only 1.8 if in the surrounding matrix is included as much phosphorus as indium $Y/X_w = 1$.

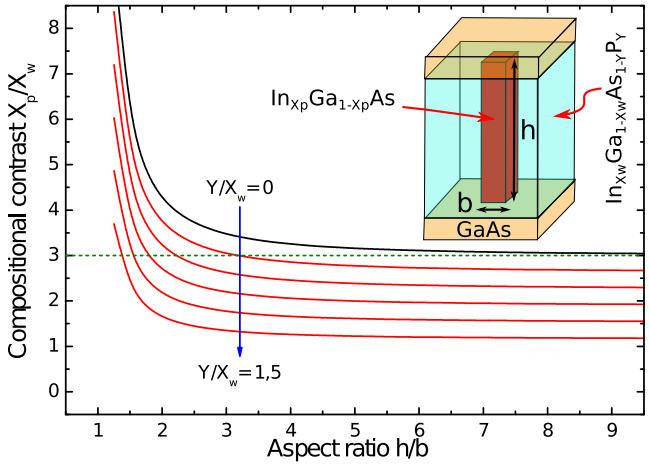

Figure 6.31: Calculated polarization compositional contrast needed to achieve the TM/TE balance as a function of the aspect ratio and the P to In ratio in the matrix.

The quantitative predictions of the above result are probably quite

different in a real system, given the amount of approximations we have made, however, we believe that the general trends described here as a result of including P in the matrix still hold. If we summarize the results we have obtain in this chapter on strain balanced QPs, we can see that using P for its fabrication could be very beneficial:

- The structure becomes partly strain balanced which should lead to better optical and structural properties and allow the fabrication of larger stacks of nanostructures without degradation.
- Phosphorus has a size filtering effect, as shown in Sections 5.2 and 6.2, which increases the homogeneity of the nanostructures and leads to narrower PL emission.
- Given that P alloys with the WLs of the superlattice, the bandgap of the matrix region around QPs increases which might lead to better thermal stability by partly preventing carrier scape from the nanostructures.
- The presence of P in the matrix favours the HH and LH bands mixing, allowing to reach the TM/TE balance with smaller QPs. This in turn, allows to increase the number of nanostructures that can fit in a given active region of a device.

Despite all this advantages, it should be noted that P also have some side effects, such as the possibly lateral composition modulation or the increase of the PL emission energy, which might be undesirable if long wavelengths are required.

6.5 Conclusions

In summary, our results on strain balanced QPs points out a number of interesting fundamental properties. On the one hand, we have shown that is feasible to fabricate QPs using the strain balanced technique. The addition of P leads to a blueshift of the QPs related PL signal, but also reduces the inhomogeneous linewidth by homogenizing the QPs sizes and prevents the formation of defects.

The fabrication of large nanostructures which exceed the size of any preceding result also becomes possible with this technique, demonstrating the growth of 120 nm high QPs. The analysis of the PL reveals that these structures have a 1D-like density of states, indeed, becoming similar to vertical quantum wires. The study of the carrier recombination dynamics indicate that, despite the strain balanced process, defect formation in the upper part of the structure is affecting the QPs properties. This suggest that an optimization of the growth conditions and the sample structure itself must be done in order to take advantage of the extraordinary length of this nanostructures.

Finally, the polarization properties of these large QPs have revealed large polarization anisotropy factors combining the expected increase in the TM component of the PL emitted by the edge of the sample with the effect of in-plane shape anisotropy with a possible composition modulation in the surrounding matrix or bond symmetry issues. Nevertheless, the effect of P in the polarization properties of QPs have been shown to be of capital importance in achieving nanostructures with TM/TE balance, which paves the way for the fabrication of polarization independent devices with improved characteristics.

Bibliography

[1] O. Demichel, V. Calvo, A. Besson, P. Noé, B. Salem, N. Pauc, F. Oehler, P. Gentile, and N. Magnea, "Surface Recombination Velocity Measurements of Efficiently Passivated Gold-Catalyzed Silicon Nanowires by a New Optical Method," *Nano Letters*, vol. 10, no. 7, pp. 2323–2329, 2010.

[2] O. Demichel, M. Heiss, J. Bleuse, H. Mariette, and A. F. i Morral, "Impact of surfaces on the optical properties of GaAs nanowires," vol. 97, no. 20, p. 201907, 2010.

[3] J. He, R. Nötzel, P. Offermans, P. M. Koenraad, Q. Gong, G. J. Hamhuis, T. J. Eijkemans, and J. H. Wolter, "Formation of columnar (In,Ga)As quantum dots on GaAs(100)," *Applied Physics Letters*, vol. 85, no. 14, pp. 2771–2773, 2004.

[4] J. He, H. J. Krenner, C. Pryor, J. P. Zhang, Y. Wu, D. G. Allen, C. M. Morris, M. S. Sherwin, and P. M. Petroff, "Growth, structural, and optical properties of self-assembled (In,Ga)as quantum posts on GaAs.," *Nano Letters*, vol. 7, no. 3, pp. 802–6, 2007.

[5] L. Li, G. Patriarche, M. Rossetti, and A. Fiore, "Growth and characterization of InAs columnar quantum dots on GaAs substrate," *Journal of Applied Physics*, vol. 102, p. 033502, 2007.

[6] P. Ridha, L. Li, M. Rossetti, G. Patriarche, and A. Fiore, "Polarization dependence of electroluminescence from closely-stacked and columnar quantum dots," *Optical and Quantum Electronics*, vol. 40, no. 2-4, pp. 239–248, 2008.

[7] H. J. Krenner, C. E. Pryor, J. He, and P. M. Petroff, "A semiconductor exciton memory cell based on a single quantum nanostructure.," *Nano Letters*, vol. 8, no. 6, pp. 1750–5, 2008.

[8] M. Sugawara, H. Ebe, N. Hatori, M. Ishida, Y. Arakawa, T. Akiyama, K. Otsubo, and Y. Nakata, "Theory of optical signal amplification and processing by quantum-dot semiconductor optical amplifiers," *Physical Review B*, vol. 69, no. 23, pp. 4–6, 2004.

[9] T. Kita, O. Wada, H. Ebe, Y. Nakata, and M. Sugawara, "Polarization-Independent Photoluminescence from Columnar InAs/GaAs Self-Assembled Quantum Dots," *Japanese Journal of Applied Physics*, vol. 41, no. Part 2, No. 10B, pp. L1143–L1145, 2002.

[10] L. H. Li, P. Ridha, G. Patriarche, N. Chauvin, and a. Fiore, "Shape-engineered epitaxial InGaAs quantum rods for laser applications," *Applied Physics Letters*, vol. 92, no. 12, p. 121102, 2008.

[11] P. Howe, E. Le Ru, E. Clarke, R. Murray, and T. Jones, "Quantification of segregation and strain effects in InAs/ GaAs quantum dot growth," *Journal of applied physics*, vol. 98, p. 113511, 2005.

[12] M. U. González, Y. González, and L. González, "Study of the relaxation process during InGaAs/GaAs (001) growth from in situ real-time stress measurements," *Applied Physics Letters*, vol. 81, no. 22, pp. 4162–4164, 2002.

[13] Y. I. Mazur, Z. M. Wang, G. G. Tarasov, V. P. Kunets, G. J. Salamo, Z. Y. Zhuchenko, and H. Kissel, "Tailoring of high-temperature photoluminescence in InAs-GaAs bilayer quantum dot structures," *Journal of Applied Physics*, vol. 98, no. 5, p. 053515, 2005.

[14] P. Alonso-González, J. Martín-Sánchez, Y. González, B. Alén, D. Fuster, and L. González, "Formation of Lateral Low Density In(Ga)As Quantum Dot Pairs in GaAs Nanoholes," *Crystal Growth & Design*, vol. 9, pp. 2525–2528, May 2009.

[15] J. T. Ng, U. Bangert, and M. Missous, "Formation and role of defects in stacked large binary InAs/GaAs quantum dot structures," *emicond. Sci. Technol.*, vol. 22, no. 2, pp. 80–85, 2007.

[16] G. Sek, P. Podemski, J. Misiewicz, L. H. Li, a. Fiore, and G. Patriarche, "Photoluminescence from a single InGaAs epitaxial quantum rod," *Applied Physics Letters*, vol. 92, no. 2, p. 021901, 2008.

[17] J. Matthews and A. Blakeslee, "Defects in epitaxial multilayers: I. misfit dislocations," *Journal of Crystal Growth*, vol. 27, pp. 118–125, 1974.

[18] E. Fitzgerald, "Dislocations in strained-layer epitaxy: theory, experiment, and applications," *Materials Science Reports*, vol. 7, pp. 87–142, Nov. 1991.

[19] M. González, Y. González, and L. González, "In situ detection of an initial elastic relaxation stage during growth of $In_{0.2}Ga_{0.8}As$ on GaAs(0 0 1)," *Applied Surface Science*, vol. 188, no. 1-2, pp. 128–133, 2002.

[20] N. Ekins-Daukes, K. Kawaguchi, and J. Zhang, "Strain-Balanced Criteria for Multiple Quantum Well Structures and Its Signature in X-ray Rocking Curves," *Crystal Growth & Design*, vol. 2, no. 4, pp. 287–292, 2002.

[21] J. Singh, *Electronic and optoelectronic properties of semiconductor structures*. Cambridge University Press, 2003.

[22] D. Fuster, J. Martínez-Pastor, L. González, and Y. González, "Exciton recombination dynamics in InAs-InP self-assembled quantum wires," *Physical Review B*, vol. 71, pp. 1–7, May 2005.

[23] K. Herz, G. Bacher, A. Forchel, H. Straub, G. Brunthaler, W. Faschinger, G. Bauer, and C. Vieu, "Recombination dynamics in dry-etched CdZnSe/ZnSe nanostructures: Influence of exciton localization," *Physical Review B*, vol. 59, no. 4, pp. 2888–2893, 1999.

[24] B. Alén, J. Martínez-Pastor, D. Granados, and J. M. García, "Continuum and discrete excitation spectrum of single quantum rings," *Physical Review B*, vol. 72, p. 155331, Oct 2005.

[25] J. M. Ripalda, D. Alonso-Álvarez, B. Alén, A. G. Taboada, J. M. García, Y. González, and L. González, "Enhancement of the room temperature luminescence of InAs quantum dots by GaSb capping," *Applied Physics Letters*, vol. 91, no. 1, p. 012111, 2007.

[26] S. L. Chuang, *Physics of Photonics Devices*. Wiley, 2nd ed. ed., 2009.

[27] J. Marzin and G. Bastard, "Calculation of the energy levels in quantum dots," *Solid State Communications*, vol. 92, no. 5, pp. 437–442, 1994.

[28] M. Grundmann, O. Stier, and D. Bimberg, "InAs/GaAs pyramidal quantum dots: Strain distribution, optical phonons, and electronic structure," *Physical Review B*, vol. 52, no. 16, pp. 11969–11981, 1995.

[29] B. Alén, J. Martínez-Pastor, A. García-Cristobal, L. González, and J. M. García, "Optical transitions and excitonic recombination in InAs/InP self-assembled quantum wires," *Applied Physics Letters*, vol. 78, no. 25, p. 4025, 2001.

[30] T. Guillet, R. Grousson, V. Voliotis, X. Wang, and M. Ogura, "Local disorder and optical properties in v-shaped quantum wires: Toward one-dimensional exciton systems," *Physical Review B*, vol. 68, pp. 1–8, July 2003.

[31] D. Oberli, M. Dupertuis, F. Reinhardt, and E. Kapon, "Effect of disorder on the temperature dependence of radiative lifetimes in v-groove quantum wires," *Physical Review B*, vol. 59, no. 4, p. 2910, 1999.

[32] A. Feltrin, V. Savona, J. L. Staehli, and B. Deveaud, "Temperature dependence of the photoluminescence lifetime in disordered quantumwires," *Physica Status Solidi (C)*, vol. 1, pp. 442–445, Feb. 2004.

[33] X. H. Zhang, S. J. Chua, a. M. Yong, H. Y. Yang, S. P. Lau, S. F. Yu, X. W. Sun, L. Miao, M. Tanemura, and S. Tanemura, "Exciton radiative lifetime in zno nanorods fabricated by vapor phase transport method," *Applied Physics Letters*, vol. 90, no. 1, p. 013107, 2007.

[34] D. Alonso-Álvarez, B. Alén, J. M. Ripalda, A. Rivera, A. G. Taboada, J. M. Llorens, Y. González, L. González, and F. Briones, "In-situ accumulated stress measurements: application to strain balanced quantum dots and quantum posts." 2011.

[35] N. Yasuoka, K. Kawaguchi, H. Ebe, T. Akiyama, M. Ekawa, S. Tanaka, K. Morito, A. Uetake, M. Sugawara, and Y. Arakawa, "Demonstration of transverse-magnetic dominant gain in quantum dot semiconductor optical amplifiers," vol. 92, no. 10, p. 101108, 2008.

[36] P. Podemski, G. Sck, K. Ryczko, J. Misiewicz, S. Hein, S. Höfling, A. Forchel, and G. Patriarche, "Columnar quantum dashes for an active region in polarization independent semiconductor optical amplifiers at 1.55μm," vol. 93, no. 17, p. 171910, 2008.

[37] P. Jayavel, H. Tanaka, T. Kita, O. Wada, H. Ebe, M. Sugawara, J. Tatebayashi, Y. Arakawa, Y. Nakata, and T. Akiyama, "Control of optical polarization anisotropy in edge emitting luminescence of InAs/GaAs self-assembled quantum dots," *Applied Physics Letters*, vol. 84, no. 11, p. 1820, 2004.

[38] H. Saito, K. Nishi, S. Sugou, and Y. Sugimoto, "Controlling polarization of quantum-dot surface-emitting lasers by using structurally anisotropic self-assembled quantum dots," vol. 71, no. April, pp. 590–592, 1997.

[39] P. Ridha, L. H. Li, M. Mexis, P. M. Smowton, J. Andrzejewski, G. Sek, J. Misiewicz, E. P. O'Reilly, G. Patriarche, and A. Fiore, "Polarization Properties

of Columnar Quantum Dots: Effects of Aspect Ratio and Compositional Contrast," *IEEE Journal of Quantum Electronics*, vol. 46, pp. 197–204, Feb. 2010.

[40] J. Andrzejewski, G. Sek, E. O'Reilly, A. Fiore, and J. Misiewicz, "Eight-band kp calculations of the composition contrast effect on the linear polarization properties of columnar quantum dots," *Journal of Applied Physics*, vol. 107, no. 7, p. 073509, 2010.

[41] G. Costantini, A. Rastelli, C. Manzano, R. Songmuang, G. Katsaros, O. G. Schmidt, and K. Kern, "Interplay between Thermodynamics and Kinetics in the Capping of InAs/GaAs(001)Quantum Dots," *Physical Review Letters*, no. 96, p. 226106, 2006.

[42] R. Hong-Wen, M. Sugisaki, S. Sugou, K. Nishi, A. Gomyo, and Y. Masumoto, "Lateral composition modulation induced optical anisotropy in InP/GaInP quantum dot system," *Japanese Journal of Applied Physics*, vol. 38, no. 4, pp. 2438–2441, 1999.

[43] G. Sek, "Quantum dashes and quantum rods: Optical properties and application prospects," *Acta Physica Polonica A*, vol. 116, pp. 36–41, 2009.

[44] P. Yu, W. Langbein, K. Leosson, J. Hvam, N. Ledentsov, D. Bimberg, V. Ustinov, A. Egorov, A. Zhukov, A. Tsatsul'nikov, and Y. Musikhin, "Optical anisotropy in vertically coupled quantum dots," *Physical Review B*, vol. 60, pp. 16680–16685, Dec. 1999.

[45] P. Pearah, A. Chen, and A. Moy, "Algainp multiple quantum wire heterostructure lasers prepared by the strain-induced lateral-layer ordering process," *IEEE Journal of Quantum Electronics*, vol. 30, no. 2, pp. 608–618, 1994.

[46] J. M. Millunchick, R. D. Twesten, S. R. Lee, D. M. Follstaedt, E. D. Jones, S. P. Ahrenkiel, Y. Zhang, H. M. Cheong, and a. Mascarenhas, "Spontaneous lateral composition modulation in AlAs/InAs short period superlattices via the growth front," *Journal of Electronic Materials*, vol. 26, no. 9, pp. 1048–1052, 1997.

[47] O. Krebs, D. Rondi, J. Gentner, L. Goldstein, and P. Voisin, "Inversion asymmetry in heterostructures of zinc-blende semiconductors: Interface and external potential versus bulk effects," *Physical Review Letters*, vol. 80, no. 26, pp. 5770–5773, 1998.

[48] L. L. Li, W. Xu, and F. M. Peeters, "Intrinsic optical anisotropy of [001]-grown short-period InAs/GaSb superlattices," *Physical Review B*, vol. 82, p. 235422, Dec 2010.

[49] J. Martin-Regalado, F. Prati, M. San Miguel, and N. Abraham, "Polarization properties of vertical-cavity surface-emitting lasers," *Quantum Electronics, IEEE Journal of*, vol. 33, no. 5, pp. 765–783, 1997.

[50] T. Mukaihara, N. Ohnoki, Y. Hayashi, N. Hatori, F. Koyama, and K. Iga, "Polarization control of vertical-cavity surface emitting lasers using a birefringent metal/dielectric polarizer loaded on top distributed bragg reflector," *Selected Topics in Quantum Electronics, IEEE Journal of*, vol. 1, no. 2, pp. 667–673, 1995.

[51] K. Choquette and R. Leibenguth, "Control of vertical-cavity laser polarization with anisotropic transverse cavity geometries," *Photonics Technology Letters, IEEE*, vol. 6, no. 1, pp. 40–42, 1994.

[52] T. Yoshikawa, H. Kosaka, K. Kurihara, M. Kajita, Y. Sugimoto, and K. Kasahara, "Complete polarization control of 8x8 vertical-cavity surface-emitting laser matrix arrays," vol. 66, no. 8, pp. 908–910, 1995.

[53] H. Saito, K. Nishi, I. Ogura, S. Sugou, and Y. Sugimoto, "Room-temperature lasing operation of a quantum dot vertical cavity surface emitting laser," vol. 69, no. 21, pp. 3140–3142, 1996.

[54] D. L. Huffaker, G. Park, Z. Zou, O. B. Shchekin, and D. G. Deppe, "1.3 μm room-temperature GaAs-based quantum-dot laser," *Applied Physics Letters*, vol. 73, no. 18, p. 2564, 1998.

[55] J. Tatebayashi, Y. Arakawa, N. Hatori, H. Ebe, M. Sugawara, H. Sudo, and A. Kuramata, "InAs/GaAs self-assembled quantum-dot lasers grown by metalorganic chemical vapor deposition—Effects of postgrowth annealing on stacked InAs quantum dots," *Appl. Phys. Lett.*, vol. 85, no. 6, pp. 1024–1026, 2004.

[56] F. Suárez, D. Granados, M. L. Dotor, and J. M. García, "Laser devices with stacked layers of InGaAs/GaAs quantum rings," *Nanotechnology*, vol. 15, no. 4, p. S126, 2004.

Chapter 7

Conclusions - Conclusiones

English version

Along this thesis work we have addressed many topics related with the growth, characterization and modelling of strain balanced QDs and QPs in the InAs/GaAs material system. Some of them were of a fundamental character thus contributing to the better understanding of the physics these structures involve. Others were related with their technological application in light emitting devices, infrared photodetectors and solar cells or for its possible application in memory devices, with the aim of improving their optoelectronic properties.

The main results that we have obtained in this thesis are the following:

- We have used the mechano-optical stress sensor technique to characterize the growth process of InAs/GaAs QDs. From these studies, which extend the work of other authors, we have experimentally observed the migration of In atoms from the WL to the capping and the QDs themselves during its coverage.
- The same technique applied to the study of the growth of QPs has demonstrated also the migration of In from the WL to the QPs but, in this case, enhanced by the partial melting of the sample surface during In deposition.
- We have pioneered the application of the MOSS technique as a tool to evaluate the stress accumulation during the growth of strain balanced

nanostructures, using it to optimize the growth conditions.

- The use of the MOSS technique as strain balance criterion has allowed us to fabricate full strain balanced QDs samples. The study of their properties have led us to the conclusion that the 3D shape of QDs severely affects the formation of the compensating layer and that other parameters apart from reaching a correct compensation (such as the material or the position of the compensating layer) must be taken into account in order to obtain good quality QDs stacks.

- As an outcome of the previous analysis, we have fabricated a sample containing 50 closely stacked, strain balanced QDs layers exhibiting improved characteristics compared with uncompensated samples.

- We have used, for the first time, the strain balanced technique for the fabrication of QPs. The application of this technique has demonstrated the feasibility of reaching QPs heights above 100 nm thus becoming comparable to vertical quantum wires.

- The study of the low temperature exciton extraction and recombination dynamics in QPs has highlighted the importance of the In content in the material quality and the key role that tunnelling plays in the carrier extraction from these nanostructures.

- We have also discussed the importance that the presence of P might have in the polarization properties of QPs and the advantage it could represent for the fabrication of polarization controlled VCSELs and polarization insensitive devices.

The above results pave the way for the development of a good number of research lines that can be exploited in the years to come. Among future work that can be envisaged, we can outline the following:

- The 50 QDs layers sample showed reasonably good optical properties but it was only partly strain balanced and there was plenty of room for improvement in terms of both structural and optoelectronic characteristics. The goal, in this case, would be to exploit the MOSS characterization and the knowledge acquired in the strain balancing of QDs to reach such improvement by enhancing the phosphorus

incorporation in the thin compensating layers and optimizing the sample structure.

The resulting structure we consider that will outperform any previous design and could be implemented with excellent results in quantum dot infrared photodetectors.

- The fabrication of extremely large QPs is one of the most important milestones achieved in this work thanks to the inclusion of phosphorus in the growth sequence. Despite the pioneer work we have done in this area, the optoelectronic properties we have observed suggest that the quality of the material could be improved, aiming to longer decay times in order to exploit them in storage devices. Thus we consider that, after demonstrating the successful fabrication of InAs/GaAsP QPs, an optimization process of the growth parameters and the superlattice structure will lead to the desired improved properties.

  After that work, the optimal structure will show not only the 1D-like character but also exceptionally large carrier storage times that could be tuned with an electric field, thus enabling the fabrication of memory devices with them.

- The use of phosphorus to manipulate polarization properties of QPs we believe will be a real breakthrough in the development of polarization controlled devices. Two lines might open here, one devoted to the application of strain balanced QPs in vertical-cavity surface-emitting lasers in which the giant in-plane polarization anisotropy is the magnitude of interest, and other dedicated to the achievement of polarization insensitive semiconductor optical amplifiers, where the aspect ratio and compositional contrast have a key role.

Versión en español

A lo largo de este trabajo de tésis hemos estudiado numerosos temas relacionados con la fabricación, la caracterización y el modelado de QDs y QPs compensados en tensión en el sistema material InAs/GaAs. Algunos de nuestros resultados tienen un caracter fundamental que esperamos contribuyan a una mejor comprensión de la física subyacente a estas nanoestructruras. Otros están directamente relacionados con su aplicación tecnológica con el objeto de mejorar sus propiedades optoelectrónicas, ya sea en dispositivos emisores de luz, detectores de infrarrojo, células solares o memorias.

Los principales resultados que hemos obtenido a lo largo de este trabajo pueden resumirse en los siguientes:

- Hemos usado la técnica del sensor de tensión mecano-óptico para caracterizar el proceso de fabricación de QDs de InAs/GaAs. En estos estudios, que amplian los trabajos llevados a cabo por otros autores, hemos observado experimentalmente la migración de los átomos de In desde la capa de mojado tanto al recubrimiento como a los propios QDs, proceso asistido por la presencia de fuertes campos de deformación.

- Aplicando la misma técnica al estudio de la fabricación de QPs hemos demostrado esa misma migración de In pero, en este caso, favorecida además por un fundido parcial de la superficie de la muestra que tiene lugar durante el depósito de InAs.

- Hemos sido pioneros en la aplicación de la técnicas MOSS como herramienta para evaluar la acumulación de tensión durante la fabricación de nanoestructuras compensadas en tensión, usando esa técnica, además, para optimizar dichas condicones de compensación.

- La utilización de MOSS como criterio de compensación de tensión ha permitido la fabricación de estructruas de QDs completamente compensadas. El estudio de sus propiedades nos ha llevado a concluir que la forma tridimensional de los QDs afecta severamente a la formación de la capa compesadora y que otros parámetros (como el material o la posción de dicha capa) deben ser tenidos en cuenta a la hora de obtener apilamientos de QDs con buena calidad.

- Como resultado del anterior análisis, hemos fabricado una muestra que contiene 50 capas apiladas de QDs comenensados con unas propie-dades que mejoran extraordinariamente los resultados previos, apoyando las hipótesis realizadas.
- Hemos usado, también de forma pionera, la técnica de compensación de tensión para la fabricación de QPs. La aplicación de esta técnica ha demostrado la posibilidad de fabricar QPs con aturas que exceden los 100 nm, haciéndolos comparables a hilos cuánticos verticales.
- El estudio de los procesos de extracción y recombinación excitónica a baja temperatura ha resaltado la importancia que tiene el contenido de In en los QPs en la calidad optica de la muestra así como el papel protagonista del escape tunel en la extracción de los portadores desde las nanoestructuras.
- Finalmente, hemos discutido la importancia que la presencia de fosforo en la estructura puede tener en sus propiedades de polarización, resaltando la ventaja que su utilización podría representar para el control de la polarización en VCSELs y dispositivos independientes de la polarización.

Estos resultados allanan el camino para el desarrollo de un buen número de diferentes líneas de investigación que podrán ser explotadas en los próximos años. Entre las optiones de trabajo futuro posible que se pueden plantear, nos gustaría resaltar las siguientes:

- La muestra de 50 capas apiladas mostró unas propiedades opticas razonablemente buenas. Sin emabargo, su compensación de tensión era sólo parcial lo que deja bastante marjen para mejorar sus características tanto estructurales como optoelectrónicas. El objetivo, en este caso, sería explotar la técnica MOSS y el conocimiento recientemente adquirido en la compensación de QDs para alcanzar dicha mejora mediante el aumento de la incorporación de P en las delgadas capas compensadoras y el optimizado general de la estructura.

  Creemos que el resultado de esta optimización podría superar cualquier otro diseño previo y podría ser incorporado con excelentes resultados en dispositivos detectores de infrarrojo.

- La fabricación de QPs extremadamente largos es uno de los hitos más importantes alcanzados en este trabajo. Sin embargo, las características optoelectrónicas que obtuvimos no estuvieron a la altura de las espectativas de largos tiempos de vida y almacenamiento de portadores. Dado que el problema ha sido identificado con una degradación del QPs y no con una limitación intrínseca de este tipo de nanoestructuras, y dado que estos eran nuestros primeros trabajos en esta línea de investigación, creemos que la calidad del material puede mejorarse enormemente mediante la optimización de los párametros de fabricación y de la estructura de la superred.

  Tras este trabajo de mejora consideramos que las estructuras óptimas no solo mostrarán el característico comportamiento unidimensional (algo ya alcanzado) sino que además los portadores tendrán el extraordinario tiempo de vida esperado y la posibilidad de modificarlo mediante la aplicación de los correspondientes campos eléctricos. Esto permitiría su aplicación en dispositivos de memoria, tal y como se había planteado.

- El uso de fosforo para manipular las propiedades de polarización de los QPs creemos que puede ser una revolución para el desarrollo de dispositivos con control de polarización. A partir de este punto quedan abiertas dos lineas. Una de ellas estaría dedicada a la aplicación de QPs en VCSELs para explotar su natural y gigantesca anisotropía de polaricación en el plano. La otra estaría dedicada al desarrollo de dispositivos insensibles a la polarización, mediante la mayor flexibilidad que podría ofrecer en la elección del contraste de composición y relación de aspecto de los QPs.

Appendix

Appendix A

Material parameters and universal constants

A.1 Material parameters

In this section we include the values of the material parameters used along this work, from lattice constants to bandgap values. The values for alloys, such as InGaAs, are generally derived using Vegard's law. Namely if an alloy $A_xB_{(1-x)}$ is made of a combination of materials A and B, the value of a certain parameter P for that alloy is approximated by:[1]

$$P_{A_xB_{(1-x)}} = P_A x + P_B(1-x) \tag{A.1}$$

with P_A and P_B the parameters for the binary materials. The exception to this rule are the electronic band structure parameters which have a more complex dependence with the alloy composition that includes a bowing parameter. However, in those cases Nextnano Software Package is used, which takes into account those variables.[2, 3]

All parameters have been taken either from the Ioffe Physico-Technical Institute semiconductor properties database or Vurgaftman *et al.*[4–6]

A.1.1 GaAs

- Lattice constant: $5.65325 + 3.88 \times 10^{-5}(T - 300)$ Å
- Stiffness constants:
  - $C_{11} = 122.1$ GPa
  - $C_{12} = 56.6$ GPa
  - $C_{44} = 60$ GPa
- Energy Gap: $E_g(LT) = 1.519$ eV, $E_g(300K) = 1.42 - 1.435$ eV
- Effective masses:
  - Electrons: $m_e = 0.063m_0$
  - Heavy Holes: $m_{hh} = 0.51m_0$
  - Light Holes: $m_{lh} = 0.082m_0$

A.1.2 InAs

- Lattice constant: $6.0583 + 2.74 \times 10^{-5}(T - 300)$ Å
- Stiffness constants:
  - $C_{11} = 83.3$ GPa
  - $C_{12} = 45.2$ GPa
  - $C_{44} = 39.6$ GPa
- Energy Gap: $E_g(LT) = 0.417$ eV, $E_g(300K) = 0.354$ eV
- Effective masses:
  - Electrons: $m_e = 0.023m_0$
  - Heavy Holes: $m_{hh} = 0.41m_0$
  - Light Holes: $m_{lh} = 0.026m_0$

A.1.3 GaP

- Lattice constant: $5.4505 + 2.92 \times 10^{-5}(T - 300)$ Å
- Stiffness constants:
  - $C_{11} = 140.5$ GPa
  - $C_{12} = 62$ GPa
  - $C_{44} = 70.3$ GPa
- Energy Gap: $E_g(LT) = 2.34$ eV, $E_g(300K) = 2.26$ eV (indirect bandgap)
- Effective masses:
  - Electrons: $m_l = 1.12m_0$ and $m_t = 0.22m_0$ (X-valley)
  - Heavy Holes: $m_{hh} = 0.6m_0$
  - Light Holes: $m_{lh} = 0.089m_0$

A.1.4 InP

- Lattice constant: $5.8697 + 2.79 \times 10^{-5}(T - 300)$ Å
- Stiffness constants:
  - $C_{11} = 101.1$ GPa
  - $C_{12} = 56.1$ GPa
  - $C_{44} = 45.6$ GPa
- Energy Gap: $E_g(LT) = 1.421$ eV, $E_g(300K) = 1.344$ eV
- Effective masses:
  - **Electrons**: $m_e = 0.08m_0$
  - **Heavy Holes**: $m_{hh} = 0.6m_0$
  - **Light Holes**: $m_{lh} = 0.089m_0$

A.2 Universal constants

We finally include the universal constants used along this thesis. Although they can be found in multiple places with higher precision, we have collected here as a quick reference.

- Special numbers:
  - $\pi = 3.14159$
  - $\mathbf{e} = 2.71828$
- Universal constants:
  - **Boltzman constant**: $k = 1.38 \times 10^{-23}$ J/K $= 8.6 \times 10^{-5}$ eV/K
  - **Planck constant**: $h = 6.626 \times 10^{-34}$ Js
  - **Reduced Planck constant**: $\hbar = \frac{h}{2\pi} = 1.055 \times 10^{-34}$ Js
  - **Speed of light**: $c = 3 \times 10^{8}$ m/s
- Fundamental quantities:
  - **Unit charge**: $e = 1.602 \times 10^{-19}$ C
  - **Electron mass**: $m_0 = 9.109 \times 10^{-34}$ Kg

Bibliography

[1] A. R. Denton and N. W. Ashcroft, "Vegard's law," *Phys. Rev. A*, vol. 43, pp. 3161–3164, Mar 1991.

[2] "Nextnano++ Software Package." `http://www.wsi.tum.de/nextnanoplus`, 2011.

[3] S. Birner, S. Hackenbuchner, M. Sabathil, G. Zandler, J. Majewski, T. Andlauer, T. Zibold, R. Morschl, A. Trellakis, and P. Vogl, "Modeling of semiconductor nanostructures with nextnano3," *Acta Physica Polonica Series A*, vol. 110, no. 2, p. 111, 2006.

[4] "Ioffe Physico-Technical Institute semiconductor properties database:." `http://www.ioffe.rssi.ru/SVA/NSM/Semicond/index.html`.

[5] M. Levinshtein, S. Rumyantsev, and M. Shur, *Handbook Series on Semiconductor Parameters*. No. v. 2 in Handbook Series on Semiconductor Parameters, World Scientific, 1997.

[6] I. Vurgaftman, J. Meyer, and L. Ram-Mohan, "Band parameters for III-V compound semiconductors and their alloys," *Journal of applied physics*, vol. 89, no. 11, p. 5815, 2001.

Appendix B

Curriculum vitae

B.1 List of publications

B.1.1 First author

1. **Optical investigation of type II GaSb/GaAs self assembled quantum dots**, D. Alonso-Álvarez, B. Alén, Jorge M. García and J. M. Ripalda, *Applied Physics Letters*, **91**, 263103 (2007).

2. **Carrier recombination effects in strain compensated quantum dot stacks embedded in solar cells**, D. Alonso-Álvarez, A. G. Taboada, J. M. Ripalda, B. Alén, Y. González, L. González, J. M. García, F. Briones, A. Martí, A. Luque, A. M. Sánchez and S. I. Molina, *Applied Physics Letters*, **93**, 123114 (2008).

3. **Strain balanced quantum posts**, D. Alonso-Álvarez, B. Alén, J. M. Ripalda, J. M. Llorens, A. G. Taboada, Y. González, L. González, F. Briones, M. A. Roldán, J. Hernández-Saz, D. Hernández, M. Herrera and S.I.Molina, *Applied Physics Letters*, **98**, 173106 (2011).

4. **Strain balanced epitaxial stacks of quantum dots and quantum posts**, D. Alonso-Álvarez, J. M. Ripalda, B. Alén, J. M. Llorens and F. Briones, *Advanced Materials*, In press (2011).

B.1.2 Co-author

5. **Enhancement of the room temperature luminescence of InAs quantum dots by GaSb capping**, J. M. Ripalda, D. Alonso-Álvarez, B. Alén, A. G. Taboada, Jorge M. García, Y. González and L. González, *Applied Physics Letters*, **91**, 012111 (2007).

6. **Structural changes induced by antimony on InAs/GaAs (001) quantum dots**, A. G. Taboada, A. M. Sánchez, A. M. Beltrán, M. Bozkurt, D. Alonso-Álvarez, B. Alén, A. Rivera, J. M. Ripalda, J.M. Llorens, J. Martín-Sánchez, Y. González, J.M. Ulloa, J. M. García, S. I. Molina, P.M. Koenraad, *Physical Review B*, **82**, 235316 (2010).

B.1.3 Conference Proceedings

7. **Stress compensation by GaP monolayers for stacked InAs/GaAs quantum dots solar cells**, D. Alonso-Álvarez, A. G. Taboada, Y. González, J. M. Ripalda, B. Alén, L. González, J. M. García, F. Briones, A. Martí, A. Luque, A. M. Sánchez and S. I. Molina, *Proceedings 33rd IEEE Photovoltaic Specialist Conference*, San Diego (USA) (11-16 May 2008).

8. **Strain balanced quantum posts for intermediate band solar cells**, D. Alonso-Álvarez, B. Alén, J. M. Ripalda, J. M. Llorens, A. G. Taboada, Y. González, L. González, F. Briones, M. A. Roldán, J. Hernández-Saz, M. Herrera and S.I.Molina, *Proceedings 35th IEEE Photovoltaic Specialist Conference*, Honolulu (USA) (20-25 June 2010).

9. **Strain issues in stress compensated quantum dots for intermediate band solar cells**, D. Alonso-Álvarez, J. M. Ripalda, B. Alén, A. Rivera, A. G. Taboada, J. M. Llorens, Y. González, L. González, F. Briones, *Proceedings 25th European Photovoltaic Solar Energy Conference and Exhibition*, Valencia (Spain) (6-10 September 2010).

10. **Theoretical modelling of quaternary GaInAsSb/GaAs self-assembled quantum dots**, J. M. Llorens, A. G. Taboada, J. M. Ripalda, D. Alonso-Álvarez, B. Alén, J. Martín-Sánchez, J. M. García, Y. González, A. M. Sánchez, A. M. Beltrán, P. L. Galindo and S I Molina, *Journal of Physics: Conference Series. (Quantum Dot 2010)*, **245**, 012081, Nottingham (UK) (26-30 April 2010).

B.1.4 Other publications

11. **Epitaxial quantum dots for sunlight harvesting**, D. Alonso-Álvarez, B. Alén and J. M. Ripalda, *Acta Futura*, **4**, 69 (2011).

B.1.5 Unpublished works

12. **Influence of the buffer layer growth mode on the optical properties of site controlled InAs quantum dots**, J. Herranz, J. Canet-Ferrer, Y. González, B. Alén, G. Muñoz-Matutano, D. Fuster, D. Alonso-Álvarez, J. Martín-Sánchez, P. Alonso-González, L. González, and J. Martínez-Pastor. Submitted to *Nanoscale Research Letters* (2011).

13. **Strain driven migration of In during the growth of InAs/GaAs quantum posts**, D. Alonso-Álvarez, B. Alén, J. M. Ripalda, A. Rivera, A. G. Taboada, J. M. Llorens, Y. González, L. González and F. Briones. To be submitted to *Physical Review Letters*. Available at *arXiv*: `http://arxiv.org/abs/1108.1768`.

14. **In-situ accumulated stress measurements: application to strain balanced quantum dots and quantum posts**, D. Alonso-Álvarez, B. Alén, J. M. Ripalda, A. Rivera, A. G. Taboada, J. M. Llorens, Y. González, L. González and F. Briones. To be submitted to *Physical Review B*. Available at *arXiv*: `http://arxiv.org/abs/1102.4944`.

B.2 Participation in conferences

B.2.1 Oral presentations

1. **Photodetector applications of InAsSb/GaAs self-assembled quantum dots**, D. Alonso-Álvarez, A. G. Taboada, B. Alén, J. M. Ripalda, D Granados and J. M. García, *6ª Conferencia de dispositivos electrónicos (CDE 2007)*, l Escorial, Spain (February 2007).

2. **Compacting InAs/GaAs quantum dots layers by GaP strain compensation for photovoltaic applications**, D. Alonso-Álvarez, A. G. Taboada, Y. González, J. M. Ripalda, B. Alén, L. González, J. M. García, F. Briones, A. Martí, A. Luque, A. M. Sánchez and S. I. Molina, *Workshop on Recent Advances of Low Dimensional Structures and Devices*, Nottingham, United Kingdom (April 2008).

3. **Epitaxial growth of strain balanced semiconductor nanostructures for solar cells**, D. Alonso-Álvarez, J. M. Ripalda, B. Alén, A. Rivera, A. G. Taboada, J. M. Llorens, Y. González, L. González, F. Briones, *Nanoscale devices for enviromental and energy applications (NDEEA10)*, San Sebastian, Spain (26-27 April 2010).

4. **Strain balanced quantum posts for intermediate band solar cells**, D. Alonso-Álvarez, B. Alén, J. M. Ripalda, J. M. Llorens, A. G. Taboada, Y. González, L. González, F. Briones, M. A. Roldán, J. Hernández-Saz, M. Herrera and S.I.Molina, *35th IEEE Photovoltaic Specialist Conference*, Honolulu (USA) (20-25 June 2010).

5. **Strain balanced technique for the growth of very high aspect ratio quantum posts**, D. Alonso-Álvarez, B. Alén, J. M. Ripalda, J. Llorens, A. G. Taboada, Y. González, L. González, F. Briones, M. A. Roldán, J. Hernández-Saz, M. Herrera, and S. I. Molina, *EuroMBE 2011*, L'Alpe d'Huez, France (20-24 Marzo 2011).

B.2.2 Poster presentations

6. **Electro-optical characterization of self-assembled InAs/GaAs Quantum Rings embedded in p-i-n and Schottky diodes**, A.G. Taboada, F. Suárez, D. Granados, D. Alonso-Álvarez, B. Alén, M.L. Dotor J.M. García, T. J. Badcock, D. J. Mowbray and K. M. Groom, *International Conference on the Physics of Semiconductors (ICPS 2006)*, Viena (Austria) (24th-28th July 2006).

7. **Absorption Properties on InAs quantum dots with Ga(As)Sb capping**, D. Alonso-Álvarez, B. Alén, J. M. Ripalda, A. G. Taboada and J. M. García, *Long Wavelength Quantum Dots (LWQD 2007)*, Rennes (France) (July 2007).

8. **Stress compensation by GaP monolayers for stacked InAs/GaAs quantum dots solar cells**, D. Alonso-Álvarez, A. G. Taboada, Y. González, J. M. Ripalda, B. Alén, L. González, J. M. García, F. Briones, A. Martí, A. Luque, A. M. Sánchez and S. I. Molina, *33rd IEEE Photovoltaic Specialist Conference*, San Diego (USA) (11-16 May 2008).

9. **Strain issues in stress compensated quantum dots for intermediate band solar cells**, D. Alonso-Álvarez, J. M. Ripalda, B. Alén, A. Rivera, A. G. Taboada, J. M. Llorens, Y. González, L. González, F. Briones, *25th European Photovoltaic Solar Energy Conference and Exhibition*, Valencia (Spain) (6-10 September 2010).

B.3 Other merits

B.3.1 Short stays abroad

- **Imperial College London**, Experimental Solid State Physics Group

  - June-August 2009

  - Title: "Study of intraband optical absorption properties of quantum dots for its application in intermediate band solar cells"

  - Supervisor: N. Ekins-Daukes

B.3.2 Courses

- **Installer of Solar Energy Systems**
  - Centro de Estudios CEAC S.L.
  - 650 hours
  - September 2007 - September 2010